



## AN ABSTRACT OF THE DISSERTATION OF

Geneva Laurita-Plankis for the degree of Doctor of Philosophy in Chemistry presented on December 8, 2014.

Title: Investigation of the Structural Influence on the Properties of Functional Inorganic Oxides

Abstract approved:

---

Munirpallam A. Subramanian

While properties are extremely important from an application point of view, it is crucial to have a detailed understanding of the underlying structural influence. Once a concrete correlation between the structure and the observed property is established, rational design of novel materials with optimized properties can be realized. These optimized materials lead to advancements in technology in a variety of applications, including new building materials, faster electronic devices, and more efficient catalysts. This dissertation examines the structural influence on the observed properties in a series of metal oxide materials for electronic and energy applications.

A series of pyrochlores  $\text{Ag}_{1-nx}\text{M}^n_x\text{SbO}_3$  ( $\text{M} = \text{Na}^+, \text{K}^+, \text{Tl}^+, \text{and Cd}^{2+}$ ) has been studied to evaluate the structural influence on the samples' photocatalytic activity. A complete solid solution between the anion-deficient pyrochlore  $\text{Ag}_2\text{Sb}_2\text{O}_6$  and the ideal pyrochlore  $\text{Cd}_2\text{Sb}_2\text{O}_7$  has been synthesized through the standard solid state ceramic method. Each composition has been characterized by various different techniques, including powder X-ray diffraction, optical spectroscopy, electron paramagnetic resonance and  $^{121}\text{Sb}$  Mössbauer spectroscopy. Computational methods based on density functional theory complement this investigation.

Photocatalytic activity has been studied, and transport properties have been measured on pellets densified by spark plasma sintering. The analysis of the data collected from these various techniques enables a comprehensive characterization of the complete solid solution and revealed an anomalous behavior in the Cd-rich end of the solid solution, which has been proposed to arise from a possible radical  $O^-$  species in small concentrations. Polycrystalline samples of the pyrochlore series  $Ag_{1-nx}M^n_xSbO_3$  ( $M = Na^+, K^+$  and  $Tl^{+/3+}$ ) have been structurally analyzed through total scattering techniques and evaluated for photocatalytic activity. The upper limits of  $x$  obtained are 0.08 for Na, 0.16 for K, and 0.17 for Tl. The  $Ag^+$  cation occupies a site with inversion symmetry on a 3-fold axis. When the smaller  $Na^+$  cation substitutes for  $Ag^+$ , it is displaced by about 0.6 Å perpendicular to the 3-fold axis to achieve shorter Na-O bond distances. When the larger  $Tl^+$  cation substitutes for  $Ag^+$ , it is displaced by about 1.14 Å along the 3-fold axis and achieves an environment typical of a lone pair cation. Some of the  $Tl^{3+}$  from the precursor remains unreduced, leading to a formula of  $Ag_{0.77}Tl^{+}_{0.13}Tl^{3+}_{0.04}SbO_{3.04}$ . The position of the  $K^+$  dopant was effectively modeled assuming that  $K^+$  occupied the same site as  $Ag^+$ . The expansion of the lattice caused by substitution of the larger  $K^+$  and  $Tl^+$  cations results in longer Ag-O bond lengths, which would reduce the overlap of the Ag  $4d$  and O  $2p$  orbitals that compose the valence band maximum. Substitution of the smaller  $Na^+$  results in a decrease in the Ag-O bond distance, thus increasing the overlap of the Ag  $4d$  and O  $2p$  orbitals. An increase in the photocatalytic activity has been observed for the nominal composition  $Ag_{0.8}Na_{0.2}SbO_3$  made through solid state synthesis, and this is attributed to both the slight decrease in the band gap and the increase in pore dimensions compared to the parent compound  $AgSbO_3$ .

The structural transitions in  $Cd_2Nb_2O_{7-x}S_x$  ( $x = 0, 0.25, 0.5,$  and  $0.7$ ) have been studied to determine the origin of ferroelectricity in pyrochlore oxides. For  $x = 0, 0.25,$  and  $0.5$  peak

splitting indicative of a transition to orthorhombic symmetry is observed below the transition temperature. In the  $x = 0.7$  sample, the evolution of new peaks suggest a cubic space group is retained below the phase transition accompanied by a loss of the face-centering symmetry. The observed lowering of symmetry may be responsible for the transition into a ferroelectric phase, and may be driven by a strong displacement of both the Nb and Cd from the high- to low-symmetry structures. The S content may drive the stability of different ferroelectric phases, as no trend was observed with increasing content in the ferroelectric Curie temperatures of the samples.

The structure of the hollandites  $A_xRu_4O_8$  ( $A = K^+, Rb^+$ ) has been studied through total scattering techniques upon cation exchange with  $Na^+$  on the A-site to evaluate the effect on the quasi-one dimensional (Q1D) nature of these materials. It is observed that the A-site of the hollandite structure is not fully occupied when  $A = K^+, Rb^+$ , and full A-site occupancy is achieved after ion exchange with  $NaNO_3$ . All samples exhibit Pauli paramagnetism, and this is primarily due to a large low temperature range of metallic conduction. The double chains of edge-shared  $RuO_6$  octahedra and corner shared double chains found in the channel of the hollandite structure promotes two conduction mechanisms:  $\rho_{\parallel}$  (intra-chain metallic) and  $\rho_{\perp}$  (inter-chain hopping). The coexistence of  $\rho_{\parallel}$  and  $\rho_{\perp}$  gives rise to metallic conductivity below  $T_{max}$  (suppressed hopping at lower temperature) and semiconductivity above  $T_{max}$  (intra-chain mean free path becomes smaller than the inter-chain hopping distance), exhibiting the Q1D conduction at lower temperatures. The inter-chain distance is larger in the Rb-containing samples, and consequently the region dominated by intra-chain metallic conduction increases, along with an increase in  $T_{max}$ .

©Copyright by Geneva Laurita-Plankis  
December 8, 2014  
All Rights Reserved

Investigation of the Structural Influence on the Properties of Functional Inorganic  
Oxides

by  
Geneva Laurita-Plankis

A DISSERTATION

submitted to

Oregon State University

in partial fulfillment of  
the requirements for the  
degree of

Doctor of Philosophy

Presented December 8, 2014  
Commencement June 2015

Doctor of Philosophy dissertation of Geneva Laurita-Plankis presented on December 8, 2014

APPROVED:

---

Major Professor, representing Chemistry

---

Chair of the Department of Chemistry

---

Dean of the Graduate School

I understand that my dissertation will become part of the permanent collection of Oregon State University libraries. My signature below authorizes release of my dissertation to any reader upon request.

---

Geneva Laurita-Plankis, Author

## ACKNOWLEDGEMENTS

The past four and a half years has been an incredible journey, and I know that it would have been impossible without the support of many amazing individuals. I hope to be able to express my sincerest gratitude to everyone who contributed to this monumental task.

To begin, I would like to acknowledge and thank Dr. Mas Subramanian, who has served as an advisor and mentor to me since my undergraduate research internship at Oregon State University. The resources provided inside his lab have allowed me to improve and grow confident in my skills as a solid state chemist. With Dr. Subramanian's unwavering support, I have had the opportunity to explore new areas of research and tackle new techniques, and never once did he discourage me to pursue something I was interested in. Dr. Subramanian has provided multiple avenues for my professional development: involvement in the Center for Sustainable Materials Chemistry (CSMC), participation in summer workshops, and attendance to multiple prestigious solid state conferences. Through these experiences I have been able to build and expand an invaluable professional network for my future endeavors.

During my time here I had the incredible honor of working with Dr. Arthur Sleight on several projects. Not only did he serve on my committee, but was willing to meet with me on numerous occasions to discuss my research. During these meeting I learned an invaluable amount of information about structural analysis, and his insight was crucial for helping me learn and understand PDF analysis. I would additionally like to thank Dr. Michael Lerner, Dr. Janet Tate, and Dr. Ronald Adams for their time and commitment as my committee members through this process. I have greatly benefited from many insightful discussions on their various areas of expertise, and I know I am a better scientist for interacting with them.

I would like to acknowledge and thank the CSMC not only for the financial support for my research, but for the countless opportunities for professional and personal development. In particular, I would like to thank Bettye Maddux and Andy Bedingfield for organizing a plethora of useful and interesting workshops and outreach opportunities. Being a part of such a large yet tight-knit organization was an irreplaceable experience, and I know the connections I made through my involvement will be of paramount importance in my future.

I am beyond grateful to all of the past and present students in Dr. Subramanian's group. Although it has changed throughout the years, there was always a sense of support

and togetherness as we went through our own separate journeys. I would especially like to thank the other two members of the “Maskeeters”: Dr. Whitney Schmidt and Dr. Rosa Grajczyk. We have been together from the beginning, and even though they graduated before me, they have both continued to be a constant support system in the conclusion of my graduate work. I would like to specifically acknowledge Dr. Romain Berthelot, Dr. Sean Muir, Dr. James Eilertsen, and Dr. Jun Li. I cannot express how pivotal these individuals were in my graduate studies, and my knowledge of solid state chemistry would be incomplete without the numerous research (and life) discussions held between us. I would like to thank Dr. Andrew Smith, Dr. Alvin Gatimu, Dr. Peng Jiang, Dr. June Siritanon, and Dr. Krishnendu Biswas for training me in various aspects of lab. I would also like to thank my undergraduate mentee Matt Stolt for not only being an excellent researcher, but for being a lot of fun to work with in the lab. Additionally, I would like to thank all of my past and present office mates who I have not yet mentioned: Elena Medina, Song Yi Kim, Joseph Tang, and Joshua Flynn. They provided an immeasurable amount of support and comradery through all the experiences that graduate school had to offer.

Throughout my time here I have had the pleasure to make connections and friends throughout the department and community. I would like to specifically thank those who helped me review various parts of this massive document: Dr. Whitney Schmidt, Joseph Tang, Joshua Flynn, Ryan McQuade, Wesley Surta, Shawn Decker, Dr. Romain Berthelot, Dr. Jun Li, Dr. Rosa Grajczyk, and Dr. Benjamin Hanken. I would additionally like to thank Dylan Fast for great discussions and memorable trips to Argonne National Lab, and Lauren Fullmer for being a wonderful friend throughout this past year.

I would like to thank the incredible staff of instrument scientists at various national laboratories for their patience and assistance during my user visits: Dr. Kate Page (currently and Oak Ridge National Laboratory) and Dr. Joan Siewenie at Los Alamos National Laboratory, Dr. Jörg Neuefiend and Dr. Mikhail Feygenson at Oak Ridge National Laboratory, and Kevin Beyer and Dr. Karena Chapman at Argonne National Laboratory.

I want to express my sincerest gratitude to my high school chemistry teacher Mr. Jeremy Johnson. He sparked my interest in chemistry (and Weezer), and without him, I would most certainly not be a chemist. I would also like to acknowledge and thank my undergraduate advisor Dr. Robin Macaluso. She inspired me to pursue graduate education in

solid state chemistry and has continued to serve as a mentor and friend throughout my studies.

Last but certainly not least I would like to thank my family for being a solid foundation and support system throughout my life. Mom, Dad, and Emily: you have provided daily advice and have been only a phone call away whenever I needed to talk. The support from my extended family has provided the inspiration to complete each task in front of me. Finally and most importantly I would like to thank my husband, Peter. There is absolutely no way this would have been possible without your love and support. You have been there for me every single day and have shown your willingness to do what it takes to help me achieve my dreams.

## CONTRIBUTION OF AUTHORS

Chapter 3: Dr. Mas Subramanian contributed in the preparation and review of the two manuscripts on which this chapter is primarily based; Laurita, G., Vielma, J., Berthelot, R., Largeteau, A., Winter, F., Pöttgen, R., Schneider, G., and Subramanian, M. A. From  $\text{Ag}_2\text{Sb}_2\text{O}_6$  to  $\text{Cd}_2\text{Sb}_2\text{O}_7$ : investigations on an anion-deficient to ideal pyrochlore solid solution. *Journal of Solid State Chemistry* **2013**, 210, 65 – 73 and Laurita, G., Page, K., Sleight, A. W., and Subramanian, M. A. Investigation of the anion-deficient pyrochlore  $\text{AgSbO}_3$  through total scattering techniques. *Inorganic Chemistry* **2013**, 52, 11530-11537. For the first manuscript, Dr. Jason Vielma and Dr. Guenter Schneider contributed computational studies and manuscript review, Dr. Romain Berthelot assisted in TGA studies and manuscript review, Dr. Alain Largeteau performed spark plasma sintering on samples and contributed to manuscript review, Florian Winter and Dr. Rainer Pöttgen collected Mössbauer Spectroscopy measurements and contributed manuscript review. For the second manuscript, Dr. Kate Page assisted in the data analysis and manuscript review and Dr. Arthur Sleight contributed to the preparation and review of the manuscript.

Chapter 4: Dr. Mas Subramanian and Dr. Arthur Sleight contributed in discussions on the manuscript in preparation on which this chapter is primarily based. Dr. Robin Macaluso assisted in the data collection and data analysis, and Dr. Jun Li provided many helpful discussions in regard to the data analysis and manuscript layout.

Chapter 5: Dr. Mas Subramanian and Dr. Arthur Sleight contributed in discussions on the manuscript in preparation on which this chapter is primarily based. Matt Stolt and Italo

Coutinho assisted in sample synthesis and preparation for property measurements. Dr. Rosa Grajczyk performed and analyzed magnetic susceptibility measurements and contributed to manuscript review.

Appendix 1: Dr. Michelle Dolgos served as the Primary Investigator for this project. Hans Chiang and Dr. John Wager provided amorphous samples for analysis, and T. J. Mustard, Dr. Benjamin Hanken, and Dr. Paul Cheong contributed to computational studies.

Appendix 2: Dr. Jaeseok Heo and Dr. Douglas Keszler drafted the manuscript on which this Appendix is based on: Heo, J., Laurita, G., Muir, S., Subramanian, M. A., and Keszler, D. A. Enhanced thermoelectric performance of synthetic tetrahedrites. *Chemistry of Materials* **2014**, 26, 2047 – 2051. Dr. Jaeseok Heo synthesized the samples and completed optical and specific heat measurements on the samples, Dr. Sean Muir performed magnetic susceptibility measurements, and Dr. Mas Subramanian contributed to manuscript preparation and review.

## TABLE OF CONTENTS

	<u>Page</u>
1 Introduction to Structure-Property Relationships in a Material .....	1
1.1 Scope of Dissertation .....	1
1.2 The Structure of Crystalline Materials .....	1
1.2.1 Describing a Structure through Close Packing .....	1
1.2.2 Describing a Structure through Symmetry Operations.....	6
1.3 Structure Types in this Dissertation .....	9
1.3.1 The Pyrochlore Structure .....	9
1.3.2 The Hollandite Structure .....	13
1.3.1 The YbFe <sub>2</sub> O <sub>4</sub> Structure.....	15
1.4 References.....	18
2 Fundamentals of Solid State Chemistry: Synthesis, Material Properties, and Characterization methods.....	20
2.1 Sample Synthesis.....	20
2.1.1 Standard Solid State Synthesis.....	20
2.1.2 Molten Salt Ion Exchange.....	21
2.2 Structural Characterization .....	22
2.2.1 Scattering in Materials .....	22
2.2.2 Powder Diffraction .....	26
2.2.2.1 X-ray Diffraction .....	26
2.2.2.2 Neutron Diffraction.....	30

## TABLE OF CONTENTS (Continued)

	<u>Page</u>
2.2.3 Total Scattering Techniques.....	31
2.2.4 Structural Modeling from Scattering Data.....	34
2.2.4.1 Average Structure Modeling.....	34
2.2.4.2 Local Structure Analysis: Small and Large Box Modeling.....	36
2.2.5 Characterization of Amorphous Materials.....	38
2.3 Thermogravimetric Analysis of Materials.....	41
2.4 Transport Properties.....	42
2.4.1 Electronic Properties of Materials.....	42
2.4.2 Electronic Characterization Techniques.....	45
2.4.3 Thermal Transport Properties.....	48
2.5 Magnetic Properties.....	50
2.6 Optical Properties.....	52
2.7 Sample Morphology.....	54
2.7.1 Grain Size from PXRD.....	54
2.7.2 Scanning Electron Microscopy.....	55
2.7.3 BET Surface Area Analysis.....	57
2.8 Photocatalytic Activity.....	59
2.9 Computational Methods.....	63
2.10 Other Spectroscopic Techniques in this Dissertation.....	64
2.10.1 Inductively Coupled Plasma-Atomic Emission Spectroscopy.....	64
2.10.2 Electron Paramagnetic Resonance.....	65

## TABLE OF CONTENTS (Continued)

	<u>Page</u>
2.10.3 Mössbauer Spectroscopy .....	65
3 Substitutions into the Anion-Deficient Pyrochlore $\text{Ag}_2\text{Sb}_2\text{O}_6$ .....	69
3.1 Introduction to $\text{Ag}_2\text{Sb}_2\text{O}_6$ .....	71
3.2 Investigation of the Solid Solution between $\text{Ag}_2\text{Sb}_2\text{O}_6$ and $\text{Cd}_2\text{Sb}_2\text{O}_7$ .....	72
3.2.1 Motivation for the Solid Solution .....	72
3.2.2 Structural Characterization .....	73
3.2.3 Thermogravimetric Analysis .....	74
3.2.4 Optical Characterization .....	77
3.2.5 Computational Results .....	78
3.2.6 Transport Properties .....	81
3.2.7 Photocatalytic Activity .....	82
3.2.8 Investigation of the Cadmium-Rich End of the Solid Solution .....	84
3.2.9 Conclusions .....	88
3.3 Characterization of $\text{Ag}_{1-x}\text{M}^n_x\text{SbO}_{3+x[(n-1)/2]}$ ( $\text{M} = \text{Na}^+, \text{K}^+, \text{Tl}^{+/3+}$ ) .....	89
3.3.1 Motivation for Substitution .....	89
3.3.2 Structural Analysis .....	90
3.3.3 Sample Morphology .....	105
3.3.4 Optical Characterization .....	107
3.3.5 Photocatalytic Activity .....	107
3.3.6 Discussion .....	108
3.3.7 Conclusions .....	110

## TABLE OF CONTENTS (Continued)

	<u>Page</u>
3.4 Chapter Conclusions .....	111
3.5 Materials and Methods .....	111
3.6 References .....	115
4 Determination of the low-temperature structural phases of the ferroelectric pyrochlore $\text{Cd}_2\text{Nb}_2\text{O}_{7-x}\text{S}_x$ .....	
4.1 Introduction to $\text{Cd}_2\text{Nb}_2\text{O}_{7-x}\text{S}_x$ .....	121
4.1.1 Introduction to Ferroelectricity.....	121
4.1.2 Introduction to the Ferroelectric Pyrochlore Series $\text{Cd}_2\text{Nb}_2\text{O}_{7-x}\text{S}_x$ .....	122
4.2 Structural Characterization of $\text{Cd}_2\text{Nb}_2\text{O}_{7-x}\text{S}_x$ at Room Temperature .....	124
4.3 Structural Characterization of $\text{Cd}_2\text{Nb}_2\text{O}_{7-x}\text{S}_x$ at 100 K .....	128
4.3.1 Qualitative Analysis of $\text{Cd}_2\text{Nb}_2\text{O}_{7-x}\text{S}_x$ at 100 K .....	128
4.3.2 Structural Characterization of $\text{Cd}_2\text{Nb}_2\text{O}_7$ at 100 K.....	130
4.3.3 Structural Characterization of $\text{Cd}_2\text{Nb}_2\text{O}_{7-x}\text{S}_x$ ( $x = 0.25, 0.7$ ) at 100 K .....	134
4.5 Structural Characterization of $\text{Cd}_2\text{Nb}_2\text{O}_{7-x}\text{S}_x$ at 100 K .....	138
4.6 Conclusions .....	139
4.7 Materials and Methods .....	139
4.8 References .....	139
5 Probing the local structure of Na-exchanged hollandites using total scattering techniques: $\text{A}_x\text{Ru}_4\text{O}_8$ ( $A = \text{K}, \text{Rb}$ ) .....	
5.1 Introduction to Quasi-one Dimensional Structures .....	144
5.2 Structural Analysis .....	145

## TABLE OF CONTENTS (Continued)

	<u>Page</u>
5.3 Physical Property Characterization .....	151
5.3.1 Electrical Characterization.....	151
5.3.2 Magnetic Characterization .....	155
5.4 Conclusions .....	156
5.5 Materials and Methods .....	156
5.6 References .....	158
General Conclusions and Future work.....	160
Bibliography .....	162
Appendix A Investigation of the Local Cation Environments in Thin Films of Amorphous IGZO.....	167
A.1 Introduction to Amorphous IGZO .....	167
A.2 Structural Characterization .....	168
A.2.1 Qualitative Analysis of the Experimental PDFs .....	168
A.2.2 Reverse Monte Carlo Simulations.....	172
A.3 Discussion and Future Directions .....	176
A.4 Conclusions .....	177
A.5 Materials and Methods .....	177
A.6 References .....	179
Appendix B Thermoelectric Characterization of Tetrahedrites $\text{Cu}_{10}\text{TM}_2\text{Sb}_4\text{S}_{13}$ (TM = Mn, Fe, Co, Ni, Zn).....	180

## TABLE OF CONTENTS (Continued)

	<u>Page</u>
B.1 Introduction .....	180
B.1.1 Introduction to Thermoelectricity .....	180
B.1.2 The Tetrahedrite Structure .....	181
B.2 Results and Discussion .....	182
B.2.1 Electrical Properties .....	182
B.2.2 Thermal Conductivity .....	184
B.2.3 Figures of Merit .....	186
B.3 Conclusion .....	189
B.4 Methods and Materials .....	189
B.5 References .....	190

## LIST OF FIGURES

<u>Figure</u>	<u>Page</u>
1.1 Layering scheme of “ABCABC...” for cubic close packed spheres (top) and “ABAB...” for hexagonal close packed spheres (bottom) .....	2
1.2 Left: Location of an octahedral hole (shown by the black dot) between two layers of close packed atoms (top) and an expanded view of the octahedral arrangement of the atoms around the void (bottom). Right: Location of a tetrahedral hole (shown by the black dot) between two layers of close packed atoms (top) and an expanded view of the tetrahedral arrangement of the atoms around the void (bottom).....	3
1.3 a) The rocksalt structure NaCl, described as a CCP array of anions (Cl <sup>-</sup> ) with all octahedral holes filled by Na <sup>+</sup> . b) The spinel structure MgAl <sub>2</sub> O <sub>4</sub> , described as a CCP array of O <sup>2-</sup> with ½ of the octahedral holes occupied by Al <sup>3+</sup> and ¼ of the tetrahedral holes filled with Mg <sup>2+</sup> .....	5
1.4 Extended crystalline lattice of NaCl with unit cell outlined, left, and enlarged unit cell of NaCl, right .....	7
1.5 The pyrochlore structure A <sub>2</sub> M <sub>2</sub> O <sub>6</sub> O'. The “A” cations are found in the black 16 <i>d</i> site, the “M” cations in the blue 16 <i>c</i> site, and the oxygen, O and O', found in the green 48 <i>f</i> and red 8 <i>b</i> , respectively .....	9
1.6 The pyrochlore structure (c) as derived from the fluorite structure (a) by removal of one of the oxygen atoms (b) in a 2 x 2 x 2 fluorite supercell .....	10
1.7 The pyrochlore structure described as two interpenetrating networks of corner-shared MO <sub>6</sub> octahedra and A <sub>2</sub> O' chains .....	11
1.8 Interpenetrating networks of A <sub>4</sub> (a) and M <sub>4</sub> (b) tetrahedra around O atoms to describe the pyrochlore structure (c).....	12
1.9 The ideal pyrochlore A <sub>2</sub> M <sub>2</sub> O <sub>6</sub> O' with all sites filled (left), the anion-deficient pyrochlore A <sub>2</sub> M <sub>2</sub> O <sub>6</sub> with vacant 8 <i>b</i> site (middle), and the defect pyrochlore AM <sub>2</sub> O <sub>6</sub> with vacant 16 <i>d</i> site (right) .....	13
1.10 a) The 1 x 1 x 1 x 1 channel structure of rutile, formed by corner-shared chains of edge-shared octahedra; b) the 2 x 2 x 2 channel found in the hollandite structure composed of two chains of edge-shared octahedral linked together through corner-sharing .....	14

## LIST OF FIGURES (Continued)

<u>Figure</u>	<u>Page</u>
1.11 The hollandite structure $A_xM_4O_8$ , shown here with $x = 1$ . “A” atoms are shown in purple, “M” in charcoal, and “O” in red .....	15
1.12 The two offset HCP layers in the hexagonal $ABO_3$ structure (a) with “A” cations, blue, in octahedral sites and “B” cations, green, in trigonal bipyramidal sites (b).....	15
1.13 a) The hexagonal $AMO_3$ structure described as alternating layers of edge-shared distorted $AO_6$ octahedra (shown in green) and corner-shared $MO_5$ trigonal bipyramids (shown in purple). In this structure, the “M” cation sits directly in the middle of the trigonal bipyramidal site. b) The hexagonal $AM_2O_4$ structure with alternating layers of edge-shared $AO_6$ octahedra (shown in green) and edge-shared double layers of $MO_5$ trigonal bipyramids (shown in purple). This double layer of trigonal bipyramids results in an off-center shift of the M cation .....	16
1.14 A unit cell of crystalline $InGaZnO_4$ with space group symmetry $R\bar{3}m$ consists of alternating layers of edge-shared $InO_6$ octahedra and edge-shared $Ga/ZnO_5$ trigonal bipyramids. The Ga and Zn atoms are disordered in the trigonal bipyramid sites .....	17
2.1 Reaction interface of two particles of starting reagents. Figure adapted from [1] .....	21
2.2 Pictorial representation of an idealized topotactic ion exchange process.....	22
2.3 Schematic of the derivation of $Q$ from an elastic scattering event ( $k_i = k_f$ ).....	23
2.4 Interaction of an electron through the repulsive force of an atom’s electrons (a), X-ray through electromagnetic interaction with an electron (b), and neutrons through dipole interactions with the nucleus and magnetic interactions with unpaired electrons (c and d, respectively) .....	24
2.5 Normalized scattering cross sections of X-rays (black) and neutrons (red) as a function of atomic number .....	25
2.6 Schematic Diagram of an X-ray tube .....	27
2.7 Basic schematic diagram of a Rigaku Miniflex-II diffractometer .....	28
2.8 Schematic of Bragg’s Law in relation to an incident and diffracted beam from a lattice.....	28

## LIST OF FIGURES (Continued)

<u>Figure</u>	<u>Page</u>
2.9 Diffraction peaks generated from the (200) lattice plane (blue) and the (220) lattice plane (green) in NaCl .....	28
2.10 Examples of a) an average structure that is representative of the local structure, b) long –range correlated local displacements that are shown as a static displacement in the average structure, and c) disordered local displacements with some local correlations represented as enlarged thermal parameters in the average structure. ....	32
2.11 The atomic pair distribution function of graphite. Each ring corresponds to a C-C correlation in the PDF .....	33
2.12 Illustration of the structure (top boxes) and the generated PDF (blue dotted line) against the experimental data (solid black line) through the RMC modeling process .....	38
2.13 Types of materials based on various degrees of disorder .....	39
2.14 a) Structure of crystalline SiO <sub>2</sub> $\alpha$ -quartz (top) and the calculated diffraction pattern (bottom); b) the structure of randomized $\alpha$ -quartz to simulate an amorphous SiO <sub>2</sub> glass (top) and the resulting calculated diffraction pattern (bottom).....	40
2.15 TGA plot of mass vs. temperature reveals the various decomposition steps in Calcium Oxalate .....	42
2.16 Energy vs Density of States (DOS) for a metal (a), semiconductor (b), and insulator (c) .....	43
2.17 Location of donor states in a <i>p</i> -type semiconductor (a) and acceptor states in an <i>n</i> -type semiconductor (b).....	45
2.18 Attachment points for electrodes on a sintered bar for four-probe resistivity measurements.....	46
2.19 Illustration of the simultaneous measurement of four-probe resistivity and Seebeck coefficient in a sintered bar sample .....	47
2.20 Parallel capacitor plate setup for a dielectric measurement .....	48
2.21 Components of a Laser Flash instrument for thermal diffusivity measurements .....	49

## LIST OF FIGURES (Continued)

<u>Figure</u>	<u>Page</u>
2.22 Magnetic ordering of unpaired electrons in a material: a) paramagnetic, b) ferromagnetic, c) antiferromagnetic, and d) ferrimagnetic .....	50
2.23 Illustration of the Pauli paramagnetic interaction of electrons in a metal to an external magnetic field. In the absence of a magnetic field, no net magnetic moment is observed (a). Upon application of a magnetic field, the electrons will shift energy based on spin (b) and a small net magnetic moment is observed (c) .....	52
2.24 Specular and diffuse reflection of an incident beam of light from a packed powder surface .....	53
2.25 The full-width-half-max (FWHM) of a diffraction peak .....	55
2.26 Schematic diagram of the components of a scanning electron microscope....	57
2.27 Idealized adsorption isotherm for surface area extraction from BET analysis .....	59
2.28 Photocatalytic process in a semiconducting photocatalyst particle .....	60
2.29 Diagram of the constructed reactor setup for photocatalysis evaluation .....	61
2.30 a) Data for the photolysis correction applied to all samples; b) example of data for the adsorption correction applied to samples of $Ag_{1-x}M^n_xSbO_{3+x}[(n-1)/2]$ (M = Na, K and Tl) in Chapter 3 .....	62
3.1 PXRD data collected on the nominal series $(Ag_{1-x}Cd_x)_2Sb_2O_{6+x}$ (left). Lattice parameter evolution of the series (right) reveals a relatively unchanging unit cell .....	73
3.2 Thermogravimetric analysis of the nominal series $(Ag_{1-x})_2(Cd_x)_2Sb_2O_{6+x}$ indicating the weight gain as the samples are formed.....	75
3.3 A summary of the theoretical and experimental overall mass gained during formation as a function of Cd content in the series. A linear gain of O as Cd content increase is assumed for this model, with a deviation from linearity in the Cd-rich end. Systematic instrumental error in the mass gain has been removed from the theoretical models to facilitate comparison .....	76

## LIST OF FIGURES (Continued)

<u>Figure</u>	<u>Page</u>
3.4 Images of the powders (left) reveal a change in color as the nominal series $(\text{Ag}_{1-x})_2(\text{Cd}_x)_2\text{Sb}_2\text{O}_{6+x}$ progresses. Diffuse reflectance data transformed with the Kubelka-Munk equation (right) reveal a changing band gap accompanying the color change.....	77
3.5 Band structure diagrams using DFT with HSE06 of the defect pyrochlore $\text{Ag}_2\text{Sb}_2\text{O}_6$ and the ideal pyrochlore $\text{Cd}_2\text{Sb}_2\text{O}_7$ . Both diagrams are shifted down such that 0 eV coincides with the valence band maximum (dotted line) .....	79
3.6 Partial and Total Electronic Density of States (DOS) using DFT with HSE06 for $\text{Ag}_2\text{Sb}_2\text{O}_6$ (a) and $\text{Cd}_2\text{Sb}_2\text{O}_7$ (b). The total DOS is in black, the s-states in red, the p-states in green, and the d-states in blue. Top plot is the total DOS, and the bottom three are the partial DOS of each atom. Each partial DOS shows how much the y-axis is scaled. DOS are shifted to set the Fermi energy to 0 eV .....	80
3.7 Partial DOS for the two types of oxygen atoms in $\text{Cd}_2\text{Sb}_2\text{O}_7$ . It can be seen that the band closest to the Fermi level originates from the oxygen in the 8b site.....	80
3.8 High temperature resistivity and Seebeck data collected on the samples with a density 70% or greater of that of the theoretical values.....	82
3.9 Degradation of methylene blue over a two-hour irradiation period, monitored by the normalized maximum absorbance of the dye at various time intervals .....	83
3.10 EPR spectra for $\text{Ag}_{0.5}\text{Cd}_{1.5}\text{Sb}_2\text{O}_{6+\delta}$ (red) and $\text{Ag}_{0.2}\text{Cd}_{1.8}\text{Sb}_2\text{O}_{6+\delta}$ (blue). Spectra indicate a small radical species is present, but is not indicative of $\text{Ag}^{2+}$ .....	85
3.11 Experimental and simulated $^{121}\text{Sb}$ Mössbauer spectra of the $\text{Sb}^{5+}$ pyrochlores $\text{Ag}_2\text{Sb}_2\text{O}_6$ , $\text{AgCdSb}_2\text{O}_{6+\delta}$ , $\text{Ag}_{0.4}\text{Cd}_{1.6}\text{Sb}_2\text{O}_{6+\delta}$ , and $\text{Cd}_2\text{Sb}_2\text{O}_7$ at 78 K .....	86
3.12 Lattice parameter evolution determined from neutron diffraction Rietveld analysis as cations Na, K, and Tl are doped into $\text{AgSbO}_3$ . Error bars are contained within the points.....	90

## LIST OF FIGURES (Continued)

<u>Figure</u>	<u>Page</u>
3.13 Average Rietveld (top) and local PDF (bottom) structure fits to the neutron data for the parent compound $\text{AgSbO}_3$ . Refinements indicate the atomic displacement of the $\text{Ag}^+$ cation is parallel to the three-fold rotation axis of the structure (top, inset).....	94
3.14 Partial atom-atom contributions to the PDF function in the range of 1.7-5 Å. Peaks within the PDF can be assigned to various atom-atom correlations in the anion-deficient pyrochlore $\text{AgSbO}_3$ . The black curve represents the total PDF, while colored curves correspond to specific partial contributions ...	95
3.15 Schematic representation of the available sites for the A cation within the $\text{MO}_6$ channel structure. The ideal position for the A cation is $16d$ . Red atoms at $8b$ indicate regular pyrochlore locations for the $\text{O}'$ positions. Arrows along the 3-fold rotation axis indicate the displacement direction of the $32e$ site, shown in navy.....	96
3.16 Rietveld refinement fits for nominal $\text{Ag}_{0.9}\text{Na}_{0.1}\text{SbO}_3$ with $\text{Na}^+$ in the $16d$ site, left, and the $96h$ site, right.....	98
3.17 Local refinement fit results to neutron data for the various sodium models. Refinement fits for the sample $\text{Ag}_{0.96(1)}\text{Na}_{0.05(1)}\text{SbO}_3$ where sodium sits in the $16d$ site (left) and $96h$ site (right) .....	98
3.18 Rietveld (left) and PDF (right) refinements for $\text{Ag}_{0.76(4)}\text{K}_{0.24(4)}\text{SbO}_3$ .....	99
3.19 Coordination environment for $\text{Tl}^+$ in $16d$ (left) vs. $32e$ (right). When located in $16d$ , $\text{Tl}^+$ has six equivalent $\text{Tl-O}$ bonds (2.579 Å), whereas when located in the $32e$ site, short (bonds #1, 2.636 Å) and long (bonds #2, 2.98 Å) $\text{Tl-O}$ bonds are observed. Movement into $32e$ results in a displacement of 1.14 Å off of the $16d$ site .....	100
3.20 Rietveld refinement fit for nominal $\text{Ag}_{0.8}\text{Tl}_{0.2}\text{SbO}_3$ with $\text{Tl}^+$ in (a) $16d$ , (b) $\text{Tl}^+$ in $32e$ , (c) $\text{Tl}^+$ in $32e$ and oxygen in $8b$ , and (d) $\text{Tl}^+$ in $32e$ , $\text{Tl}^{3+}$ in $16d$ and oxygen in $8b$ .....	100
3.21 Local refinement fits for nominal $\text{Ag}_{0.8}\text{Tl}_{0.2}\text{SbO}_3$ . Top, left: Fit with $\text{Tl}^+$ in $16d$ . Top, right: Fit with $\text{Tl}^+$ in $32e$ . Bottom, left: Fit with $\text{Tl}^+$ in $32e$ and oxygen in $8b$ . Bottom, right: Fit with $\text{Tl}^+$ in $32e$ , $\text{Tl}^{3+}$ in $16d$ and oxygen in $8b$ .....	101

## LIST OF FIGURES (Continued)

<u>Figure</u>	<u>Page</u>
3.22 Overlay of the PDF data in the range of 1.7-3 Å. Peaks within the PDF can be assigned to various atom-atom correlations in the defect pyrochlore AgSbO <sub>3</sub> . The black curve corresponds to the total PDF, while colored curves correspond to various samples in the series Ag <sub>1-x</sub> M <sup>n</sup> <sub>x</sub> SbO <sub>3+x[(n-1)/2]</sub> (M = Na, K and Tl). For M=K, the atom-atom correlation curve for Ag <sub>0.76(4)</sub> K <sub>0.24(4)</sub> SbO <sub>3</sub> is shown.....	103
3.23 Ag-O bond length (top, left), Sb-O bond length (bottom, left), Ag-O-Ag bond angle (top, right) and Sb-O-Sb bond angle (bottom, right) evolution in the series Ag <sub>1-x</sub> M <sup>n</sup> <sub>x</sub> SbO <sub>3+x[(n-1)/2]</sub> (M = Na, K and Tl) as determined by Rietveld refinement of the neutron data. Error bars are contained within the point for plots a, b and d .....	105
3.24 SEM images of the series Ag <sub>1-x</sub> M <sup>n</sup> <sub>x</sub> SbO <sub>3+x[(n-1)/2]</sub> (M = Na, K and Tl) prepared by standard solid state (top row) and ion exchange (bottom row) reactions. ....	106
3.25 Optical spectra and powders for the series Ag <sub>1-x</sub> M <sup>n</sup> <sub>x</sub> SbO <sub>3+x[(n-1)/2]</sub> (M = Na, K and Tl) .....	107
3.26 Degradation of Methylene Blue in the presence of Ag <sub>1-x</sub> Na <sub>x</sub> SbO <sub>3</sub> (left), Ag <sub>1-x</sub> K <sub>x</sub> SbO <sub>3</sub> (middle), and Ag <sub>1-x</sub> Tl <sub>x</sub> SbO <sub>3</sub> (right).....	108
4.1 Sketch of the observance of $T_c$ in ferroelectric material .....	121
4.2 Left: The crystal structure of the ferroelectric perovskite BaTiO <sub>3</sub> . Right: An enlarged TiO <sub>6</sub> octahedra that illustrates the axial displacement of Ti, giving rise to the permanent dipole in this ferroelectric material.....	122
4.3 The ferroelectric pyrochlore Cd <sub>2</sub> Nb <sub>2</sub> O <sub>6</sub> S at room temperature, space group $Fd\bar{3}m$ .....	123
4.4 Room temperature Rietveld fits and unit cells for the series Cd <sub>2</sub> Nb <sub>2</sub> O <sub>7-x</sub> S <sub>x</sub> . Labels for x are nominal values.....	125
4.5 Lattice parameter evolution for the series Cd <sub>2</sub> Nb <sub>2</sub> O <sub>7-x</sub> S <sub>x</sub> . Deviation from a linear trend in the nominal x = 0.25 (red outlined box) and x = 0.5 (blue outlined box) can be attributed to large amounts of strain in the samples, which were modeled through multiple pyrochlore phases .....	127
4.6 Bond valence sums of Cd (black) and Nb (magenta) as a function of S-content (x) for the series Cd <sub>2</sub> Nb <sub>2</sub> O <sub>7-x</sub> S <sub>x</sub> at room temperature.....	128

## LIST OF FIGURES (Continued)

<u>Figure</u>	<u>Page</u>
4.7 Comparison of the room temperature and 100 K diffraction data for the series $\text{Cd}_2\text{Nb}_2\text{O}_{7-x}\text{S}_x$ .....	129
4.8 Comparison of the room temperature and 100 K data for the series $\text{Cd}_2\text{Nb}_2\text{O}_{7-x}\text{S}_x$ . Enlarged areas from 8-10 ° 2 $\theta$ highlight the structural changes observed in each sample. For $\text{Cd}_{1.96(2)}\text{Nb}_2\text{O}_7$ (blue outline), $\text{Cd}_2\text{Nb}_2\text{O}_{6.88(1)}\text{S}_{0.22(1)}$ (orange outline), and $\text{Cd}_2\text{Nb}_2\text{O}_{6.36(1)}\text{S}_{0.64(1)}$ (green outline) various degrees of peak splitting are observed. While no peak splitting is present in $\text{Cd}_2\text{Nb}_2\text{O}_{6.28(1)}\text{S}_{0.72(1)}$ (yellow outline), the emergence of new peaks is observed .....	129
4.9 Subgroups of the $Fd\bar{3}m$ subgroup. Space groups in red indicate non-centrosymmetric groups.....	130
4.10 Phase transition from $Fd\bar{3}m$ at 330 K (left) to $Ima2$ at 100 K for nominal $\text{Cd}_2\text{Nb}_2\text{O}_7$ .....	131
4.11 a) Cd-O' chain (top) and $\text{OCd}_4$ tetrahedra (bottom) in nominal $\text{Cd}_2\text{Nb}_2\text{O}_7$ obtained from the room temperature refinement in space group $Fd\bar{3}m$ . b) Cd1-O' and Cd2-O' chains (top) and $\text{OCd}_4$ tetrahedra (bottom) in nominal $\text{Cd}_2\text{Nb}_2\text{O}_7$ obtained from the 100 K refinement in space group $Ima2$ .....	132
4.12 a) $\text{NbO}_6$ network in the room temperature $Fd\bar{3}m$ phase and b) in the $Ima2$ phase at 100 K.....	133
4.13 Room temperature (a) and 100 K data (b) for $\text{Cd}_2\text{Ta}_2\text{O}_7$ .....	134
4.14 Le Bail fits with $Ima2$ , $Fddd$ , and $Fdd2$ space groups for nominal $\text{Cd}_2\text{Nb}_2\text{O}_{6.75}\text{S}_{0.25}$ at 100 K.....	135
4.15 Rietveld fits with $Fddd$ , and $Fdd2$ space groups for nominal $\text{Cd}_2\text{Nb}_2\text{O}_{6.75}\text{S}_{0.25}$ at 100 K .....	135
4.16 Phase transition from 330 K (left) to 100 K (right) for the networks in nominal $\text{Cd}_2\text{Nb}_2\text{O}_{6.75}\text{S}_{0.25}$ .....	137

## LIST OF FIGURES (Continued)

<u>Figure</u>	<u>Page</u>
4.17 Le Bail fits for nominal $\text{Cd}_2\text{Nb}_2\text{O}_{6.3}\text{S}_{0.7}$ at 100K: a) LeBail fit with space group $Fd\bar{3}m$ results in poor profile fits for major peaks and many smaller peaks remain unindexed; b) Le Bail fit with space group $F\bar{4}3m$ provides a better peak profile peak, but many smaller peaks still remain unindexed; c) Le Bail fit with space group $P\bar{4}3m$ is able to index all peaks present and provide the best peak profile fit.....	137
4.18 Dielectric measurements for $\text{Cd}_2\text{Nb}_2\text{O}_7$ (a), $\text{Cd}_2\text{Nb}_2\text{O}_{6.88(1)}\text{S}_{0.22(1)}$ (b), and $\text{Cd}_2\text{Nb}_2\text{O}_{6.28(1)}\text{S}_{0.72(1)}$ (c).....	134
5.1 The tetragonal hollandite structure $\text{A}_x\text{M}_4\text{O}_8$ . Edge-shared double chains of $\text{MO}_6$ octahedra form a 1D tunnel structure which houses the A-cation.....	144
5.2 Q1D structures of $\text{K}_{0.3}\text{MoO}_3$ (a) and $\text{Nb}_3\text{Se}_4$ (b).....	145
5.3 Unit cells obtained from Rietveld refinement of the neutron diffraction data for $\text{K}_x\text{Ru}_4\text{O}_8$ (a), $\text{K}_{1-x}\text{Na}_x\text{Ru}_4\text{O}_8$ (b), $\text{Rb}_x\text{Ru}_4\text{O}_8$ (c), and $\text{Rb}_{1-x}\text{Na}_x\text{Ru}_4\text{O}_8$ (d). For $\text{K}_{1-x}\text{Na}_x\text{Ru}_4\text{O}_8$ , the A-site refined to full occupancy, but the degree of Na substitution requires X-ray analysis and is currently under investigation .....	146
5.4 Anisotropic displacements of the A-site cations parallel to the $\text{RuO}_6$ channel structure for $\text{K}_x\text{Ru}_4\text{O}_8$ (a), $\text{K}_{1-x}\text{Na}_x\text{Ru}_4\text{O}_8$ (b), $\text{Rb}_x\text{Ru}_4\text{O}_8$ (c), and $\text{Rb}_{1-x}\text{Na}_x\text{Ru}_4\text{O}_8$ (d).....	147
5.5 Fits to the neutron PDF data for $\text{K}_x\text{Ru}_4\text{O}_8$ (a), $\text{K}_{1-x}\text{Na}_x\text{Ru}_4\text{O}_8$ (b), $\text{Rb}_x\text{Ru}_4\text{O}_8$ (c), and $\text{Rb}_{1-x}\text{Na}_x\text{Ru}_4\text{O}_8$ (d). Insets: Resulting units cells from the neutron PDF refinements.....	148
5.6 Partial contributions to the neutron PDF for samples $\text{A}_x\text{Ru}_4\text{O}_8$ (A = $\text{Na}^+$ , $\text{K}^+$ , and $\text{Rb}^+$ ).....	151
5.7 TGA curves up to 500 ° C under $\text{N}_2$ flow for hollandite samples $\text{A}_x\text{Ru}_4\text{O}_8$ (A = $\text{Na}^+$ , $\text{K}^+$ , and $\text{Rb}^+$ ).....	152
5.8 Left: Resistivity vs. temperature for polycrystalline samples of $\text{K}_x\text{Ru}_4\text{O}_8$ and $\text{Rb}_x\text{Ru}_4\text{O}_8$ . Right: conduction pathways in the hollandite structure .....	153
5.9 Microscope image of the small needle-shaped single crystals of $\text{K}_x\text{Ru}_4\text{O}_8$ .....	153
5.10 A shift in the $T_{max}$ observed in the resistivity data (left) can be explained by a change in the inter-chain distance, $d$ , or the distance between Ru-Ru atoms in the corner-shared chains .....	154

## LIST OF FIGURES (Continued)

<u>Figure</u>	<u>Page</u>
5.11 Magnetic susceptibility (a) and modified Curie-Weiss fits (b) for hollandite samples $ARu_4O_8$ ( $A = Na^+, K^+, \text{ and } Rb^+$ ).....	155
A.1 Overlay of the variable temperature synchrotron PDF for an amorphous film of IGZO. The sample was heated at a ramp rate of $10^\circ\text{C}/\text{min}$ up to $750^\circ\text{C}$ , and data was collected every minute. ....	169
A.2 Comparison of the simulated crystalline M-O partials (left) and M-M partials (right) to the experimental data collected at $30^\circ\text{C}$ and $750^\circ\text{C}$ . Simulated total and partial PDFs are represented by lines and experimental data by open circles. Zn-O partials fall directly underneath the Ga-O partials due to same site-occupancy in the crystal structure.. ....	170
A.3 Comparison of the X-ray (top) and neutron (bottom) $G(r)$ reveals the X-ray sample has more peaks present in the higher- $r$ range, indicating more mid-range order than in the neutron sample.. ....	171
A.4 Least-squares refinements of the synchrotron diffraction (top) and PDF (bottom) data collected at $750^\circ\text{C}$ on an amorphous film of IGZO.....	172
A.5 Starting configurations for RMC simulations generated by creating (a) a $17 \times 17 \times 2$ supercell of crystalline $\text{InGaZnO}_4$ and (b) a $2 \times 2 \times 2$ supercell of a randomized structure of $\text{InGaZnO}_4$ obtained through MD simulations.. ....	173
A.6 Total RMC fit against the X-ray PDF of an amorphous IGZO film with a crystalline starting configuration (a) and a MD starting configuration (b). Calculated partials from the crystalline (c) and MD fit (d), and final configurations obtained from the crystalline (e) and MD (f) fit... ..	175
B.1 Crystal structure of the tetrahedrite, $\text{Cu}_{12}\text{Sb}_4\text{S}_{13}$ and b) isolated $\text{CuS}_3$ and $\text{SbS}_3$ polyhedron.....	181
B.2 Temperature dependences of (a) power factor (PF), (b) electrical conductivity ( $\sigma$ ), and (c) Seebeck Coefficient (S) for $\text{Cu}_{10}\text{TM}_2\text{Sb}_4\text{S}_{13}$ (TM = Mn, Fe, Co, Ni, Cu, Zn).....	183
B.3 (a) Total thermal conductivity ( $\kappa$ ), (b) lattice thermal conductivity ( $\kappa_L$ ), and (c) the thermoelectric figure of merit ZT for $\text{Cu}_{10}\text{TM}_2\text{Sb}_4\text{S}_{13}$ (TM = Mn, Fe, Co, Ni, Cu, Zn) as a function of temperature.....	185

## LIST OF FIGURES (Continued)

<u>Figure</u>	<u>Page</u>
B.4 (a) The thermoelectric figure of merit ZT, (b) electrical conductivity ( $\sigma$ ), and (c) thermopower (S) for $\text{Cu}_{12-x}\text{Mn}_x\text{Sb}_4\text{S}_{13}$ ( $0 \leq x \leq 2$ ) as a function of temperature.....	187
B.5 (a) Thermoelectric figure of merit ZT (black filled squares), (b) thermal conductivity ( $\kappa$ , black filled circles), power factor (PF, blue open circles), (c) electrical conductivity electrical conductivity ( $\sigma$ , black filled triangles), and thermopower (S, blue open triangles) as a function of Mn concentration in $\text{Cu}_{12-x}\text{Mn}_x\text{Sb}_4\text{S}_{13}$ ( $0 \leq x \leq 2$ ) at 575 K.....	188

## LIST OF TABLES

<u>Table</u>	<u>Page</u>
3.1	Summary of the estimated band gaps of the samples .....78
3.2	Summary of the densities of solid state and SPS-prepared samples .....81
3.3	Fitting parameters of $^{121}\text{Sb}$ Mössbauer spectroscopic measurements of several $\text{Sb}^{5+}$ pyrochlores at 78 K. $\delta$ = isomer shift and $\Gamma$ = experimental line width .....87
3.4	Crystallographic data from the Rietveld refinement of neutron diffraction data for the series $\text{Ag}_{1-x}\text{M}^n_x\text{SbO}_{3+x[(n-1)/2]}$ (M = Na, K and Tl) ....91
3.5	Refined atomic positional and displacement parameters from average (Rietveld) and local (PDF) structure refinements for the series $\text{Ag}_{1-x}\text{M}^n_x\text{SbO}_{3+x[(n-1)/2]}$ (M = Na, K and Tl) from neutron data. PDF refinements were completed on the r-range 1.7-10Å .....92
3.6	Summary of refined local parameters for the series $\text{Ag}_{1-x}\text{M}^n_x\text{SbO}_{3+x[(n-1)/2]}$ (M = Na, K and Tl) over r=1.7-10Å .....93
3.7	Comparison of the refined atomic positional and displacement parameters from average (Rietveld) and local (PDF) structure refinements for the series $\text{Ag}_{1-x}\text{M}^n_x\text{SbO}_{3+x[(n-1)/2]}$ (M = Na, K and Tl) from neutron data. PDF refinements were completed on the r-range 1.7-10Å .....97
3.8	Comparison of the refined atomic positional and displacement parameters from average (Rietveld) and local (PDF) structure refinements for the series $\text{Ag}_{1-x}\text{Tl}_x\text{SbO}_3$ . PDF refinements were completed on the r-range 1.7-10Å ..... 102
3.9	Selected bond lengths and angles from average (Rietveld) and local (PDF) structure refinements for the series $\text{Ag}_{1-x}\text{M}^n_x\text{SbO}_{3+x[(n-1)/2]}$ (M = Na, K and Tl) from neutron data. PDF refinements were completed on the r-range 1.7-10Å..... 104
4.1	Refined crystallographic details for the series $\text{Cd}_2\text{Nb}_2\text{O}_{7-x}\text{S}_x$ ..... 125
4.2	Comparison of room temperature and 100 K data for nominal $\text{Cd}_2\text{Nb}_2\text{O}_7$ ..... 131

## LIST OF TABLES (Continued)

<u>Table</u>	<u>Page</u>
4.3 Comparison of room temperature and 100 K data for nominal $\text{Cd}_2\text{Nb}_2\text{O}_{6.75}\text{S}_{0.25}$ .....	136
4.4 Observed and literature ferroelectric Curie temperatures for the series $\text{Cd}_2\text{Nb}_2\text{O}_{7-x}\text{S}_x$ .....	138
5.1 Select crystallographic data from the powder neutron diffraction data .....	146
5.2 Comparison of the refined parameters for the local structure (refined over an r-range of 10 Å) and average structure (refined through Rietveld analysis) against neutron scattering data).....	149
5.3 Inter-chain Ru-Ru distance ( $d$ ) and corresponding observed and predicted $T_{max}$ values .....	155

## DEDICATION

To Peter,  
It's been a grand adventure  
And I'm glad it was  
With you

## CHAPTER 1

### Introduction to Structure-Property Relationships in a Material

#### 1.1 Scope of Dissertation

Crystallography and its application towards the study of materials has revolutionized the design of materials for targeted applications. This year has been termed the “International Year of Crystallography” as it commemorates the 100<sup>th</sup> year since the discovery of X-ray diffraction by William Lawrence Bragg and William Henry Bragg, for which both were awarded the Nobel Prize in physics in 1915.[1,2] Crystallography allows for a detailed understanding of a material’s structure, which is crucial for advancements in technology. In particular, an intimate knowledge of how the structure of a material influences the observed properties are of paramount importance. Once this relationship is established, it can be manipulated in order to tune or enhance a desired property, driving the design of optimized materials for peak performance in applications. This dissertation aims to highlight the structural influence on the properties of a series of metal oxide materials for electronic and energy applications. This chapter will address how to describe crystal structures and the particular structure types encountered in this dissertation: the pyrochlore structure  $A_2M_2O_7$ , the hollandite structure  $A_xM_4O_8$ , and the  $YbFe_2O_4$  structure.

#### 1.2 The Structure of Crystalline Materials

##### 1.2.1 *Describing a Structure through Close Packing*

To establish the structure-property relationships in a material, one must have an understanding of how to build and describe its structure. Many structures can be described by a close packed array of atoms with the subsequent filling of void spaces in the packing scheme. If atoms are considered as spheres, there is one arrangement in two dimensions that allows for maximum packing density of the spheres, shown as

Layer “A” in Figure 1.1. Each atom in this layer has a coordination number (CN) of 6, indicating it is in contact with six surrounding atoms. By building layers of this two-dimensional (2D) arrangement, three-dimensional (3D) close packed structures can be realized. The overall packing scheme of a material is defined by how these 2D arrangements are layered to form the 3D structure. Figure 1.1 illustrates the various options for placement of the second layer, either the green or yellow positions. If this layer is placed on the yellow positions, the stacking sequence is “AB”. The third layer has two options for placement, above the green positions or directly above the first blue layer. Placement of the third layer above the green positions results in a stacking sequence “ABC”, and if this sequence continues, the material is considered a cubic close packed (CCP) structure. If the third layer is placed directly above the first, the stacking sequence is “ABA”, and a repeated sequence of “ABAB...” is called a hexagonal close packed (HCP) structure.

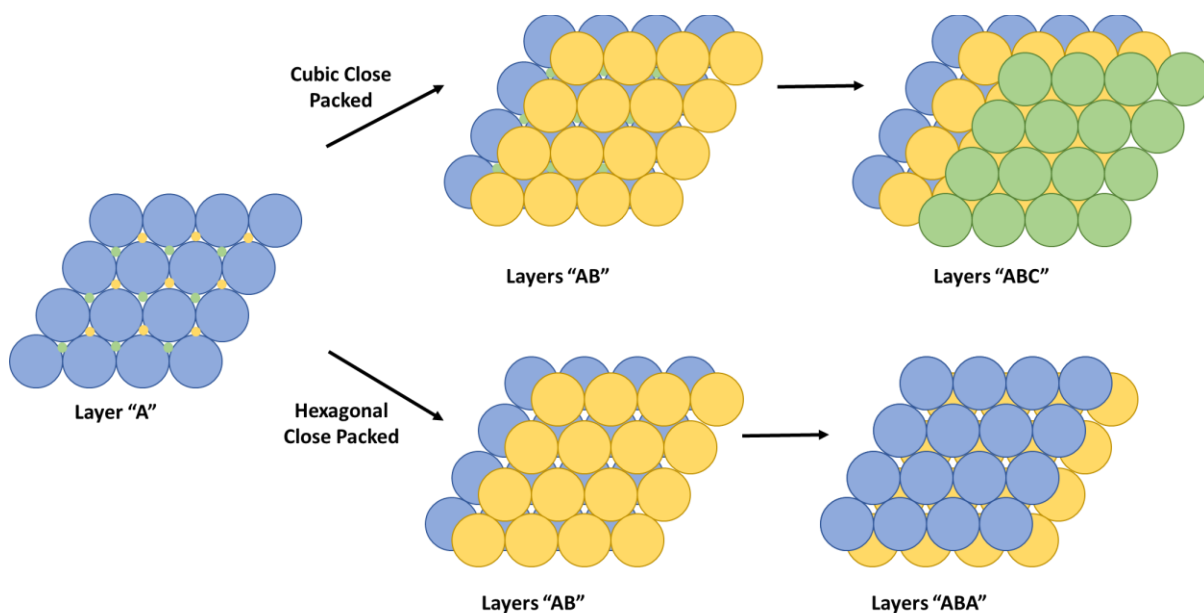


Figure 1.1 Layering scheme of “ABCABC...” for cubic close packed spheres (top) and “ABAB...” for hexagonal close packed spheres (bottom).

While close packing optimizes the density of packed spheres of the same size, there is still 25.95% void space in this configuration. Each void space can be described by the number of atoms surrounding it. Consider two void spaces shown in Figure 1.2. The void space on the left is surrounded by six neighboring atoms, or has a CN of 6. These six atoms form an octahedral coordination around the void space, and thus this void is referred to as an octahedral hole. The void space on the right only has a CN of 4, therefore a tetrahedral arrangement of the atoms is observed, creating a tetrahedral hole. Both holes can be occupied by atoms of various sizes; based on a geometrical considerations, the octahedral hole will accommodate larger atoms than the tetrahedral hole.

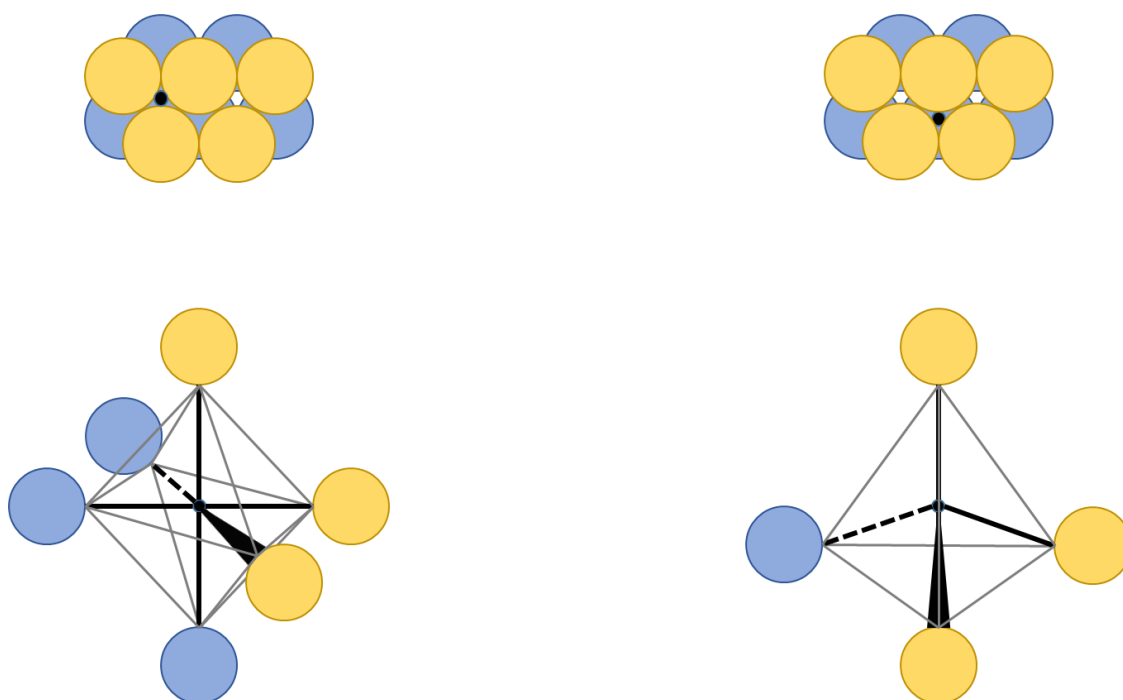


Figure 1.2 Left: Location of an octahedral hole (shown by the black dot) between two layers of close packed atoms (top) and an expanded view of the octahedral arrangement of the atoms around the void (bottom). Right: Location of a tetrahedral hole (shown by the black dot) between two layers of close packed atoms (top) and an expanded view of the tetrahedral arrangement of the atoms around the void (bottom).

Once a close packing and void filling scheme is established, a crystal structure can be built. It is common to start with the close packing scheme of anions. A closed packed arrangement of anions generates one octahedral hole and two tetrahedral holes per anion; therefore, filling of the holes can be inferred from the chemical formula. For example, a material with the formula  $\text{MX}_2$  either has  $\frac{1}{2}$  of the octahedral holes or  $\frac{1}{4}$  of the tetrahedral holes filled with a cation. Differentiation of these filling schemes is dependent on the size and chemistry of the M cation present. To determine the preference of each cation, a common radius ratio rule can be applied. This radius ratio rule is defined as the ratio of the radius of the cation to the radius of the anion, or  $r_{\text{cation}}/r_{\text{anion}}$ . In general, a radius ratio between  $\sim 0.2$  and  $\sim 0.4$  will result in tetrahedral hole filling, while a radius ratio between  $\sim 0.4$  and  $\sim 0.7$  will result in cation occupancy of the octahedral hole. While there are plenty of exceptions to this rule, it serves as a good guideline for determining how a structure will form.

An example of a simple structure described through packing schemes and hole filling is the rocksalt structure ( $\text{NaCl}$ ) shown in Figure 1.3a. If starting with a CCP array of Cl atoms, based on the formula, either all octahedral holes or  $\frac{1}{2}$  tetrahedral holes are filled. By determining the radius ratio of  $\text{Na}^+$  to  $\text{Cl}^-$  ( $\text{Na}^+_{\text{r}} = 1.16 \text{ \AA}$ ,  $\text{Cl}^-_{\text{r}} = 1.67 \text{ \AA}$ ), [3] a radius ratio of 0.695 is obtained, indicating  $\text{Na}^+$  will occupy octahedral holes. A succinct description of the rocksalt structure is therefore a CCP array of anions with all octahedral holes filled. The HCP analog of this is the Nickel Arsenide structure: an HCP array of anions with all octahedral holes filled. This method of building structures can also be applied to more complex structures, such as the spinel structure, shown in example 1.3b as  $\text{MgAl}_2\text{O}_4$ . The  $\text{MgAl}_2\text{O}_4$  spinel is a good example of an exception to the radius ratio rule. The radius ratios for  $\text{Al}^{3+}$  and  $\text{Mg}^{2+}$  are 0.378 and 0.514, respectively, which indicate that  $\text{Al}^{3+}$  should occupy tetrahedral sites and  $\text{Mg}^{2+}$  should occupy the octahedral site. In reality, Al occupies octahedral sites, while Mg occupies the tetrahedral sites. To explain this, one must look beyond the radius ratio rule and towards other factors. For ionic spinels, an octahedral

site preference energy has been calculated to determine which cation will fill the octahedral site. This preference energy,  $P$ , takes into account the Coloumbic energy, the Madelung energy, the crystal field stabilization energy, and the valence of the cation. For  $\text{Al}^{3+}$ ,  $P = -0.11$  and for  $\text{Mg}^{2+}$ ,  $P = -0.22$ ; as  $\text{Al}^{3+}$  has the greater preference energy, it will occupy the octahedral site, leaving  $\text{Mg}^{2+}$  to occupy the tetrahedral site. Based on this reasoning, the  $\text{MgAl}_2\text{O}_4$  spinel is described as a CCP array of oxygen atoms where  $\frac{1}{2}$  of the octahedral holes are filled with Al atoms, and  $\frac{1}{4}$  of the tetrahedral holes are filled with Mg.  $\text{MgAl}_2\text{O}_4$  serves as an excellent example of why radius ratio rules are only to be used as a guideline, and careful consideration of the cation chemistry is highly important in structure prediction.

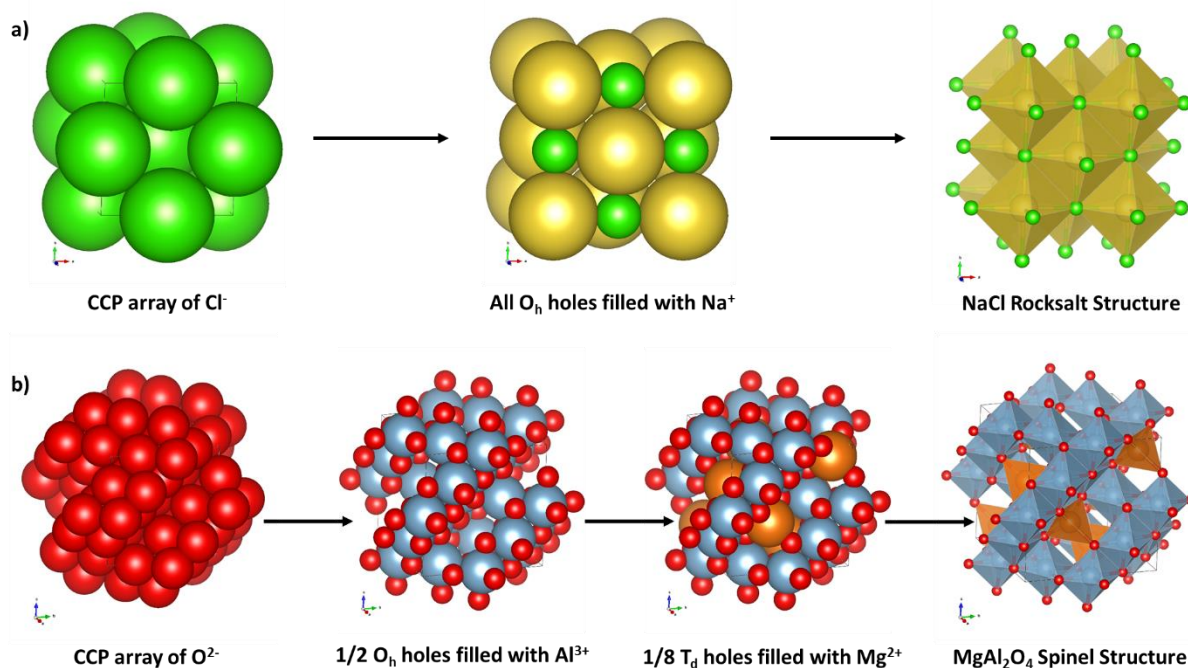


Figure 1.3 a) The rocksalt structure  $\text{NaCl}$ , described as a CCP array of anions ( $\text{Cl}^-$ ) with all octahedral holes filled by  $\text{Na}^+$ . b) The spinel structure  $\text{MgAl}_2\text{O}_4$ , described as a CCP array of  $\text{O}^{2-}$  with  $\frac{1}{2}$  of the octahedral holes occupied by  $\text{Al}^{3+}$  and  $\frac{1}{4}$  of the tetrahedral holes filled with  $\text{Mg}^{2+}$ .

### 1.2.2 Describing a Structure through Symmetry Operations

A crystalline material consists of atoms arranged in a lattice, or a periodically repeating 3D array. This periodic repetition of a crystal can be described by the unit cell, which is defined as the smallest repeating unit that contains all symmetry operations necessary to generate the extended lattice. The symmetry of the unit cell can be described according to a crystal system and space group. There are seven crystal systems, derived from 32 point groups that can be used to describe a unit cell (listed from highest to lowest symmetry): cubic, hexagonal, trigonal/rhombohedral, tetragonal, orthorhombic, monoclinic, and triclinic. These crystal systems can be further divided into 14 Bravais Lattices by identifying the unit cell as primitive (*P*), base-centered (*A*, *B*, or *C*), body-centered (*I*), or face-centered (*F*). The symmetry of a crystal contained in a unit cell is described by a space group, which describes the Bravais lattice and the highest symmetry operations present in the lattice along axes dependent on the crystal system. For example, rock salt NaCl crystallizes in a unit cell with space group symmetry  $Fm\bar{3}m$ . Written in the Hermann-Mauguin notation, the first letter of a space group represents the lattice type, which in this case is face-centered. The unit cell of NaCl is cubic; the next term in the Hermann-Mauguin notation indicates symmetry with respect to the *x*, *y*, and *z* axes ("*m*", indicating a mirror plane), followed by the three-fold symmetry of the body diagonals (" $\bar{3}$ ", indicating a three-fold inversion axis), followed by symmetry with respect to the face diagonals ("*m*", indicating a mirror plane). In theory, a crystal is generated when the unit cell is repeated to infinity, and this forms the highly ordered crystalline lattice. The unit cell and crystalline lattice of NaCl is illustrated in Figure 1.4.

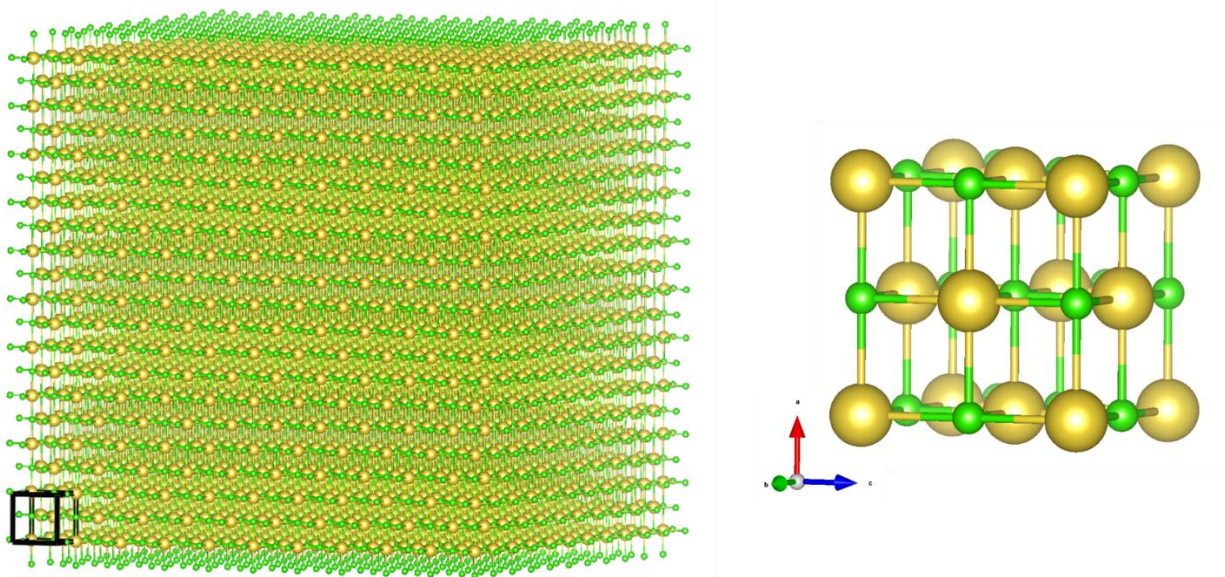


Figure 1.4 Extended crystalline lattice of NaCl with unit cell outlined, left, and enlarged unit cell of NaCl, right.

### 1.2.3 Considerations for Structure Prediction: Pauling's Rules

While there are no absolute rules for predicting how a crystal structure will form, there are some guidelines that can be considered when designing new materials. In "The Principles Determining the Structure of Complex Ionic Crystals", Linus Pauling states "The elucidation of the factors determining the relative stability of alternative crystalline structures of a substance would be of the greatest significance in the development of the theory of the solid state." This manuscript outlines some basic rules for structure prediction that can serve as a good reference.[4]

Pauling's first rule is the radius ratio rule discussed in section 1.2.1; in reality, this rule has such a large number of exceptions, and it is rarely consulted when predicting a new material. Pauling's second rule carries more credibility and states that the bond valence sum of each ion should equal its oxidation state. The bond valence sum (BVS) of an atom can be calculated according to equation 1.1

$$V_i = \sum s_{ij} \quad (1.1)$$

where  $V_i$  is the oxidation state of atom "i" and  $s_j$  is the valence of each bond, which can be calculated by the valence of the central atom divided by the number of surrounding bonds. As illustrated in Equation 1.1, BVS couples both the coordination number and the bonds lengths surrounding an atom. This can be useful when quantifying the degree of ionicity or covalency of a bond in a material, and it is often applied to validate new structures in terms of chemical sensibility. An example of the application of Pauling's second rule can be seen in Chapter 3.3.2 where the BVS of cations in various positions are calculated to determine the most stable position based on the oxidation state of the cation.

Pauling's third, fourth, and fifth rules describe guidelines for the arrangement and occupation of polyhedra in a structure. The third rule states that sharing of faces and edges of polyhedra decreases the stability of a structure, and is illustrated by Pauling in the case of the polymorphs of  $\text{TiO}_2$ . Stoichiometric compounds of  $\text{TiO}_2$  crystallizes in the rutile, anatase, and brookite structures. The rutile structure is the most stable of the three, in which the  $\text{TiO}_6$  octahedra share two edges with adjacent octahedra. In anatase and brookite, the  $\text{TiO}_6$  octahedra share three and four edges, respectively, with their neighboring octahedra, and as a result are less stable. This is especially true for cations with high valence and small coordination numbers, and according to the fourth rule, such cations do not share adjacent polyhedra. For example, Pauling describes the structure of olivine ( $\text{MgFeSiO}_4$ ), which contains isolated  $\text{SiO}_4$  tetrahedral units. The fifth and final rule is often referred to as "the rule of parsimony" and explains that even though a variety of coordination environments are possible, most crystals will only exhibit a small number of possible sites in their structure.

While useful as a baseline for structure prediction, many structures violate Pauling's rules and must therefore be used only as guidelines. For example, the lyonsite structure contains cations in tetrahedral, octahedral, and trigonal prismatic sites, pushing the rule of parsimony.[5] In addition to structure prediction, these rules can provide explanation for the observed crystal structure of a material, such as the honeycomb ordering observed in layered  $\text{A}_3\text{M}_2\text{XO}_6$  compounds.[6–8] They can additionally be

used to help validate or disprove a new structure. For example, if the BVS of the Na position in a new structure results in an oxidation state of +3 for Na, there must be an error with the structural model. Pauling's rules provide a reference tool for the solid state chemist and should be taken into consideration during any structural analysis problem.

### 1.3 Structure Types in this Dissertation

#### 1.3.1 The Pyrochlore Structure

Oxides which crystallize in the pyrochlore structure form a family of materials with fascinating properties, such as the ferroelectric  $\text{Cd}_2\text{Nb}_2\text{O}_7$ [9] and the superconducting  $\text{Cd}_2\text{Re}_2\text{O}_7$ [10]. This cubic structure is highly symmetric, belonging to the space group of  $Fd\bar{3}m$ . It is often represented with the formula  $\text{A}_2\text{M}_2\text{O}_7$ , which can be rewritten as  $\text{A}_2\text{M}_2\text{O}_6\text{O}'$  as oxygen is found on two distinct crystallographic Wyckoff sites:  $48f$  and  $8b$ . The "A" cations are found in the  $16d$  site, and the "M" cations are found in  $16c$ . A representation of the various sites in the pyrochlore structure is shown in Figure 1.5.

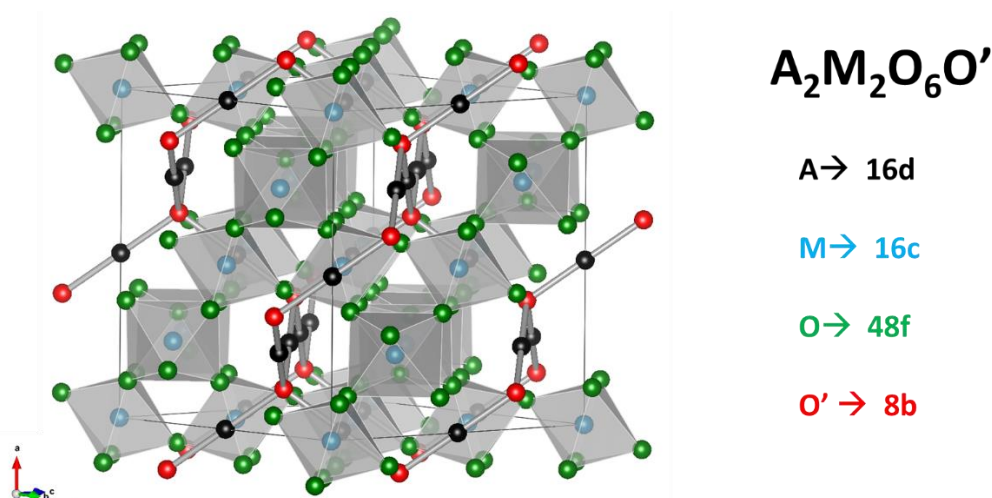


Figure 1.5 The pyrochlore structure  $\text{A}_2\text{M}_2\text{O}_6\text{O}'$ . The "A" cations are found in the black  $16d$  site, the "M" cations in the blue  $16c$  site, and the oxygen, O and O', found in the green  $48f$  and red  $8b$ , respectively.

The pyrochlore structure can be described in several different ways. One is as an anion-deficient fluorite structure, shown in Figure 1.6.[11] In the fluorite structure  $AX_2$ , shown in Figure 1.6a, the cations form a CCP array and the anions occupy all tetrahedral holes. The cations are coordinated to the anions in a cubic configuration. If the unit cell is expanded to a  $2 \times 2 \times 2$  supercell, the resultant formula will be  $A_4X_8$ . The removal of one oxygen from the formula unit, i. e. an oxygen from one of the corners of the cube, an octahedral coordination is formed, illustrated in Figure 1.6b. This results in two distinct crystallographic cation sites and a formula of  $A_2M_2X_7$ . In the pyrochlore structure, shown in Figure 1.6c, the “A” cation site becomes modified from a perfect cubic to a distorted cubic, depending on the position of the  $48f$  oxygen atoms, while the “M” cation occupies the octahedral site.

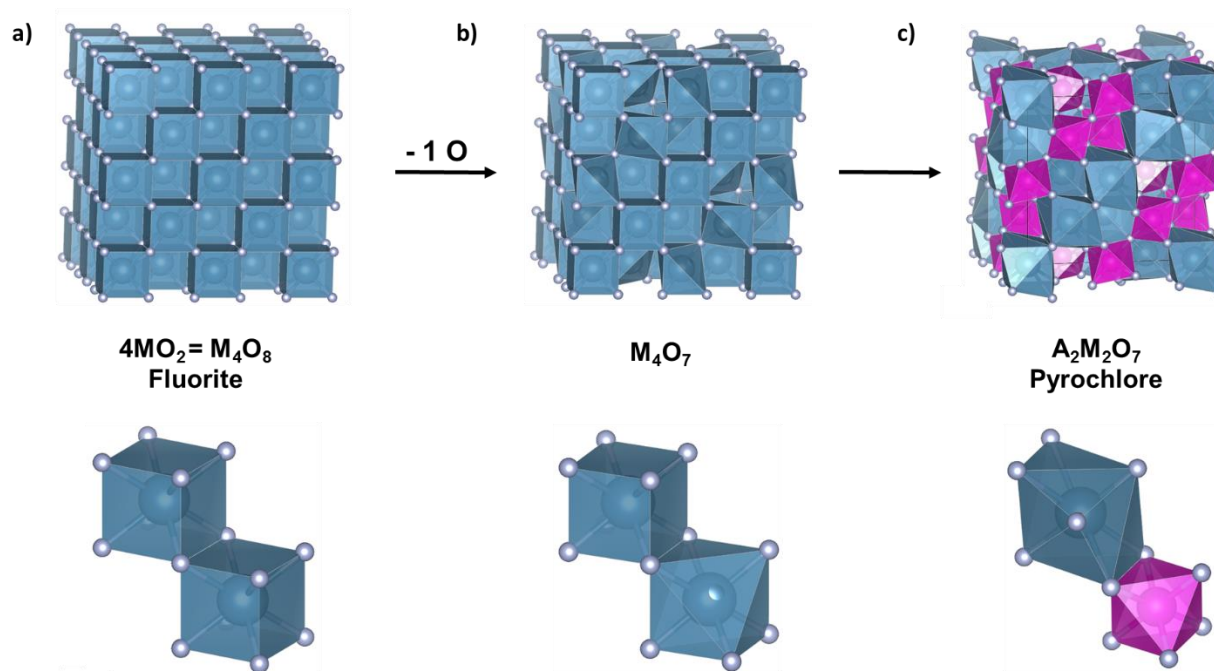


Figure 1.6 The pyrochlore structure (c) as derived from the fluorite structure (a) by removal of one of the oxygen atoms (b) in a  $2 \times 2 \times 2$  fluorite supercell.

It is also common to describe the pyrochlore structure as two interpenetrating 3D networks: a network of corner-sharing  $\text{MO}_6$  octahedra and a network of linearly-coordinated A-atoms, which are linked together by a framework of  $\text{O}'$ -centered tetrahedra (Figure 1.7).[11,12] Additionally, the pyrochlore structure can be described as two interpenetrating networks of corner-sharing A and M tetrahedra, shown in Figure 1.8. The subunits of this structure allow for some of the unique characteristics found in this family. For instance, the tetrahedral arrangement of the A and M atoms can lead to a frustrated lattice, giving rise to interesting magnetic properties, such as spin glass and spin ice behavior.[13]

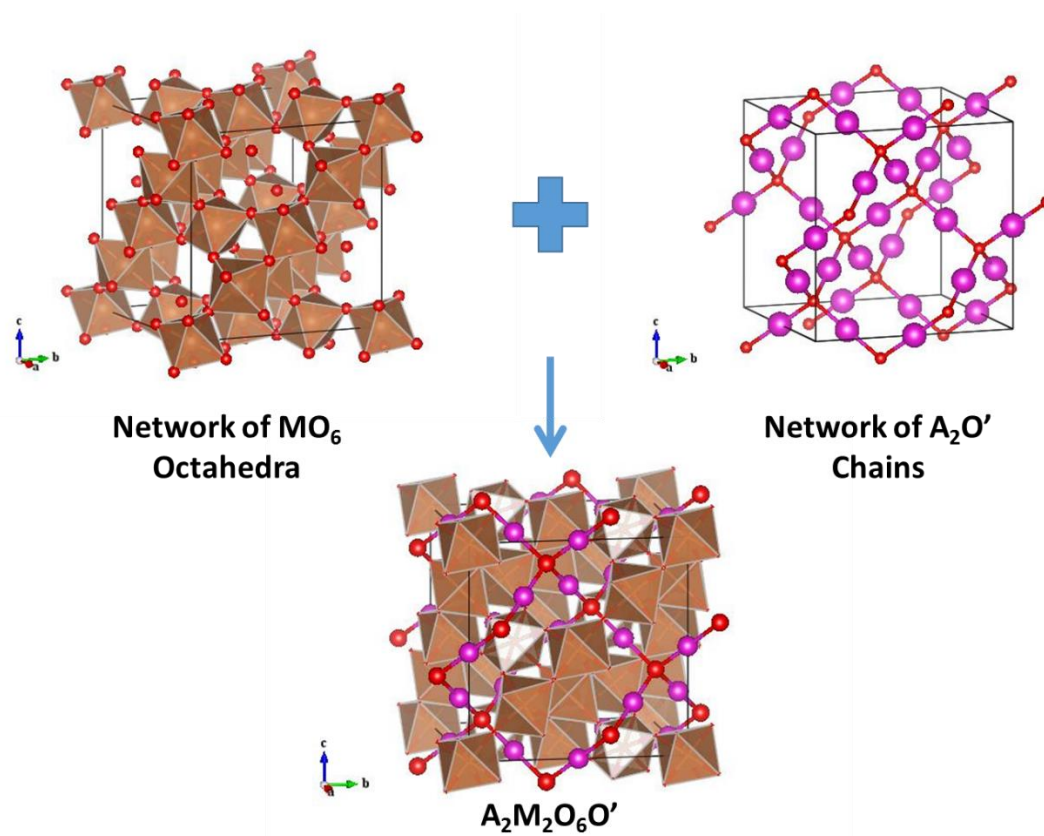


Figure 1.7 The pyrochlore structure described as two interpenetrating networks of corner-shared  $\text{MO}_6$  octahedra and  $\text{A}_2\text{O}'$  chains.

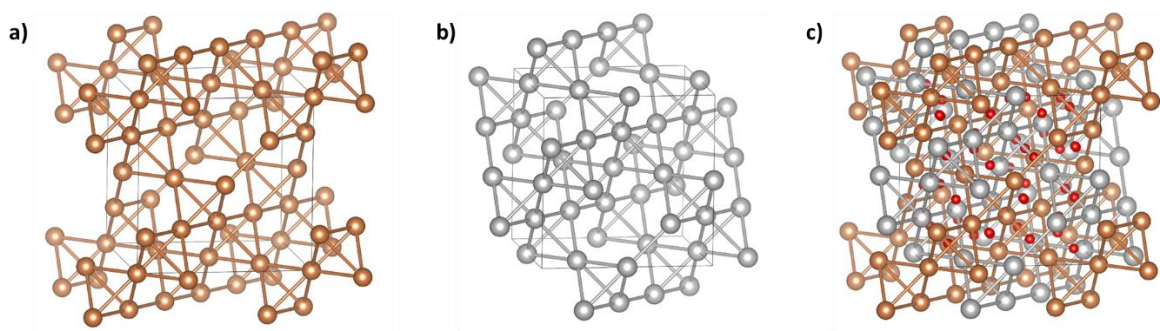


Figure 1.8 Interpenetrating networks of  $A_4$  (a) and  $M_4$  (b) tetrahedra around O atoms to describe the pyrochlore structure (c).

The network of  $MO_6$  octahedra is fairly rigid, facilitating variations in the chemistry of the A-site cation. This rigid framework also allows for the structure to tolerate defects in the channels where the  $A_2O'$  chains are found. In the ideal pyrochlore, the A atoms are located in the  $16d$  site that is central to the  $MO_6$  channel structure, and the  $O'$  atoms are found in the  $8b$  sites along this channel (Figure 1.9, left). In the anion-deficient pyrochlore structure, the  $8b$  sites are vacant, and the resulting formula is  $A_2M_2O_6$ , often shortened to  $AMO_3$  (Figure 1.9, middle). Another defect pyrochlore is the  $AM_2O_6$  defect pyrochlore, where the  $O'$  atom and one of the A site cations are missing. The  $MO_6$  octahedral network remains intact, and the A cation occupies the  $8b$  site, leaving the  $16d$  site vacant (Figure 1.9, right). To stabilize this configuration, a large  $A^+$  cation, such as  $Rb^+$  or  $Cs^+$ , must be present. A comparison of the ideal and defect pyrochlores can be seen in Figure 1.9.

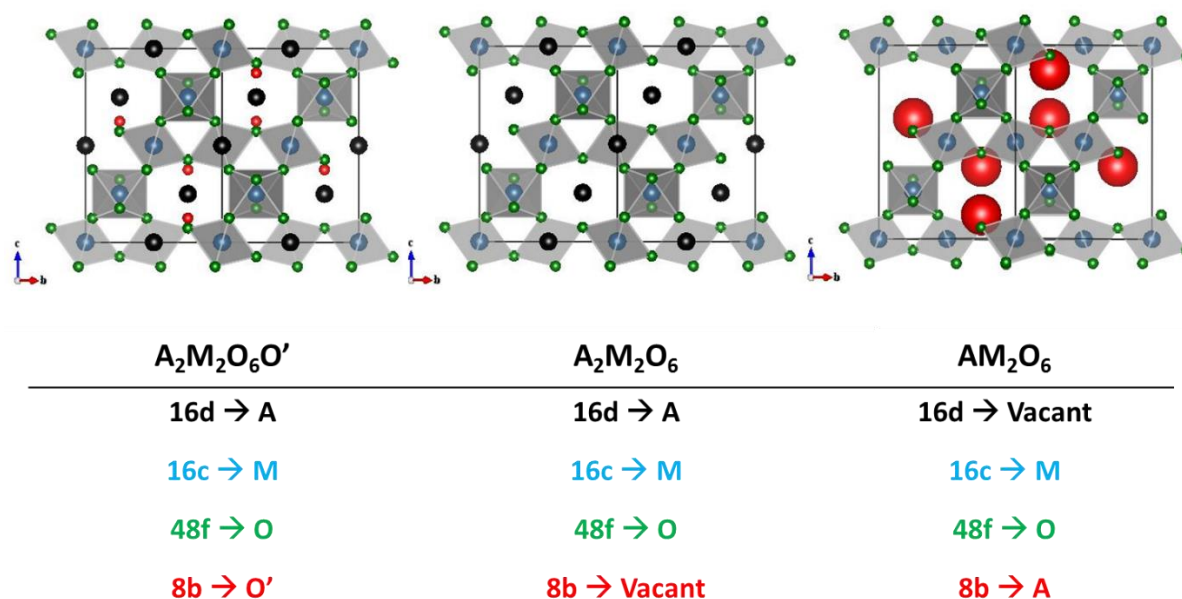


Figure 1.9 The ideal pyrochlore  $A_2M_2O_6O'$  with all sites filled (left), the anion-deficient pyrochlore  $A_2M_2O_6$  with vacant  $8b$  site (middle), and the defect pyrochlore  $AM_2O_6$  with vacant  $16d$  site (right).

While the pyrochlore structure has the ability to accommodate a large range of elements and tolerate defects, most members of the pyrochlore family crystallize in the ideal pyrochlore structure. Very few compounds can form in this family with the vacancy on the  $8b$  site, and as a result, the literature on  $A_2M_2O_6$  pyrochlores is relatively small. Substitutions into the anion-deficient pyrochlore  $Ag_2Sb_2O_6$  will be discussed in detail in Chapter 3 to evaluate the effect of structural substitutions on the observed photocatalytic activity of the samples. The phase transitions of the ideal pyrochlore solid solution  $Cd_2Nb_2O_{7-x}S_x$  will be discussed in Chapter 4 to help elucidate the origin of ferroelectricity in this system.

### 1.3.2 The Hollandite Structure

The hollandite structure can be understood by first describing the rutile structure, typified by the oxide  $TiO_2$ . The rutile structure, shown in Figure 1.10a, is described an HCP lattice of anions with  $\frac{1}{2}$  of the

octahedral holes filled. The  $\text{TiO}_6$  octahedra form edge-sharing chains that can be viewed down the  $b$ -direction of multiple unit cells. These chains are additionally connected by corner-sharing octahedra, and a 1 chain x 1 chain x 1 chain x 1 chain channel structure is formed. In the hollandite structure  $\text{A}_x\text{M}_4\text{O}_8$ , the  $\text{MO}_6$  octahedra retain the edge- and corner-sharing characteristics of the rutile structure, but the channel is created by two edge-shared chains (Figure 1.10b), creating a 2 x 2 x 2 x 2 channel.

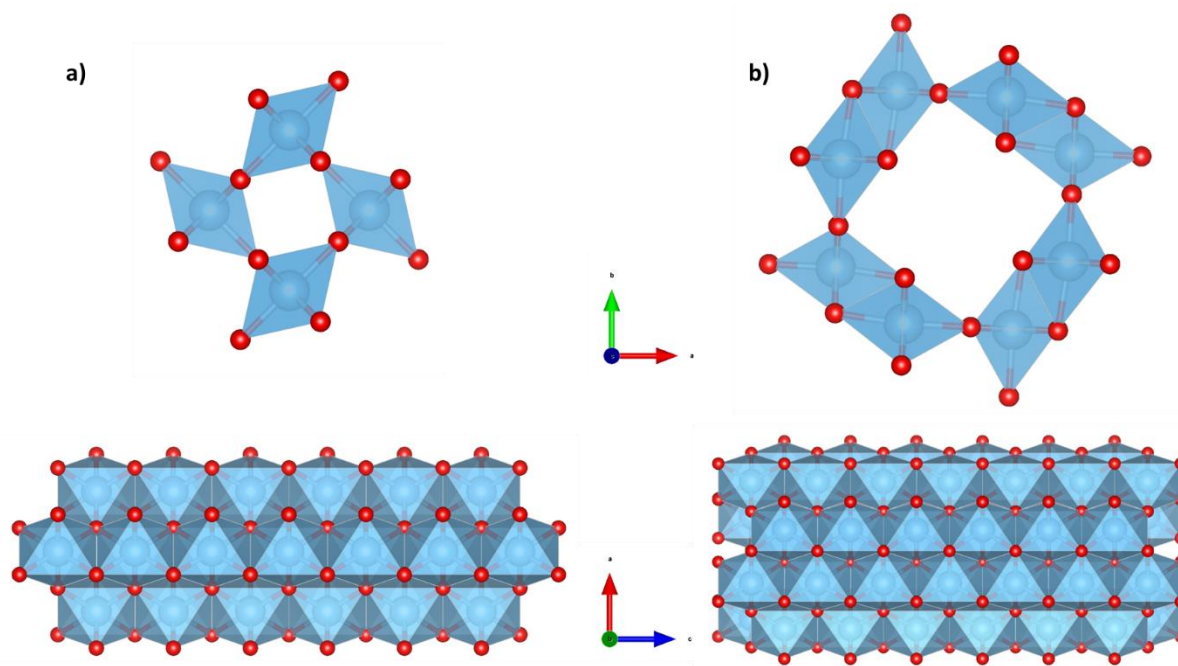


Figure 1.10 a) The 1 x 1 x 1 x 1 channel structure of rutile, formed by corner-shared chains of edge-shared octahedra; b) the 2 x 2 x 2 x 2 channel found in the hollandite structure composed of two chains of edge-shared octahedra linked together through corner-sharing.

The hollandite  $\text{A}_x\text{M}_4\text{O}_8$  crystallizes in a tetragonal structure with space group symmetry  $I4/m$  (Figure 1.11). The M transition metals found on the variable  $8h$  site include Ti, Cr, Mn, Mo, Rh, or Ru. The tunnel formed by the corner-shared double chains of edge-shared  $\text{MO}_6$  octahedra can house a large A cation in the fixed  $2b$  site, such as  $\text{K}^+$ ,  $\text{Rb}^+$ , or  $\text{Cs}^+$ . The substitution of smaller cations into this lattice is sustained by the ordered co-presence of one of these large cations. An example of an ordered hollandite

is  $\text{Cs}_{0.8}\text{Li}_{0.2}\text{Ru}_4\text{O}_8$ . [14–17] Chapter 5 will focus on the effect of Na-substitution into the A-site of hollandites  $\text{ARu}_4\text{O}_8$  ( $A = \text{Na}^+, \text{K}^+, \text{Rb}^+$ ) to evaluate the effect on the quasi-one dimensional conduction displayed by these materials.

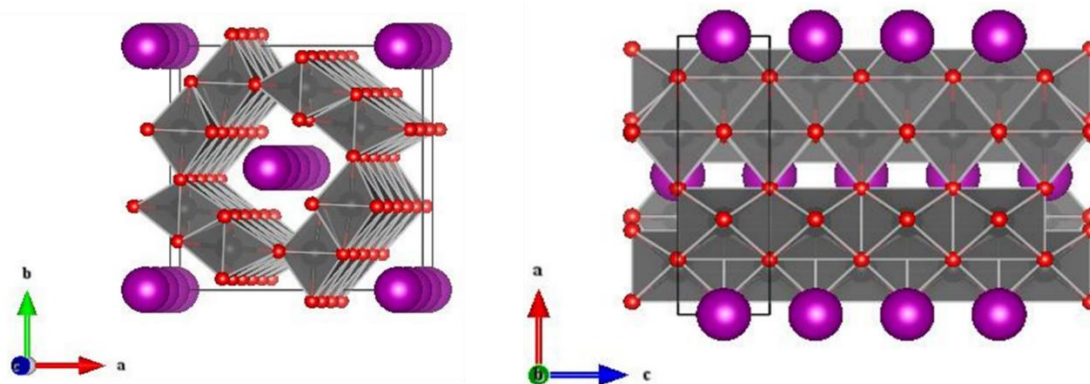


Figure 1.11 The hollandite structure  $A_xB_4O_8$ , shown here with  $x = 1$ . “A” atoms are shown in purple, “B” in charcoal, and “O” in red.

### 1.3.3 The $\text{YbFe}_2\text{O}_4$ Structure

The final structure type discussed in this dissertation is the  $\text{YbFe}_2\text{O}_4$  structure. To describe this structure it is helpful to begin with describing the  $\text{YAlO}_3$  structure. This structure can be referred to as a hexagonal  $\text{AMO}_3$  structure, and is a variant of HCP packed anions. The packing scheme is not strictly HCP, but consists of two offset “ABA” layers, shown in Figure 1.12a. The A cations occupy octahedral sites, and the B cation sits in a trigonal bipyramidal (TBP) site, shown in Figure 1.12b.

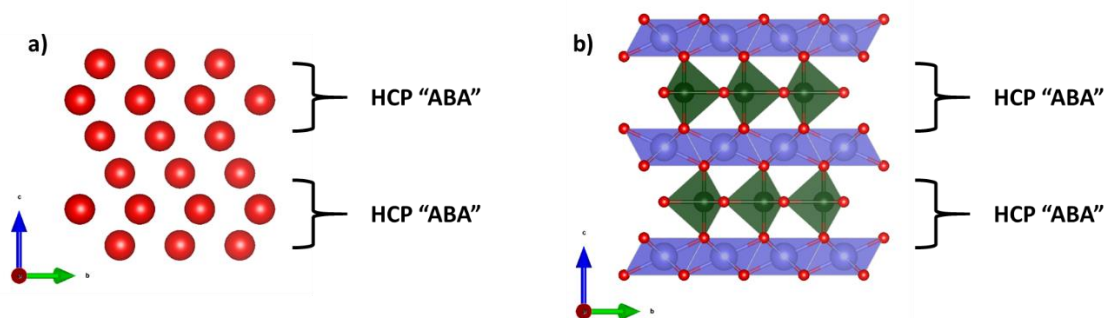


Figure 1.12 The two offset HCP layers in the hexagonal  $\text{AMO}_3$  structure (a) with “A” cations, blue, in octahedral sites and “M” cations, green, in trigonal bipyramidal sites (b).

Due to the complicated packing scheme, it is easier to describe the hexagonal  $AMO_3$  structure in terms of polyhedral layers. This structure is composed of alternating layers of edge-shared distorted  $AO_6$  octahedra (described in some literature as trigonal antiprisms) and corner-shared  $MO_5$  TBPs, shown in Figure 1.13a.[18–21] The  $AM_2O_4$  structure (Figure 1.13b), typified by  $YbFe_2O_4$ , retains the layers of  $AO_6$  octahedra, but the alternating layer is a double-layer of edge shared TPBs. This new configuration creates octahedra that are less distorted than in  $YAlO_3$ , and the M cation displaces from the center of the trigonal bipyramidal site. These changes are accompanied by a change in space group from  $P6_3/mmc$  to  $R\bar{3}m$ .

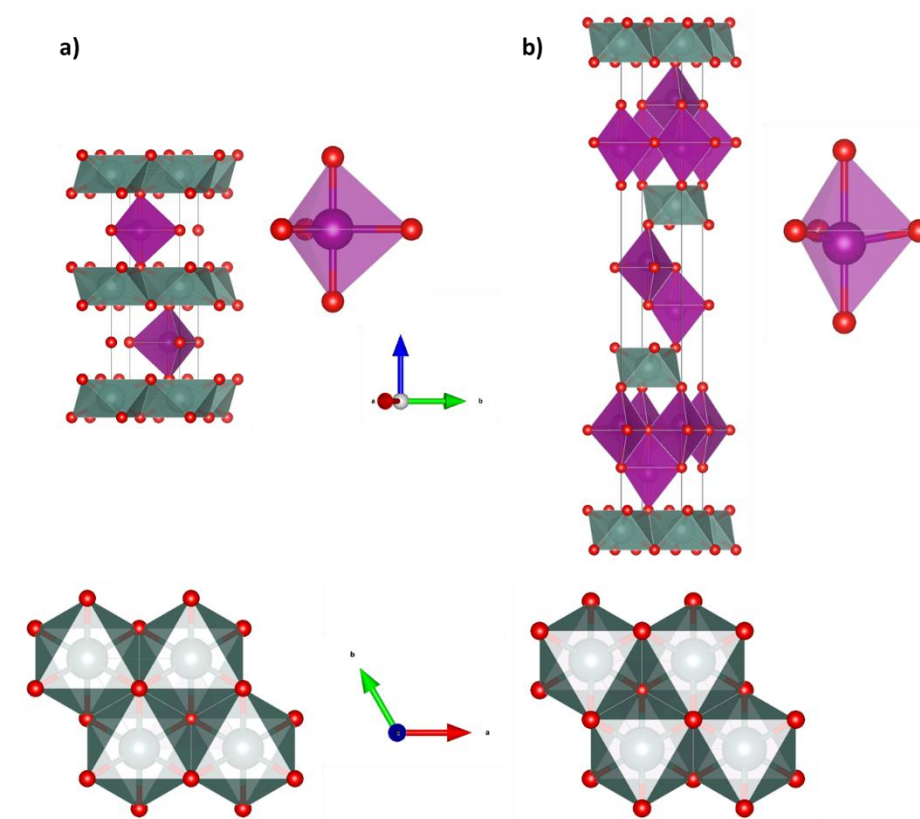


Figure 1.13 a) The hexagonal  $AMO_3$  structure described as alternating layers of edge-shared distorted  $AO_6$  octahedra (shown in green) and corner-shared  $MO_5$  trigonal bipyramids (shown in purple). In this structure, the “M” cation sits directly in the middle of the trigonal bipyramidal site. b) The hexagonal  $AM_2O_4$  structure with alternating layers of edge-shared  $AO_6$  octahedra (shown in green) and edge-shared double layers of  $MO_5$  trigonal bipyramids (shown in purple). This double layer of trigonal bipyramids results in an off-center shift of the M cation.

The  $\text{YbFe}_2\text{O}_4$  structure can be re-written as  $(\text{A}^{3+}\text{M}^{3+}\text{O}_3)(\text{M}^{2+}\text{O})$  to reflect the insertion of an additional TBP layer into the unit cell. In general,  $\text{A}^{3+}$  is typically a rare-earth atom, In, or Sc. Reported  $\text{M}^{3+}$  cations include Fe, Mn, Ga, Lu, and Al, and  $\text{M}^{2+}$  cations include Fe, Mg, Mn, Cd, Co, Cu, and Zn.[22] One compound of interest in the  $\text{YbFe}_2\text{O}_4$  family is the transparent conducting oxide  $\text{InGaZnO}_4$ , shown in Figure 1.14. In this compound the In atoms occupy the octahedral sites and the Ga and Zn atoms are disordered in the TBP sites. Appendix A focuses on the modeling of amorphous films of  $\text{InGaZnO}_4$  for electronic applications based on this crystalline structure.

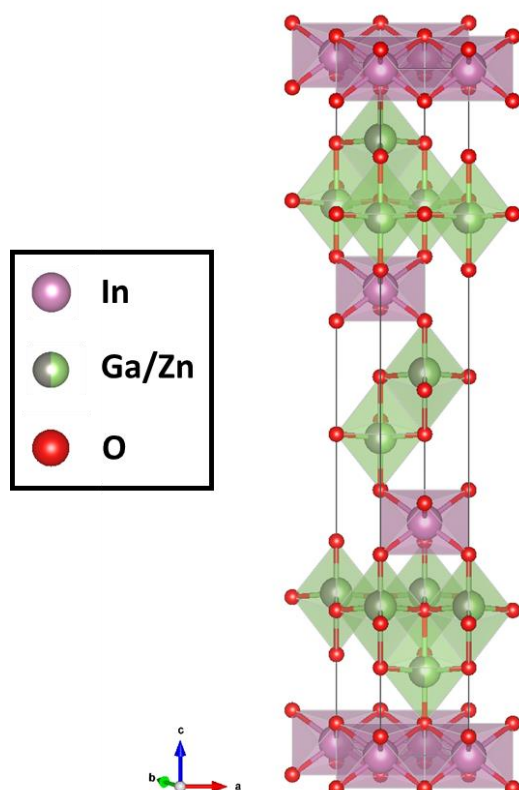


Figure 1.14 A unit cell of crystalline  $\text{InGaZnO}_4$  with space group symmetry  $R\bar{3}m$  consists of alternating layers of edge-shared  $\text{InO}_6$  octahedra and edge-shared  $\text{Ga/ZnO}_5$  trigonal bipyramids. The Ga and Zn atoms are disordered in the trigonal bipyramid sites.

#### 1.4 References

- [1] International Union of Crystallography, <http://www.iucr2014.org/> (2014).
- [2] N. Media, [http://www.nobelprize.org/nobel\\_prizes/physics/laureates/1915/index.html](http://www.nobelprize.org/nobel_prizes/physics/laureates/1915/index.html) (2014).
- [3] R.D. Shannon, *Acta Crystallogr. Sect. A Found.* 32 (1976) 751.
- [4] L. Pauling, *J. Am. Chem. Soc.* 51 (1929) 1010.
- [5] J.P. Smit, P.C. Stair, K.R. Poeppelmeier, *Chemistry* 12 (2006) 5944.
- [6] S.M.A. Greaves, C. Katib, *Mater. Res. Bull.* 25 (1990) 1175.
- [7] A.R. Mather, G. C. Smith, R. I., Skakle, J. M. S Fletcher, J. G Castellanos, M. A. Gutierrez, M. P. West, *J. Solid State Chem.* 10 (2000) 2219.
- [8] R. Berthelot, W. Shmidt, S. Muir, J. Eilertsen, L. Etienne, A.W. Sleight, M.A. Subramanian, *Inorg. Chem.* 51 (2012) 5377.
- [9] F. Jona, G. Shirane, R. Pepinsky, *Phys. Rev.* 98 (1955) 903.
- [10] R. Jin, J. He, S. McCall, C. Alexander, F. Drymiotis, D. Mandrus, *Phys. Rev. B Condens. Matter* 64 (2001) 180503.
- [11] M.A. Subramanian, G. Aravamudan, G.V. Subba Rao, *Prog. Solid State Chem.* 15 (1983) 55.
- [12] A.W. Sleight, *Inorg. Chem.* 7 (1968) 1704.
- [13] J.E. Greedan, *J. Mater. Chem.* 11 (2001) 37.
- [14] M.. Foo, W.-L. Lee, T. Siegrist, G. Lawes, a. . Ramirez, N.. Ong, R.. Cava, *Mater. Res. Bull.* 39 (2004) 1663.
- [15] W. Kobayashi, *Phys. Rev. B* 79 (2009) 155116.
- [16] T. Toriyama, M. Watanabe, T. Konishi, Y. Ohta, *Phys. Rev. B* 83 (2011) 195101.
- [17] A. Pautrat, W. Kobayashi, *EPL* 97 (2012) 67003.
- [18] H.L. Yakel, W.C. Koehler, E.F. Bertaut, E.F. Forrat, *Acta Crystallogr.* 16 (1963) 957.
- [19] B. van Akin, A. Meetsma, T. Palstra, *Acta Crystallogr. Sect. C Cryst. Struct. Commun.* 57 (2001) 230.
- [20] B. van Akin, A. Meetsma, T. Palstra, *Cond. Mat.* (2001) 0106298.

[21] B. van Akin, A. Meetsma, T. Palstra, *Acta Crystallogr. Sect. E Struct. Reports Online* 57 (2001) 87.

[22] R. Graczyk, M.A. Subramanian, *Prog. Solid State Chem.* (2014).

## CHAPTER 2

### Fundamentals of Solid State Chemistry: Synthesis, Material Properties, and Characterization Methods

#### 2.1 Sample Synthesis

##### 2.1.1 *Standard Solid State Synthesis*

The majority of the materials in this dissertation were synthesized through the standard solid state synthesis method. Also referred to as “shake-and-bake” or “beat-and-heat”, this method relies on elevated temperatures for atomic diffusion and reaction. This synthesis route begins with a stoichiometric amount of powdered starting materials, typically metal oxides or metal carbonates. These powders are mechanically ground together in a mortar and pestle or ball milled and then pressed into a pellet before heat treatment. This treatment provides smaller particle sizes and maximum contact between particles, facilitating atomic diffusion between the starting reagents. Once prepared, the sample is heated to temperatures between 400-1500°C. The target temperature is governed by the elemental composition of the sample, and properties such as volatility, melting point, and reactivity (with both either starting reagents and reaction container) must be taken into consideration. The reaction may be a slow process, so subsequent grinding, pressing, and heating processes may be needed for reaction completion.

The formation of materials through this route is both a combination of kinetics and thermodynamics, but can be thermodynamically predicted through the consultation of phase diagrams. High-temperature synthesis is employed to overcome diffusion barriers and lattice enthalpies, and diffusion is often the limiting factor of reactivity. A typical solid state reaction begins at the interfaces between particles of starting reagents, and product formation occurs at this interface, illustrated in Figure 2.1. Further reaction of the starting materials is facilitated by diffusion through the product phase, and it is here that diffusion rates are limited. For this reason intermediate grinding between successive heating

intervals are crucial for complete product formation, as it creates new interfaces of unreacted starting material for product formation.

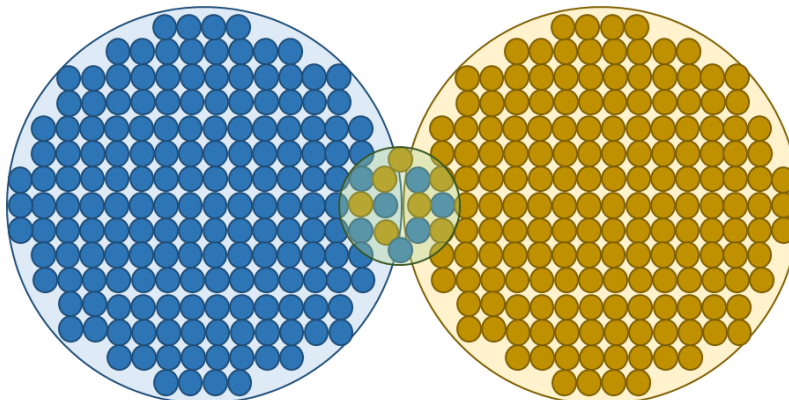


Figure 2.1 Reaction interface of two particles of starting reagents. Figure adapted from [1].

### 2.1.2 Molten Salt Ion Exchange

Another major synthesis method employed in this dissertation is molten salt ion exchange. This method relies on the topotactic exchange of ions in a structure, illustrated in Figure 2.2. In a topotactic reaction, one of the reactants acts as a host structure, and ions (in this case cations) from the host phase are exchanged for those from the surrounding phase. Molten salt ion exchange uses a water-soluble salt with low a low melting point, such as alkali halides or nitrates as the liquid media and source of exchange ions. For the exchange reaction, the parent compound is combined with the alkali salt in an excess molar ratio of the salt. Once thoroughly combined, the mixture is placed in an appropriate reaction vessel and heated above the melting point of the salt. Once in a liquid state, diffusion of the alkali cations into the host structure can occur, with counter-diffusion of host structure cations into the molten liquid phase. After cooling, any excess alkali salt or salt from the exchanged host cation can be removed by washing with water.

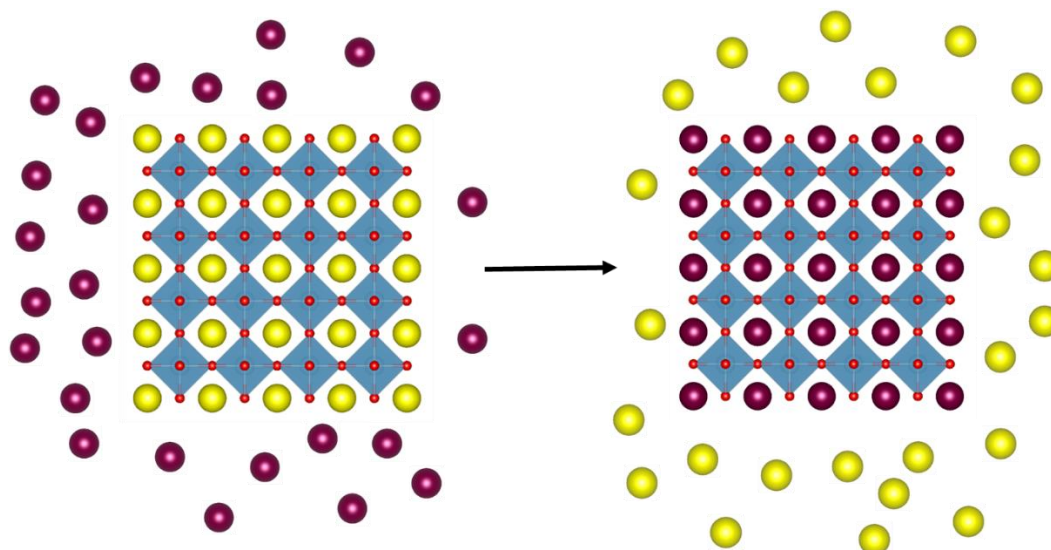


Figure 2.2 Pictorial representation of an idealized topotactic ion exchange process.

Once synthesized, the structure of a material can be determined through various scattering techniques outlined in the following section.

## 2.2 Structural Characterization

### 2.2.1 *Scattering in Materials*

A highly effective way of determining the structure of a material is to irradiate a sample with a beam of particles and observe the interaction with the material. A particle beam can interact with an atom through either elastic or inelastic scattering events. In an elastic scattering event, there is a complete momentum and energy transfer from the incident to the scattered beam, or  $k_i$  is equal to  $k_f$  (Figure 2.3). In an inelastic scattering event, some of the momentum and energy is lost to the interaction. While

inelastic scattering can provide information about a material (for example, phonon dispersion curves in inelastic neutron scattering), this dissertation will focus on experiments employing elastic scattering.

Based on the wavelength of the particle beam,  $\lambda$ , and the scattering angle,  $\theta$ , the magnitude of the momentum transfer (or the scattering vector),  $Q$ , can be determined according to Equation 2.1 [2]:

$$Q = \frac{4\pi\sin\theta}{\lambda} \quad (2.1)$$

This relationship is illustrated in Figure 2.3. The momentum transfer  $Q$  is a useful quantity, as it can facilitate structure comparison between radiation sources with varying wavelength.

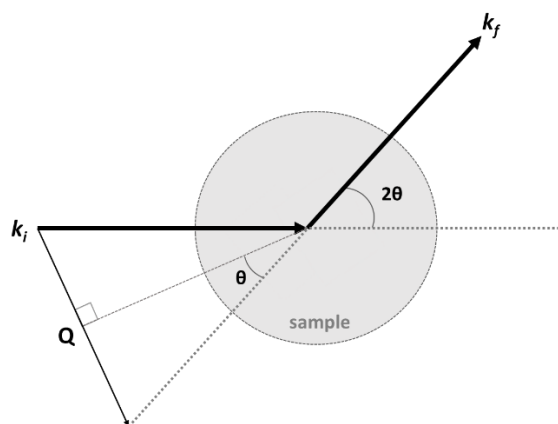


Figure 2.3 Schematic of the derivation of  $Q$  from an elastic scattering event ( $k_i = k_f$ ).[2]

The structural probe used for a scattering experiment must have the appropriate wavelength for interaction, and for characterization on the atomic scale, this limits the wavelength of the particle beam to 0.1 – 100 Å. Based on these criteria, the best candidates for structural analysis are electrons, neutrons, and X-rays. These particles interact with the atoms in the material differently, and this must be taken into account when planning a scattering experiment. Illustrated in Figure 2.4, the various particles have varying penetration depths into the material. An electron beam, shown in 2.4a, interacts with the electrons of an atom through electrostatic repulsion. This repulsive force is very strong, and the result is a shallow

penetration depth of the electron beam. This type of scattering is useful for surface characterization, but cannot give information on the inner structure of a material. As this dissertation focuses on bulk structural characterization, studies involving electron scattering were not performed and will not be further discussed. X-rays can be scattered by the electrons of an atom through electromagnetic interactions (Figure 2.4b). Unlike an electron beam, an X-ray is not charged, and thus exhibits a farther penetration depth into the material. Neutrons interact with the nucleus of a material (Figure 2.4c), and can achieve the farthest penetration depth because they are not affected by the Coulombic barrier of an electron surrounding an atom. Neutrons possess a magnetic dipole, and if there are any unpaired electrons in a system, the neutrons will exhibit a dipole-dipole interaction with the electron (Figure 2.4d), giving rise to magnetic scattering. Both X-rays and neutrons exhibit penetration depths that allow for analysis of the bulk of the structure, and the choice between these two probes depends on the atoms present in the material.

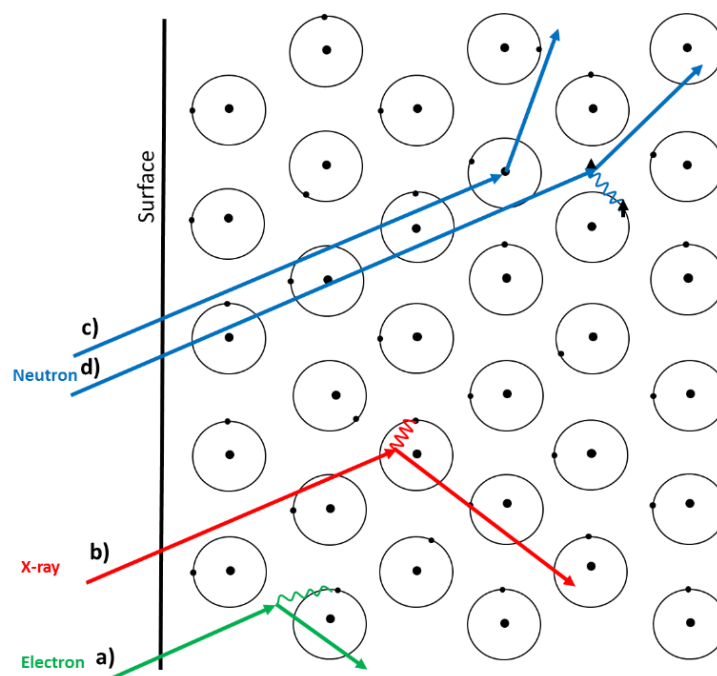


Figure 2.4 Interaction of an electron through the repulsive force of an atom's electrons (a), X-ray through electromagnetic interaction with an electron (b), and neutrons through dipole interactions with the nucleus and magnetic interactions with unpaired electrons (c and d, respectively). [2]

The fact that X-rays and neutrons interact with different parts of the atom has very important implications on the choice of probe used for structural studies, and often complementary scattering experiments are performed to gather information on different aspects of the structure. As X-ray radiation interacts with the electrons in a material, the scattering strength of an atom is proportional to the number of electrons it possesses (Figure 2.5, black data points). This means that X-rays are scattered very well by atoms with a high atomic number, and can prove to be problematic when trying to study a material with both light and heavy atoms present, such as PbO. The scattering strength of a neutron, however, is not dependent on the atomic number (Figure 2.5, red data points), and the use of neutron scattering can be employed to lessen the contrast between atoms with large differences in atomic numbers. This is especially crucial when trying to determine the position and site occupancy of lighter atoms such as hydrogen and oxygen.

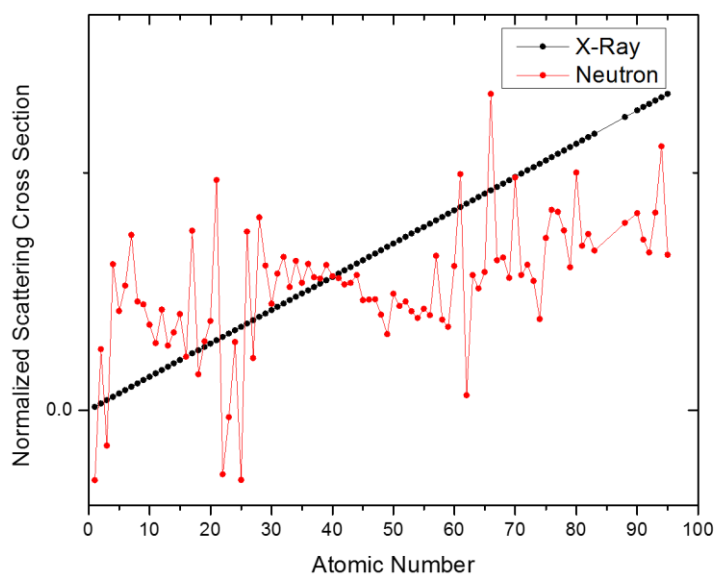


Figure 2.5 Normalized scattering cross sections of X-rays (black) and neutrons (red) as a function of atomic number.

Neutrons can also provide contrast where X-rays cannot; for example, if a material contains both Ni and Cu (atomic numbers 28 and 29, respectively), X-ray scattering is unable to provide enough contrast to determine positional and occupational differences between the two. The neutron scattering lengths of Ni and Cu (10.3 and 7.718 barn, respectively) provide enough contrast to accurately determine the position and occupancy of each. [3] Careful consideration of the atoms in a material and the nature of the data needed must be exercised when choosing a scattering probe, and only then can various techniques be employed to accurately study the structure.

## 2.2.2 Powder Diffraction

### 2.2.2.1 X-ray Diffraction

A powerful tool for the study of crystalline materials is powder X-ray diffraction (PXRD). A PXRD experiment requires a source of X-ray radiation; this is commonly an X-ray tube or a synchrotron particle accelerator. Laboratory X-ray diffractometers utilize an X-ray tube consisting of a metal target, which acts as the anode, and a source of electrons (typically a tungsten filament) acts as the cathode. A schematic of an X-ray tube is illustrated in Figure 2.6. To generate X-rays, a large voltage potential is applied across the anode and the cathode, resulting in a flow of high speed electrons from the filament to the metal target. Upon collision with the metal target, a continuous spectrum of X-rays is generated. This continuous spectrum of radiation is a result of the rapid acceleration and deceleration of electrons interacting with the target, and is called white radiation or Bremsstrahlung, which means “braking radiation”.

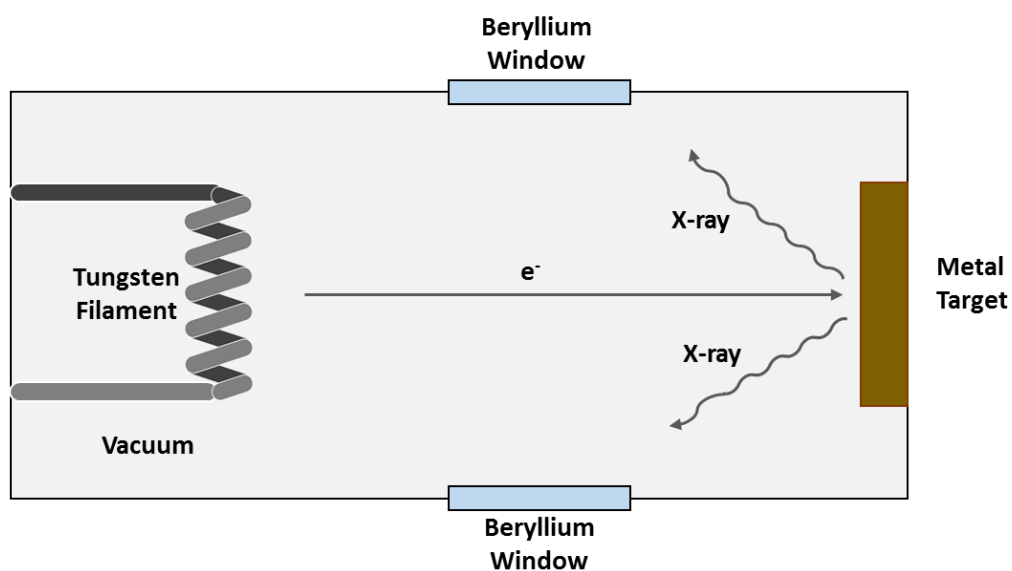


Figure 2.6 Schematic Diagram of an X-ray tube.

If a high enough voltage is applied, the generated electrons can displace electrons from the inner shell of the metal target. Electrons in a higher energy shell will relax to fill this hole, and X-ray radiation will be generated. This type of X-ray radiation is monochromatic and called characteristic radiation, as the precise wavelength is dependent on the identity of the metal target. Targets used in laboratory X-ray diffractometers include Cu, Mo, Co, Fe, Cr, W, and Ag, as the characteristic radiation is on the order of atomic distances (0.1 – 100 Å). The most common target used is Cu, which emits three characteristic radiation wavelengths:  $K\alpha_1$  ( $\lambda = 1.54041 \text{ \AA}$ ),  $K\alpha_2$  ( $\lambda = 1.54443 \text{ \AA}$ ), and  $K\beta_1$  ( $\lambda = 1.3927 \text{ \AA}$ ). The  $K\beta_1$  is typically filtered out at the expense of some intensity of the  $K\alpha$  radiation, but allows for easier data analysis. The generated characteristic radiation exits the X-ray tube through beryllium windows, and may be passed through a series of focusing optics, such as monochromators or slits. Once the X-rays pass through the focusing optics, they will reach the sample stage and then diffract to the detector. A general schematic of an X-ray diffractometer is shown in Figure 2.7.

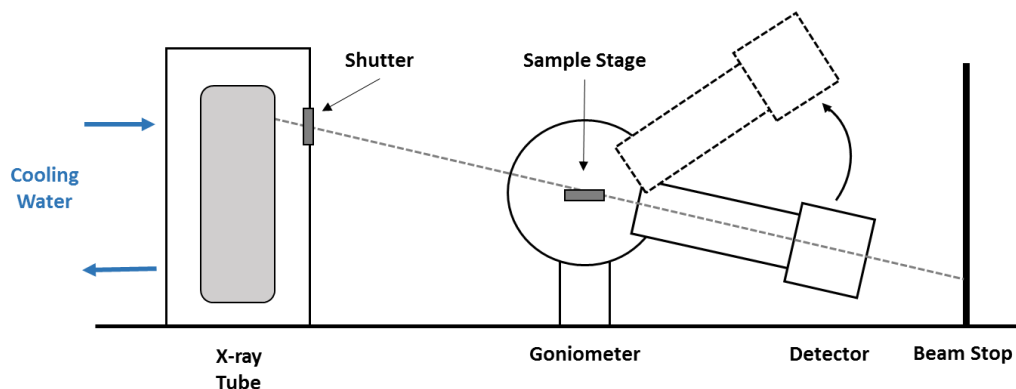


Figure 2.7 Basic schematic diagram of a Rigaku Miniflex-II diffractometer.[4]

As discussed in section 2.2.1, X-rays interact with the electrons of an atom through electromagnetic waves. In a crystalline material, the incident X-rays are scattered in all directions, and this scattering can either be in phase (constructive) or out of phase (destructive). Diffraction occurs in a crystalline material when constructive interference is observed in accordance with Bragg's Law, shown below in Equation 2.2 and illustrated in Figure 2.8.

$$n\lambda = 2d\sin\theta \quad (2.2)$$

In Bragg diffraction, X-ray radiation with a wavelength  $\lambda$  is scattered from periodic planes of atoms with a spacing distance  $d$ . The constructive scattered beam is diffracted at the same angle  $\theta$  (with respect to the plane of the atom) at the incident beam.

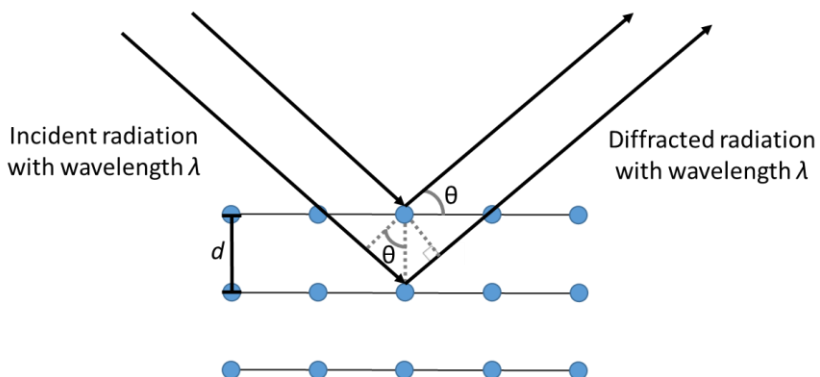


Figure 2.8 Schematic of Bragg's Law in relation to an incident and diffracted beam from a lattice.

The Bragg condition for various planes are accessed at different values of  $\theta$ , and a PXRD pattern displays the intensity of the diffracted X-rays as a function of  $2\theta$ . The diffracted X-rays are collected at the detector of the diffractometer and by sweeping a range of  $\theta$ , a complete diffraction pattern can be obtained for a crystalline sample. From this pattern, information about the unit cell, including cell dimensions, atomic positions, atomic thermal vibrations, and site occupancy can be determined. The diffraction pattern of NaCl is shown as an example in Figure 2.9. Each peak in the pattern arises from diffraction off of different lattice planes in the material, defined by Miller indices ( $hkl$ ). For NaCl, the two strongest peaks arise from interaction with the (200) plane of atoms (shown in blue) at  $2\theta = 31.8^\circ$  and the (220) plane of atoms (shown in green) at  $2\theta = 45.6^\circ$ .

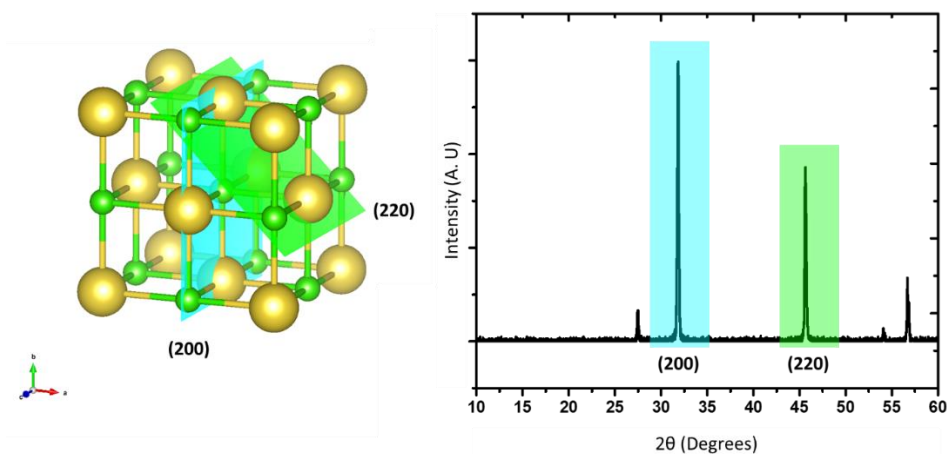


Figure 2.9 Diffraction peaks generated from the (200) lattice plane (blue) and the (220) lattice plane (green) in NaCl.

Based on the exact  $2\theta$  value of the various  $hkl$  planes observed in a diffraction pattern, the unit cell dimensions  $a$ ,  $b$ , and  $c$  can be calculated for a cubic unit cell using equation 2.3 in conjunction with Bragg's Law:

$$\frac{1}{d_{hkl}^2} = \frac{h^2 + k^2 + l^2}{a^2} \quad (2.3)$$

Information about the atomic positions, thermal vibrations, and occupancies can be extracted from the peak intensity, and will be further covered in section 2.2.4.1.

PXRD diffraction experiments using synchrotron radiation differs from a X-ray tube experiment in the way that the X-rays are generated. At a synchrotron source, electrons are generated by an electron gun such as the LINAC system at the Advanced Photon Source, Argonne National Laboratory. These electrons are then accelerated in a booster ring, and then transferred to a storage ring. A continuous spectrum of electromagnetic radiation is generated as the electron beam passes through bending magnets, and high energy X-rays are separated at various beam lines by passing the electromagnetic radiation through wigglers or undulators. The wavelength of the X-ray beam is then selected with a Laue double-crystal monochromator, and after passing through focusing optics, the sample is irradiated. Although the phenomenon of Bragg diffraction will still occur, synchrotron radiation has advantages of higher intensity, better counting statistics, faster acquisition time, and higher resolution than can be obtained with an X-ray tube. X-ray experiments for this dissertation were performed at Oregon State University (OSU) (all chapters) and at the Advanced Photon Source, Argonne National Laboratory (Chapter 4 and Appendix A).

### 2.2.2.2 *Neutron Diffraction*

Neutron diffraction is often used as a complementary technique to PXRD when a very detailed structural analysis is needed. In neutron and X-ray diffraction, the concept of diffraction is essentially the same, as defined by Bragg's Law. Neutron diffraction can be used to determine the structural and atomic parameters of materials that have both light and heavy atoms present. It can provide contrast between atoms with similar atomic numbers, as well as contrast between different isotopes of the same atom. Neutron diffraction can provide additional information about the magnetic structure of a material:

neutrons exhibit a dipole moment and can therefore interact with unpaired electrons in a magnetic material. The magnetic ordering of a material will manifest itself in neutron diffraction. For example, ferromagnetic ordering in a material results in a change in the peak intensity of peaks already present that arise from magnetic atoms, whereas antiferromagnetic ordering results in the emergence of new peaks that were not present before the magnetic transition temperature. A more detailed discussion of the types of magnetic interactions in a material can be found in section 2.5.

Neutrons can be generated through either a nuclear fission or spallation process, and experiments can be performed at either a reactor or spallation source, respectively. Neutrons at a reactor have the advantage of easier data analysis due to their monochromatic nature, and give better resolution at higher  $d$ -spacing. Neutrons produced at a spallation source have a higher incident flux as more neutrons with appropriate energy are released via spallation than fission. In a spallation process, a metal target is bombarded by pulses of a proton beam, and the neutrons are released in pulses. This results in a polychromatic beam of neutrons, which is measured by the time it takes for each neutron to travel to a detector. As such, spallation radiation is called time-of-flight (TOF), and the nature of this must be considered in data analysis. TOF neutron experiments for this dissertation were performed at the Lujan Neutron Scattering Center, Los Alamos National Laboratory (Chapter 3) and the Spallation Neutron Source, Oakridge National Laboratory (Chapter 5 and Appendix 1).

### 2.2.3 *Total Scattering Techniques*

Bragg's Law is an extremely powerful tool that led to the advent of the field of crystallography and has allowed generations of scientists to determine the structure of numerous crystalline materials. Although powerful, Bragg diffraction relies on a perfectly periodic lattice and in reality no such materials exist. Even in a highly crystalline material, defects and atom-atom interactions gives rise to disorder in a

material. These short range, or local, atom-atom interactions result in what is called diffuse scattering. Bragg diffraction gives information about the average structure of a material, as it is a result of interactions over an infinite distance, or has a long-range correlation. The local structure, however, only relies on short-range interactions and can deviate significantly from the average structure. Consider the examples in Figure 2.10. Figure 2.10a shows octahedra with central atoms that are correlated, or ordered, over a long range and as a result, the average structure determined by Bragg diffraction is the same as the local octahedron. In Figure 2.10b, the central atom in the octahedra are displaced to the right, and this displacement is correlated over long ranges, and is therefore reflected in the average structure as a static displacement of the central atom. Contrary to the first two examples, Figure 2.10c illustrates a case in which the central atom is disordered about the center of the octahedra. This is represented in the average structure as an enlarged thermal parameter, but there are still local atomic correlations that give rise to diffuse scattering can have important implications on the properties of a material.

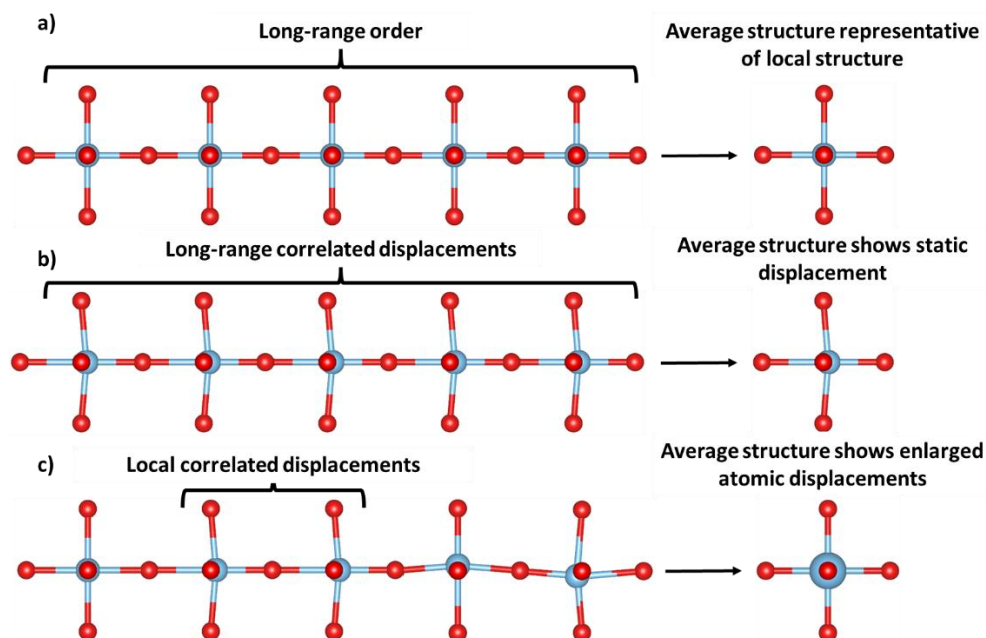


Figure 2.10 Examples of a) an average structure that is representative of the local structure, b) long –range correlated local displacements that are shown as a static displacement in the average structure, and c) disordered local displacements with some local correlations represented as enlarged thermal parameters in the average structure.

In the analysis of diffraction data, diffuse scattering is usually ignored and dealt with through background modeling. In the total scattering technique, all scattering events, both Bragg and diffuse, are utilized to study a structure via its pair distribution function (PDF). The PDF of a material yields a real-space distribution of the interatomic distances and describes the “probability” of finding atomic pairs separated by a distance  $r$  in Angstroms.[5] As an example, the PDF of graphite is shown in Figure 2.11.

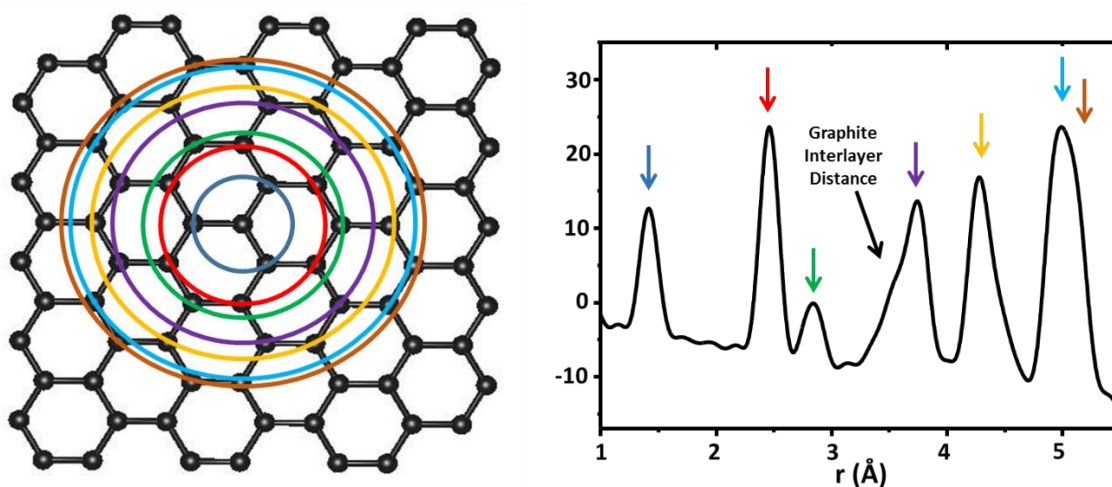


Figure 2.11 The atomic pair distribution function of graphite. Each ring corresponds to a C-C correlation in the PDF.

The analysis of PDFs has traditionally been applied to liquids and glasses where only short range order is present, but this technique has been increasingly utilized to gain insight into crystalline materials that may show local disorder in the form of thermal vibrations, static atomic displacements, mixed valency, and crystalline defects. To perform a total scattering experiment the data is collected in a very similar manner to that of a diffraction experiment, but specific instrumental conditions must be taken into account. To obtain a high quality PDF data needs to be collected to high  $Q$  values, in the range of 20-40  $\text{\AA}^{-1}$ . Therefore, a standard laboratory diffractometer with a Cu X-ray source, which only achieves a maximum  $Q$  of 8  $\text{\AA}^{-1}$ , cannot be used to obtain a good PDF. Typically total scattering experiments are performed at a

synchrotron or neutron source, which produce particles with maximum  $Q$  values between 35-40  $\text{\AA}^{-1}$ . A total scattering experiment must have good  $Q$ -resolution, good counting statistics, and low instrument background for successful data collection. After performing the scattering experiment, the raw data,  $I(Q)$ , is obtained. This must first be treated to remove all background and instrumental contributions to the collected scattering. This includes absorption corrections, multiple scattering, Compton scattering, and any data normalization that is required. After all of these corrections are applied the resulting data is called the total scattering structure function,  $S(Q)$ , and only contains scattering contributions from the sample. To convert between the reciprocal-space  $S(Q)$  to the real-space PDF,  $G(r)$ , a Fourier transform must be performed on the  $S(Q)$  according to Equation 2.4 [5]:

$$G(r) = \frac{2}{\pi} \int_{Q=0}^{Q=\infty} Q[S(Q) - 1] \sin Qr dQ \quad (2.4)$$

Experimental limitations do not allow for an integration over all  $Q$  values, so realistically  $G(r)$  must be integrated over a  $Q_{min}$  to  $Q_{max}$  range.  $Q_{max}$  must be chosen so that a proper balance is obtained between resolution of the peaks in the PDF and artificial termination ripples from the transform cutoff.

#### 2.2.4 Structural Modeling from Scattering Data

Once the data is collected, properly corrected, and normalized, modeling of the structure can be performed. This is typically done by comparison with an initial structural model, which is then refined through a least-squares process to improve the goodness of fit, defined as the difference between the experimental data and the calculated scattering data from the model. The average structure is typically modeled first by a two-step process: Le Bail whole pattern fitting followed by Rietveld analysis. After a good average structure model is obtained, the local structure can be analyzed through either small or large box modeling.

### 2.2.4.1 Average Structure Modeling

A common method of structural refinement from powder diffraction data is the Rietveld refinement method. The peak intensity in an observed diffraction peak is dependent on the scattering power of atoms in the diffraction plane. This scattering power is described by an atom  $j$ 's form factor,  $f_j$ , which in X-ray diffraction is dependent on the number of electrons in the atom. When diffracted from a lattice plane  $hkl$ , the scattered wave is defined by the structure factor of the plane,  $F_{hkl}$ :

$$F_{hkl} = \sum_j f_j e^{-2\pi i(hx_j + ky_j + lz_j)} \quad (2.5)$$

where the coordinates for atom  $j$  are  $x_j$ ,  $y_j$ , and  $z_j$ . [6] Based on structure factors of a model, the Bragg intensity ( $I_k$ ) of all reflections  $k$  at a given data point  $i$  can be calculated. From this the calculated intensity of each point in the diffraction pattern,  $Y_{calc_i}$ , is determined according to Equation 2.6:

$$Y_{calc_i} = Y_{bkg_i} + \sum_k G_{ki} I_k \quad (2.6)$$

where  $Y_{bkg_i}$  is the background intensity at point  $i$ ,  $G_{ki}$  is the value of the normalized peak function at point  $i$  for collective reflections  $k$ . From  $Y_{calc_i}$  the total observed intensity,  $I_{obs}$ , is determined from the structure model and used for least-squares fitting against the experimental diffraction data. [6] For a neutron scattering experiment, the process is the same except the form factor is determined by the atom's neutron scattering length and any magnetic scattering contributions. The largest strength of the Rietveld algorithm is the ability to resolve and calculate intensities from overlapping peaks, leading to more accurate structure determination. [7]

In general the Rietveld process proceeds by refinement of the following parameters: instrumental background, lattice parameters, peak shape (including peak broadening from sample size or strain), atomic positions, atomic displacements, and site occupancies. Additional refinement of instrumental zero and broadening may be performed if these parameters are unknown, but it is recommended to collect

data on a sample that is free of size and strain broadening (for example, a NIST Si Standard) and use the refined instrumental zero and broadening parameters for sample refinement. Rietveld analysis is only applicable if a decent starting structural model is known. However, some structural information can be extracted through the Le Bail method if the only knowledge about the material is the space group.

The method of Le Bail whole pattern fitting is designed to assign reflection positions and estimate their intensities in the absence of a detailed structural model. This method uses the Rietveld algorithm but is modified so that all  $F_{hkl}$  values are set to 1 and peak intensities will be generated where peak reflections occur.[8] Peak reflections are generated based on the space group and lattice parameters of the unit cell, and their position is adjusted through least-squares refinements of the lattice parameters and any instrumental “zero” errors. It is in this step where impurity phases, if present, can be identified and factored into the analysis. The intensity of the peak is simulated by fitting the profile of the peak shape, and this is adjusted by refining peak broadening due to instrumental affects and peak broadening due to sample particle size and structural strain. Based on the profile function chosen to model, peaks are modeled as Gaussian, Lorentzian, or often as a mixture of both. Proper peak shape requires accurate modeling of the data’s background, and several mathematical functions can be applied to do so. Once a good profile fit is obtained, instrumental effects and lattice parameters have been properly determined, and modeling of the atomic parameters can be performed through Rietveld analysis.

As a note, Rietveld analysis can be used without performing a Le Bail fit, but performing a LeBail fit first provides a better starting model for Rietveld analysis, allowing for more accurate structure determination. Average structural analysis through the Le Bail and Rietveld methods can be found in Chapters 3, 4, 5, and Appendix A.

#### 2.2.4.2 Local Structure Analysis: Small and Large Box Modeling

Different methods of structural modeling against a PDF can be performed based on the degree of local disorder in a material. If small amounts of local disorder are present in a material, a least-squares approach similar to the Le Bail and Rietveld method, where the instrumental and unit cell parameters are adjusted until the best goodness-of-fit is obtained, can be used. As this is based on the unit cell, which is typically less than 200 atoms, this is referred to as small box modeling. Examples of small box modeling against PDF data can be found in Chapters 3 and 5. In order to reach convergence in the refinement, a starting model that is reasonably close to the real structure must be used. In the case of a completely unknown structure or large amounts of local disorder, large box modeling approaches such as Reverse Monte Carlo (RMC) modeling must be employed.

To begin an RMC simulation a cell of  $N$  atoms with periodic boundary conditions is generated (Figure 2.12a, top). In cases where the average structure is known but local deviations are too large for small box modeling, a good starting cell would be a supercell of the average structure unit cell. This starting cell can have thousands of atoms, hence the name large box modeling. From this starting configuration the partial PDFs are calculated and then Fourier transformed to obtain the partial structure factors. These partial structure factors are summed to obtain the total structure factor of the starting configuration (Figure 2.12a, bottom), and the difference between the calculated and experimental structure factor,  $\chi^2$ , is determined. To proceed with the RMC simulation, an atom is moved at random (either through translation or swapping), and the cycle of partial PDFs to the goodness-of-fit is repeated (Figure 2.12b). If the goodness-of-fit improves, or  $\chi^2_n < \chi^2_0$ , the move is accepted and this will become the new “starting configuration”. If the goodness-of-fit does not improve, or  $\chi^2_{\text{final}} > \chi^2_{\text{initial}}$ , and is within the probability  $\exp[-(\chi^2_{\text{final}} - \chi^2_{\text{initial}})]$ , the move will be accepted; if it is not within the probability, the move is rejected. This cycle of randomly moving and accepting/rejecting moves is repeated (Figure 2.12c) until  $\chi^2$

is minimized (Figure 2.13d). The basic RMC algorithm is a variation of the Metropolis Monte Carlo Method, but instead of adjusting a structure until energy is minimized, the structure is adjusted to minimize the goodness-of-fit parameter.[9] Unlike Rietveld analysis and small box PDF modeling, RMC modeling does not result in a unique structural solution. While constraints such as coordination numbers and bond valence sums can be applied to guide the RMC process, it is highly advisable to perform an RMC simulation against multiple data sets. The application of RMC modeling of amorphous thin films can be found in Appendix A.

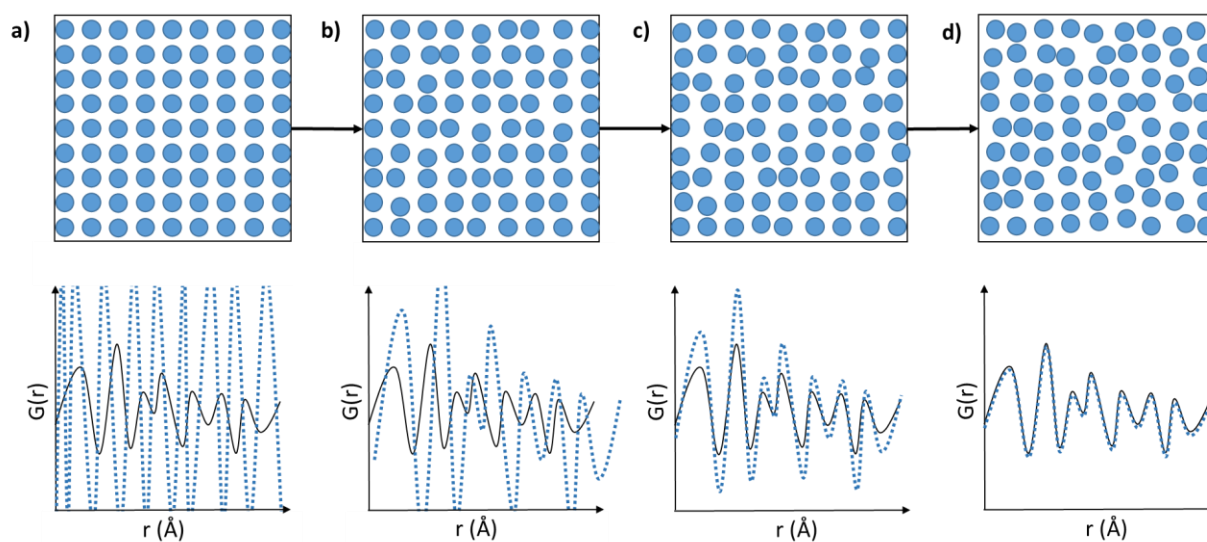


Figure 2.12 Illustration of the structure (top boxes) and the generated PDF (blue dotted line) against the experimental data (solid black line) through the RMC modeling process.

### 2.2.5 Characterization of Amorphous Materials

Crystalline materials exhibit a long range periodicity, allowing for the analysis of their structure through traditional crystallographic methods such as diffraction. While still crystalline, many materials exhibit defects in their structure which can lead to disorder in their structure. The extent of these defects can lead to varying degrees of disorder, creating a range of disordered materials, shown in Figure 2.13.

On the high end of disorder is an amorphous material, which completely lacks any kind of medium or long range order.

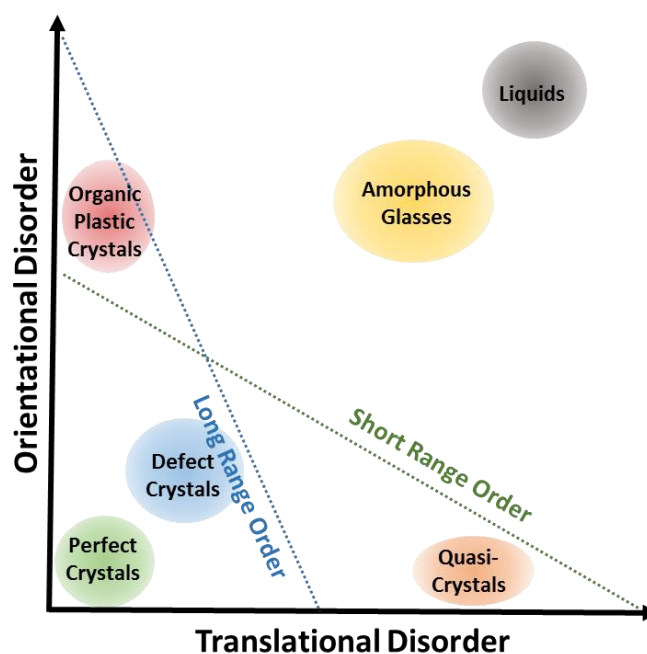


Figure 2.13 Types of materials based on various degrees of disorder. Figure adapted from [10].

An example of crystalline vs. amorphous  $\text{SiO}_2$  is shown in Figure 2.14. The phase of crystalline  $\text{SiO}_2$  depicted in Figure 2.14a ( $\alpha$ -quartz) crystallizes in the space group  $P3_121$  and consists of a periodic array of corner-linked  $\text{SiO}_4$  tetrahedra. This crystalline motif gives rise to two distinct diffraction peaks between  $10\text{-}30^\circ 2\theta$ , and the structure can be easily characterized through analysis of a complete diffraction pattern. However, if we were to randomize the structure as shown in Figure 2.14b, the disappearance of these peaks can be observed. This randomized structure represents that of an amorphous glass, such as fused silica in the case of  $\text{SiO}_2$ .

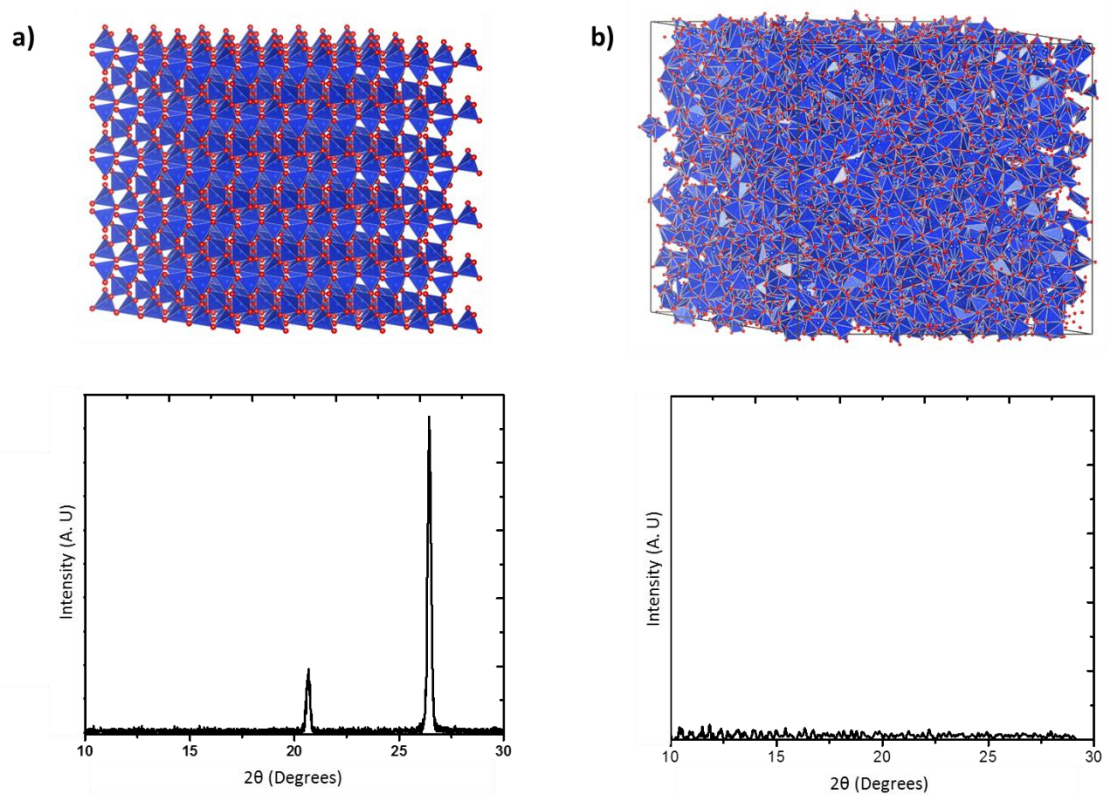


Figure 2.14. a) Structure of crystalline  $\text{SiO}_2$   $\alpha$ -quartz (top) and the calculated diffraction pattern (bottom); b) the structure of randomized  $\alpha$ -quartz to simulate an amorphous  $\text{SiO}_2$  glass (top) and the resulting calculated diffraction pattern (bottom).

Amorphous materials do not possess a symmetry higher than P1, and the lack of translational order in the form of lattice planes makes amorphous materials impossible to study via diffraction techniques.[5] However, there are plenty of local atomic correlations present, making amorphous solids excellent candidates for pair distribution function analysis. Amorphous samples are commonly synthesized through deposition routes such as atomic layer deposition and chemical vapor deposition. [11] Additionally, films can be made through solution processing routes, for example sol-gel or prompt inorganic condensation.[12] However, the principles behind these synthesis routes are outside of the scope of this dissertation.

While diffraction is not an effective technique to study the structure of amorphous films, other techniques have been successfully employed to characterize local atomic interactions. Spectroscopic techniques including XAFS, NMR, IR and Raman spectroscopy can be used to analyze coordination environments of atoms in the material, providing insight into the immediate short range order of an amorphous films.[13–16] However, any information on the presence or extent of mid-range order in the films cannot be provided through these techniques. Not only can the PDF corroborate short-range information, but it contains crucial information on the medium-range order exhibited by the sample. This mid-range order can provide insight the observed bulk properties, such as providing an explanation for a conduction mechanism or correlation lengths for magnetic ordering. When used jointly in an RMC simulation, a detailed understanding of the short- and medium-range order in an amorphous material can be compiled.[17–22] This understanding is paramount for the development of advanced films for optimal device performance. The application of RMC modeling of amorphous thin films of  $\text{InGaZnO}_4$  for electronic applications can be found in Appendix A.

### **2.3 Thermogravimetric Analysis of Materials**

Thermal analysis of a material can provide useful insight into the processes observed in a sample, such as the mass gained during a reaction procedure, the mass lost during a dehydration process, the detection of phase transformations that occur upon heating, and the temperature of sample decomposition. One method of thermal analysis utilized in this work is thermogravimetric analysis (TGA), which sensitively measures the mass of a sample as a function of temperature or time. A plot of the TGA of calcium oxalate ( $\text{CaC}_2\text{O}_4$ ) is shown in Figure 2.15. As  $\text{CaC}_2\text{O}_4$  is heated, three distinguishable mass losses are observed at approximately 160 °C, 470 °C, and 700 °C, corresponding to the loss of water, carbon monoxide (CO), and carbon dioxide ( $\text{CO}_2$ ), respectively. TGA collected at OSU is employed in Chapter 3 to

monitor the weight and corresponding oxygen gain as product formation occurs and in Chapter 5 to monitor sample stability at elevated temperatures.

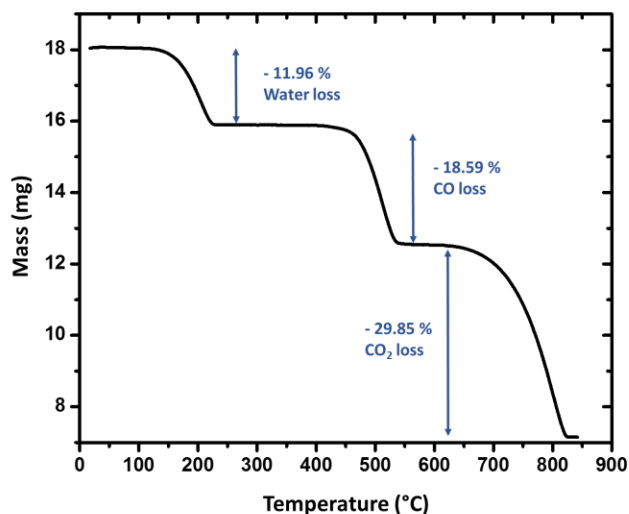


Figure 2.15 TGA plot of mass vs. temperature reveals the various decomposition steps in Calcium Oxalate.

## 2.4 Transport Properties

### 2.4.1 Electronic Properties of Materials

The structural arrangement of atoms in a material has important implications on the observed electronic properties. In Molecular Orbital (MO) theory, linear combinations of atomic orbitals results in molecular orbitals that are either lower (bonding) or higher in energy (anti-bonding) depending on the interactions of the involved atomic orbitals. This concept can be extended to solid materials, but instead of the formation of discrete molecular orbitals, atomic overlap in a solid results in bands composed of a large number of orbitals that are very close in energy. An analog to the Highest Occupied Molecular Orbital (HOMO) in MO theory, the highest energy band of orbitals that contains electrons is called the valence band. The unoccupied band of the next-highest energy is called the conduction band, and the energy

separating the valence and conduction bands is called the band gap ( $E_g$ ). In a metal, illustrated in Figure 2.16a, the highest occupied band is not completely full, and no band gap is present. In semiconductors and insulators (Figure 2.16b and 2.16c, respectively), the valence band is completely occupied, and the magnitude of  $E_g$  differentiates the two. The Fermi Level,  $E_f$ , is the energy level at which there is a 50% probability that an electron will occupy that level. In a metal,  $E_f$  lies in a conducting, delocalized band, while in a semiconductor and insulator  $E_f$  lies within the band gap.

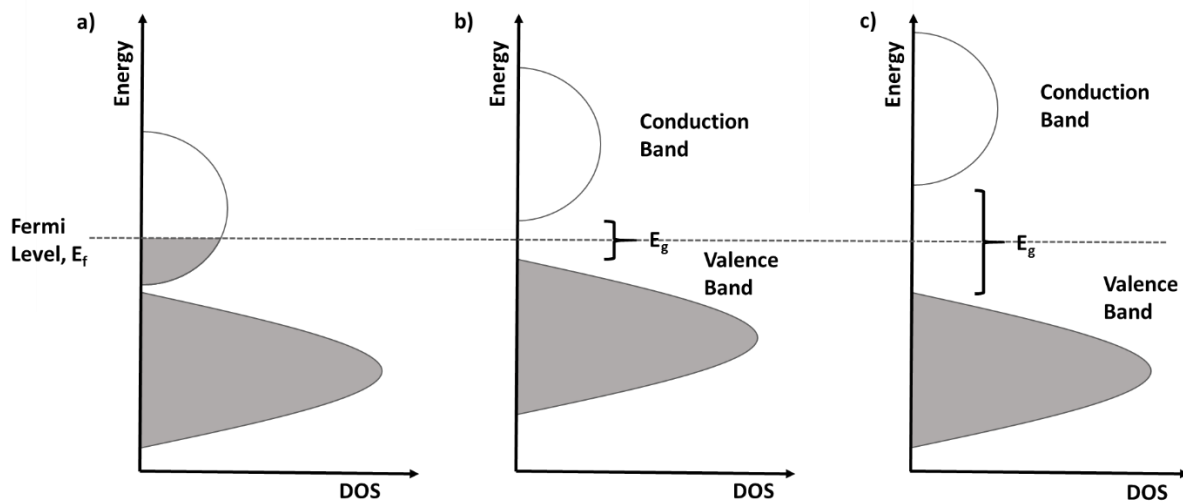


Figure 2.16 Energy vs Density of States (DOS) for a metal (a), semiconductor (b), and insulator (c).

Metals exhibit high conductivity, a result of delocalized electrons that act as a “sea of electrons”.

The electronic conductivity,  $\sigma$ , of a metal can be modeled according to Equation 2.7:

$$\sigma = \frac{e^2 n \tau}{m_e^*} \quad (2.7)$$

where  $e$  is the electron charge,  $n$  is the number of mobile electrons,  $\tau$  is the relaxation time (time between two successive scattering events of the electron), and  $m_e^*$  is the effective mass of the electron.[23] Often the relaxation time and effective mass are modeled as the electron mobility,  $\mu_e$  (Equation 2.8):

$$\mu_e = \frac{e\tau}{m_e^*} \quad (2.8)$$

and the conductivity can be modeled as:

$$\sigma = ne\mu_e \quad (2.9)$$

In a metal the resistivity ( $\rho = 1/\sigma$ ), arises from scattering of the mobile electrons with lattice vibrations, called phonons. As the temperature increases, collisions with phonons become more present, and the resistivity increases. Electrons can also be scattered from defects in a material, including impurities and grain boundaries. For this reason, polycrystalline metals exhibit higher resistivity than their single crystal counterparts.

Both semiconductors and insulators have a valence and conduction band separated by the band gap. In intrinsic semiconducting materials,  $E_g$  is small enough that electrons can be promoted from the valence band to the conduction band. As this is a thermal effect, promotion becomes more energetically favorable at higher temperatures, and consequently conductivity increases with temperature. If  $E_g$  is too large for an electron to cross, the resulting material is an insulator and will exhibit high electronic resistivity. However, an insulator can be modified through doping to become an extrinsic semiconductor. Doping a material with an element that has fewer electrons is called hole doping, and this effectively creates empty acceptor levels above the valence band (Figure 2.17a). These acceptor levels are easily accessible by electrons in the valence band and upon filling, a hole is left in the electron's place. This facilitates conduction in the valence band, and as the carrier is a positive hole, this type of material is called a  $p$ -type semiconductor. Conversely, if an insulator is doped with an element with more electrons, donor levels of electrons are present below the conduction band (Figure 2.17b). These donor electrons can be promoted into the conduction band, and as the charge carrier is now an electron, the material is classified as an  $n$ -type semiconductor.

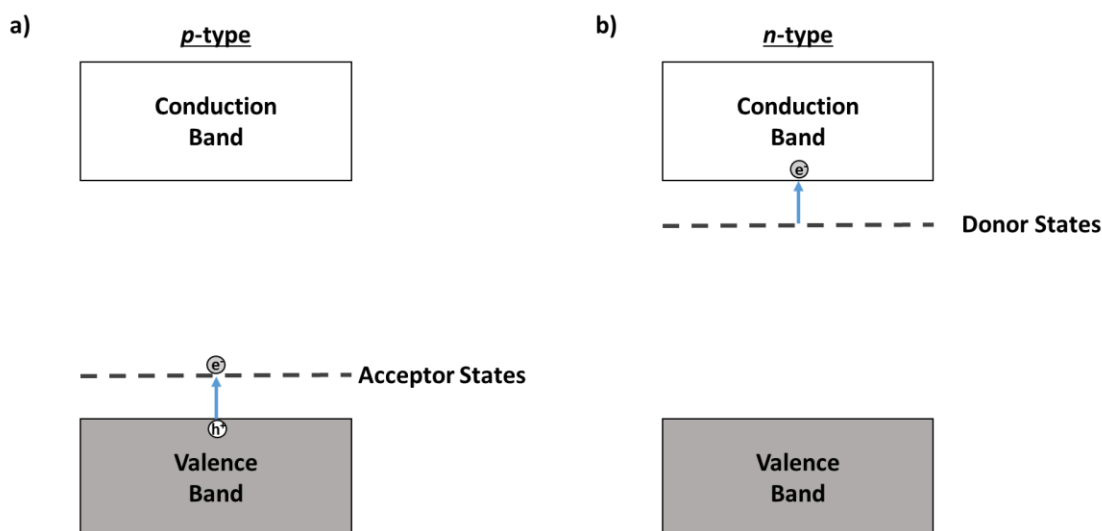


Figure 2.17 Location of donor states in a  $p$ -type semiconductor (a) and acceptor states in an  $n$ -type semiconductor (b).

The composition of the valence and conduction band is based on the geometrical arrangement of atoms in a material, which is dictated by the structure. In oxide materials, bands are often composed of orbital contributions between metal  $d$ -orbitals and oxygen  $p$ -orbitals. Substitution by atoms of varying size and electronegativity can change the bond lengths and angles in a material, having an effect on the orbital overlap that composes the various bands in the electronic structure. Through substitution and subsequent manipulation of the orbital overlap, electronic properties can be tuned for optimized material performance.

#### 2.4.2 Electronic Characterization Techniques

To differentiate metals or semiconductors experimentally, four-probe resistivity measurements can be performed over a varied temperature range. For polycrystalline samples, a well-sintered bar must be synthesized. Density will have a large effect on the observed conductivity and an attempt should be made to acquire the densest bars possible. This can be improved through sintering aids such as an organic

binding agent or techniques such as spark plasma sintering (See Chapter 3). Once the sample bar is attained, four leads are attached according to the schematic in Figure 2.18. A current is applied to the sample across electrodes  $I^-$  and  $I^+$  while the voltage is measured across  $V^-$  and  $V^+$ . The resistance of the sample,  $R$ , is determined according to Ohm's law,  $V = IR$ , and  $\rho$  of the sample is determined by incorporating the sample dimensions  $l$ ,  $w$ , and  $h$  according to:

$$R = \rho \frac{l}{w \cdot h} \quad (2.10)$$

The four-probe method has the advantage over two-probe measurements as it eliminates lead and contact resistance.[24]

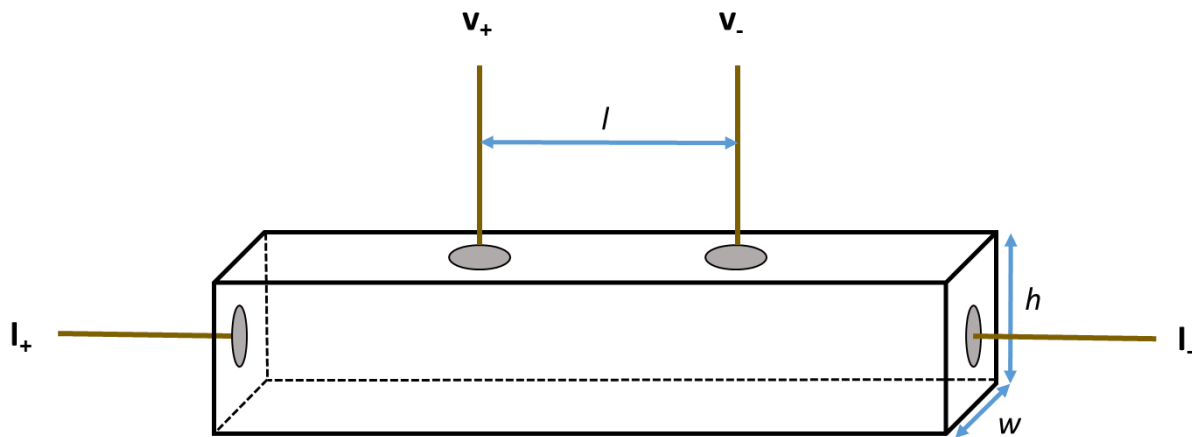


Figure 2.18 Attachment points for electrodes on a sintered bar for four-probe resistivity measurements.

Further characterization of semiconducting materials can be performed by determining the Seebeck Coefficient of the material. Similar to a four-probe resistivity experiment, a well-sintered bar is placed between four electrodes, illustrated in Figure 2.19. Seebeck characterization takes advantage of the Seebeck effect, which is the generation of a voltage when a thermal gradient is applied across a sample.[25] The Seebeck coefficient,  $\alpha$ , is the ratio of the generated voltage to the temperature difference:

$$\alpha = \frac{\Delta V}{\Delta T} \quad (2.11)$$

and often the Seebeck coefficient and sample resistivity are measured simultaneously. The Seebeck coefficient is primarily used in thermoelectric measurements (see Appendix B), but the sign of  $\alpha$  can be used to determine the carrier type. A positive  $\alpha$  indicates a *p*-type material, while a negative  $\alpha$  indicates *n*-type. Carrier identification plays a role of Seebeck characterization in Chapter 3 of this dissertation.

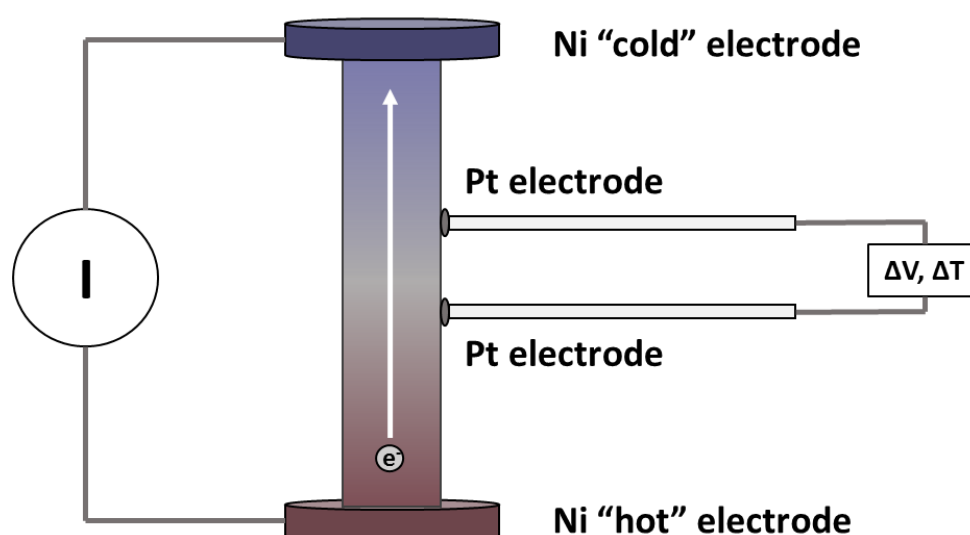


Figure 2.19 Illustration of the simultaneous measurement of four-probe resistivity and Seebeck coefficient in a sintered bar sample.

While not conducting, insulators can be characterized by their response to an applied external electric field. As with resistivity and Seebeck measurements, a well-sintered sample is needed. Instead of a bar, sample geometry is in a cylindrical pellet shape. The pellet is placed between two parallel capacitor plates (Figure 2.20), and often the surfaces of the pellet in contact with the plate are painted with Ag electrodes. When a differential voltage is applied across the sample, a polarization of the static charge in the material is observed. The degree of polarization is characterized through the derivation of the relative

permittivity,  $\epsilon_r$ , which is also referred to as the dielectric constant. To determine  $\epsilon_r$  the capacitance of free space,  $C_0$ , is first measured:

$$C_0 = \frac{\epsilon_0 A}{d} \quad (2.12)$$

where  $\epsilon_0$  is the permittivity of free space,  $8.854 \times 10^{-12} \text{ Fm}^{-1}$ ,  $A$  is the area of the capacitor plates, and  $d$  is the distance between the two plates, which is equivalent to the sample thickness. [23] The capacitance of the sample,  $C_s$ , is then measured similarly, and from the relationship between the capacitance of free space and the sample, the dielectric constant is determined:

$$\epsilon_r = \frac{C_s}{C_0} \quad (2.13)$$

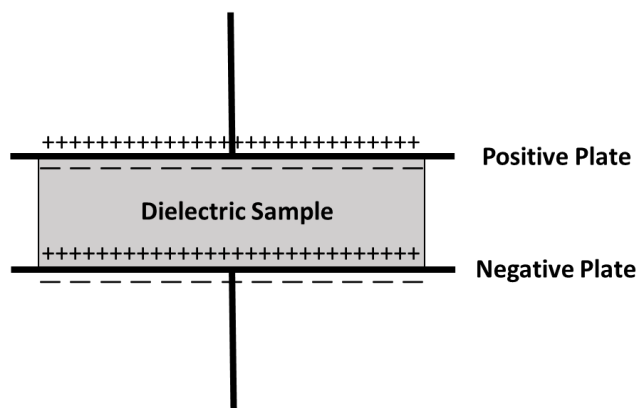


Figure 2.20 Parallel capacitor plate setup for a dielectric measurement.

The polarization of a dielectric material is lost once the applied voltage has been removed from the sample. However, there are special classes of dielectric materials which can behave differently in response to the electric field. For example, in a ferroelectric material this charge is retained upon removal of the voltage. The ferroelectric pyrochlore  $\text{Cd}_2\text{Nb}_2\text{O}_{7-x}\text{S}_x$  will be discussed in detail in Chapter 4. Low temperature four-probe resistivity measurements are utilized in Chapter 5, high temperature resistivity and Seebeck measurements in Chapter 3, and dielectric constant measurements in Chapter 4, all collected at OSU.

### 2.4.3 Thermal Transport Properties

The ability of a material to conduct heat can be characterized by determining a material's thermal conductivity. This can be done by measuring the thermal diffusivity of the sample using a Laser Flash instrument. Once again, a well-sintered pellet of the sample is needed for measurement. Once placed in the measurement apparatus (Figure 2.21), a laser pulse is applied normal to the sample. This pulse heats the sample on the bottom side, and a temperature signal is detected above the sample as a function of time. This process is performed over a variable temperature range, and to improve even heating across the sample face, a layer of graphite is often applied to the sample prior to measurement. The time of the half maximum temperature signal,  $t_{1/2}$ , and the sample thickness,  $d$ , is then used to calculate the thermal diffusivity,  $\alpha$ [26]:

$$\alpha = 0.1388 * \frac{d^2}{t_{1/2}} \quad (2.14)$$

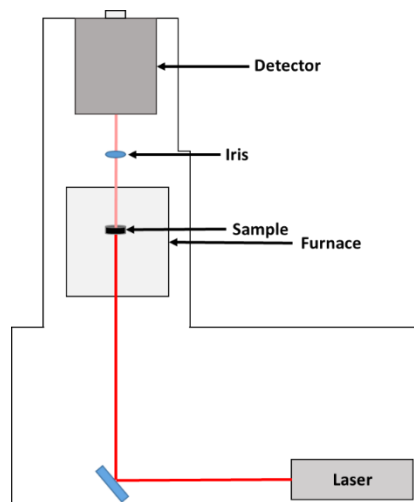


Figure 2.21 Components of a Laser Flash instrument for thermal diffusivity measurements.

If the sample density,  $\rho$ , and specific heat,  $c_p$ , are known, the thermal diffusivity can be related to the thermal conductivity,  $\kappa$ :

$$\kappa = \alpha \rho c_p \quad (2.15)$$

Thermal conductivity is an important factor in thermoelectric materials. The thermal diffusivity, in conjunction with high-temperature resistivity and Seebeck measurements, were performed at OSU to evaluate the thermoelectric properties of synthetic tetrahedrite materials, and a more detailed discussion can be found in Appendix B.

## 2.5 Magnetic Properties

All materials exhibit a response when exposed to a magnetic field. In the case of a diamagnetic material, where there are no unpaired electrons, a small repulsion of the magnetic field from the electrons is observed with no further response. Paramagnetic materials, in contrast, possess unpaired electrons; these electrons tend to align with an applied magnetic field, resulting in a net magnetic moment. However, due to thermal agitation, only a portion of these electrons will align. Consequently, a lowering of the temperature will result in an increase in the net moment. In certain materials, lower temperatures can cause spontaneous long-range ordering of electron spins. If the unpaired spins are aligned parallel to one another, the material is called ferromagnetic. An antiparallel alignment of spins equal in magnitude is called antiferromagnetic ordering, while antiparallel spins of unequal magnitude is called ferrimagnetic ordering. A pictorial representation of the types of magnetic ordering can be found in Figure 2.22.

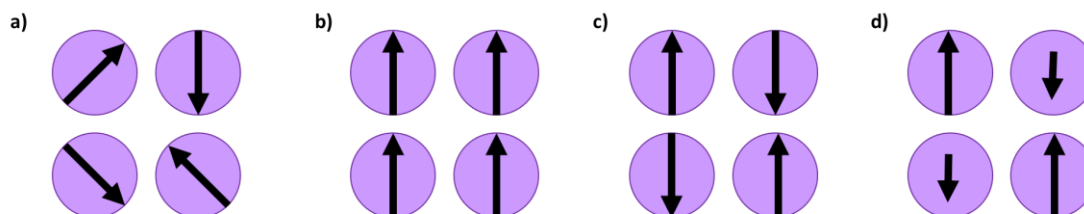


Figure 2.22 Magnetic ordering of unpaired electrons in a material: a) paramagnetic, b) ferromagnetic, c) antiferromagnetic, and d) ferrimagnetic.

To determine the magnetic ordering in a material, a sample is placed in an external magnetic field  $H$ . This magnetic field is related to the magnetic permeability of the sample,  $\mu$ , by the magnetic induction in the sample,  $B$ :

$$B = \mu H \quad (2.16)$$

From this expression the magnetization of the sample,  $M$ , can be determined:

$$B = \mu_0 H + \mu_0 M \quad (2.17)$$

where  $\mu_0$  is the magnetic permeability constant.[26] The magnetic susceptibility of the sample,  $\chi$ , can be extracted from the magnetization:

$$\chi = \frac{M}{H} \quad (2.18)$$

The magnetic susceptibility of a material is an important quantity, as it can be used to determine the magnetic ordering of a material as a function of temperature,  $T$ , according to the Curie-Weiss law:

$$\chi = \frac{C}{(T + \theta)} \quad (2.19)$$

In this relation  $C$  and  $\theta$  are the Curie and Weiss constants, respectively. When this law is obeyed, a plot of the inverse magnetic susceptibility as a function of temperature will yield a straight line. From this plot the Curie constant (the inverse of the slope of the line) and the Weiss constant (the x-intercept of the line) can be extracted. From the Curie constant the magnetic moment of the sample  $\mu_{\text{eff}}$  can be determined, which gives insight into the number of spins contributing to the magnetic response. The Weiss constant can be used to determine the magnetic ordering in a sample: a Weiss constant of zero indicates paramagnetism, a negative value corresponds to antiferromagnetic ordering, and a positive value to ferromagnetic ordering.[23]

Magnetic ordering is usually only exhibited in semiconducting and insulating materials. In a metallic material, the electrons act as a free electron gas with an equal number of spin up and spin down states, resulting in no net magnetic moment, illustrated in Figure 2.23a. Upon the application of a small

magnetic field, the electrons with spins parallel to the magnetic field will be lowered in energy, while the antiparallel spins will be raised, see Figure 2.23b. Consequently, the spin down electrons near  $E_f$  will overflow into the spin up states to equalize  $E_f$ , and in the process will flip their spin (Figure 2.23c). This gives rise to a net magnetic moment in the metallic material,  $2\mu_B$ . This weak, temperature-independent response is called Pauli Paramagnetism.[27] Magnetic susceptibility measurements on Pauli Paramagnetic samples in Chapter 5 were collected at OSU and modeled with a modified Curie-Weiss law by Dr. Rosa Grajczyk.

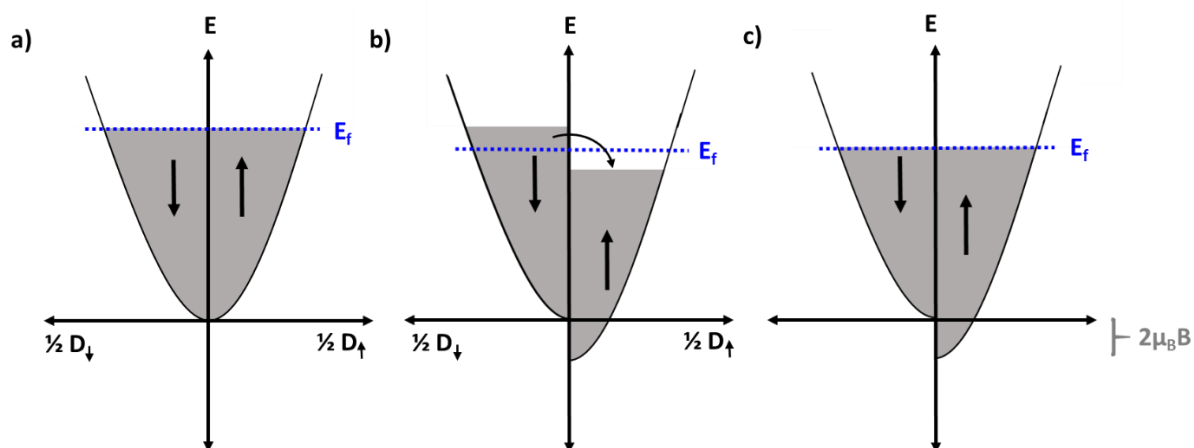


Figure 2.23 Illustration of the Pauli paramagnetic interaction of electrons in a metal to an external magnetic field. In the absence of a magnetic field, no net magnetic moment is observed (a). Upon application of a magnetic field, the electrons will shift energy based on spin (b) and a small net magnetic moment is observed (c).

## 2.6 Optical Properties

The interaction of light with a material can give rise to very interesting optical properties. Probably the most striking and observable optical property of a material is its color; the source of which, in addition to other information about the electronic and optical structure of the material, can be determined

through diffuse reflectance measurements. When a light source interacts with a material, four primary effects can take place: specular reflection, diffuse reflection, absorption, and/or transmission.[28] Both specular and diffuse reflection are elastic events, illustrated in Figure 2.24. In specular reflection the light is reflected from a smooth surface of a material at the same angle as the incident light. Diffuse reflection occurs when the light is scattered in all directions from scattering centers beneath the surface.[29]

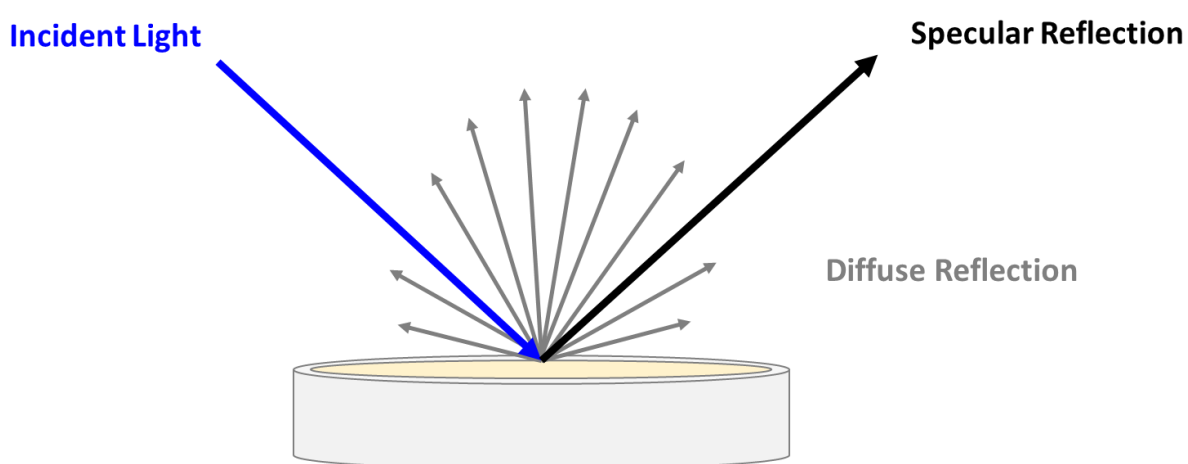


Figure 2.24 Specular and diffuse reflection of an incident beam of light from a packed powder surface.

In a diffuse reflectance measurement only the scattering due to diffuse reflection is collected via an integrating sphere or bifurcated optic cable. The diffuse reflection of a white reference (such as  $\text{BaSO}_4$  or  $\text{MgO}$ ) and dark reference (no light) is collected along with the sample data and used to determine the calculated diffuse reflectance of the sample,  $R_{calc}$ . This calculated diffuse reflectance can then be transformed through the Kubelka-Munk equation to obtain the absorbance of the sample,  $f(R)$  [30]:

$$f(R) = \frac{(1-R_{calc})^2}{2R_{calc}} \quad (2.20)$$

A plot of  $f(R)$  as a function of energy (in eV) will yield a spectrum that can provide information on the optical and electronic structure of the material. From this plot, an estimation of the band gap,  $E_g$ , can be

performed by extrapolating the linear region of the absorption onset to the x-axis. This is only an estimation of  $E_g$ , and can be useful for qualitative evaluations, such as the trends observed in  $E_g$  throughout a solid solution. For more accurate determination of  $E_g$ , linear extrapolation can be performed on a plot of  $f(R)^2$  vs. energy for a direct band gap material or  $f(R)^{1/2}$  vs. energy for an indirect band gap material. Diffuse reflectance measurements performed on samples in Dr. David McIntyre's laboratory in the OSU Physics Department and subsequent  $E_g$  estimation are presented in Chapter 3.

## 2.7 Sample Morphology

Chapter 3 discusses the analysis of the photocatalytic semiconductor  $\text{AgSbO}_3$  through substitution of the Ag with various metals. As discussed in the previous sections, detailed structural analysis can provide a large amount of insight on properties that are effected directly by the orbital overlap, such as optical and electrical properties. As photocatalysis is a surface reaction, it is crucial to be able to characterize the morphology of the surface of the photocatalyst. A combined investigation of the structure and morphology of potential photocatalysts can provide a complete analysis of observed changes in the photocatalytic activity of semiconducting materials. A detailed discussion of photocatalysis can be found in section 2.5.

### 2.7.1 Grain Size from PXRD

An approximation of the average grain size can be acquired from proper fitting of the peak shape of powder diffraction data. There are multiple ways the grain size can be evaluated, but this dissertation utilizes the Scherrer Method and analysis of the Lorentzian size broadening term in GSAS. Both of these methods relate the crystallite size to the broadness of the peaks in the diffraction pattern.

The Scherrer method applies the Scherrer equation (Equation 2.21):

$$\tau = \frac{K\lambda}{\beta \cos\theta} \quad (2.21)$$

where  $\tau$  is the average crystallite size,  $K$  is the dimensionless Scherrer factor (typically 0.9),  $\beta$  is the full width half maximum (FWHM) of the peak, and  $\theta$  is the diffraction angle of the peak.[6] The FWHM is the width due to broadening of the peak at half of the maximum intensity of the peak, illustrated in Figure 2.25.

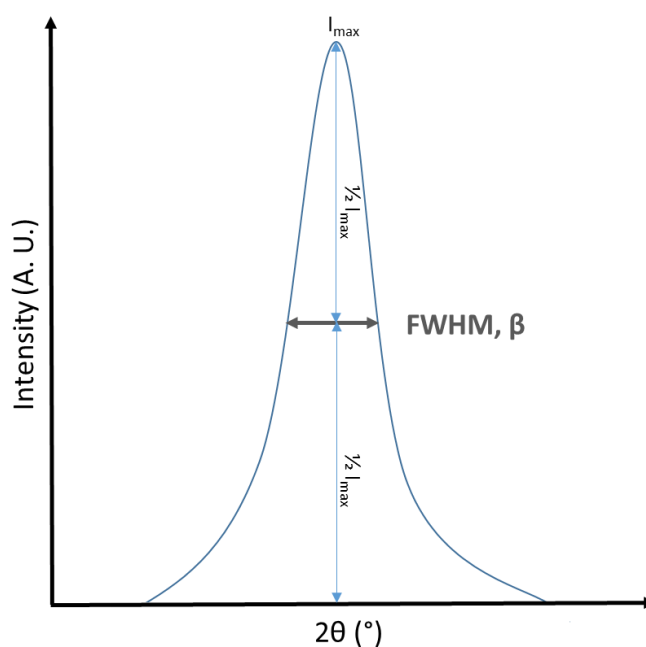


Figure 2.25 The full-width-half-max (FWHM) of a diffraction peak.

The Scherrer method approximates the crystallite size from direct analysis of the broadness of the diffraction peak, but a large shortcoming is that it attributes all broadening to sample size effects and does not take instrumental or sample strain broadening into account. By utilizing Rietveld software programs such as GSAS or FullProf, the size and strain broadening components can be extracted from the

profile fitting terms.[31,32] Details of crystallite size extraction from GSAS can be found in the “Materials and Methods” section of Chapter 3.

### 2.7.2 *Scanning Electron Microscopy*

Scanning electron microscopy (SEM) employs a focused beam of electrons to generate an image of the sample.[33] This image can be analyzed to observe changes in the sample’s surface morphology such as grain size, porosity, and agglomeration. To obtain an SEM image on a non-conductive sample, the sample is first prepared by applying a layer of conductive material to the surface. This will provide an electrical ground to avoid the accumulation of electrostatic charge on the surface, which can lead to issues when trying to image the sample. Conductive coatings include gold, gold/palladium, platinum, and graphite. To collect the image electrons are generated by an electron gun (typically a tungsten filament) and passed through a series of magnetic optics to produce a finely focused beam. The sample is then irradiated with the electron beam through a scanning motion which is controlled by magnetic coils in the magnetic objective lens. Through these scan control coils an image of the entire sample can be collected. When the electron beam interacts with the sample, a variety of signals are generated: backscattered electron, secondary electrons, and X-ray radiation, all of which can be analyzed by respective detectors. A schematic of SEM instrumentation can be found in Figure 2.26.

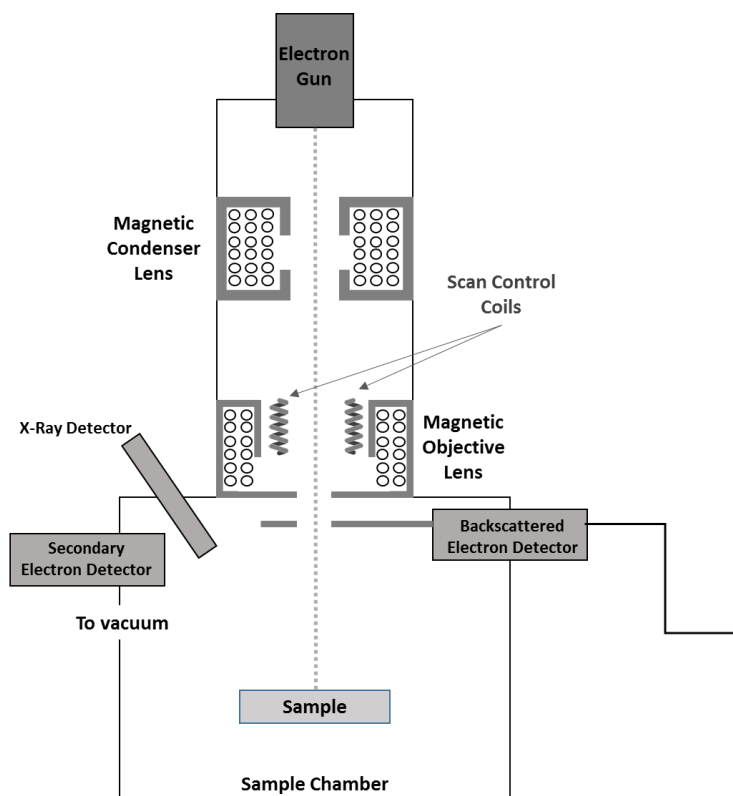


Figure 2.26 Schematic diagram of the components of a scanning electron microscope.

The generated backscattered electrons are produced through elastic scattering events with the sample surface, and can be used to provide contrast in a sample with areas of differing elemental composition. Secondary electrons are generated from inelastic scattering events with the sample surface and are the primary source of imaging the sample. X-ray generation from interaction with the electron beam can be further analyzed through energy- or wavelength dispersive X-ray spectroscopy, which can provide information on the elemental composition of the sample. SEM images in Chapter 3 were collected at OSU with the help of Dr. Jun Li to image the grain morphology of polycrystalline samples in the series  $\text{Ag}_{1-x}\text{M}^n_x\text{SbO}_{3+x[(n-1)/2]}$  ( $\text{M} = \text{Na}^+, \text{K}^+$  and  $\text{Tl}^{+/3+}$ ).

### 2.7.3 BET Surface Area Analysis

A crucial aspect in the study of morphology for catalytic applications is the surface area and pore dimensions. A commonly-employed technique used to determine the specific surface area of a powder is through the Brunauer-Emmett-Teller (BET) method.[34] Through this method the surface area is determined by calculating the amount of gas that is adsorbed to the surface of a powdered sample. To determine the surface area the BET equation (Equation 2.22) is applied:

$$\frac{1}{V_a \left( \frac{P_0}{P} - 1 \right)} = \frac{C-1}{V_m C} \times \frac{P}{P_0} + \frac{1}{V_m C} \quad (2.22)$$

where  $V_a$  is the volume (mL) of gas adsorbed at STP,  $P$  is the partial vapor pressure (Pa) of the adsorbed gas in equilibrium with the surface at 77.4 K (boiling point of liquid  $N_2$ ),  $P_0$  is the saturated pressure (Pa) of the adsorbed gas,  $V_m$  is the volume (mL) of gas adsorbed at STP to produce an adsorbed monolayer on the sample surface, and  $C$  is the dimensionless BET constant which is related to the enthalpy of absorption of gas to sample surface. The BET equation is referred to as the adsorption isotherm and can be plotted with  $\frac{1}{V_a \left( \frac{P_0}{P} - 1 \right)}$  on the  $y$ -axis and  $\frac{P}{P_0}$  on the  $x$ -axis, see Figure 2.27. The volume of the adsorbed gas,  $V_m$ , and the BET constant,  $C$ , can be calculated using the slope ( $M$ ) and the  $y$ -intercept ( $B$ ), and the total surface area,  $S_T$ , and BET surface area,  $S_{BET}$  can be calculated according to Equations 2.23 and 2.24, respectively:

$$S_T = \frac{V_m N s}{V} \quad (2.23)$$

$$S_{BET} = \frac{S_T}{a} \quad (2.24)$$

where  $N$  is Avogadro's number,  $s$  is the adsorption cross section of the adsorbed gas,  $V$  is the molar volume of the adsorbed gas, and  $a$  is the mass of the solid sample.

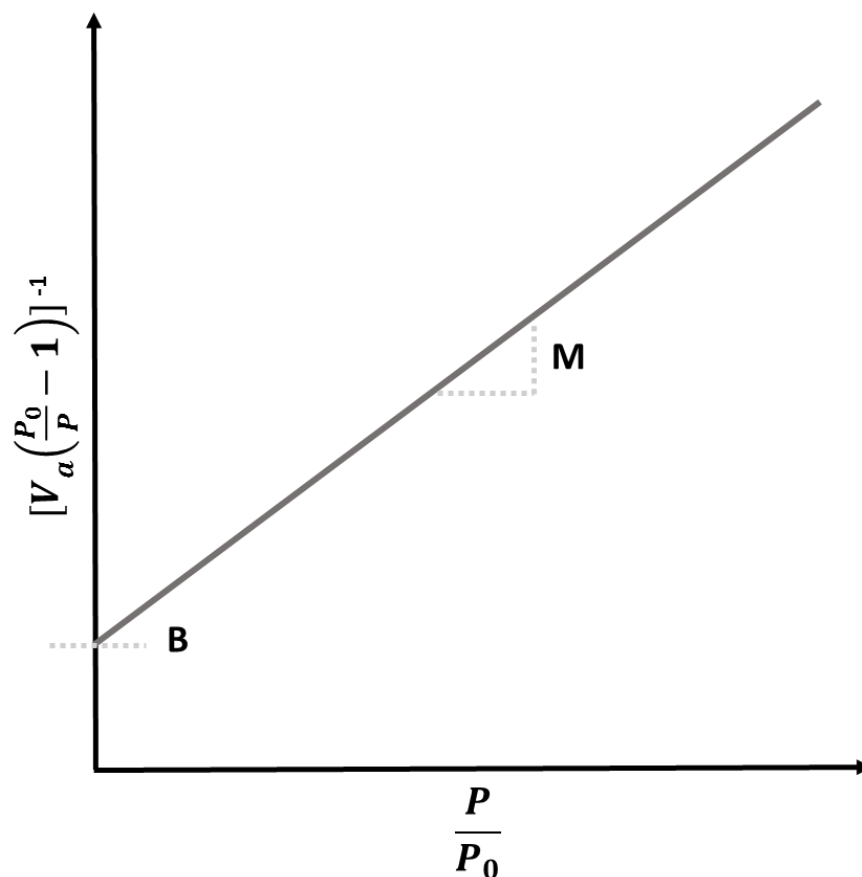


Figure 2.27 Idealized adsorption isotherm for surface area extraction from BET analysis.

BET surface area measurements were collected at OSU by Nick Wannemacher and employed for surface area and pore size analysis on samples in Chapter 3.

## 2.8 Photocatalytic Activity

Photocatalytic activity is a material property that converts light into chemical energy, which is used to catalyze a reaction. The main goal of this research is to find an efficient way to utilize ambient solar and lamp-produced light for energy and environmental applications. Some potential applications include breaking down water to produce  $H_2$  fuels, degradation of harmful organic solvents, and

environmental remediation. Metal oxide photocatalysts have the particular advantages of being cost-effective materials with high stability. There has been a significant amount of research and advancement using  $\text{TiO}_2$  as a photocatalyst, but the major disadvantage of this material is that the photocatalytic activity is observed with wavelengths in the UV region of light sources.[35] As a large portion of ambient light has wavelengths that are in the visible region of the electromagnetic spectrum, efficient utilization necessitates a photocatalyst that is activated by visible wavelengths of light. One such visible-light photocatalyst is  $\text{AgSbO}_3$ , and is the subject of Chapter 3 of this dissertation.[36]

The photocatalytic process of a semiconductor is illustrated in Figure 2.28. A photocatalytic reaction occurs when a sample is irradiated with light that has a wavelength with an energy that is slightly greater than the optical band gap of the material. Upon radiation, an electron is excited into the conduction band, creating an exciton pair. This generated pair migrates to an active site on the surface of the semiconducting particle, where simultaneous reduction and oxidation reactions occur with molecules adsorbed to the surface.[35]

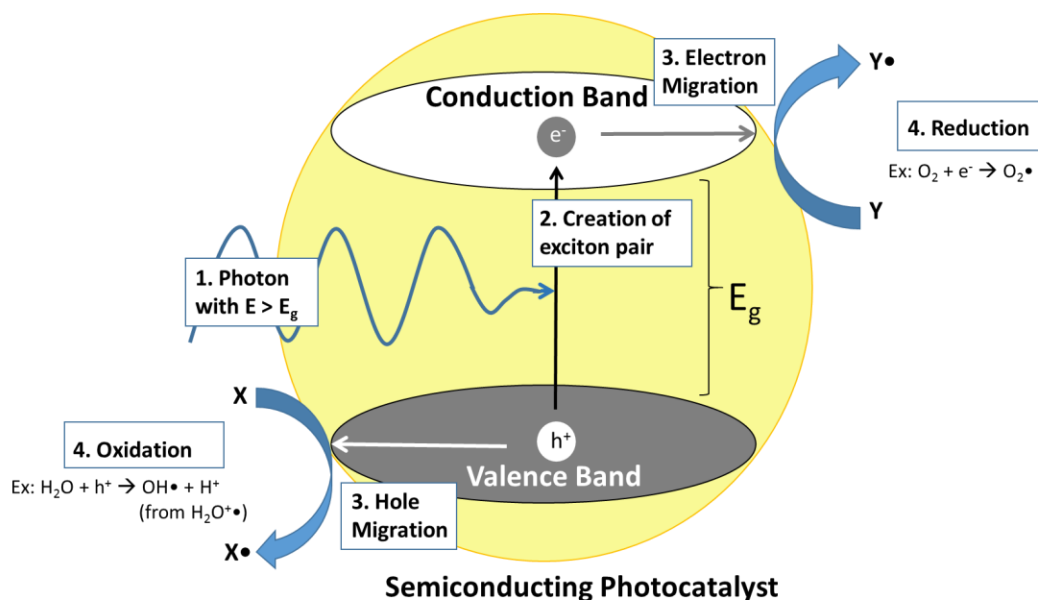


Figure 2.28 Photocatalytic process in a semiconducting photocatalyst particle.

When designing and testing a photocatalytic material, there are several factors to consider. For the photocatalytic material, the engineering of key properties drives the design: the band gap, the carrier transport efficiencies and mechanisms, the surface area and adsorption sites, and the chemical stability. When testing a material, several experimental aspects can be tuned to optimize performance: concentration of the semiconductor, reactive surface area (directly related to particle size), concentration of electron donors and acceptors, incident light intensity, pH, and temperature.

To evaluate the photocatalytic activity of powdered materials, a reactor setup was designed for use in conjunction with UV-vis spectroscopy, illustrated in Figure 2.29. The powdered sample and a solution containing the target material for degradation are placed in a quartz reactor flask with an optically flat side. The reactor flask is placed on a stir plate, and both the flask and stir plate are enclosed in a dark box. The only source of light in the dark box is from a xenon arc lamp at time of irradiation for the photocatalysis experiment. Options for gas flow and light filters have been included in the setup.

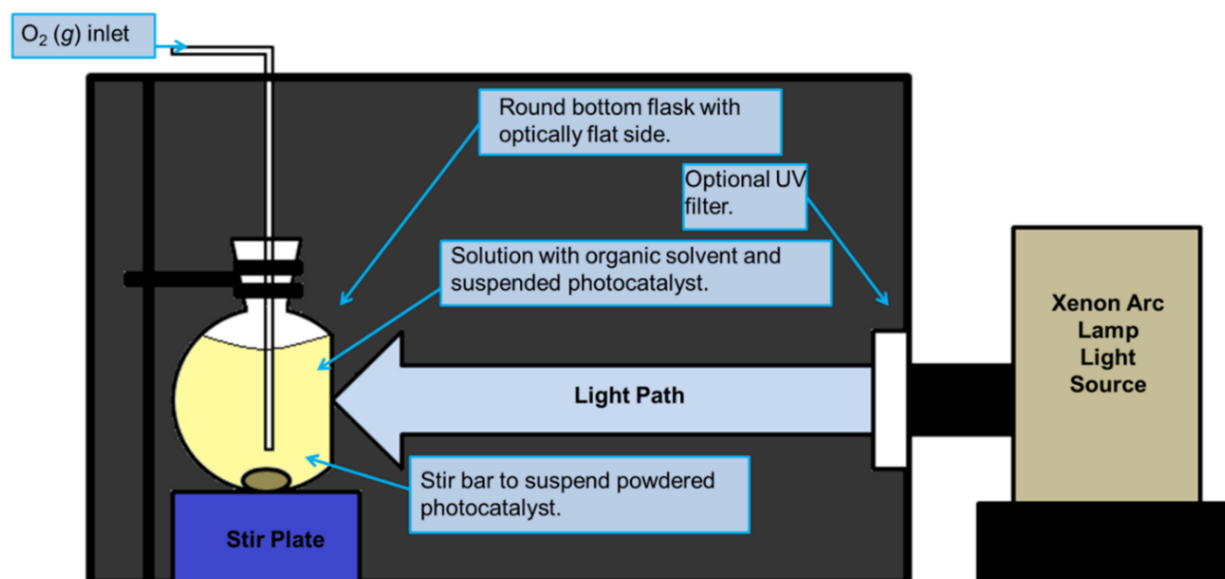


Figure 2.29 Diagram of the constructed reactor setup for photocatalysis evaluation.

To evaluate the photocatalytic activity of a material, a solution of methylene blue dye was chosen as the target molecule. The degradation of this molecule is well-documented and easily analyzed with a standard UV-vis spectrometer due to the strong absorbance of the region by the dye.[37,38] The first experiment performed with the setup was the evaluation of the degradation of the dye due to photolysis. Several experiments were performed to establish the experimental error of the setup. It was determined that  $11.5 \pm 0.7\%$  of the dye was degraded over an irradiation period of 2 hours (Figure 2.30a). This data is applied to the overall sample degradation as a photolysis correction. The next experiment is a sample-specific adsorption experiment. For this experiment, the powder sample is suspended in a solution of methylene blue and placed in the dark box. It is important that the sample mass is the same amount that will be used for the photocatalysis experiment. The sample is then allowed to stir for the same time that sample irradiation will take place. Sample aliquots were withdrawn every 10-15 minutes followed by centrifugation to remove the powdered samples from the solution. After analysis of the solution via UV-vis spectroscopy, the amount of Methylene Blue lost to surface adsorption can be determined and applied to the photocatalysis experiment as an adsorption correction. This correction is usually small in powders synthesized through standard solid state reactions; for example, the adsorption data for samples from Chapter 3 are shown in Figure 2.30b.

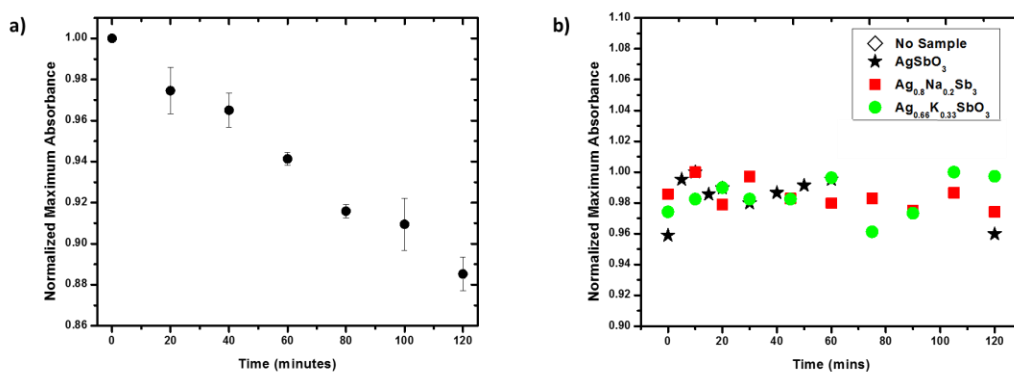


Figure 2.30 a) Data for the photolysis correction applied to all samples; b) example of data for the adsorption correction applied to samples of  $\text{Ag}_{1-x}\text{M}^n_x\text{SbO}_{3+x[(n-1)/2]}$  ( $\text{M} = \text{Na}, \text{K}$  and  $\text{TI}$ ) in Chapter 3.

For the photocatalysis experiment, approximately 0.0200 g of a powdered sample is suspended in a  $2.0 \times 10^{-5}$  M solution of methylene blue and stirred in the dark box for two hours to allow for adsorption of the dye onto to the surface of the sample. The reactor is then irradiated with light from a 300 W Xenon lamp source under constant stirring. The intensity of the lamp is regulated with a power and energy meter to ensure all samples received the same irradiated intensity, with the power output kept constant at 155 mW at the reactor face. Sample aliquots are withdrawn every 10-15 minutes followed by centrifugation. The solution is then analyzed with an Ocean Optics ISS-UV-Vis spectrometer to determine the maximum absorption and concentration of the methylene blue. The photolysis and adsorption corrections are then applied to each data point, and the overall degradation of methylene blue is calculated. To test the sample setup, a sample of Degussa P25  $\text{TiO}_2$  was analyzed via irradiation for one hour, and the UV-vis spectra and degradation is shown in Figure 2.31. By plotting the maximum absorbance of methylene blue ( $\sim 667$  nm) vs. time, it can be seen that nearly all of the dye is degraded after an irradiation time of two hours. The constructed setup and outlined procedure was performed on samples in Chapter 3.

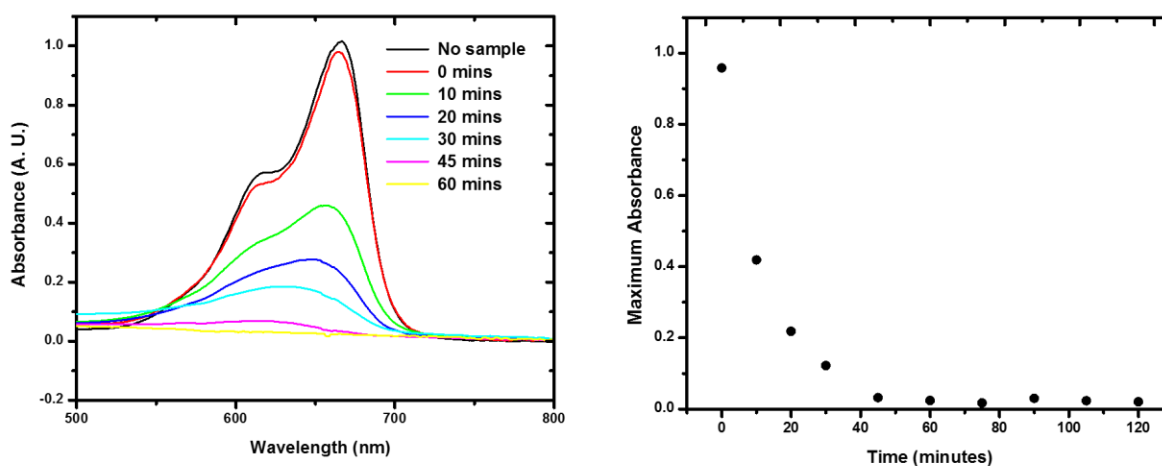


Figure 2.31 UV-Vis spectra (left) and overall degradation (right) of Methylene Blue with a Degussa P25  $\text{TiO}_2$  powdered sample collected over two hours of irradiation time.

## 2.9 Computational Methods

Computational methods can provide valuable information about the synthesis, structure, and properties of a material. These methods can also be used as a method of prediction for phenomena and materials, helping to drive the advancement of new materials. While not a main focus of this dissertation, Density Functional Theory (DFT) and Molecular Dynamics (MD) computational methods have been employed to aid the studies presented in Chapter 3 and Appendix A.

DFT is a method for approximating a solution to the Schrodinger equation for an extended, many-body system.[39] Once approximated, a variety of material properties such as structural (lattice parameters, defects structures), electronic (density of states, band structures), and spectroscopic (optical absorption, Raman scattering) can be calculated. Hybrid DFT calculations on the electronic structure of materials in Chapter 3 were performed by Dr. Jason Vielma at OSU's Physics Department.

Molecular Dynamic (MD) simulations calculate the time-dependent physical movements and interactions of  $N$  atoms in a system.[40] One focused application of MD simulations is rapid quenching from elevated temperatures to obtain an amorphous structural model. In this process  $N$  atoms are placed within a box and heated to high temperatures ( $\sim 4000$  K) to equilibrate the atomic positions. The box is then rapidly quenched to 300 K, and a disordered, or amorphous, structural model is generated for use in subsequent calculations. Structural models obtained through MD simulated annealing for Appendix A were performed by Dr. Benjamin Hanken at OSU's Chemistry Department.

## 2.10 Other Spectroscopic Techniques in this Dissertation

### 2.10.1 Inductively Coupled Plasma-Atomic Emission Spectroscopy

Inductively coupled plasma – atomic emission spectroscopy (ICP-AES) is a sensitive analytical technique that can be used to accurately determine the concentration of even trace amounts of metals in a solution.[33] ICP-AES utilizes an argon plasma to excite atoms or ions which emit characteristic radiation upon relaxation. The intensity of this from the sample radiation is compared to a calibration curve of previously measured intensities obtained from solutions with known concentrations of the metal in question. ICP-AES analysis on solutions from ion exchanged samples is presented in Chapters 3 and 5 were collected with the assistance of Dr. Whitney Schmidt and Matt Stolt in the teaching lab at OSU's Chemistry Department.

### 2.10.2 Electron Paramagnetic Resonance

In addition to magnetic susceptibility measurements, unpaired electrons can be studied through Electron Paramagnetic Resonance (EPR), also known as Electron Spin Resonance (ESR). EPR is similar to nuclear magnetic resonance (NMR), but instead of interacting with nuclear spins, EPR interacts with the permanent magnetic dipoles of unpaired electrons. In addition to the detection of small concentrations of unpaired spins, EPR can be used to determine the oxidation state, electronic configuration, and coordination number of the ion giving rise to the signal, as well as any structural distortions, such as that observed in Jahn-Teller active ions.[26] EPR measurements were performed Dr. Joshua Telser at Roosevelt University in Chapter 3 to investigate the presence of  $\text{Ag}^{2+}$  in the samples.

### 2.10.3 Mössbauer Spectroscopy

Mössbauer spectroscopy utilizes nuclear transitions and the Doppler Effect to produce a spectrum of  $\gamma$ -ray absorption of a sample.[26] The Mössbauer effect operates on the principle of “recoilless emission”, where  $\gamma$ -rays are produced via radioactive decay of atoms in a bound crystal. In a Mössbauer experiment, a solid sample is irradiated with a beam of  $\gamma$ -rays and the transmitted rays are detected. For this to work, the atoms emitting the rays (the source) must be the same as the atoms absorbing them (the sample). Only a few atoms exhibit decay that is suitable for the generation of  $\gamma$ -rays, and as a result, Mössbauer spectroscopy can only be performed on a few elemental isotopes, the most common being  $^{57}\text{Fe}$ ,  $^{119}\text{Sn}$ , and  $^{121}\text{Sb}$ .

Multiple important parameters can be extracted from a Mössbauer spectrum that can provide insight into the oxidation state, coordination environment, and bond character of the ion in question. If not in an identical environment to the source, a shift in the peak position will be observed. This is known as the isomer shift (also called the chemical shift,  $\delta$ ) and provides information regarding the coordination environment of the ion. If an ion contains a nuclear spin quantum number  $I > \frac{1}{2}$ , the peak in the spectrum will be split into doublets. This quadrupole splitting, measured by  $\Delta$ , gives insight into the local structure and oxidation state of the ion. An additional type of splitting, magnetic hyperfine Zeeman splitting, arises when an ion is exposed to a magnetic field. This type of splitting can give information on the type of magnetic ordering present.  $^{121}\text{Sb}$  Mössbauer spectroscopy measurements were performed on samples in Chapter 3 by Florian Winter and Dr. Rainer Pöttgen at the Institut für Anorganische und Analytische Chemie, Universität Münster to analyze the oxidation state and coordination environments of  $\text{Sb}^{n+}$  ions in the sample.

## 2.11 References

- [1] S.A. Corr, R. Seshadri, in: Compr. Inorg. Chem. II, Second, Elsevier, 2013, pp. 1–15.

- [2] D.S. Sivia, *Elementary Scattering Theory for X-Ray and Neutron Users*, Oxford University Press, 2011.
- [3] A. Munter, NIST Center for Neutron Research Neutron Scattering Lengths and Cross Sections, [Http://www.ncnr.nist.gov/resources/n-lengths/](http://www.ncnr.nist.gov/resources/n-lengths/), 2011.
- [4] Rigaku, *X-Ray Diffractometer Miniflex II Instruction Manual*, Manual No. ME14966A02, 2006.
- [5] T. Egami, S.J.L. Billinge, *Underneath the Bragg Peaks: Structural Analysis of Complex Materials*, Pergamon, New York, 2003.
- [6] B.D. Cullity, S.R. Stock, *Elements of X-Ray Diffraction*, 3rd ed., Prentice Hall, Upper Saddle River, NJ, 2001.
- [7] H.M. Rietveld, *J. Appl. Crystallogr.* 2 (1969) 65.
- [8] A. Le Bail, *Powder Diffr.* 20 (2005) 316.
- [9] R.L. McGreevy, *J. Phys. Condens. Matter* 13 (2001) R877.
- [10] J.K.R. Weber, C.J. Benmore, a. N. Taylor, S.K. Tumber, J. Neuefeind, B. Cherry, J.L. Yarger, Q. Mou, W. Weber, S.R. Byrn, *Chem. Phys.* 424 (2013) 89.
- [11] J. George, *Preparation of Thin Films*, M. Dekker, New York, NY, 1993.
- [12] D. Mitzi, *Solution Processing of Inorganic Materials*, Wiley, Hoboken, NJ, 2009.
- [13] K. Nomura, T. Kamiya, H. Ohta, T. Uruga, M. Hirano, H. Hosono, *Phys. Rev. B* 75 (2007) 035212.
- [14] M. Inukai, Y. Noda, K. Takeda, *J. Magn. Reson.* 213 (2011) 192.
- [15] P.G. Pai, *J. Vac. Sci. Technol. A Vacuum, Surfaces, Film.* 4 (1986) 689.
- [16] E. Bonera, G. Scarel, M. Fanciulli, *J. Non. Cryst. Solids* 322 (2003) 105.
- [17] C. Fan, P. Liaw, V. Haas, J. Wall, H. Choo, A. Inoue, C. Liu, *Phys. Rev. B* 74 (2006) 014205.
- [18] N. Yan, X.Q. Liu, L. Zhang, Z. Zhang, X.D. Han, *Chem. Phys. Lett.* 556 (2013) 108.
- [19] M. Winterer, *J. Appl. Phys.* 88 (2000) 5635.
- [20] K.B. Borisenko, Y. Chen, S.A. Song, D.J.H. Cockayne, *Chem. Mater.* 21 (2009) 5244.
- [21] K.B. Borisenko, Y. Chen, D.J.H. Cockayne, S.A. Song, H.S. Jeong, *Acta Mater.* 59 (2011) 4335.
- [22] T. Arai, K. Tani, R.L. McGreevy, *J. Phys. Condens. Matter* 22 (2010) 404204.

- [23] Anthony R. West, *Basic Solid State Chemistry*, 2nd ed., John Wiley & Sons. Ltd., New York, 1999.
- [24] S.M. Sze, K.N. Kwok, *Physics of Semiconductor Devices*, John Wiley & Sons. Ltd., 2008.
- [25] R. Tilley, *Understanding Solids: The Science of Materials*, John Wiley & Sons. Ltd., West Sussex, 2004.
- [26] Anthony R. West, *Solid State Chemistry and Its Applications*, Second, John Wiley & Sons. Ltd., West Sussex, 2014.
- [27] C. Kittel, *Introduction to Solid State Physics*, John Wiley & Sons. Ltd., Hoboken, NJ, 2005.
- [28] J.A. Russell, *Measurement of Optical Bandgap Energies of Semiconductors*, 2011
- [29] P. Hanrahan, W. Krueger, *SIGGRAPH '93 Proceedings*, J. T. Kajiya 27 (1993) 165.
- [30] P. Kubelka, F. Munk, *Zeitschrift Für Tech. Phys.* 12 (1931) 593.
- [31] A.C. Larson, R.B. Von Dreele, *Los Alamos Nat. Lab. Rep. LAUR* (1994) 89.
- [32] J. Rodríguez-Carvajal, *Phys. B Condens. Matter* 192 (1993) 55.
- [33] D.A. Skoog, F.J. Holler, S.R. Crouch, *Principles of Instrumental Analysis*, Sixth, Thompson Higher Education, Belmont, CA, 2007.
- [34] S. Brunauer, P.H. Emmett, E. Teller, *J. Am. Chem. Soc.* 60 (1938) 309.
- [35] M. Kaneko, I. Okura, *Photocatalysis: Science and Technology*, Springer, New York, NY, 2002.
- [36] T. Kako, N. Kikugawa, J. Ye, *Catal. Today* 131 (2008) 197.
- [37] P. T. Hang, G. W. Brindley, *Clays and Clay Min.* 18 (1970) 203.
- [38] A. Houas, H. Lachheb, M. Ksibi, E. Elaloui, C. Guillard, J. Herrmann, 31 (2001) 145.
- [39] P. Seminario, *Modern Density Functional Theory: A Tool for Chemistry*, Elsevier, New York, NY, 1995.
- [40] B.J. Alder, T.E. Wainwright, *J. Chem. Phys.* 31 (1959) 459.

## CHAPTER 3

### Substitutions into the Anion-Deficient Pyrochlore $\text{Ag}_2\text{Sb}_2\text{O}_6$

#### Abstract

The anion-deficient pyrochlore  $\text{Ag}_2\text{Sb}_2\text{O}_6$  (synonymous with  $\text{AgSbO}_3$ ) has been investigated through substitution with various cations according to the formula  $\text{Ag}_{1-nx}\text{M}^n_x\text{SbO}_3$  ( $\text{M} = \text{Na}^+, \text{K}^+, \text{Tl}^+, \text{and Cd}^{2+}$ ) with the goal of enhancing the photocatalytic activity of the parent compound. A complete solid solution between the anion-deficient pyrochlore  $\text{Ag}_2\text{Sb}_2\text{O}_6$  and the ideal pyrochlore  $\text{Cd}_2\text{Sb}_2\text{O}_7$  has been synthesized through standard solid state ceramic methods. Compositions were characterized by powder X-ray diffraction, optical spectroscopy, electron paramagnetic resonance,  $^{121}\text{Sb}$  Mössbauer spectroscopy, photocatalytic activity and transport property measurements. This study resulted in a comprehensive characterization of the complete solid solution and revealed an anomalous behavior in the Cd-rich end of the solid solution, proposed to arise from a possible radical  $\text{O}^-$  species in small concentrations. Polycrystalline samples of the series  $\text{Ag}_{1-nx}\text{M}^n_x\text{SbO}_3$  ( $\text{M} = \text{Na}^+, \text{K}^+ \text{ and } \text{Tl}^+$ ) have been structurally analyzed through total scattering techniques and evaluated for photocatalytic activity. The upper limits of  $x$  obtained are 0.08 for  $\text{Na}^+$ , 0.16 for  $\text{K}^+$ , and 0.17 for  $\text{Tl}^+$ , and an increase in the lattice parameter was observed for the larger  $\text{K}^+$  and  $\text{Tl}^+$  ions. An increase in the photocatalytic activity has been observed for nominal  $\text{Ag}_{0.8}\text{Na}_{0.2}\text{SbO}_3$  made through solid state synthesis, and this is attributed to both the slight decrease in the band gap from stronger  $\text{Ag } 4d - \text{O } 2p$  orbital overlap and the increase in pore dimensions compared to the parent compound  $\text{AgSbO}_3$ . This chapter presents the first study on  $\text{AgSbO}_3$  through neutron total scattering techniques.

Publications based on this chapter:

- 1) Laurita, G., Vielma, J., Berthelot, R., Largeteau, A., Winter, F., Pöttgen, R., Schneider, G., and Subramanian, M. A. From  $\text{Ag}_2\text{Sb}_2\text{O}_6$  to  $\text{Cd}_2\text{Sb}_2\text{O}_7$ : investigations on an anion-deficient to ideal pyrochlore solid solution *Journal of Solid State Chemistry* **2013**, 210, 65 – 73
- 2) Laurita, G., Page, K., Sleight, A. W., and Subramanian, M. A. Investigation of the anion-deficient pyrochlore  $\text{AgSbO}_3$  through total scattering techniques *Inorganic Chemistry* **2013**, 52, 11530-11537
- 3) Laurita, G. Stolt, M., Berthelot, R., Subramanian, M. A. Synthesis and characterization of  $\text{Ag}_{1-x}\text{M}_x\text{SbO}_3$  ( $\text{M}=\text{K}^+, \text{Na}^+, \text{Tl}^+$ ) for visible-light photocatalysis, *Manuscript in Preparation*

### 3.1. Introduction to $\text{Ag}_2\text{Sb}_2\text{O}_6$

The compound  $\text{Ag}_2\text{Sb}_2\text{O}_6$  (commonly referred to as  $\text{AgSbO}_3$ ) was first reported in 1938, and structurally characterized as a defect pyrochlore in 1969.[1,2] Further XRD characterization through Rietveld analysis revealed that  $\text{Ag}^+$  sits in the center of the channel in the anion-deficient pyrochlore structure.[3] Interest in the pyrochlore  $\text{AgSbO}_3$  increased when photocatalytic activity was observed by powdered samples in the presence of a gaseous mixture of dry air and 2-propanol. After adsorption equilibrium was established, the sample and gaseous mixture was irradiated with visible light. Gas chromatography revealed the 2-propanol had been decomposed into acetone and molecular oxygen.[4] This visible-light response is facilitated by a narrow band gap of approximately 2.6 eV, which also led to studies of  $\text{AgSbO}_3$  as a potential transparent conducting oxide.[4–6]

Photoemission studies of  $\text{AgSbO}_3$  thin-films demonstrated that the top of the valence band was primarily composed of O 2*p* and Ag 4*d* orbitals.[5] Further theoretical calculations confirmed this valence band composition, and detailed that the valence band in the anion-deficient pyrochlore was constructed of the overlap between these orbitals. This Ag 4*d*-O 2*p* orbital overlap is attributed to raising the energy of the valence band, resulting in the narrow band gap that is observed.[4,7] Theoretical studies also conclude the conduction band minimum is primarily composed of diffuse Ag 5*s* and Sb 5*s* orbitals, which also contributes to the formation of the narrow band gap that gives rise to the observed optical properties of this material.[4,6,7] Increased photocatalytic activity has been observed in the illmenite polymorph,[8] and photocatalysis has been observed in  $\text{AgSbO}_3$  prepared via ion exchange with a  $\text{NaSbO}_3$  precursor.[9] In-depth studies of the pyrochlore and illmenite band structures have been performed through hybrid-DFT methods to compare and contrast the two photocatalysts.[7]

Fundamentally, this material is an  $\text{Ag}^+$  ion conductor, and additionally displays *n*-type conductivity in bulk powders and amorphous thin-films.[5,10] The thermoelectric properties of pure  $\text{AgSbO}_3$  and

copper-doped  $\text{AgSbO}_3$  have been systematically studied to show a maximum thermoelectric figure-of-merit,  $zT$ , of 0.06 at 873 K in pure  $\text{AgSbO}_3$ . [11,12] Copper doping increased the power factor of  $\text{AgSbO}_3$ , but  $zT$  was not calculated due to the absence of thermal conductivity measurements. Further studies characterized  $\text{AgSbO}_3$  through scanning electron microscopy, X-ray photoelectron spectroscopy, and electron diffraction. [9]

### 3.2 Investigation of the Solid Solution between $\text{Ag}_2\text{Sb}_2\text{O}_6$ and $\text{Cd}_2\text{Sb}_2\text{O}_7$

#### 3.2.1 Motivation for the Solid Solution

$\text{Cd}_2\text{Sb}_2\text{O}_7$  was first reported in 1945 and has been structurally characterized and determined to adopt the pyrochlore structure. [13–15] Both  $\text{Ag}_2\text{Sb}_2\text{O}_6$  and  $\text{Cd}_2\text{Sb}_2\text{O}_7$  crystallize in the pyrochlore structure with similar covalency, lattice, and synthesis parameters. The primary difference is that  $\text{Ag}_2\text{Sb}_2\text{O}_6$  forms an anion-deficient pyrochlore, whereas  $\text{Cd}_2\text{Sb}_2\text{O}_7$  forms the ideal pyrochlore structure. A study on the electrical conductivity of sintered samples determined  $\text{Cd}_2\text{Sb}_2\text{O}_7$  to be an  $n$ -type semiconductor, [16] but there have not previously been further reports on the electronic properties of  $\text{Cd}_2\text{Sb}_2\text{O}_7$ .

Although a partial solid solution  $(\text{Cd}_{1-x}\text{Ag}_x)\text{Sb}_2\text{O}_{6.8}$  ( $x=0.00-0.15$ ) has been studied as a potential alcohol gas-sensing material, including a study of the observed conductivities in the solution, [17] to the best of the authors' knowledge there is no report of a full solid solution between  $\text{Ag}_2\text{Sb}_2\text{O}_6$  and  $\text{Cd}_2\text{Sb}_2\text{O}_7$ . For these reasons, the compositions between  $\text{Ag}_2\text{Sb}_2\text{O}_6$  and  $\text{Cd}_2\text{Sb}_2\text{O}_7$  were investigated in an attempt to tune the band structure and the properties of  $\text{Ag}_2\text{Sb}_2\text{O}_6$  by changing the orbital overlap between the Ag  $4d$  and O  $2p$  orbitals. As the solid solution progresses, a transition between the anion-deficient to ideal pyrochlore is expected, accompanied by an increase in the oxygen content within the unit cell. This section presents the first report of the full solid solution between the anion-deficient pyrochlore  $\text{Ag}_2\text{Sb}_2\text{O}_6$  and the ideal pyrochlore  $\text{Cd}_2\text{Sb}_2\text{O}_7$ , and aims to qualitatively study the solid solution through X-ray diffraction

(XRD), thermogravimetric analysis, density functional theory, diffuse reflectance optical properties, transport properties (on samples densified by spark plasma sintering), electron paramagnetic resonance and  $^{121}\text{Sb}$  Mossbauer spectroscopy.

### 3.2.2 Structural Characterization

XRD patterns obtained for the nominal series  $(\text{Ag}_{1-x}\text{Cd}_x)_2\text{Sb}_2\text{O}_{6+x}$ ,  $x = 0.0, 0.2, 0.4, 0.6, 0.8$  and  $1.0$  are shown in Figure 3.1 and evidence a complete solid solution. Indeed all diffraction peaks can be indexed to a cubic lattice with the  $Fd\bar{3}m$  space group, indicating the pyrochlore structure is retained through the series.

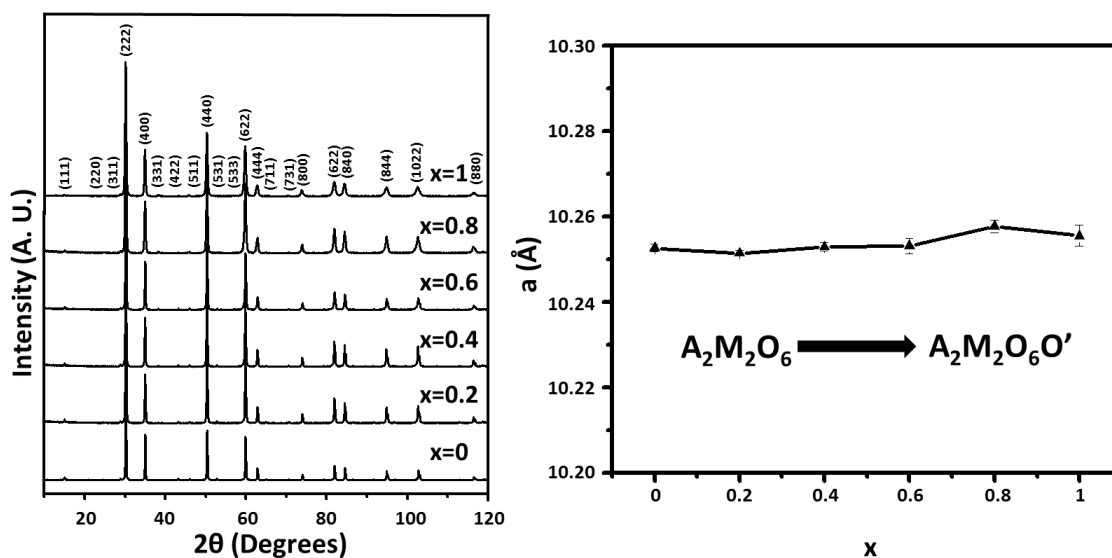


Figure 3.1 PXR D data collected on the nominal series  $(\text{Ag}_{1-x}\text{Cd}_x)_2\text{Sb}_2\text{O}_{6+x}$  (left). Lattice parameter evolution of the series (right) reveals a relatively unchanging unit cell.

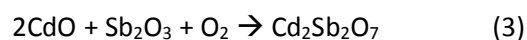
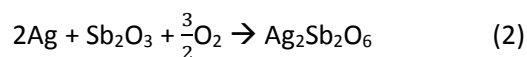
Le Bail analysis of the patterns shows that the lattice parameter remains relatively unchanged throughout the solid solution, as is expected based on the reported unit cell dimensions of the end

members. However, it does seem surprising that as the smaller Cd cation is substituted for the larger Ag cation, the lattice parameter does not change. Therefore, there must be a compensating factor to account for the observed trend in the lattice parameter evolution. As the solution progresses from an anion-deficient pyrochlore to an ideal pyrochlore, the oxygen content in the unit cell increases according to the formula  $(\text{Ag}_{1-x}\text{Cd}_x)_2\text{Sb}_2\text{O}_{6+x}$ , as illustrated in the following section. Consequently, the unchanging lattice parameter evolution is a result of the two counterbalancing processes: the substitution of a smaller cation (Cd) into the lattice, accompanied by an increase in the number of atoms in the unit cell (addition of O).

### 3.2.3 Thermogravimetric Analysis

Analysis through XRD reveals that a solid solution between Ag and Cd is obtained with the pyrochlore structure. However, as stated in the introduction,  $\text{Ag}_2\text{Sb}_2\text{O}_6$  is an anion-deficient pyrochlore, whereas  $\text{Cd}_2\text{Sb}_2\text{O}_7$  is an ideal pyrochlore. It can be assumed that the O content as the series progresses from anion-deficient to ideal is variable. Quantification of the O content using XRD is unfavorable due to its low scattering factor. Neutron diffraction is unfavorable as well due to the high absorption cross section of Cd (2520 barn).[18] Therefore, alternative methods must be employed to gain insight into the amount of O in each particular composition in the solution. One way to analyze the O composition is by monitoring the mass gain during the synthesis reaction.

The reactions for  $\text{Ag}_2\text{Sb}_2\text{O}_6$ , from either  $\text{Ag}_2\text{O}$  or Ag metal, and  $\text{Cd}_2\text{Sb}_2\text{O}_7$  are as follows:



For the Cd end-member, there is a total theoretical mass gain of 5.83%. For the Ag end-member, there is a theoretical mass gain of 6.12% with a precursor of Ag<sub>2</sub>O (equation 1) or 9.46% with a precursor of Ag metal (equation 2). Therefore, the use of Ag metal as a Ag precursor is preferred as it allows a greater differentiation between the mass change of the two end members. Figure 3.2 shows the TGA curves obtained for varying Cd content with the use of Ag metal as the Ag precursor.

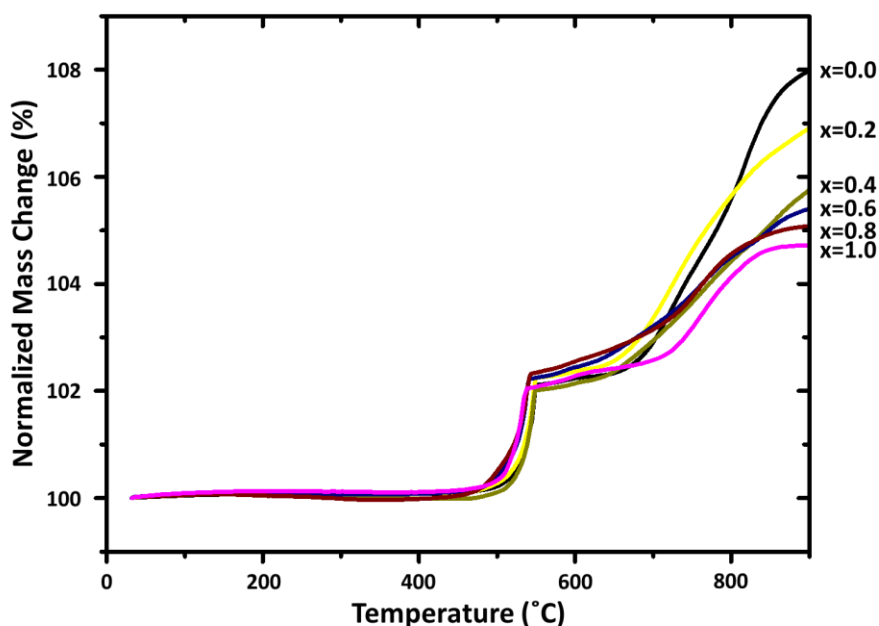


Figure 3.2 Thermogravimetric analysis of the nominal series  $(Ag_{1-x})_2(Cd_x)_2Sb_2O_{6+x}$  indicating the weight gain as the samples are formed.

All curves exhibit two distinct increases in mass, indicating that the pyrochlore formation is a two-step process. The first mass gain around 550 °C represents a mass increase between 2 to 2.5%, and is uniform and very rapid in all curves. The second mass gain is more gradual as a function of temperature (between 650 and 900 °C). It exhibits a large variation from the Cd-rich end (approximately a 6% total gain for Cd<sub>2</sub>Sb<sub>2</sub>O<sub>7</sub>) to the Ag-rich end (up to approximately a 10% total increase for Ag<sub>2</sub>Sb<sub>2</sub>O<sub>6</sub>). XRD analysis after the TGA runs confirmed that the pyrochlore phase is formed in each case.

According to the two distinct mass gains, the two step process during the pyrochlore formation of the pyrochlore compounds can be hypothesized as the following: between 500-550 °C, half of the  $\text{Sb}^{3+}$  is oxidized to  $\text{Sb}^{5+}$ , resulting in the formation of  $\text{Sb}_2\text{O}_4$  and a theoretical weight gain of 3.20%. Further TGA experiments stopped after this first gain, coupled with XRD analysis confirmed the presence of  $\text{Sb}_2\text{O}_4$ , while Ag metal is still unchanged. The second mass gain between 600-900 °C is the formation of the pyrochlore phase, with a simultaneous oxidation of the remaining  $\text{Sb}^{3+}$  to  $\text{Sb}^{5+}$  and  $\text{Ag}^0$  to  $\text{Ag}^+$ . This represents the additional theoretical weight gain of 6.26% for  $\text{Ag}_2\text{Sb}_2\text{O}_6$  and 2.36% for  $\text{Cd}_2\text{Sb}_2\text{O}_7$  (only Sb oxidation). Using TGA, it appears to be impossible to differentiate the oxidation of Ag metal with the oxidation of the second half of  $\text{Sb}^{3+}$ , as they occur in the same temperature range.

The summarized mass gain as compared to the theoretical value is shown in Figure 3.3. It appears that there is a linear mass gain in the Ag-rich end of the series, suggesting that in this region the O content strictly follows that of the Cd. Therefore, the general synthesis equation can be modeled linearly as

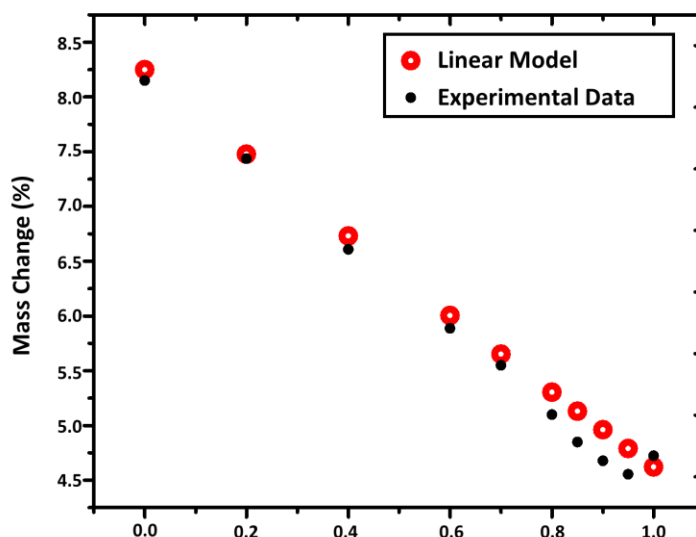
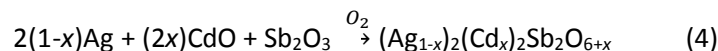


Figure 3.3 A summary of the theoretical and experimental overall mass gained during formation as a function of Cd content in the series. A linear gain of O as Cd content increase is assumed for this model, with a deviation from linearity in the Cd-rich end. Systematic instrumental error in the mass gain has been removed from the theoretical models to facilitate comparison.

### 3.2.4 Optical Characterization

It was noticed that the increase in Cd content was accompanied by a color change from yellow ( $\text{Ag}_2\text{Sb}_2\text{O}_6$ ) to violet/grey ( $\text{Ag}_{0.4}\text{Cd}_{0.8}\text{Sb}_2\text{O}_{6+\delta}$ ) to tan ( $\text{Cd}_2\text{Sb}_2\text{O}_7$ ). This observation prompted the collection of optical data on the series to analyze the apparently changing band gap (Figure 3.4). Grain size calculations (from the Scherrer[19] equation) reveal particle sizes within the same order of magnitude (200-600 nm), suggesting that the observed color progression is not a result of the particle size, but of the changing band structure.

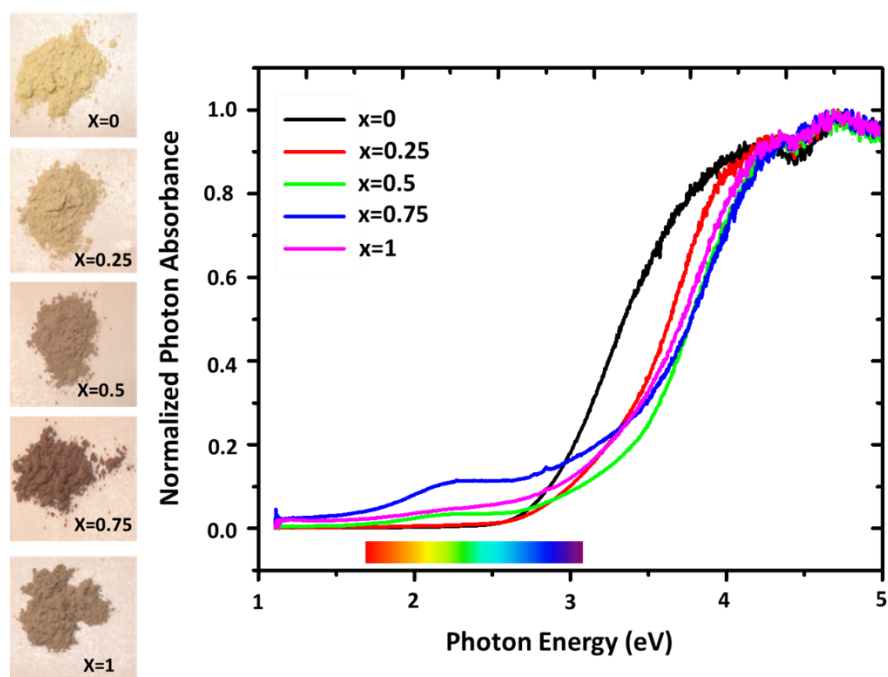


Figure 3.4 Images of the powders (left) reveal a change in color as the nominal series  $(\text{Ag}_{1-x})_2(\text{Cd}_x)_2\text{Sb}_2\text{O}_{6+x}$  progresses. Diffuse reflectance data transformed with the Kebulka-Munk equation (right) reveal a changing band gap accompanying the color change.

After transforming the collected data using the Kebulka-Munk equation, the band gap was estimated by extrapolating the linear portion of the absorption onset to the x-axis in a plot of absorption

versus energy, following the work of Mizoguchi *et al.*[6] Table 3.1 shows the estimated band gaps, as well as a comparison to the band gaps for  $\text{Ag}_2\text{Sb}_2\text{O}_6$  and  $\text{Cd}_2\text{Sb}_2\text{O}_7$  from the literature.[6,20]

Table 3.1 Summary of the estimated band gaps of the samples.

<b>Compound</b>	<b>Estimated Main-Gap Band Gap (eV)</b>
<b><math>\text{Ag}_2\text{Sb}_2\text{O}_6</math></b>	2.70
	2.7[6]
<b><math>(\text{Ag}_{0.9})_2(\text{Cd}_{0.1})_2\text{Sb}_2\text{O}_{6+\delta}</math></b>	2.69
<b><math>(\text{Ag}_{0.8})_2(\text{Cd}_{0.2})_2\text{Sb}_2\text{O}_{6+\delta}</math></b>	2.73
<b><math>(\text{Ag}_{0.7})_2(\text{Cd}_{0.3})_2\text{Sb}_2\text{O}_{6+\delta}</math></b>	2.91
<b><math>(\text{Ag}_{0.6})_2(\text{Cd}_{0.4})_2\text{Sb}_2\text{O}_{6+\delta}</math></b>	2.79
<b><math>(\text{Ag}_{0.5})_2(\text{Cd}_{0.5})_2\text{Sb}_2\text{O}_{6+\delta}</math></b>	2.90
<b><math>(\text{Ag}_{0.4})_2(\text{Cd}_{0.6})_2\text{Sb}_2\text{O}_{6+\delta}</math></b>	2.92
<b><math>(\text{Ag}_{0.3})_2(\text{Cd}_{0.7})_2\text{Sb}_2\text{O}_{6+\delta}</math></b>	2.94
<b><math>(\text{Ag}_{0.2})_2(\text{Cd}_{0.8})_2\text{Sb}_2\text{O}_{6+\delta}</math></b>	3.05
<b><math>(\text{Ag}_{0.1})_2(\text{Cd}_{0.9})_2\text{Sb}_2\text{O}_{6+\delta}</math></b>	3.09
<b><math>\text{Cd}_2\text{Sb}_2\text{O}_7</math></b>	3.16
	2.7[6] - 3.0[20]

An increasing band gap as the series progresses from  $\text{Ag}_2\text{Sb}_2\text{O}_6$  to  $\text{Cd}_2\text{Sb}_2\text{O}_7$  is experimentally observed. Upon further analysis, it is noted that at an approximate nominal composition of  $\text{AgCdSb}_2\text{O}_{6.5}$ , an additional absorption band emerges and is observed until a nominal composition of  $\text{Cd}_2\text{Sb}_2\text{O}_7$ .

### 3.2.5 Computational Results

The equilibrium lattice parameters for  $\text{Ag}_2\text{Sb}_2\text{O}_6$  and  $\text{Cd}_2\text{Sb}_2\text{O}_7$  using DFT with HSE06 are 10.22 Å and 10.23 Å, respectively, which are very close to both the experimental equilibrium lattice constants of

10.25 Å. DFT with PBE give equilibrium lattice constants of 10.43 Å and 10.44 Å for  $\text{Ag}_2\text{Sb}_2\text{O}_6$  and  $\text{Cd}_2\text{Sb}_2\text{O}_7$ , respectively. Figure 3.5 gives the band structure diagrams of both compounds. DFT with HSE06 gives band gaps of 2.26 eV for  $\text{Ag}_2\text{Sb}_2\text{O}_6$  and 2.50 eV for  $\text{Cd}_2\text{Sb}_2\text{O}_7$ . DFT/PBE portray  $\text{Ag}_2\text{Sb}_2\text{O}_6$  as being a metal and  $\text{Cd}_2\text{Sb}_2\text{O}_7$  with a band gap of 0.39 eV. When using DFT with HSE06, the bottom of the conduction band is shifted up greatly in both compounds, while the rest of the valence bands are only shifted slightly from literature DFT with PBE calculations.

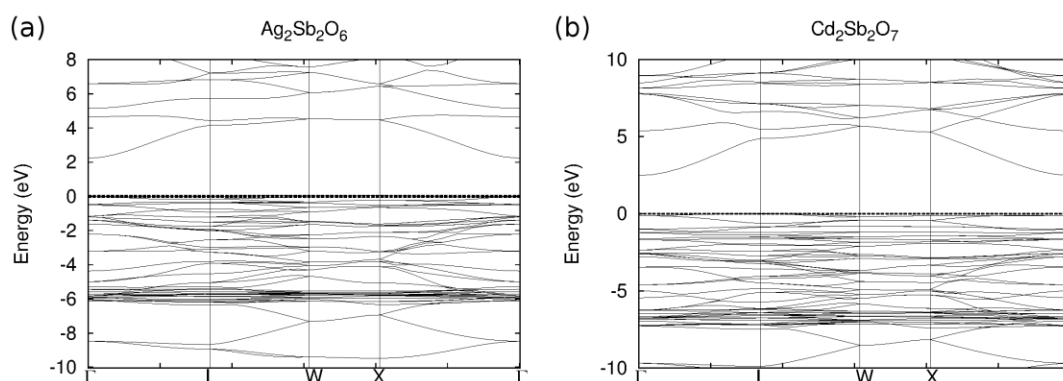


Figure 3.5 Band structure diagrams using DFT with HSE06 of the defect pyrochlore  $\text{Ag}_2\text{Sb}_2\text{O}_6$  and the ideal pyrochlore  $\text{Cd}_2\text{Sb}_2\text{O}_7$ . Both diagrams are shifted down such that 0 eV coincides with the valence band maximum (dotted line).

Figure 3.6 gives the total and partial density of states (DOS) for both compounds. For  $\text{Ag}_2\text{Sb}_2\text{O}_6$ , the valence band maximum is dominated by Ag 4d and O 2p states, and the conduction band minimum is composed of Sb 5s and O 2p states, in agreement with Allen *et al.*[7] For  $\text{Cd}_2\text{Sb}_2\text{O}_7$ , the conduction band minimum is also composed of Sb 5s and O 2p states, but the valence band maximum is primarily made of O 2p states. The top of the Cd 4d states are located 6 eV below the valence band maximum.

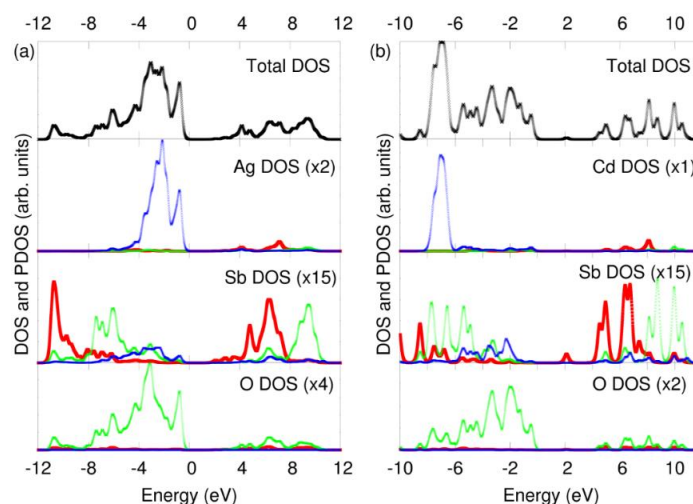


Figure 3.6 Partial and Total Electronic Density of States (DOS) using DFT with HSE06 for  $\text{Ag}_2\text{Sb}_2\text{O}_6$  (a) and  $\text{Cd}_2\text{Sb}_2\text{O}_7$  (b). The total DOS is in black, the s-states in red, the p-states in green, and the d-states in blue. Top plot is the total DOS, and the bottom three are the partial DOS of each atom. Each partial DOS shows how much the y-axis is scaled. DOS are shifted to set the Fermi energy to 0 eV.

The orbital contributions at the VBM of  $\text{Cd}_2\text{Sb}_2\text{O}_7$  have been further analyzed by calculating the partial contributions to the DOS near the Fermi level of the two types of O atoms (48f and 8b). By comparing the partial DOS (Figure 3.7), it can be seen that the orbitals closest to the Fermi level originate from the O' in the 8b site. The absence of these partials from the DOS of  $\text{Ag}_2\text{Sb}_2\text{O}_6$  indicates that it is indeed the O' that is being acquired as the series progresses from  $\text{Ag}_2\text{Sb}_2\text{O}_6$  to  $\text{Cd}_2\text{Sb}_2\text{O}_7$ .

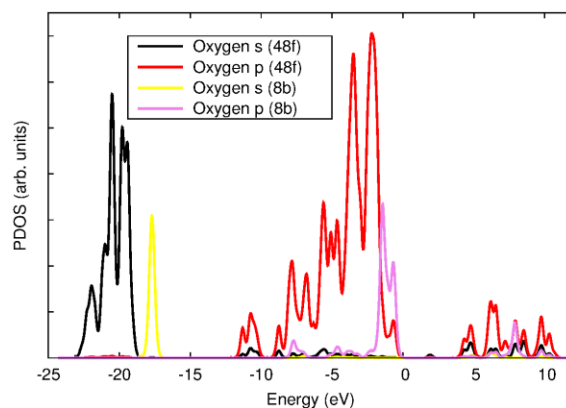


Figure 3.7 Partial DOS for the two types of oxygen atoms in  $\text{Cd}_2\text{Sb}_2\text{O}_7$ . It can be seen that the band closest to the Fermi level originates from the oxygen in the 8b site.

### 3.2.6 Transport Properties

Obtaining high-density samples seems to be very difficult, in agreement with the literature in the case of  $\text{Ag}_2\text{Sb}_2\text{O}_6$ . [11] Samples prepared through conventional solid state routes yields densities of only 50% of that of the theoretical values. [6] To increase the density of the samples, spark plasma sintering (SPS) was applied to the samples. Densification was variable by composition, and at longer sintering time, higher temperature, and higher pressures, decomposition of the samples was evident. However, phase pure samples were obtained through SPS, and a summary of the increased densities can be seen in Table 3.2.

Table 3.2 Summary of the densities of solid state and SPS-prepared samples.

Cadmium Content ( $\text{Ag}_{1-x}\text{Cd}_x$ ) $_2\text{SbO}_{6+6}$	Conventional Solid State Reaction		Spark Plasma Sintering	
	Density ( $\text{g}/\text{cm}^3$ )	% Theoretical (based off nominal composition)	Density ( $\text{g}/\text{cm}^3$ )	% Theoretical (based on nominal composition)
0 (Theoretical[6])	6.81	--	--	--
0	3.42	50.2	5.21	<b>76.5</b>
0.1	3.38	49.4	3.78	55.2
0.2	3.28	47.7	5.14	<b>74.8</b>
0.3	3.27	47.4	--	--
0.4	3.31	47.7	4.82	<b>69.5</b>
0.5	3.43	49.2	3.83	54.9
0.6	3.20	45.7	4.10	58.5
0.7	3.14	44.6	--	--
0.8	3.28	46.4	4.04	57.1
0.9	3.76	52.9	3.99	56.2
1.0	3.10	43.4	3.76	52.7
1.0 (Theoretical[6])	7.14	--	--	--

The highest densities observed after sintering were between 70-75% of the theoretical values. High temperature resistivity and Seebeck measurements indicate that as the Cd content increases, the samples retain *n*-type conductivity accompanied by an increase in the measured resistivity (Figure 3.8).

This follows the expected trend based on the electronic properties of the parent compounds  $\text{Ag}_2\text{Sb}_2\text{O}_6$  and  $\text{Cd}_2\text{Sb}_2\text{O}_7$ .

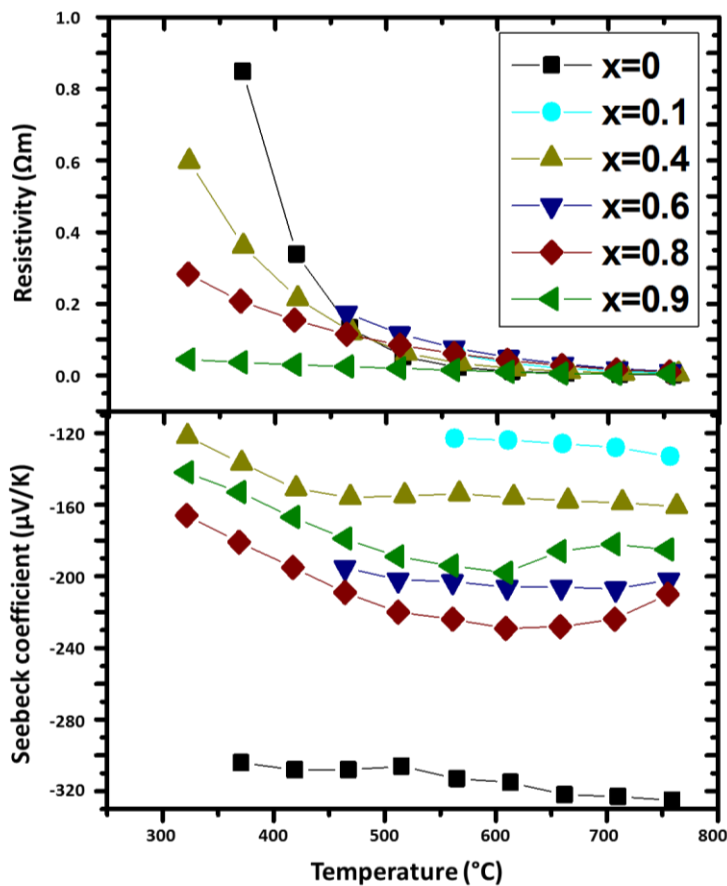


Figure 3.8 High temperature resistivity and Seebeck data collected on the samples with a density 70% or greater of that of the theoretical values.

### 3.2.7 Photocatalytic Activity:

The photocatalytic activity was evaluated for the solid solution by monitoring the degradation of methylene blue over 2 h irradiation time. The normalized data for each sample along the series is shown in Figure 3.9. It is observed that the total amount of methylene blue degraded by the sample decreases with increasing Cd content along the series.

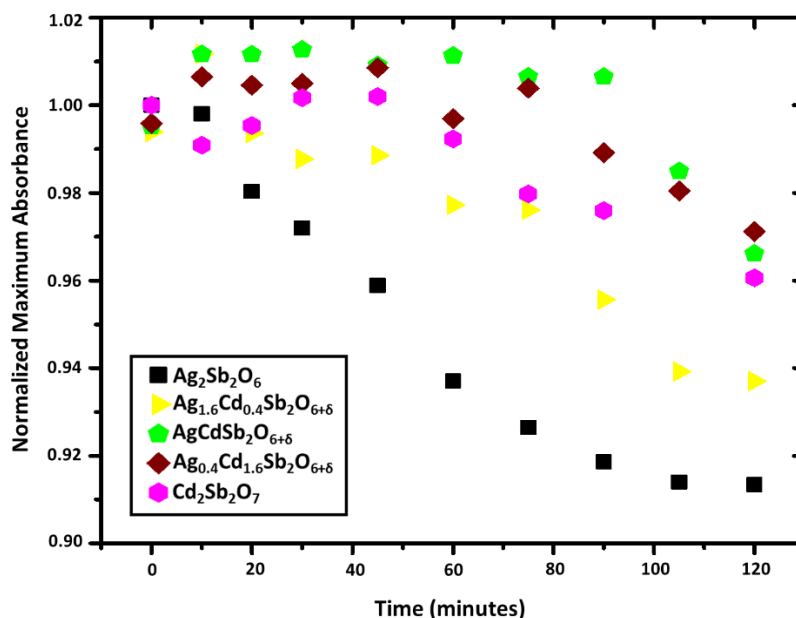


Figure 3.9 Degradation of methylene blue over a two-hour irradiation period, monitored by the normalized maximum absorbance of the dye at various time intervals.

Based on an estimation of the band gap, it was determined that an increase in the magnitude was observed with an increase in cadmium content. It was previously hypothesized that a change in the magnitude of the band gap could be induced by changing the amount of orbital overlap between the Ag  $4d$  and O  $2p$  orbitals, or in other words, by changing the Ag-O bond length. Throughout the series, it was indicated that the change in lattice parameter was minimal, and it is speculated that the change in the Ag-O bond length is minimal as well. Therefore, the evolution of the band gap throughout the series must be attributed elsewhere. Detailed DOS calculations (Figures 3.5-3.7) show that as the Cd content increases, the VBM becomes no longer dominated by Ag  $4d$ -O  $2p$  orbitals, but instead becomes dominated by primarily O orbitals. This effectively lowers the energy of the VBM, resulting in the observed increase in the magnitude of the band gap.

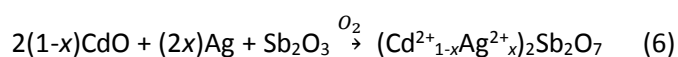
Along with the increase in the magnitude of the band gap, an increase in the resistivities of the samples was observed as the Cd content increased. Both of these properties play a large role in the

photocatalytic activity of a material, and it is observed that a decrease in the activity of the samples follows the increase in the Cd content as well. This decrease is primarily attributed to the increasing resistivity, which can also be attributed to the increase in the magnitude of the band gap. While an enhancement of the photocatalytic activity was not observed, this work illustrates the dependence of this activity not only on the magnitude of the band gap, but on the orbital composition in the VBM and CBM.

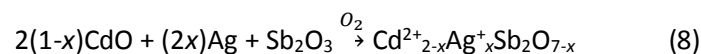
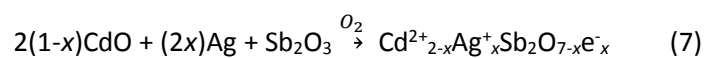
### 3.2.8 Investigation of the Cadmium-Rich End of the Solid Solution

As the series progresses from  $\text{Ag}_2\text{Sb}_2\text{O}_6$  to  $\text{Cd}_2\text{Sb}_2\text{O}_7$ , it is expected that a linear gain of O would be observed as Cd content increases. This hypothesis can be modeled by the formula  $(\text{Ag}_{1-x}\text{Cd}_x)_2\text{Sb}_2\text{O}_{6+x}$ . However, rationalizing this linear relationship near the Cd-rich end presents a problem. As previously mentioned, the ideal pyrochlore structure can be described as two interpenetrating networks: a network of  $\text{BO}_6$  octahedra, and a network of  $\text{A}_2\text{O}$  chains. For  $\text{Cd}_2\text{Sb}_2\text{O}_7$ , this would be equivalent to a network of  $\text{SbO}_6$  polyhedra and a network of  $\text{Cd}_2\text{O}$  chains. This  $\text{Cd}_2\text{O}$  chain consists of strong bonds between the alternating Cd and O atoms. As silver is introduced into this system, the  $\text{SbO}_6$  polyhedra remain unchanged, but the Ag will replace a Cd atom on the  $\text{Cd}_2\text{O}$  chain. After this substitution, based on a linear O-Cd relationship, the  $\text{A}_2\text{O}$  chain would now consist of neighboring Cd that are bonded to only one oxygen atom. This creates an unfavorable situation of severely under-bonded Cd cations in the compound, which could be alleviated by distributing charge elsewhere. Three alternative models were proposed for the Cd-rich end of the solid solution:

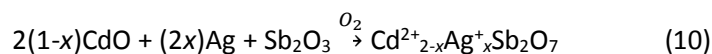
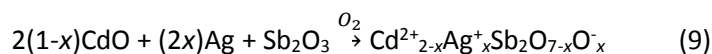
1. The formation of  $\text{Ag}^{2+}$ :



2. An  $e^-$  trapped in an  $\text{O}^{2-}$  vacancy, creating a color center:



3. A hole color center trapped on an interstitial oxygen, essentially creating an  $\text{O}^-$  species:



Electron Paramagnetic Resonance (EPR) spectra collected at Roosevelt University of the Cd-rich samples did not show evidence for the presence of  $\text{Ag}^{2+}$ , as there is no hyperfine splitting present. However, the spectra did indicate the presence of a radical species in small concentrations (Figure 3.10).[21] To further investigate the origin of the EPR signal, it was necessary to exclude other possible sources.

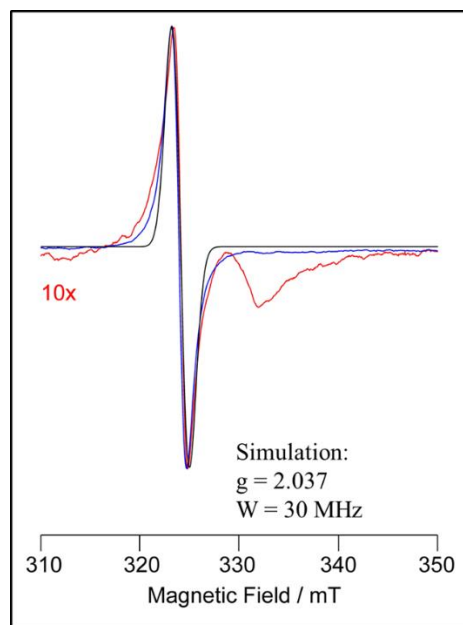


Figure 3.10 EPR spectra for  $\text{Ag}_{0.5}\text{Cd}_{1.5}\text{Sb}_2\text{O}_{6+\delta}$  (red) and  $\text{Ag}_{0.2}\text{Cd}_{1.8}\text{Sb}_2\text{O}_{6+\delta}$  (blue). Spectra indicate a small radical species is present, but is not indicative of  $\text{Ag}^{2+}$ .

In the solid solution, another possible source for an EPR signal could arise from Sb in the system that is not in the pentavalent oxidation state. One possibility is that if an electron color center is generated, it could become trapped on Sb, creating  $\text{Sb}^{4+}$ . However, due to the tendency towards disproportionation to  $\text{Sb}^{3+}$  and  $\text{Sb}^{5+}$ , this is unlikely. Another possibility is the presence of  $\text{Sb}^{3+}$  on the A-site of the pyrochlore structure, which has been reported in the literature.[22–27] Therefore, it was necessary to employ  $^{121}\text{Sb}$  Mössbauer spectroscopy to determine the oxidation and coordination of Sb throughout the series. The well-resolved  $^{121}\text{Sb}$  Mössbauer spectra of the pyrochlores  $\text{Ag}_2\text{Sb}_2\text{O}_6$ ,  $\text{AgCdSb}_2\text{O}_{6+x}$ ,  $\text{Ag}_{0.4}\text{Cd}_{1.6}\text{Sb}_2\text{O}_{6+x}$ , and  $\text{Cd}_2\text{Sb}_2\text{O}_7$  are presented in Figure 3.11 together with transmission integral fits. The corresponding fitting parameters are listed in Table 3.3.

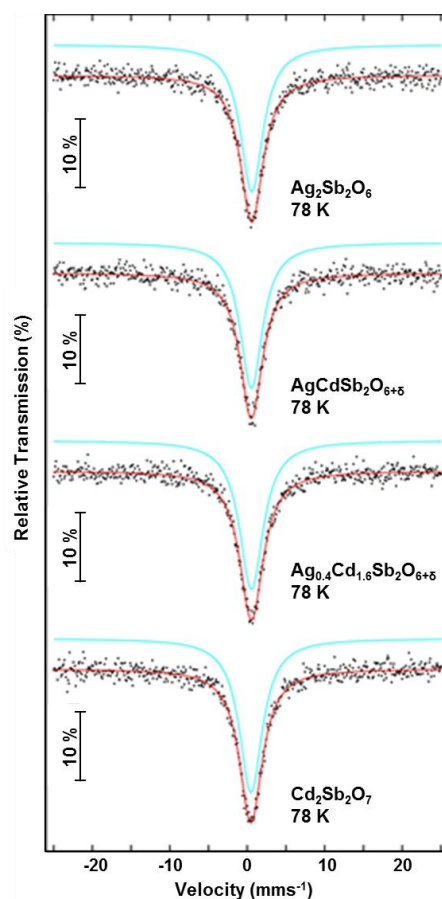


Figure 3.11 Experimental and simulated  $^{121}\text{Sb}$  Mössbauer spectra of the  $\text{Sb}^{5+}$  pyrochlores  $\text{Ag}_2\text{Sb}_2\text{O}_6$ ,  $\text{AgCdSb}_2\text{O}_{6+6}$ ,  $\text{Ag}_{0.4}\text{Cd}_{1.6}\text{Sb}_2\text{O}_{6+6}$ , and  $\text{Cd}_2\text{Sb}_2\text{O}_7$  at 78 K.

Table 3.3 Fitting parameters of  $^{121}\text{Sb}$  Mössbauer spectroscopic measurements of several  $\text{Sb}^{5+}$  pyrochlores at 78 K.  $\delta$  = isomer shift and  $\Gamma$  = experimental line width.

Compound	$\delta$ ( $\text{mm s}^{-1}$ )	$\Gamma$ ( $\text{mm s}^{-1}$ )
$\text{Ag}_2\text{Sb}_2\text{O}_6$	0.58(2)	3.55(6)
$\text{AgCdSb}_2\text{O}_{6+x}$	0.53(2)	3.53(7)
$\text{Ag}_{0.4}\text{Cd}_{1.6}\text{Sb}_2\text{O}_{6+x}$	0.54(2)	3.71(6)
$\text{Cd}_2\text{Sb}_2\text{O}_7$	0.48(2)	3.62(6)

All spectra show single signals with isomer shifts ranging from 0.48 mm/s ( $\text{Cd}_2\text{Sb}_2\text{O}_7$ ) to 0.58 mm/s ( $\text{Ag}_2\text{Sb}_2\text{O}_6$ ) which are indicative for purely pentavalent Sb.[28] The slightly smaller isomer shift of the Cd compound indicates slightly smaller 5s electron density at the Sb nuclei. Since the Sb atoms have cubic site symmetry  $Fd\bar{3}m$ , the spectra show no electric quadrupole splitting. The experimental line width parameters are all similar within the combined standard deviations and similar to many other Sb oxides and Sb intermetallics.[29–33] The spectra were recorded over the broad range of  $\pm 25$  mm/s. No signals are evident around  $-15$  mm/s, indicating stable pentavalent Sb in all samples.

Electron Paramagnetic Resonance (EPR) spectra of the Cd-rich samples disproves the existence of  $\text{Ag}^{2+}$ , as there is no hyperfine splitting present. However, a signal was detected with a g-factor of 2.037, suggesting that there may be a radical center present in relatively low concentrations. This signal was also detected in the end members of the solid solution, indicating that the EPR signal is not unique to the Cd-rich end. A qualitative comparison between literature EPR signals for classic materials that have formed an electron color center and the EPR signals for the solid solution indicate that an electron color center is not responsible for the observed signal. The formation of an electron color center is also highly unlikely due to the absence of irradiation or heating in metal vapor that is normally required for electron color center formation.[34] As no  $\text{Ag}^{2+}$ ,  $\text{Sb}^{4+}$ , or  $\text{Sb}^{3+}$  is present in the sample, it is concluded that the EPR signal is arising from a radical species present in relatively low concentrations, such as an  $\text{O}^-$  species.

The evolution of a broad absorption band in the Cd-rich samples, combined with an observation of a smoky color, also suggests that there may be the evolution of another species in the samples. It has

been shown that the smoky color in smoky quartz is a result of hole color centers in the system.[35,36] In the  $\text{SiO}_2$  network of smoky quartz, a  $\text{Si}^{+4}$  atom is replaced with an  $\text{Al}^{+3}$  atom, generating a hole. This generated hole becomes trapped on a nearby interstitial  $\text{O}^{2-}$ , effectively creating an  $\text{O}^\cdot$ . A similar mechanism may be responsible for the observed optical properties and EPR spectra of the  $\text{Ag}_2\text{Sb}_2\text{O}_6$ - $\text{Cd}_2\text{Sb}_2\text{O}_7$  solid solution.

### 3.2.9 Conclusions

A complete solid solution between  $\text{Ag}_2\text{Sb}_2\text{O}_6$  and  $\text{Cd}_2\text{Sb}_2\text{O}_7$  has been synthesized and characterized to investigate the effect of substitution upon the observed properties of the visible-light photocatalyst  $\text{Ag}_2\text{Sb}_2\text{O}_6$ . Substitution of Cd resulted in a simultaneous increase in the optical band gap and decrease in the resistivity of the samples, which are attributed to the observed decrease in the degradation rate of methylene blue upon irradiation with light. Anomalous behavior was observed in the optical data of the Cd-rich samples, and further investigation with EPR and  $^{121}\text{Sb}$  Mössbauer spectroscopy indicate that neither  $\text{Ag}^{2+}$  or  $\text{Sb}^{3+}$  are present. Therefore, the observed behavior of the Cd-rich samples is attributed to a small concentration of radical species such as  $\text{O}^\cdot$  in the samples, which is proposed to arise from a hole color center formed in the samples. Through cation substitution, the properties of  $\text{Ag}_2\text{Sb}_2\text{O}_6$  were successfully manipulated and, in combination with theoretical results, give insight to the origin of the observed photocatalytic activity of this material of interest.

### 3.3 Characterization of $\text{Ag}_{1-x}\text{M}^n_x\text{SbO}_{3+x[(n-1)/2]}$ ( $\text{M} = \text{Na}^+, \text{K}^+, \text{Tl}^{+/3+}$ )

#### 3.3.1 Motivation for Substitution

The atom-atom interactions in  $\text{AgSbO}_3$  can be manipulated by substituting metals of various electronegativities ( $\text{Na}^+$ ,  $\text{K}^+$  and  $\text{Tl}^+$ ) into the  $\text{Ag}^+$  site. In particular, the Ag-O bond length and consequently the Ag  $4d - \text{O} 2p$  orbital overlap will be manipulated, directly affecting the observed properties. Substitution will occur on the A-site of the pyrochlore structure, which sits within the large open channels of the anion-deficient pyrochlore. Upon substitution into the system, the cations on the A-site become disordered, making positional determination of the O especially difficult. As the Ag-O orbital overlap is crucial to the properties observed in this material, is it essential to employ a local probe which can sensitively identify the location of the O atoms. While well-characterized, neutron studies have not been performed on  $\text{AgSbO}_3$ . The ability to provide sensitivity to both the oxygen and the metals in this system makes neutron diffraction a crucial ingredient in the understanding of this promising material.

The use of the neutron PDF is essential for the determination of the local structure in  $\text{Ag}_{1-x}\text{M}^n_x\text{SbO}_{3+x[(n-1)/2]}$  ( $\text{M} = \text{Na}, \text{K}$  and  $\text{Tl}$ ). Employing neutron total scattering will help determine the O environment on the average and local scale, providing a better understanding of the disorder in the structure. This analysis will provide a detailed account of the effect of substitution upon the Ag-O bond length, which will give insight to how the Ag  $4d-\text{O} 2p$  orbital overlap is changing upon doping. This section aims to use total scattering techniques to determine the local and average structure of the pyrochlore  $\text{AgSbO}_3$  and to determine the effects of substitution on the observed properties. To the best of the authors' knowledge, this is the first report of neutron diffraction and PDF studies of this compound.

### 3.3.2 Structural Analysis

Initial structural lattice parameters were refined through the Le Bail method.[37] All peaks were indexed as cubic with the space group  $Fd\bar{3}m$  for nominal values of  $x = 0-0.2$  for the series  $\text{Ag}_{1-x}\text{M}^n_x\text{SbO}_{3+x[(n-1)/2]}$  ( $\text{M} = \text{Na}$  and  $\text{Tl}$ ) and  $x = 0.33$  for the series  $\text{Ag}_{1-x}\text{K}_x\text{SbO}_3$ , indicating a solubility limit in the pyrochlore structure for  $\text{Tl}$ ,  $\text{Na}$ , and  $\text{K}$ . Lattice parameters increased upon  $\text{Tl}$  and  $\text{K}$  substitution, as is expected when the larger  $\text{K}^+$  ( $r_{\text{ionic}} = 1.38 \text{ \AA}$ ) and  $\text{Tl}^+$  ( $r_{\text{ionic}} = 1.50 \text{ \AA}$ ) ions replace  $\text{Ag}^+$  ( $r_{\text{ionic}} = 1.15 \text{ \AA}$ ).[38] The lattice parameter was unchanging for  $\text{Na}$  substitution, which will be discussed further in the detailed analysis of the  $\text{Na}$ -substituted samples. An evolution of the lattice parameter upon substitution can be seen in Figure 3.12 for the neutron Rietveld refinements. Neutron lattice parameters are in reasonable agreement with XRD lattice parameters.

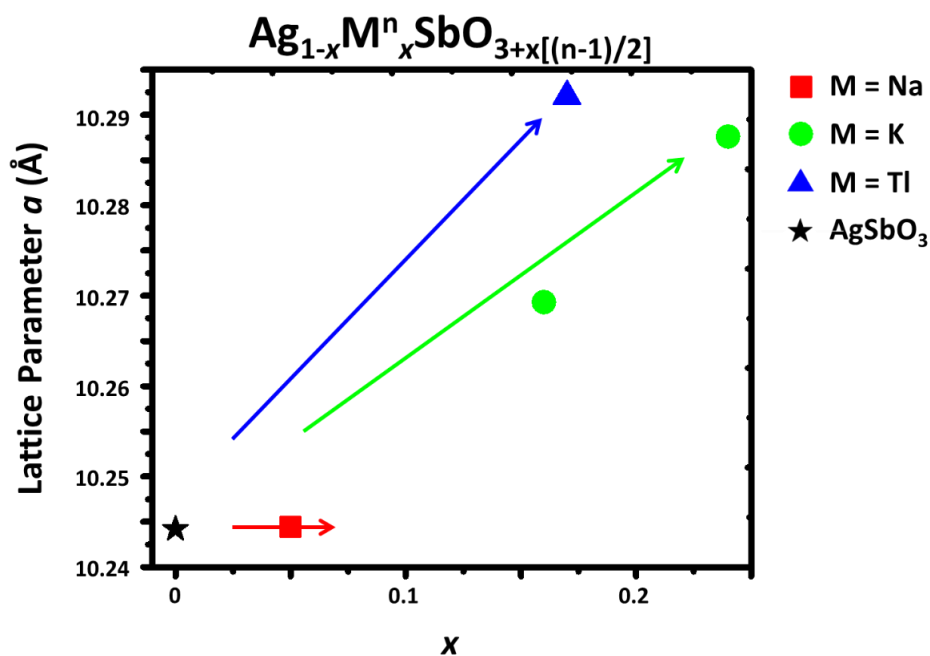


Figure 3.12 Lattice parameter evolution determined from neutron diffraction Rietveld analysis as cations Na, K, and Tl are doped into  $\text{AgSbO}_3$ . Error bars are contained within the points.

A summary of selected crystallographic parameters from the neutron Rietveld for all samples can be found in Table 3.4. Average and local structure refined atomic positional and displacement parameters for all samples are summarized in Table 3.5. Detailed results of the local PDF refinements can be found in supplemental Table 3.6. Local refinements were performed with occupancies fixed to those obtained through neutron Rietveld refinements of the average structure.

Table 3.4 Crystallographic data from the Rietveld refinement of neutron diffraction data for the series  $\text{Ag}_{1-x}\text{M}_x\text{SbO}_{3+x[(n-1)/2]}$  (M = Na, K and Tl).

Chemical Formula	$\text{AgSbO}_3$	$\text{Ag}_{0.96(1)}\text{Na}_{0.05(1)}\text{SbO}_3$	$\text{Ag}_{0.83(3)}\text{K}_{0.16(3)}\text{SbO}_3$	$\text{Ag}_{0.76(4)}\text{K}_{0.24(4)}\text{SbO}_3$	$\text{Ag}_{0.772(1)}\text{Tl}^{+0.13(2)}\text{Tl}^{+3}_{0.036(1)}\text{SbO}_{3.036(1)}$
<b>a (Å)</b>	10.2442(3)	10.2444(3)	10.2693(2)	10.2875(3)	10.292(1)
<b>Volume (Å<sup>3</sup>)</b>	1075.0(1)	1075.12(2)	1082.9(2)	1088.7(1)	1090.2(2)
<b>Z</b>	16	16	16	16	16
<b>Formula Weight</b>	277.62	274.87	266.55	261.78	298.54
<b>Space Group</b>	<i>Fd</i> $\bar{3}m$	<i>Fd</i> $\bar{3}m$	<i>Fd</i> $\bar{3}m$	<i>Fd</i> $\bar{3}m$	<i>Fd</i> $\bar{3}m$
<b>Temperature (°C)</b>	25	25	25	25	25
<b>Density<sub>calc</sub> (g/cm<sup>3</sup>)</b>	6.86	6.79	6.54	6.39	7.28
<b>R (%)</b>	2.16	2.02	2.55	2.39	2.02
<b>R<sub>wp</sub> (%)</b>	3.36	3.26	3.77	3.56	3.17

Table 3.5 Refined atomic positional and displacement parameters from average (Rietveld) and local (PDF) structure refinements for the series  $\text{Ag}_{1-x}\text{M}^n_x\text{SbO}_{3+x[(n-1)/2]}$  (M = Na, K and Tl) from neutron data. PDF refinements were completed on the r-range 1.7-10Å.

Parameter	$\text{AgSbO}_3$		$\text{Ag}_{0.96(1)}\text{Na}_{0.05(1)}\text{SbO}_3$	
	NPDF	Rietveld	NPDF	Rietveld
<b>O (48f) x</b>	0.324(1)	0.323(3)	0.324(1)	0.324(1)
<b>Na<sup>+</sup> (96h) y</b>	--	--	0.43(2)	0.458(1)
<b>Tl<sup>+</sup> (32e) x</b>	--	--	--	--
<b>Ag<sup>+</sup></b>	0.027(2)	0.027(3)	0.029(2)	0.027(1)
<b><math>U_{11}(\text{Å}^2)^*</math></b>				
<b><math>U_{12}(\text{Å}^2)^*</math></b>	0.016(2)	0.015(1)	0.016(2)	0.015(1)
<b>M <math>U_{11}(\text{Å}^2)^*</math></b>	--	--	0.03(1)	0.017(3)
<b><math>U_{12}(\text{Å}^2)^*</math></b>	--	--	0	0
<b>Sb <math>U_{iso}(\text{Å}^2)</math></b>	0.0028(2)	0.0048(2)	0.0027(2)	0.004(2)
<b>O (48f)</b>	0.0070(4)	0.009(1)	0.007(12)	0.009(1)
<b><math>U_{11}(\text{Å}^2)</math></b>				
<b><math>U_{22}(\text{Å}^2)</math></b>	0.0091(3)	0.010(1)	0.009(2)	0.0097(4)
<b><math>U_{33}(\text{Å}^2)</math></b>	0.0091(3)	0.010(1)	0.009(2)	0.0097(4)
<b><math>U_{12}(\text{Å}^2)</math></b>	0	0	0	0
<b><math>U_{13}(\text{Å}^2)</math></b>	0	0	0	0
<b><math>U_{23}(\text{Å}^2)</math></b>	0.0068(3)	0.005(1)	0.006(2)	0.005(4)
<b>O (8b)</b>	--	--	--	--
<b><math>U_{iso}(\text{Å}^2)</math></b>				

Parameter	$\text{Ag}_{0.83(3)}\text{K}_{0.16(3)}\text{SbO}_3$		$\text{Ag}_{0.76(4)}\text{K}_{0.24(4)}\text{SbO}_3$		$\text{Ag}_{0.772(1)}\text{Tl}^{+0.13(2)}\text{Tl}^{+3}_{0.036(1)}\text{SbO}_{3.036(1)}$	
	NPDF	Rietveld	NPDF	Rietveld	NPDF	Rietveld
<b>O (48f) x</b>	0.323(1)	0.323(3)	0.323(1)	0.322(2)	0.322(1)	0.3223(3)
<b>Na<sup>+</sup> (96h) y</b>	--	--	--	--	--	--
<b>Tl<sup>+</sup> (32e) x</b>	--	--	--	--	0.432(3)	0.436(2)
<b>Ag<sup>+</sup></b>	0.060(4)	0.052(2)	0.08(1)	0.076(1)	0.033(2)	0.031(2)
<b><math>U_{11}(\text{Å}^2)^*</math></b>						
<b><math>U_{12}(\text{Å}^2)^*</math></b>	0.047(4)	0.040(3)	0.07(1)	0.0064(3)	0.01(3)	0.010(2)
<b>M <math>U_{11}(\text{Å}^2)^*</math></b>	0.060(4)	0.052(2)	0.08(1)	0.076(1)	0.022(1)	0.01(1)
<b><math>U_{12}(\text{Å}^2)^*</math></b>	0.047(4)	0.040(3)	0.07(1)	0.0064(3)	0	0
<b>Sb <math>U_{iso}(\text{Å}^2)</math></b>	0.0031(2)	0.0043(1)	0.0035(2)	0.0047(1)	0.0035(3)	0.0044(1)
<b>O (48f)</b>	0.0088(1)	0.0104(1)	0.008(1)	0.0107(2)	0.008(1)	0.010(1)
<b><math>U_{11}(\text{Å}^2)</math></b>						
<b><math>U_{22}(\text{Å}^2)</math></b>	0.0097(3)	0.0098(1)	0.0095(3)	0.0096(2)	0.0102(4)	0.010(1)
<b><math>U_{33}(\text{Å}^2)</math></b>	0.0097(3)	0.0098(1)	0.0095(3)	0.0096(2)	0.0102(4)	0.010(1)
<b><math>U_{12}(\text{Å}^2)</math></b>	0	0	0	0	0	0
<b><math>U_{13}(\text{Å}^2)</math></b>	0	0	0	0	0	0
<b><math>U_{23}(\text{Å}^2)</math></b>	0.0069(1)	0.0060(1)	0.006(1)	0.0062(1)	0.007(1)	0.007(1)
<b>O (8b)</b>	--	--	--	--	0.032(3)	0.04(3)
<b><math>U_{iso}(\text{Å}^2)</math></b>						

Table 3.6 Summary of refined local parameters for the series  $\text{Ag}_{1-x}\text{M}^n_x\text{SbO}_{3+x[(n-1)/2]}$  (M = Na, K and Tl) over  $r=1.7\text{-}10\text{\AA}$ .

Parameter	$\text{AgSbO}_3$	$\text{Ag}_{0.96}\text{Na}_{0.05}\text{SbO}_3$	$\text{Ag}_{0.83}\text{K}_{0.16}\text{SbO}_3$	$\text{Ag}_{0.76}\text{K}_{0.24}\text{SbO}_3$	$\text{Ag}_{0.772}\text{Tl}^{+}_{0.13}\text{Tl}^{+3}_{0.036}\text{SbO}_{3.036}$
	$\text{Ag}^+$ in 16d	$\text{Na}^+$ in 96h	$\text{K}^+$ in 16d	$\text{K}^+$ in 16d	$\text{Tl}^+$ in 32e, $\text{O}'$ in 8b
$R_{\text{wp}}$ (%)	6.25	7.11	8.00	9.61	11.05
$a$ ( $\text{\AA}$ )	10.256(1)	10.256(1)	10.284(1)	10.302(1)	10.304(2)
$O, x$	0.3240(2)	0.3242(2)	0.3233(2)	0.3230(2)	0.3224(2)
$\text{Na}^+$ (96h) $y$	--	0.461(3)	--	--	--
$\text{Tl}^+$ (32e) $x$	--	--	--	--	0.432(3)
$\text{Ag}^+$	0.027(2)	0.029(2)	0.060(4)	0.08(1)	0.033(2)
$U_{11}(\text{\AA}^2)^*$	0.016(2)	0.016(2)	0.047(4)	0.07(1)	0.01(3)
$U_{12}(\text{\AA}^2)^*$	--	--	--	--	--
$M U_{11}(\text{\AA}^2)^*$	--	0.03(1)	0.060(4)	0.08(1)	0.022(1)
$U_{12}(\text{\AA}^2)^*$	--	0	0.047(4)	0.07(1)	0
$\text{Sb } U_{\text{iso}} (\text{\AA}^2)$	0.0028(2)	0.0027(2)	0.003(2)	0.0035(2)	0.0035(3)
$\text{O} (48f)$	0.0070(4)	0.0071(4)	0.0088(1)	0.008(1)	0.008(1)
$U_{11}(\text{\AA}^2)$	0.0091(3)	0.0089(3)	0.0097(3)	0.0095(3)	0.0102(4)
$U_{22}(\text{\AA}^2)$	0.0091(3)	0.0089(3)	0.0097(3)	0.0095(3)	0.0102(4)
$U_{33}(\text{\AA}^2)$	0	0	0	0	0
$U_{12}(\text{\AA}^2)$	0	0	0	0	0
$U_{13}(\text{\AA}^2)$	0.0068(3)	0.0060(4)	0.0069(1)	0.006(1)	0.007(1)
$U_{23}(\text{\AA}^2)$	--	--	--	--	--
$\text{O} (8b) U_{\text{iso}} (\text{\AA}^2)$	--	--	--	--	0.032(3)
$\text{Ag-O} (\text{\AA})$	2.558(1)	2.556(1)	2.570(1)	2.576(2)	2.581(2)
$\text{M-O} (\text{\AA})$	--	3.04(3) 2.61(3) 2.10(3)	2.570(1)	2.576(2)	3.02(1) 2.660(4)
$\text{Sb-O} (\text{\AA})$	1.9657(1)	1.9665(1)	1.9683(1)	1.970(1)	1.968(1)
$\text{Sb-O-Sb} (^\circ)$	134.54(2)	134.43(2)	134.93(2)	135.08(2)	135.41(2)

\*  $U_{11}=U_{22}=U_{33}$ ,  $U_{12}=U_{13}=U_{23}$

Average structure refinements of the parent compound  $\text{AgSbO}_3$  assumed full occupancy for Sb and O and all ideal positions were occupied: Ag in  $16d$ , Sb in  $16c$ , and O in  $48f$ . Rietveld analysis indicates that the ideal positions provide a good fit for the experimental data. Local refinements of  $\text{AgSbO}_3$  agree with the average model, indicating disorder of the  $\text{Ag}^+$  on the A-site within the channel structure. The displacement is evidenced through average and local fitting of the  $\text{Ag}^+$  anisotropic atomic displacement parameters. The primary displacement along the 3-fold axis is as expected, as this is the direction of the missing  $\text{O}'$  atom with respect to the  $\text{A}_2\text{B}_2\text{O}_6\text{O}'$  formula for the pyrochlore structure. The Rietveld and local fit, along with a pictorial representation of the displacement of  $\text{Ag}^+$  can be found in Figure 3.13.

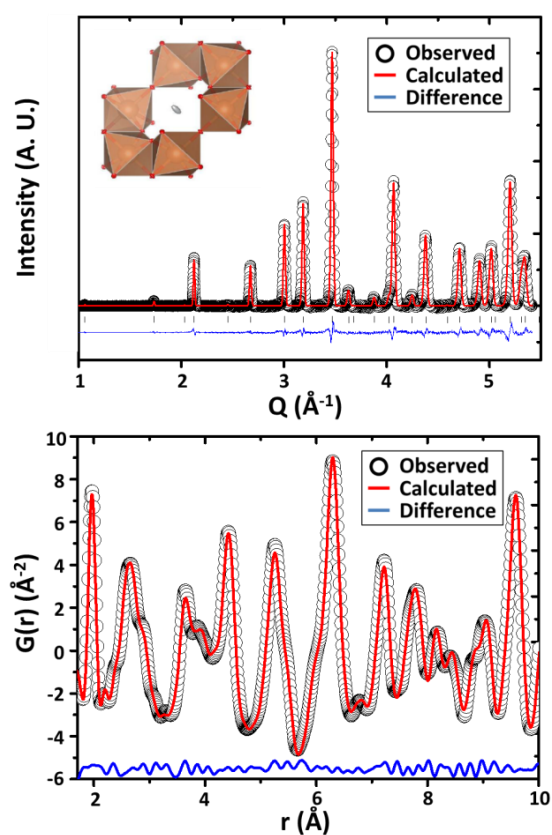


Figure 3.13 Average Rietveld (top) and local PDF (bottom) structure fits to the neutron data for the parent compound  $\text{AgSbO}_3$ . Refinements indicate the atomic displacement of the  $\text{Ag}^+$  cation is parallel to the three-fold rotation axis of the structure (top, inset).

The atom-atom correlations that form the PDF of  $\text{AgSbO}_3$  can easily be identified by calculating the individual partials of each type of atom-atom pair in the compound, shown in Figure 3.14. By referencing the partials, each peak in the PDF can be assigned to a bond length in the structure. The first peak in the PDF is formed entirely by Sb-O correlations, and this can be assigned to the basic octahedral  $\text{SbO}_6$  unit that forms the corner-sharing octahedral network. The first major Ag-O partial peak at approximately  $2.55 \text{ \AA}$  can similarly be assigned to the bonds between Ag and O that form the channel structure. This is also the bond that contributes to the valence band maximum, and is the primary bond length that will be probed through doping.

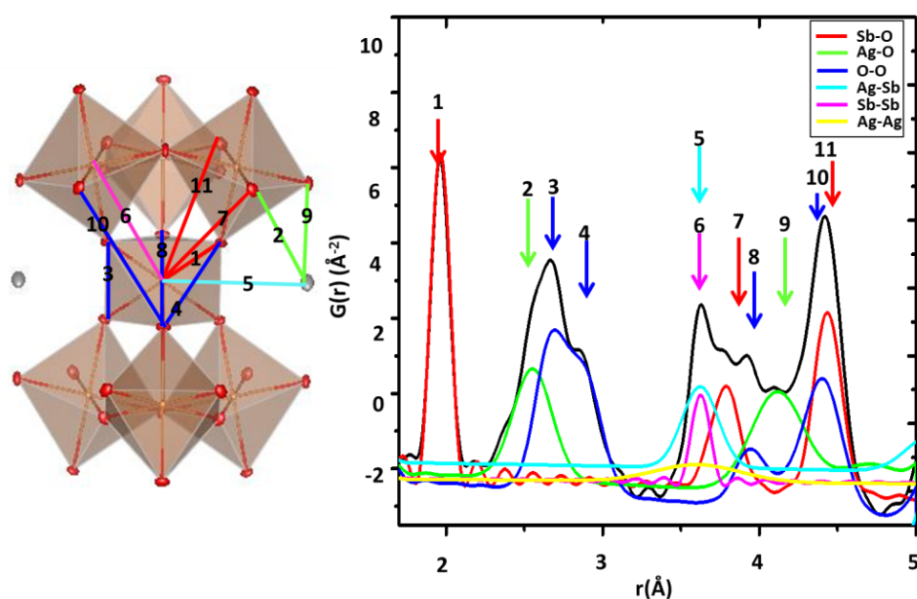


Figure 3.14 Partial atom-atom contributions to the PDF function in the range of 1.7-5  $\text{\AA}$ . Peaks within the PDF can be assigned to various atom-atom correlations in the anion-deficient pyrochlore  $\text{AgSbO}_3$ . The black curve represents the total PDF, while colored curves correspond to specific partial contributions.

Initial Rietveld refinements of the substituted samples were performed on samples assuming all cations were substituted directly for  $\text{Ag}^+$  on the  $16d$  site. Sb and O content was fixed at full occupancy, as

was done with  $\text{AgSbO}_3$ . As there is a large space within the  $\text{MO}_6$  channels, the A atom could potentially displace off of this ideal site. A displacement perpendicular to the 3-fold rotation axis of the channel results in the A atom occupying the variable  $96h$  or  $96g$  sites, and a displacement parallel to the rotation axis results in an occupancy of the variable  $32e$  site. These various displacements are shown in Figure 3.15, and will be explored as options for the location of the A cation upon substitution in the average and local structure data.

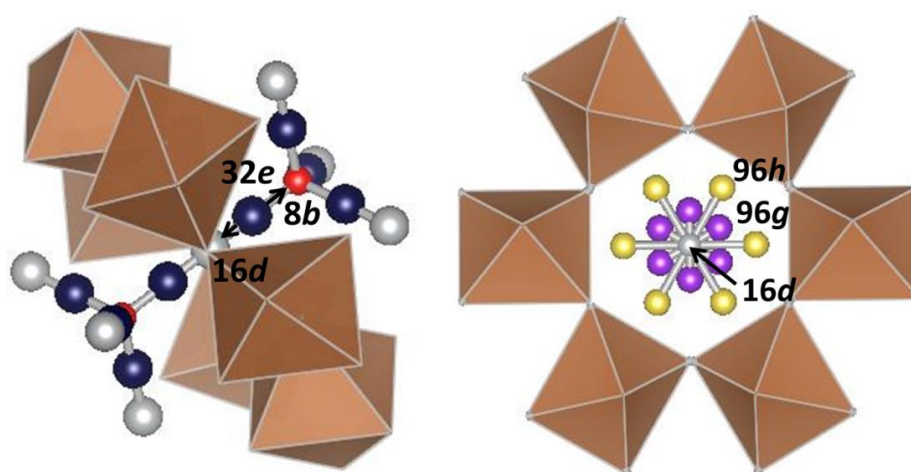


Figure 3.15 Schematic representation of the available sites for the A cation within the  $\text{MO}_6$  channel structure. The ideal position for the A cation is  $16d$ . Red atoms at  $8b$  indicate regular pyrochlore locations for the  $O'$  positions. Arrows along the 3-fold rotation axis indicate the displacement direction of the  $32e$  site, shown in navy.

The observation of unchanged lattice parameters upon  $\text{Na}^+$  substitution suggests that as  $\text{Na}^+$  is introduced into the structure, the  $\text{SbO}_6$  octahedral network remains nearly unchanged. Thus, we assumed that the displacement parameters of  $\text{Ag}^+$  should be unchanged as well upon substitution. Therefore, our model for refinement fixed the displacement parameters for  $\text{Ag}^+$  at the values obtained for  $\text{AgSbO}_3$ . The atomic displacement factor for Na was refined independently and found to be so large that a model was evaluated in which Na was statically displaced from the Ag site. The site for Ag is  $16d$  ( $\frac{1}{2}, \frac{1}{2}, \frac{1}{2}$ ), and the

96*h* site ( $\frac{1}{2}$ ,  $y$ ,  $-y$ ) allows Na to displace off this site in a direction perpendicular to the 3-fold axis, providing some shorter Na-O bonds. Rietveld refinements indicate when modeled in 96*h* there is a Na displacement of about 0.6 Å off the 3-fold axis. However, the obtained  $R_{wp}$  value of this model was very similar to that of the 16*d* model with a larger isotropic dynamic displacement, and it was difficult to determine the most accurate description of the structure through Rietveld refinements. Local modeling of Na in the 96*h* site in the PDF data revealed a reduction in both the atomic displacement of Na and  $R_{wp}$  in comparison to the 16*d* model, indicating that Na<sup>+</sup> does indeed occupy this site. Bond valence sum (BVS) calculations also support this, and a comparison between the refined values and the BVS calculations for the two models can be seen in Table 3.7. Rietveld and PDF fits of the Na sample can be seen in Figures 3.16 and 3.17, respectively.

Table 3.7 Comparison of the refined atomic positional and displacement parameters from average (Rietveld) and local (PDF) structure refinements for the series  $\text{Ag}_{1-x}\text{M}^n_x\text{SbO}_{3+x[(n-1)/2]}$  (M = Na, K and Tl) from neutron data. PDF refinements were completed on the r-range 1.7-10Å.

Parameter	$\text{Ag}_{0.96(1)}\text{Na}_{0.05(1)}\text{SbO}_3$			
	PDF		Rietveld	
	Na <sup>+</sup> in 16 <i>d</i>	Na <sup>+</sup> in 96 <i>h</i>	Na <sup>+</sup> in 16 <i>d</i>	Na <sup>+</sup> in 96 <i>h</i>
BVS, Na <sup>+</sup>	0.78	1.17	0.80	1.26
$R_{wp}$ (%)	7.45	7.11	3.26	3.26
Na <sup>+</sup> , $y$	0.5	0.461(3)	0.5	0.458(1)
Ag $U_{11}(\text{Å}^2)^*$	0.028(1)	0.029(2)	0.027(1)	0.027(1)
$U_{12}(\text{Å}^2)^*$	0.0162(2)	0.016(2)	0.015(1)	0.015(1)
Na <sup>+</sup> $U_{iso}(\text{Å}^2)$	0.22(3)	0.03(1)	0.10(1)	0.017(3)

$$* U_{11}=U_{22}=U_{33}, U_{12}=U_{13}=U_{23}$$

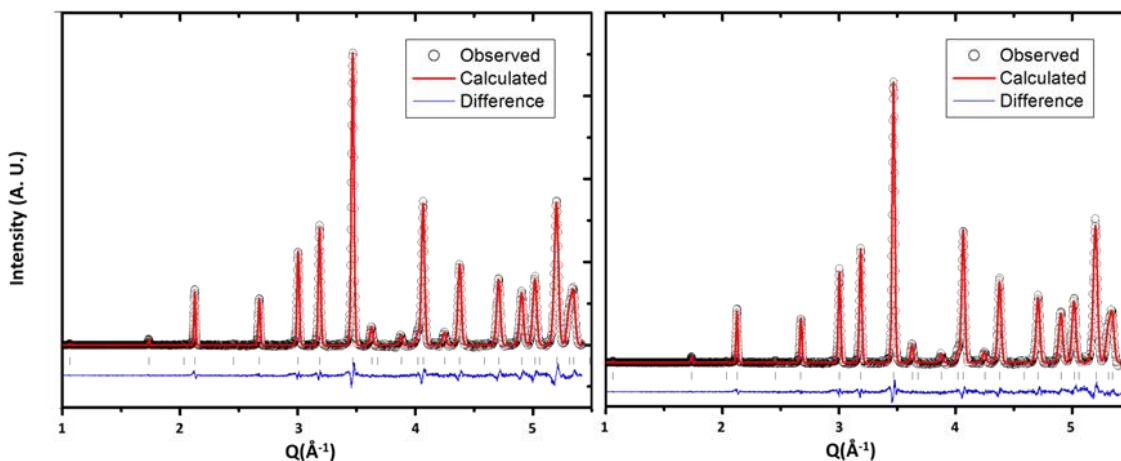


Figure 3.16 Rietveld refinement fits for nominal  $\text{Ag}_{0.9}\text{Na}_{0.1}\text{SbO}_3$  with  $\text{Na}^+$  in the  $16d$  site, left, and the  $96h$  site, right.

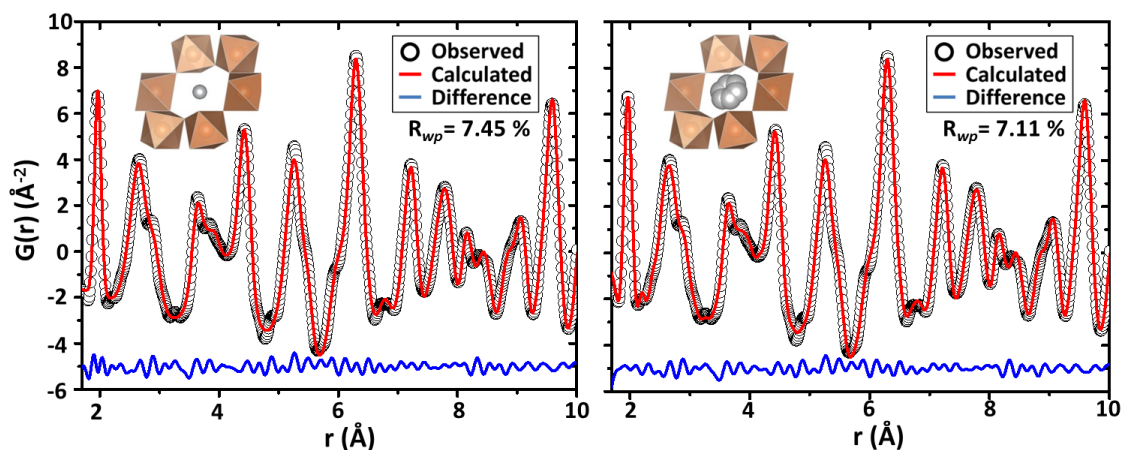


Figure 3.17 Local refinement fit results to neutron data for the various sodium models. Refinement fits for the sample  $\text{Ag}_{0.96(1)}\text{Na}_{0.05(1)}\text{SbO}_3$  where sodium sits in the  $16d$  site (left) and  $96h$  site (right).

Due to size and electronic configuration, refinements of the  $\text{K}^+$  substituted samples were performed with the assumption that  $\text{K}^+$  would behave similarly to  $\text{Ag}^+$ , and the atomic displacement parameters for the A-site cations were constrained to be equivalent during average structure modeling. The large cage at the A-site results in larger displacement factors, which remain highly anisotropic. This

high degree of anisotropic movement along the 3-fold rotation axis is also observed in the local PDF refinements. Rietveld and local PDF fits for the  $K = 0.24$  sample are illustrated in Figure 3.18.

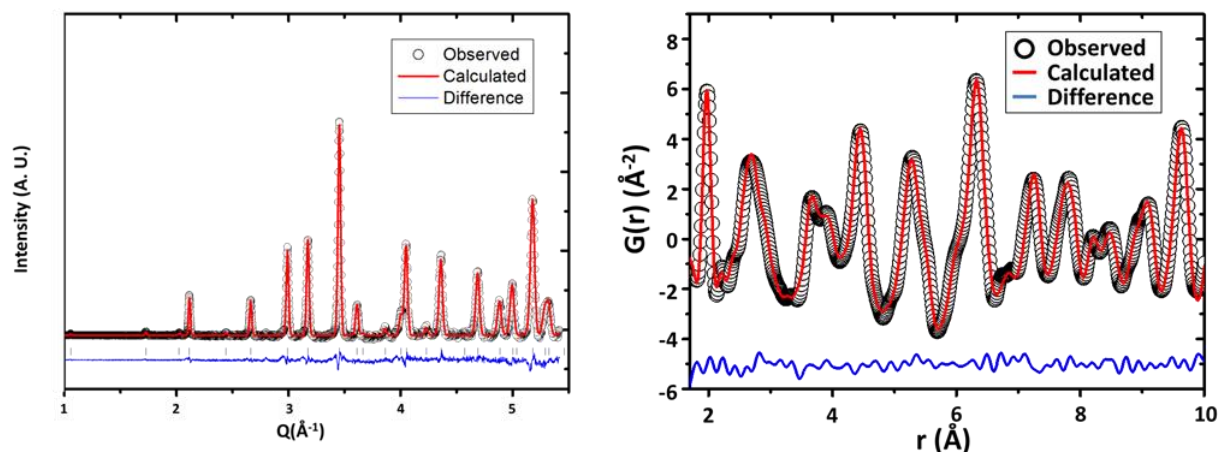


Figure 3.18 Rietveld (left) and PDF (right) refinements for  $\text{Ag}_{0.76(4)}\text{K}_{0.24(4)}\text{SbO}_3$ .

Initial refinements of the sample substituted with Tl indicated that Tl was strongly displaced from the Ag site. In this case (contrary to Na case), it was found that Tl remains on the 3-fold axis but is in the  $32e$  site very strongly displaced ( $1.14 \text{ \AA}$ ) from the  $16d$ . The Tl-O distances for  $\text{Tl}^+$  on the  $16d$  would be much too small for  $\text{Tl}^+$ , giving a Tl bond valence sum of 1.84. After the displacement of  $1.14 \text{ \AA}$  the bond valence sum for this  $\text{Tl}^+$  becomes 1.09. Since there is the possibility that some of the precursor  $\text{Tl}^{3+}$  remains unreduced, the occupancy of an O atom in the  $8b$  site was refined. The obtained value of  $0.036(1)$  indicates a formula of  $\text{Ag}_{0.772(1)}\text{Tl}_{0.13(2)}^{+}\text{Tl}_{0.036(1)}^{3+}\text{SbO}_{3.036(1)}$ . The size of  $\text{Tl}^{3+}$  is close enough to that of  $\text{Ag}^+$  that it was assumed that the  $\text{Tl}^{3+}$  would be on the  $\text{Ag}^+$  site, and the final formula was obtained with this assumption. The environment of  $\text{Tl}^+$  (Figure 3.19) with all strong bonds on one side is that expected for a lone pair cation. The lone pairs of  $\text{Tl}^+$  would be pointed in the direction of the  $8b$  site, which should be empty because the small amount of O in this site would be attracted to the vicinity of  $\text{Tl}^{3+}$ . Fits of the

Rietveld and PDF data with the various models for TI substitution are found in Figures 3.20 and 3.21 respectively, and a comparison of the refined parameters in Table 3.8.

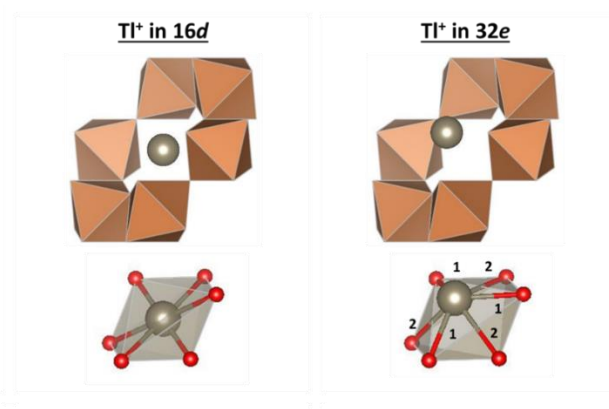


Figure 3.19 Coordination environment for TI<sup>+</sup> in 16d (left) vs. 32e (right). When located in 16d, TI<sup>+</sup> has six equivalent TI-O bonds (2.579 Å), whereas when located in the 32e site, short (bonds #1, 2.636 Å) and long (bonds #2, 2.98 Å) TI-O bonds are observed. Movement into 32e results in a displacement of 1.14 Å off of the 16d site.

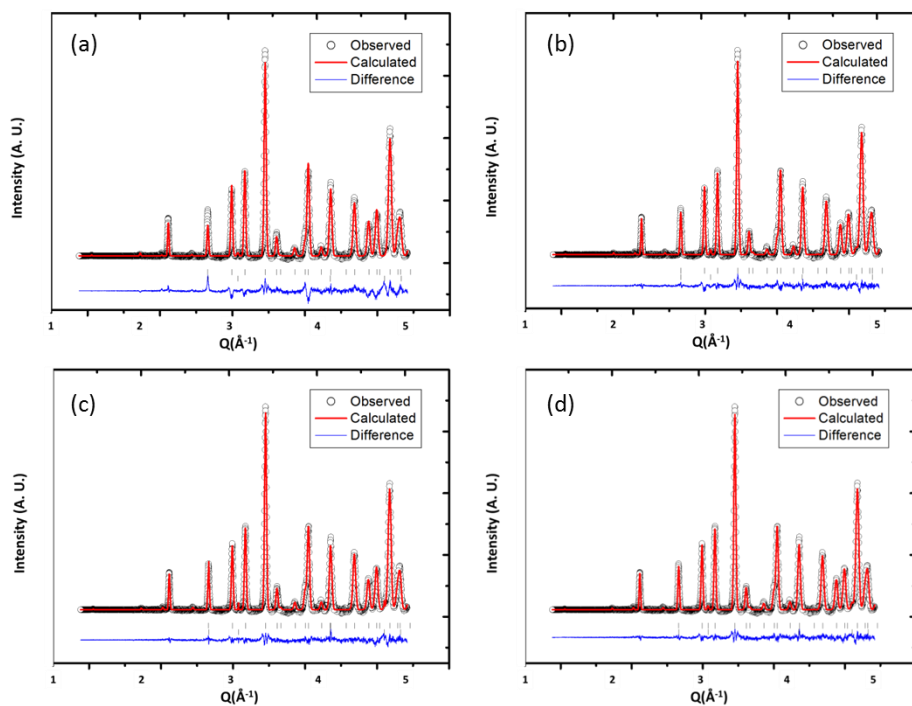


Figure 3.20 Rietveld refinement fit for nominal Ag<sub>0.8</sub>Ti<sub>0.2</sub>SbO<sub>3</sub> with TI<sup>+</sup> in (a) 16d, (b) TI<sup>+</sup> in 32e, (c) TI<sup>+</sup> in 32e and oxygen in 8b, and (d) TI<sup>+</sup> in 32e, TI<sup>3+</sup> in 16d and oxygen in 8b.

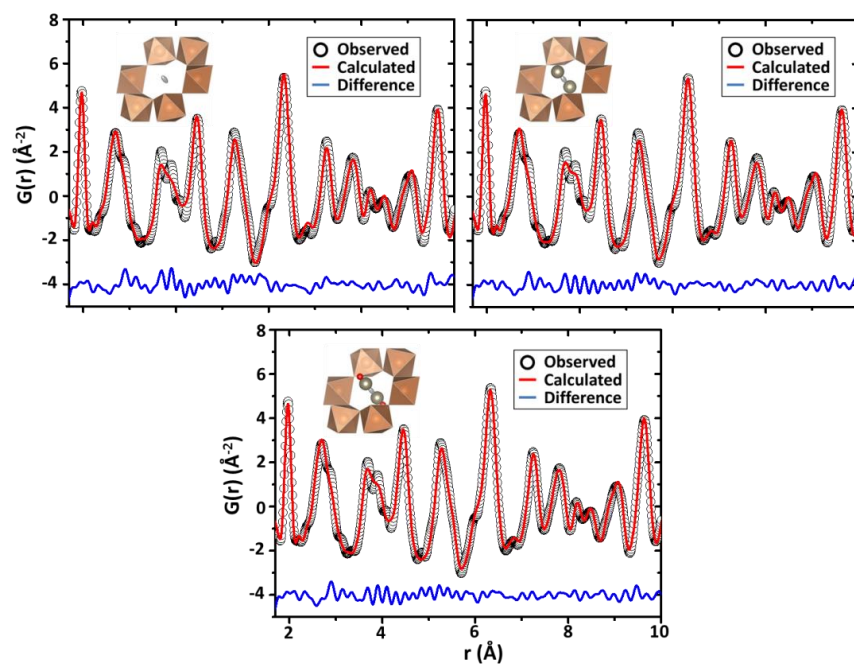


Figure 3.21 Local refinement fits for nominal  $\text{Ag}_{0.8}\text{Tl}_{0.2}\text{SbO}_3$ . Top, left: Fit with  $\text{Tl}^+$  in  $16d$ . Top, right: Fit with  $\text{Tl}^+$  in  $32e$ . Bottom, left: Fit with  $\text{Tl}^+$  in  $32e$  and oxygen in  $8b$ . Bottom, right: Fit with  $\text{Tl}^+$  in  $32e$ ,  $\text{Tl}^{3+}$  in  $16d$  and oxygen in  $8b$ .

Table 3.8 Comparison of the refined atomic positional and displacement parameters from average (Rietveld) and local (PDF) structure refinements for the series  $\text{Ag}_{1-x}\text{Tl}_x\text{SbO}_3$ . PDF refinements were completed on the r-range 1.7-10Å.

Parameter	$\text{Ag}_{0.8}\text{Tl}_{0.2}\text{SbO}_3$ Model 1: $\text{Ag}^+/\text{Tl}^+$ in 16d		$\text{Ag}_{0.8}\text{Tl}_{0.2}\text{SbO}_3$ Model 2: $\text{Ag}^+$ in 16d, $\text{Tl}^+$ in 32e		$\text{Ag}_{0.8}\text{Tl}_{0.2}\text{SbO}_3$ Model 3: $\text{Ag}^+$ in 16d, $\text{Tl}^+$ in 32e, $\text{O}'$ in 8b	
	NPDF 10Å	Rietveld	NPDF 10Å	Rietveld	NPDF 10Å	Rietveld
$wR_p$ (%)	13.71	4.06	11.40	3.42	11.05	3.17
a (Å)	10.307(4)	10.29169(16)	10.304(3)	10.29191(13)	10.304(2)	10.292(1)
O, x	0.3223(4)	0.32238(4)	0.3227(4)	0.32268(4)	0.322(1)	0.3223(3)
$\text{Tl}^+$ , x	0.5000	0.5000	0.427(5)	0.4289(4)	0.432(3)	0.436(2)
$\text{Ag}^+$ (occ.)	0.80(2)	0.92312	0.711(7)	0.897(5)	0.77(1)	0.77(1)
$\text{Tl}^+$ (occ.)	0.103(7)	0.07688	0.131(4)	0.1136(16)	0.06(1)	0.06(1)
Sb (occ.)	1.0	1.0	1.0	1.0	1.0	1.0
O (occ.)	1.0	1.0	1.0	1.0	1.0	1.0
$\text{O}'$ (occ.)	N/A	N/A	N/A	N/A	0.07(1)	0.07(1)
$\text{Ag}^+ U_{11}(\text{Å}^2)$	0.068(8)	0.061(1)	0.024(3)	0.035(2)	0.033(2)	0.031(2)
$U_{22}(\text{Å}^2)$	0.068(8)	0.061(1)	0.024(3)	0.035(2)	0.033(2)	0.031(2)
$U_{33}(\text{Å}^2)$	0.068(8)	0.061(1)	0.024(3)	0.035(2)	0.033(2)	0.031(2)
$U_{12}(\text{Å}^2)$	0.046(2)	0.044(2)	0.010(2)	0.018(2)	0.01(3)	0.010(2)
$U_{13}(\text{Å}^2)$	0.046(2)	0.044(2)	0.010(2)	0.018(2)	0.01(3)	0.010(2)
$U_{23}(\text{Å}^2)$	0.046(2)	0.044(2)	0.010(2)	0.018(2)	0.01(3)	0.010(2)
$\text{Tl}^+ U_{iso}(\text{Å}^2)$	0.009(1)	0.0200(2)	0.03(2)	0.041(2)	0.022(1)	0.01(1)
Sb $U_{iso}(\text{Å}^2)$	0.0031(5)	0.00355(13)	0.0039(6)	0.00298(9)	0.0035(3)	0.0044(1)
O (48f) $U_{11}(\text{Å}^2)$	0.009(3)	0.009(1)	0.009(2)	0.009(1)	0.008(1)	0.010(1)
$U_{22}(\text{Å}^2)$	0.009(2)	0.010(1)	0.009(2)	0.009(1)	0.0102(4)	0.010(1)
$U_{33}(\text{Å}^2)$	0.009(2)	0.010(1)	0.009(2)	0.009(1)	0.0102(4)	0.010(1)
$U_{12}(\text{Å}^2)$	0	0	0	0	0	0
$U_{13}(\text{Å}^2)$	0	0	0	0	0	0
$U_{23}(\text{Å}^2)$	0.005(1)	0.006(2)	0.006(1)	0.007(1)	0.007(1)	0.007(1)
O (8b) $U_{iso}(\text{Å}^2)$	N/A	N/A	N/A	N/A	0.032(3)	0.04(3)

As previously discussed, a very rigid and unchanging  $\text{SbO}_6$  network is present. This was initially concluded from an unchanging lattice parameter upon  $\text{Na}^+$  substitution, but can be further evidenced by directly comparing the first 3Å of the local PDF data of  $\text{AgSbO}_3$  with the highest-substituted sample for each element, shown in Figure 3.22. The primary Sb-O correlation peaks overlay almost completely, whereas the peak for the Ag-O correlation changes quite drastically. Through an analysis of the local data, it can be seen that the Sb-O correlation and consequently the  $\text{SbO}_6$  network remains relatively unchanged throughout the entire series  $\text{Ag}_{1-x}\text{M}^n_x\text{SbO}_{3+x[(n-1)/2]}$  (M = Na, K and Tl).

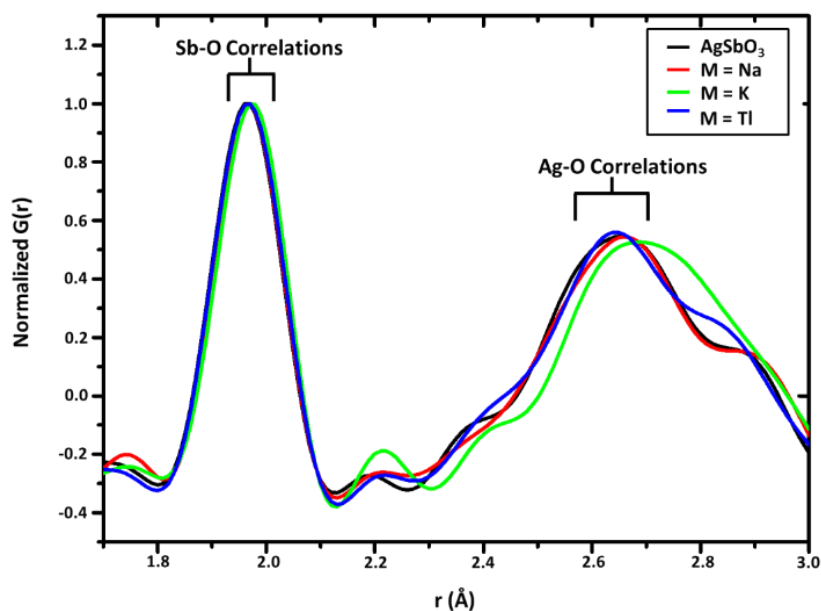


Figure 3.22 Overlay of the PDF data in the range of 1.7-3 Å. Peaks within the PDF can be assigned to various atom-atom correlations in the defect pyrochlore  $\text{AgSbO}_3$ . The black curve corresponds to the total PDF, while colored curves correspond to various samples in the series  $\text{Ag}_{1-x}\text{M}_x\text{SbO}_{3+x[(n-1)/2]}$  ( $M = \text{Na}, \text{K}$  and  $\text{Tl}$ ). For  $M=\text{K}$ , the atom-atom correlation curve for  $\text{Ag}_{0.76(4)}\text{K}_{0.24(4)}\text{SbO}_3$  is shown.

Selected bond distances and bond angles from the Rietveld and PDF fits are summarized in Table 3.9, and Figure 3.23 relates bond length and bond angle resulting from the Rietveld analysis of the samples series. In Figure 3.23a it can be seen that Ag-O bond length increases as expected as the larger  $\text{K}^+$  and  $\text{Tl}^+$  substitute for  $\text{Ag}^+$ . It can also be seen that substituting  $\text{Na}^+$  for  $\text{Ag}^+$  causes a decrease in the average Ag-O distance. This is not surprising except for the fact that there is no noticeable decrease in the lattice parameter as  $\text{Na}^+$  substitutes for  $\text{Ag}^+$ . This decrease of the Ag-O distance with no decrease in the lattice parameter can only occur if there is a compensating increase in the Sb-O distance. Such an increase does appear to occur, albeit very small. A plot of the Sb-O distance (Figure 3.23b) vs.  $x$  indicates a small but steady increase in the Sb-O distance as  $x$  increases for all samples. As the Ag-O bond length increases in the material, the amount of overlap between the Ag and O orbitals will decrease and conversely, as the

bond length decreases, the overlap will increase. While the Sb-O bond length apparently increases as the system is doped, the change is not as great in magnitude as the change upon doping of the Ag-O bond. Therefore, doping has a larger effect on the environment of the channel structure, leaving the  $\text{SbO}_6$  octahedral network relatively unchanged.

Table 3.9 Selected bond lengths and angles from average (Rietveld) and local (PDF) structure refinements for the series  $\text{Ag}_{1-x}\text{M}^n_x\text{SbO}_{3+x[(n-1)/2]}$  (M = Na, K and Tl) from neutron data. PDF refinements were completed on the r-range 1.7-10Å.

Parameter	$\text{AgSbO}_3$		$\text{Ag}_{0.96(1)}\text{Na}_{0.05(1)}\text{SbO}_3$	
	NPDF	Rietveld	NPDF	Rietveld
<b>Ag-O (Å)</b>	2.558(1)	2.555(1)	2.556(1)	2.554(1)
<b>M-O (Å)</b>	--	--	3.04(3)	3.08(2)
			2.61(1)	2.62(3)
			2.10(3)	2.06(1)
<b>Sb-O (Å)</b>	1.966(1)	1.963(1)	1.966(1)	1.963(1)
<b>Ag-O-Ag (°)</b>	62.8(1)	62.8(1)	62.9(1)	62.8(1)
<b>Sb-O-Sb (°)</b>	134.54(2)	134.57(1)	134.43(2)	134.48(1)

Parameter	$\text{Ag}_{0.83(3)}\text{K}_{0.16(3)}\text{SbO}_3$		$\text{Ag}_{0.76(4)}\text{K}_{0.24(4)}\text{SbO}_3$		$\text{Ag}_{0.772(1)}\text{Tl}^{+0.13(2)}\text{Tl}^{+3}_{0.036(1)}\text{SbO}_{3.036(1)}$	
	NPDF	Rietveld	NPDF	Rietveld	NPDF	Rietveld
<b>Ag-O (Å)</b>	2.570(1)	2.566(1)	2.576(2)	2.574(1)	2.581(2)	2.577(1)
<b>M-O (Å)</b>	2.570(1)	2.566(1)	2.576(2)	2.574(1)	2.660(4)	2.636(2)
					3.02(1)	2.98(2)
<b>Sb-O (Å)</b>	1.968(1)	1.965(1)	1.970(1)	1.966(1)	1.968(1)	1.966(1)
<b>Ag-O-Ag (°)</b>	62.8(1)	62.8(2)	62.7(2)	62.7(1)	62.7(1)	62.7(3)
<b>Sb-O-Sb (°)</b>	134.90(1)	134.86(2)	135.17(1)	135.41(1)	135.41(2)	135.33(1)

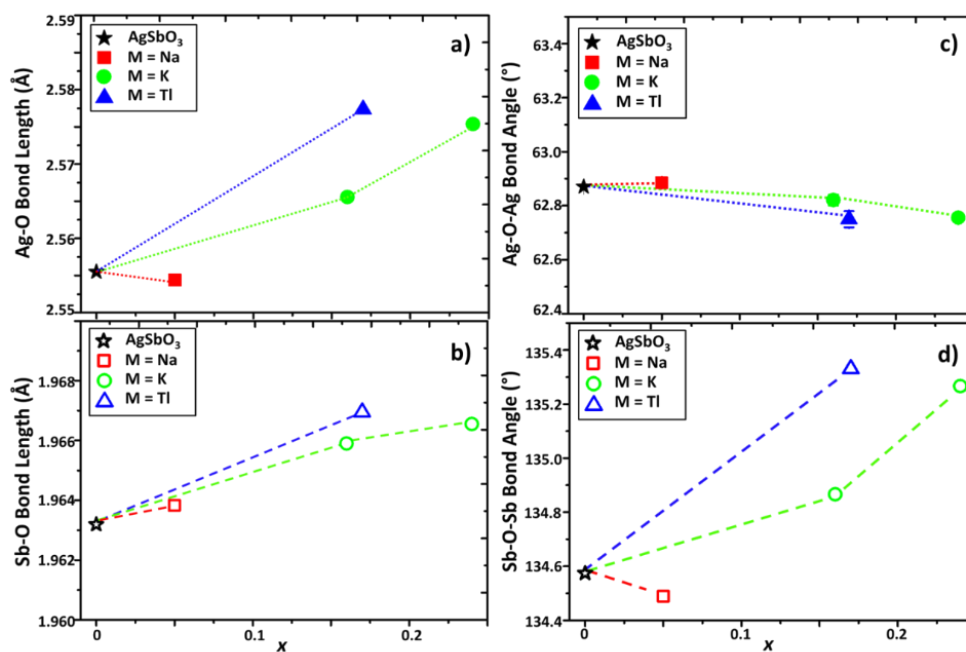


Figure 3.23 Ag-O bond length (top, left), Sb-O bond length (bottom, left), Ag-O-Ag bond angle (top, right) and Sb-O-Sb bond angle (bottom, right) evolution in the series  $\text{Ag}_{1-x}\text{M}^n_x\text{SbO}_{3+x[(n-1)/2]}$  (M = Na, K and Tl) as determined by Rietveld refinement of the neutron data. Error bars are contained within the point for plots a, b and d.

### 3.3.3 Sample Morphology

Qualitatively, SEM analysis reveals a similar grain size for all samples synthesized through solid state methods (Figure 3.24). Ion exchange synthesis appears to yield a smaller grain size for the Na-exchanged sample, and a larger grain size for the K-exchanged sample. To provide a more quantitative comparison, grain size was calculated using Le Bail profile matching through GSAS. Particle size analysis calculated through the analysis of the Lorentzian broadening term indicates particle sizes between 90 – 400 nm, with nominal  $\text{Ag}_{0.66}\text{K}_{0.33}\text{SbO}_3$  having the smallest particle size and nominal  $\text{Ag}_{0.8}\text{Tl}_{0.2}\text{SbO}_3$  having the largest. BET surface area analysis indicated similar surface areas for the solid state samples with an increase in surface area for both ion-exchanged samples. However, the ion-exchanged samples exhibit

the smallest pore width and diameter, and a large increase in pore width and diameter is observed for nominal  $\text{Ag}_{0.8}\text{Na}_{0.2}\text{SbO}_3$  in comparison to the parent compound. A summary of the morphological data can be found in Table 3.10.

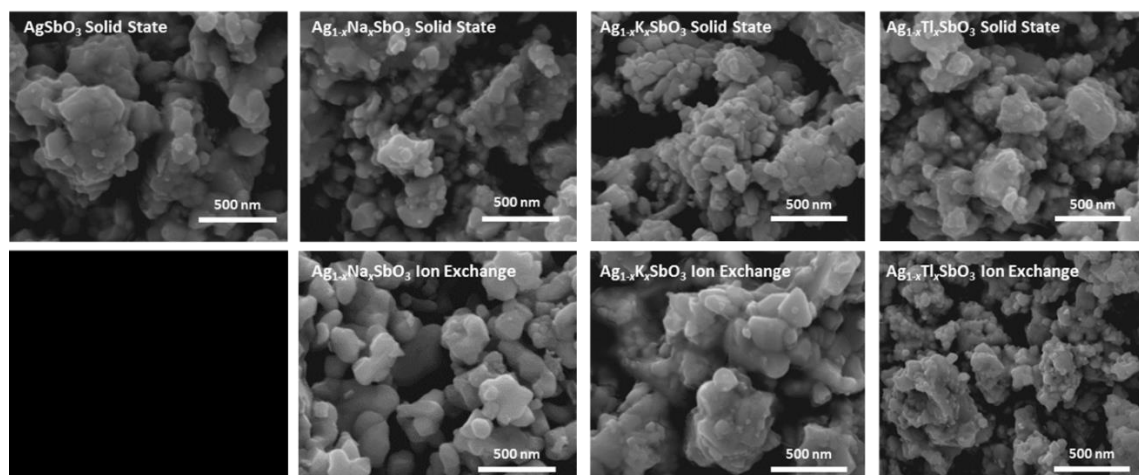


Figure 3.24 SEM images of the series  $\text{Ag}_{1-x}\text{M}^n_x\text{SbO}_{3+x[(n-1)/2]}$  ( $\text{M} = \text{Na}, \text{K}$  and  $\text{Tl}$ ) prepared by standard solid state (top row) and ion exchange (bottom row) reactions.

Table 3.10 Summary of sample particle size, surface area, and pore dimensions for the series  $\text{Ag}_{1-x}\text{M}^n_x\text{SbO}_{3+x[(n-1)/2]}$  ( $\text{M} = \text{Na}, \text{K}$  and  $\text{Tl}$ ).

Nominal Composition	Particle Size (nm)	Surface Area ( $\text{m}^2/\text{g}$ )	Pore Surface Area ( $\text{m}^2/\text{g}$ )	Pore Width ( $\text{\AA}$ )	Pore Diameter ( $\text{\AA}$ )
<b><math>\text{AgSbO}_3</math></b>	192.03	2.82	1.7	84.74	149.1
<b><math>\text{Ag}_{0.8}\text{Na}_{0.2}\text{SbO}_3</math></b>	235.13	1.88	0.6	214.60	662.4
<b><math>\text{Ag}_{1-x}\text{Na}_x\text{SbO}_3^*</math></b>	150.95	15.12	9.8	33.21	9.8
<b><math>\text{Ag}_{0.66}\text{K}_{0.33}\text{SbO}_3</math></b>	91.58	4.56	3.9	180.91	218.5
<b><math>\text{Ag}_{1-x}\text{K}_x\text{SbO}_3^*</math></b>	113.06	7.83	6.5	40.93	67.7
<b><math>\text{Ag}_{0.8}\text{Tl}_{0.2}\text{SbO}_3</math></b>	339.98	N/A	N/A	N/A	N/A
<b><math>\text{Ag}_{1-x}\text{Tl}_x\text{SbO}_3^*</math></b>	93.79	N/A	N/A	N/A	N/A

\*samples made though molten salt ion-exchange

### 3.3.4 Optical Characterization

The band gap for each sample was estimated by extrapolating the onset of the absorption curve obtained through diffuse reflectance measurements (Figure 3.25). Substitution with Na results in a small decrease in the band gap, while substitution with K results in an increase in the band gap. Substitution with Tl appears to result in a decrease in the band gap, but it must be noted that the absorption onset is more gradual in the Tl-substituted samples, giving rise to difficulty in accurate extrapolation. This is most likely due to the mixed valency of  $Tl^+$  and  $Tl^{3+}$  present in the sample. All ion exchange samples indicate minimal change in the band gap upon exchange.

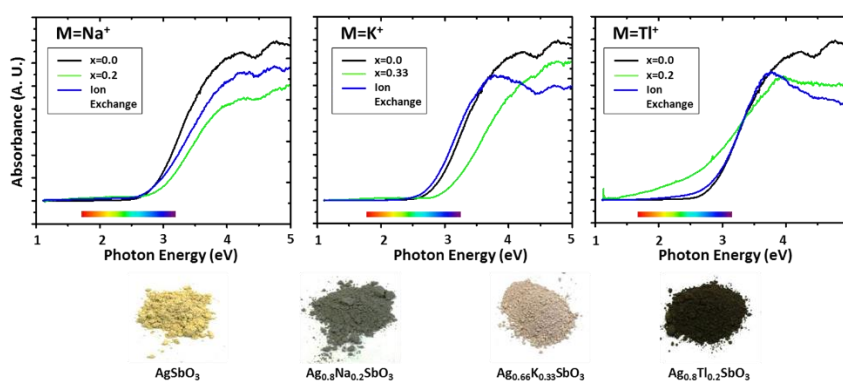


Figure 3.25 Optical spectra and powders for the series  $Ag_{1-x}M^n_xSbO_{3+x[(n-1)/2]}$  ( $M = Na, K$  and  $Tl$ ).

### 3.3.5 Photocatalytic Activity

The photocatalytic activity was evaluated with the described apparatus for a total irradiation time of 2 hours, with the maximum absorption of methylene blue evaluated at ten minute intervals. The maximum absorption was plotted as a function of time, and compared against a blank (no sample in reactor flask) and a Degussa P25  $TiO_2$  standard. The value for the degradation amount from the blank was

subtracted from each run to obtain the final degradation percentage of the methylene blue after 2 hours irradiation time. The normalized data for each sample along the series is shown in Figure 3.26.

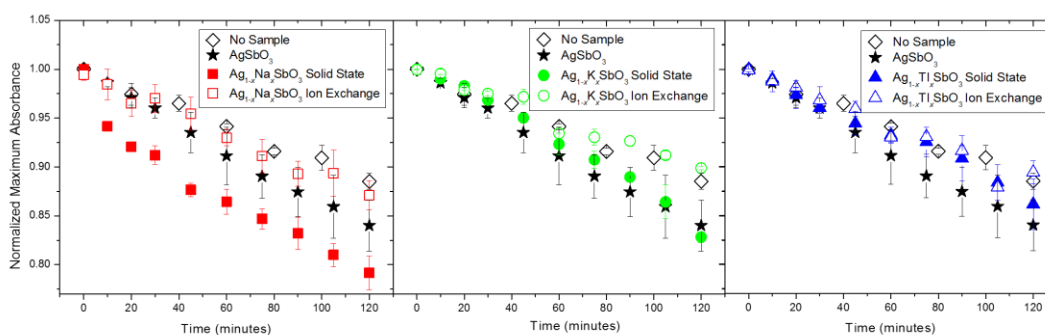


Figure 3.26 Degradation of Methylene Blue in the presence of  $\text{Ag}_{1-x}\text{Na}_x\text{SbO}_3$  (left),  $\text{Ag}_{1-x}\text{K}_x\text{SbO}_3$  (middle), and  $\text{Ag}_{1-x}\text{Tl}_x\text{SbO}_3$  (right).

Upon K and Tl substitution, no change and a decrease in methylene blue degradation after 2h is observed, respectively. However, upon Na substitution, an increase in the degradation amount after two hours is observed. A decrease in degradation percentage accompanies substitution through ion exchange for all three samples.

### 3.3.6 Discussion

As the valence band maxima is composed primarily of the orbital overlap between Ag 4s and O 2p orbitals, a manipulation of the Ag-O bond length will directly change the character of the upper valence band. With overlap between Ag 4s and O 2p, the energy of the valence band is increased, giving rise to a narrow band gap. Therefore, a decrease in the orbital overlap should result in a lowering of the energy, and an increase in the observed band gap, or vice versa. If the magnitude of the band gap is changed, this will change the wavelength of light that promotes the properties observed in  $\text{AgSbO}_3$ . The amount of

overlap will be affected not only by the M-O bond distance, but also the M-O-M bond angles. Figure 3.23c and 3.23d show the change in Ag-O-Ag and Sb-O-Sb bond angle upon doping, respectively. The Ag-O-Ag angle remains relatively unchanged, indicating the Ag-O bond distance will have the largest effect on the orbital overlap. The Sb-O-Sb angle does show a change as various metals are doped into the system, but this should not have a major influence on the Ag-O orbital overlap.

An alteration in the magnitude of the band gap will have a direct effect on the wavelength of light that promotes the photocatalytic properties observed in  $\text{AgSbO}_3$ . Therefore, by these observations, it was predicted that substitution of  $\text{K}^+$  and  $\text{Tl}^+$  will result in a weaker orbital overlap and larger band gap due to the increase bond length, while substitution by  $\text{Na}^+$  will lead to a stronger overlap and slightly smaller band gap. An increase in the band gap was indeed observed upon K-substitution, and a decrease with Na-substitution. However, Tl substitution resulted in a more gradual onset of absorption, making band gap extrapolation less straight-forward. This was most likely a result of defect states in the Tl sample, further evidenced by A-site disorder and Ag(m) impurities in the sample. Due to the increase in the band gap of the K sample, a corresponding increase in resistivity was predicted. Indeed, the K-substituted samples, in addition to all substituted samples, exhibited such high resistivity that it was outside of instrumental measurement limits. An increase in resistivity would result in less electron/hole recombination in the photocatalysis process, but such large resistivity may inhibit carrier mobility in the samples. As all samples exhibited a large increase in resistivity, but only the Na-substituted samples displayed an increase in the methylene blue degradation. This suggests that the changing band structure is not entirely responsible for increased degradation, and effects of the sample morphology must be considered.

Similar particle sizes were calculated for all samples, but variations in the surface area were present. Due to the volatility of Tl, only the surface areas of the parent compound, Na-substituted, and K-substituted samples were studied. Both samples synthesized through molten salt ion-exchange exhibited

larger surface areas than their solid state counterparts, and this is attributed to a greater porosity the samples. Indeed, the pore dimensions in these samples are much smaller than those of the solid state samples. Considerations of pore dimensions explain the decreased degradation rate of samples synthesized through ion exchange. The combination of a negligible change in band gap and a large increase in surface area compared to  $\text{AgSbO}_3$  would initially suggest an increase in degradation should be observed. However, the small pore size is most likely inhibiting adsorption of methylene blue to the surface of the samples, resulting in the observed decrease in the overall degradation. For catalysis, a higher surface area is desired for optimal catalytic activity. However, the size of the adsorbed molecule must also be considered. The relative area of methylene blue is  $130 \text{ \AA}^2$ , and therefore a larger pore size would promote a larger adsorption of methylene blue onto the surface of the photocatalyst. The observed increase in methylene blue degradation in the presence of the nominal  $\text{Ag}_{0.8}\text{Na}_{0.2}\text{SbO}_3$  is likely due to a large corresponding increase in pore dimensions compared to the parent compound in addition to the favorable electronic contributions.

### 3.3.7 Conclusions

A thorough investigation on the local and average structure of anion deficient pyrochlores with the formula  $\text{Ag}_{1-x}\text{M}^n_x\text{SbO}_{3+x[(n-1)/2]}$  ( $\text{M} = \text{Na}, \text{K}$  and  $\text{Tl}$ ) has been performed through neutron scattering techniques. The large channel of the anion deficient pyrochlore allows for large displacements of the metal cations, whether it be dynamic in the case of  $\text{Ag}^+$  and  $\text{K}^+$  (large thermal displacements parallel to the channel) or static in the case of  $\text{Na}^+$  and  $\text{Tl}^+$  (positional displacement perpendicular and parallel to the channel, respectively). These displacements result in a change in the Ag-O bonds lengths present, directly influencing the Ag  $4d$  and O  $2p$  orbital overlap and the band gap of each sample. While these changes have a strong influence on the observed photocatalytic activity, it is observed that sample morphology, in

particular pore dimensions, play a large role in the activity. All of these factors must be considered in the design and manipulation of novel photocatalysts.

### 3.4 Chapter Conclusions

Cation substitution can be a fruitful method for tuning and enhancing desired material properties. In this chapter, substitution of cations with varying valency, size, and electronegativity was employed, and it was observed that all substitutions had a measurable effect on the photocatalytic activity of the samples. Substitution with cations of higher valency than  $\text{Ag}^+$  ( $\text{Cd}^{2+}$ ,  $\text{Tl}^{3+}$ ) resulted in solid solutions between the anion-deficient and the ideal pyrochlore structure, and in the case of  $\text{Cd}^{2+}$ , anomalous behavior in the Cd-rich end attributed to small concentrations of an  $\text{O}^-$  radical species was observed. Substitution by cations with larger radii ( $\text{K}^+$  and  $\text{Tl}^+$ ) resulted in a longer Ag-O bond, directly manipulating the observed band gap and electrical resistivities of the samples. Substitution by the smaller  $\text{Na}^+$  results in a smaller Ag-O bond, and a slight decrease in the observed band gap of the material. While the change in orbital overlap and consequential electronic structure was partially responsible for the observed changes in the photocatalytic activity, it is concluded that morphological aspects of a sample play a crucial role and therefore must be strongly taken into consideration in the pursuit of novel materials for efficient photocatalysis.

### 3.5 Materials and Methods

Polycrystalline samples of  $(\text{Ag}_{1-x}\text{Cd}_x)_2\text{Sb}_2\text{O}_{6+x}$  were prepared by thoroughly grinding stoichiometric amounts of  $\text{Ag}_2\text{O}$  (Aldrich, 99+%) or Ag metal (Alfa Aesar, 325 mesh, 99.9%),  $\text{CdO}$  (Sigma Aldrich 99.99+%), and  $\text{Sb}_2\text{O}_3$  (J. T. Baker Analyzed Reagent) in an agate mortar and pestle with acetone. The samples were then pelletized and annealed in air at 900 °C for 24-48 hours in an alumina boat with intermediate

grindings. Samples of  $\text{Ag}_{1-x}\text{M}^n_x\text{SbO}_{3+x[(n-1)/2]}$  ( $\text{M} = \text{Na}, \text{K}$  and  $\text{Tl}$ ) were made through standard solid state synthesis techniques by mixing stoichiometric amounts of high purity  $\text{Ag}_2\text{O}$ ,  $\text{Sb}_2\text{O}_3$  and either  $\text{K}_2\text{CO}_3$ ,  $\text{Na}_2\text{CO}_3$ , or  $\text{Tl}_2\text{O}_3$ . After being thoroughly ground, the mixtures were pelletized and annealed at  $750^\circ\text{C}$  ( $\text{Na}, \text{K}$ ) or  $500^\circ\text{C}$  ( $\text{Tl}$ ) for 12 hours. Samples of  $\text{Ag}_{1-x}\text{M}^n_x\text{SbO}_{3+x[(n-1)/2]}$  ( $\text{M} = \text{Na}, \text{K}$  and  $\text{Tl}$ ) prepared through the molten salt ion exchange method were carried out in a porcelain crucible. Approximately 0.2000g of  $\text{AgSbO}_3$  was combined with a nitrate salt ( $\text{KNO}_3$ ,  $\text{NaNO}_3$ , or  $\text{TlNO}_3$ ) in a 1:10 silver to metal molar ratio.  $\text{K}^+$  and  $\text{Na}^+$  exchanges were performed at  $350^\circ\text{C}$  for 12 hours, and  $\text{Tl}^+$  exchange was performed at  $250^\circ\text{C}$  for 12 hours. Samples were rinsed with deionized water to remove any exchanged or excess salts.

Powders were first characterized through XRD with a Rigaku Miniflex II diffractometer using  $\text{Cu K}\alpha$  radiation and a graphite monochromator. Powder samples were loaded onto a “zero background” oriented Si single crystal sample holder (MTI corp.) to maximize the detection of minor impurity phases. Data was collected from  $10\text{-}120^\circ 2\theta$  with a step size of  $0.02^\circ 2\theta$  and a dwell time of 2.0 s. Room temperature lattice parameters were refined through the Le Bail method[39] using the GSAS software and EXPGUI user interface.[40,41] Time-of-flight (TOF) neutron scattering data was collected on powdered samples of  $\text{Ag}_{1-x}\text{M}^n_x\text{SbO}_{3+x[(n-1)/2]}$  ( $\text{M} = \text{Na}, \text{K}$  and  $\text{Tl}$ ) on the NPDF instrument at Los Alamos National Laboratory.[42] Approximately 3-4 grams of sample were placed into vanadium cans and measurements were obtained at 298 K for approximately 4 hours. Rietveld refinements were conducted using the GSAS software with the interface EXPGUI.[40,41] Due to the relatively high absorption cross-section of Ag, an absorption correction was applied to all data. Data reduction to obtain the PDF  $G(r)$  function was performed using the PDFgetN program,[43] with  $Q_{\text{max}} = 35 \text{ \AA}^{-1}$ , which was selected to balance between resolution and termination ripples in the reduced data. Least-squares refinement of reduced PDF functions were performed with PDFGUI.[44] While local refinements were performed for various ranges of real space data ( $r = 1.7\text{-}5\text{\AA}$ ,  $r = 1.7\text{-}10\text{\AA}$  and  $r = 1.7\text{-}20\text{\AA}$ ), the dependency of the parameters on

the range was determined to be negligible. Therefore, the reported PDF refinements have been completed with a 1.7 to 10 Å range.

The mass variation during the synthesis of the compounds was studied through thermogravimetric analysis (TGA) using a Metler Toledo TGA 850. Powdered starting materials were loaded in an alumina crucible and heated under O<sub>2</sub> flow to 900°C, with a ramp rate of 5°C/minute.

Sample composition of ion exchanged samples was estimated through inductively coupled plasma atomic emission spectroscopy (ICP-AES). Each sample was washed for six hours with exactly 500 ml D. I. water, and during filtration any amount of D. I. water added to wash the samples was recorded precisely. 100 ml aliquots of the filtrate was collected and combined with 2 mL of HNO<sub>3</sub> to prepare for ICP analysis. Each filtrate was analyzed for Ag content, along with a control sample of washed, non-exchanged AgSbO<sub>3</sub>. The concentration obtained from the control was subtracted from the concentrations obtained with the ion exchange samples. The Ag concentration of the samples was then compared to the hypothetical maximum possible concentration (all Ag exchanged; obtained from the mass of the AgSbO<sub>3</sub> used for the exchange) to determine a percent exchange and composition. ICP analysis was performed against a set of AgNO<sub>3</sub> standards in the appropriate concentration range.

Sample grain size was calculated by analyzing the Lorentzian broadening term LX obtained from LeBail fitting of the XRD data in GSAS with Profile Type #2 according to the equation

$$p = \frac{18,000 * K * \lambda}{\pi * LX}$$

where  $p$  is the particle size,  $\lambda$  is the radiation wavelength ( $\sim 1.54$  Å for Cu k- $\alpha$ ), and  $K$  is the Scherrer constant, 1.[40,41] Scanning Electron Microscopy (SEM) images were taken using a FEI Quanta 600F FEG SEM at an accelerating voltage of 10.00 kV. Powder samples were mounted on double-sided carbon conductive tabs and coated with Au/Pd. BET surface area and pore size measurements were performed on a Micrometrics ASAP 2020 Accelerated Surface Area and Porosimetry System. The surface area and

pore dimensions were determined by nitrogen adsorption-desorption isotherms operated at liquid nitrogen temperature after degassing for 24 h at 200 °C.

Optical spectra were determined by collecting the diffuse reflectance of the powders in the region of 200-1100 nm, using a halogen lamp source passed through a bifurcated optical fiber. The diffuse light reflected by the powders was collected with the optic cable and taken to an Ocean Optics HR4000 spectrophotometer. MgO (99.5%, Cerac) was used as a white reference. The collected data were converted to absorbance using the Kubelka-Munk equation.[45]

Density functional theory (DFT) calculations on  $\text{Ag}_2\text{Sb}_2\text{O}_6$  and  $\text{Cd}_2\text{Sb}_2\text{O}_7$  used the projector augmented plane wave method[46,47] as implemented in the Vienna *ab-initio* simulation package (VASP)[48,49] together with two different approximations for the exchange-correlation functional: the Perdew-Burker-Ernzerhoff (PBE)[50] generalized gradient approximation and the Heyd, Scuzeria, and Ernzerhoff (HSE06) hybrid functional.[51,52] It has been shown that using HSE06 for  $\text{Ag}_2\text{Sb}_2\text{O}_6$  resulted in lattice constants, volume, bond lengths, and a band gap much closer to experimentally determined parameters.[7] Additional calculation parameters include a 500 eV plane-wave cutoff (400 eV for HSE06), using Fermi-smearing with a width of 0.05 eV, and a gamma-centered 6 x 6 x 6 k-point grid.

Sample densification on samples of  $(\text{Ag}_{1-x}\text{Cd}_x)_2\text{Sb}_2\text{O}_{6+x}$  was done with spark plasma sintering (SPS) (DR. SINTER LAB Spark Plasma Sintering system, Model SPS-515S) at a sintering temperature of 850°C for a dwell time of 5 minutes in vacuum (8 Pa) under 50 MPa of pressure which was applied at the start of the sintering cycle. The constant heating and cooling rate of 100°C/min was employed for all the experiments with 2 g of powder inside graphite mold of 10 mm inner diameter. The temperature inside the graphite mold was controlled with a pyrometer. Residual graphite from the SPS process was removed from the sample by mechanical sanding of the pellets and verification of phase purity through XRD. High temperature (30-800°C) resistivity and Seebeck measurements were performed on densified samples with an ULVAC-RIKO ZEM 3 under a static helium atmosphere.

The photocatalytic activity was evaluated with a reactor setup in conjunction with UV-Vis spectroscopy. Approximately 0.0200 g of each powdered sample was suspended in a  $2.0 \times 10^{-5}$  M solution of methylene blue and stirred in a dark box for two hours to allow for adsorption of the dye onto to the surface of the sample. The reactor was then irradiated with light from a 300 W Xenon lamp source (Newport Corp.) under constant stirring. The intensity of the lamp was regulated with a Thorlabs PM100USB power and energy meter outfitted with a SC103C thermal power sensor. The power output was kept constant at 155 mW at the reactor face for all samples. Sample aliquots were withdrawn every 10-15 minutes followed by centrifugation to remove the powdered samples from the solution. The solution was then analyzed with an Ocean Optics ISS-UV-Vis spectrometer to determine the maximum absorption of the methylene blue. A photolysis and an adsorption correction were applied to each data point (see Chapter 2, "Fundamentals of Solid State Chemistry: Synthesis, Material Properties, and Characterization Methods").

A  $\text{Ba}^{121}\text{SnO}_3$  source was used for the Mössbauer spectroscopic experiments and the quoted values of the isomer shifts are given relative to this material. The measurements were carried out in the usual transmission geometry at 78 K. The temperature was controlled by a resistance thermometer ( $\pm 0.5$  K accuracy) and the Mössbauer source was kept at room temperature. The samples were enclosed in small PMMA containers at a thickness corresponding to about  $10 \text{ mg Sb/cm}^2$ . The total counting time was approximately 3 days per spectrum. Fitting of the spectra was performed with the NORMOS-90 program system.[53]

### 3.6 References

- [1] A.W. Sleight, Mater. Res. Bull. 4 (1969) 377.
- [2] N. Schrewelius, Zeitschrift Fur Anorg. Chemie 238 (1938) 241.

- [3] A.J.G. Zarbin, O.L. Alves, J.M. Amarilla, R.M. Rojas, J.M. Rojo, *Chem. Mater.* 11 (1999) 1652.
- [4] T. Kako, N. Kikugawa, J. Ye, *Catal. Today* 131 (2008) 197.
- [5] M. Yasukawa, H. Hosono, N. Ueda, H. Kawazoe, *Solid State Commun.* 95 (1995) 399.
- [6] H. Mizoguchi, H.W. Eng, P.M. Woodward, *Inorg. Chem.* 43 (2004) 1667.
- [7] J.P. Allen, M.K. Nilsson, D.O. Scanlon, G.W. Watson, *Phys. Rev. B Condens. Matter* 83 (2011) 035207.
- [8] J. Singh, S. Uma, *J. Phys. Chem. C* 113 (2009) 12483.
- [9] Z.G. Yi, Y. Liu, R.L. Withers, *J. Appl. Phys.* 108 (2010) 024911.
- [10] Y. Matsumoto, K. Funaki, J. Hombo, Y. Ogawa, *J. Solid State Chem.* 99 (1992) 336.
- [11] H.-Y. Sang, J.-F. Li, *J. Alloys Compd.* 493 (2010) 678.
- [12] S. Nishiyama, A. Ichikawa, T. Hattori, *J. Ceram. Soc. Japan* 112 (2004) 298.
- [13] A. Bystrom, B. Hok, B. Mason, *Ark. Kemi, Mineral. Och Geol.* 15B (1941) 8.
- [14] J.-Y. Moisan, J. Pannetier, J. Lucas, *Comptes Rendus Des Seances l'Academie Des Sci. Ser. C Sci. Chim.* 271 (1970) 402.
- [15] F. Brisse, D.J. Stewart, V. Seidl, O. Knop, *Can. J. Chem.* 50 (1972) 3648.
- [16] B.R. Li, J.L. Zhang, *J. Mater. Sci. Lett.* 9 (1990) 109.
- [17] Y.-F. Liu, X. Liu, J. Yu, *Sensors Actuators B Chem.* 61 (1999) 208.
- [18] A. Munter, NIST Center for Neutron Research Neutron Scattering Lengths and Cross Sections, [Http://www.ncnr.nist.gov/resources/n-lengths/](http://www.ncnr.nist.gov/resources/n-lengths/), 2011.
- [19] A. Patterson, *Phys. Rev.* 56 (1939) 978.
- [20] K. Yanagawa, Y. Ohki, T. Omata, H. Hosono, N. Ueda, H. Kawazoe, *Jpn. J. Appl. Phys.* 33 (1994) L238.
- [21] J. Telsler, *Pers. Commun.* (2012).
- [22] M. Bouchama, M. Tournoux, *Rev. Chim. Miner.* 12 (1975) 93.
- [23] M. Bouchama, M. Tournoux, *Rev. Chim. Miner.* 12 (1975) 80.

- [24] P.Y. Piffard, M. Dion, M. Tournoux, *Acta Crystallogr. Sect. B Struct. Crystallogr. Cryst. Chem.* B34 (1978) 366.
- [25] P.Y. Piffard, M. Tournoux, *Acta Crystallogr. Sect. B Struct. Crystallogr. Cryst. Chem.* B35 (1979) 1450.
- [26] D.J. Stewart, O. Knop, C. Ayasse, F.W.D. Woodhams, *Can. J. Chem.* 50 (1972) 690.
- [27] W.S. Brower, D.B. Minor, H.S. Parker, R.S. Roth, J.L. Waring, *Mater. Res. Bull.* 9 (1974) 1045.
- [28] P.E. Lippens, *Solid State Commun.* 113 (2000) 399.
- [29] T. Birchall, B. Della Valle, *Chem. Commun.* (1970) 675.
- [30] J.B. Wooten, G.G. Long, L.H. Bowen, *J. Inorg. Nucl. Chem.* 36 (1974) 2177.
- [31] Y.M. Jansen, J. Pebler, K. Dehnicke, *Zeitschrift Für Anorg. Und Allg. Chemie* 495 (1982) 120.
- [32] R. Mishra, R. Pöttgen, R.-D. Hoffmann, T. Fickenscher, M. Eschen, H. Trill, B.D. Mosel, *Zeitschrift Fuer Naturforschung, B Chem. Sci.* 57 (2002) 1215.
- [33] I. Schellenberg, T. Nilges, R. Pöttgen, 67 (2008) 1.
- [34] Anthony R. West, *Basic Solid State Chemistry*, 2nd ed., John Wiley & Sons. Ltd., New York, 1999.
- [35] O.F. Schirmer, *Solid State Commun.* 18 (1976) 1349.
- [36] R. Gillen, J. Robertson, *Phys. Rev. B* 85 (2012) 014117.
- [37] A. Le Bail, *Powder Diffr.* 20 (2005) 316.
- [38] R.D. Shannon, *Acta Crystallogr. Sect. A Found.* 32 (1976) 751.
- [39] A. Le Bail, *Powder Diffr.* 20 (2005) 316.
- [40] A.C. Larson, R.B. Von Dreele, *Los Alamos Nat. Lab. Rep. LAUR* (1994) 89.
- [41] B.H. Toby, *J. Appl. Crystallogr.* 34 (2001) 210.
- [42] T. Proffen, T. Egami, S.J.L. Billinge, A.K. Cheetham, D. Louca, J.B. Parise, *Appl. Phys. A* 74 (2002) s163.
- [43] P.F. Peterson, M. Gutmann, T. Proffen, S.J.L. Billinge, *J. Appl. Crystallogr.* 33 (2000) 1192.
- [44] C.L. Farrow, P. Juhas, J.W. Liu, D. Bryndin, E.S. Božin, J. Bloch, T. Proffen, S.J.L. Billinge, *J. Phys. Condens. Matter* 19 (2007) 335219.

- [45] P. Kubelka, F. Munk, Zeitschrift Für Tech. Phys. 12 (1931) 593.
- [46] P.E. Blochl, Phys. Rev. B 50 (1994) 17953.
- [47] G. Kresse, Phys. Rev. B 59 (1999) 1758.
- [48] G. Kresse, J. Furthmuller, Phys. Rev. B 54 (1996) 11169.
- [49] G. Kresse, J. Hafner, Phys. Rev. B 49 (1994) 14251.
- [50] J.P. Perdew, K. Burke, M. Ernzerhoff, Phys. Rev. Lett. 77 (1996) 3865.
- [51] J. Heyd, G.E. Scuseria, M. Ernzerhof, J. Chem. Phys. 118 (2003) 8207.
- [52] A. V Krukau, O. a Vydrov, A.F. Izmaylov, G.E. Scuseria, J. Chem. Phys. 125 (2006) 224106.
- [53] R. A. Brand, NORMOS Mössbauer Fitting Program, Universitat Duisburg, Duisburg, Germany, 2007.

## CHAPTER 4

### Determination of the low-temperature structural phases of the ferroelectric pyrochlore $\text{Cd}_2\text{Nb}_2\text{O}_{7-x}\text{S}_x$

#### Abstract

The room and low temperature structures of the pyrochlore series  $\text{Cd}_2\text{Nb}_2\text{O}_{7-x}\text{S}_x$  have been investigated through synchrotron diffraction studies. All room temperature data indicated crystallization in the  $Fd\bar{3}m$  space group. Low temperature analysis revealed various degrees of structural distortions in the samples. For nominal  $x = 0$ , large displacements in the positions were observed, and the structure was fit with the space group  $Ima2$ . Structural analysis of the S-substituted samples indicates the space group  $Fdd2$  for the nominal  $x = 0.25$  sample. For nominal  $x = 0.7$ , the lattice remains cubic, but the evolution of new peaks at low temperatures suggests a loss in face-centered symmetry.

Publications based on this chapter:

1. Laurita, G., Li, J., Macaluso, R., Sleight, A. W., Subramanian, M. A. Determination of the low temperature structural phases of the ferroelectric pyrochlore  $\text{Cd}_2\text{Nb}_2\text{O}_{7-x}\text{S}_x$ . *In preparation*

## 4.1 Introduction to $\text{Cd}_2\text{Nb}_2\text{O}_7\text{-xS}_x$

### 4.1.1 Introduction to Ferroelectricity

As discussed in Chapter 2, dielectric materials are completely insulating and the static charge can be polarized by the application of an external electric field. In a ferroelectric material, this polarization can be exhibited in the absence of an electric field. Ferroelectrics are in general marked with high dielectric constants and reversible polarization. Ferroelectric materials undergo a phase transition to a non-centrosymmetric space group (lacking a center of inversion) in order to achieve residual polarization. This transition is marked by the ferroelectric Curie temperature,  $T_c$ , which can be observed in a dielectric measurement by a peak in the dielectric constant (Figure 4.1).[1]

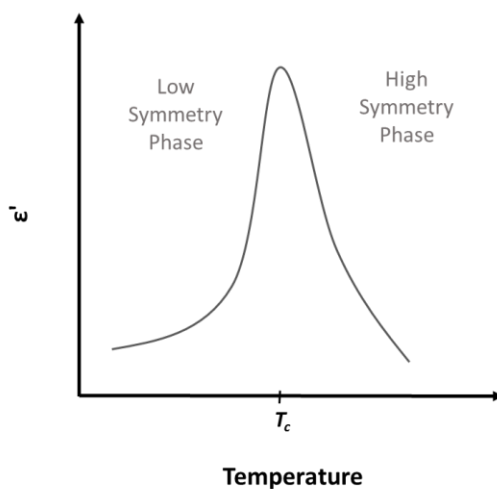


Figure 4.1 Sketch of the observance of  $T_c$  in ferroelectric material.

The transition to a ferroelectric material is described as a displacive order-disorder phase transition: below  $T_c$ , there is a preferential distortion or tilting of the polyhedra, which is either random or nonexistent above  $T_c$ . [1] Common ferroelectric materials exhibit a characteristic displacement of one of the cations in its coordination environment, typically an early transition metal such as Ti, Nb, or Zr. For

example in the ferroelectric perovskite  $\text{BaTiO}_3$ , the  $\text{Ti}^{4+}$  cations displace along the vertical axis of the  $\text{TiO}_6$  polyhedra (illustrated in Figure 4.2) generating permanent dipoles that can be aligned in an electric field.[2]

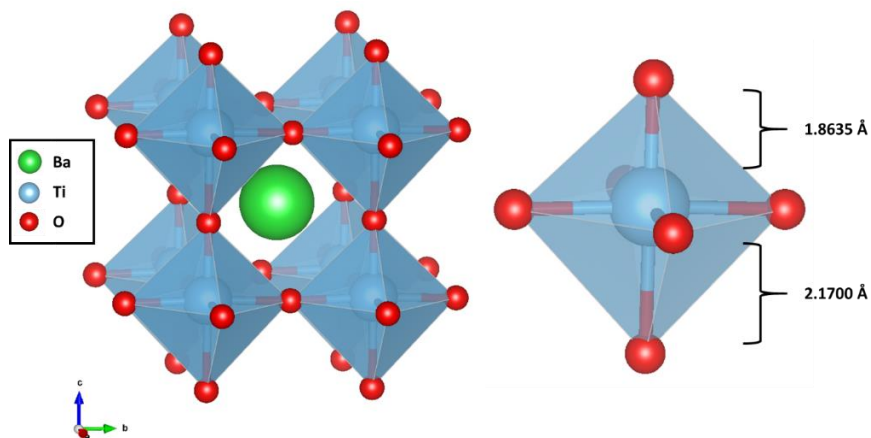


Figure 4.2 Left: The crystal structure of the ferroelectric perovskite  $\text{BaTiO}_3$ . Right: An enlarged  $\text{TiO}_6$  octahedra that illustrates the axial displacement of Ti, giving rise to the permanent dipole in this ferroelectric material.

Ferroelectricity is well known and understood in perovskite materials, but very few pyrochlores exhibit this phenomenon. While a family of numerous compositions, ferroelectricity has only been reported in  $\text{Cd}_2\text{Nb}_2\text{O}_7$  and related compounds,  $\text{Ho}_2\text{Ti}_2\text{O}_7$ ,  $\text{La}_2\text{Zr}_2\text{O}_7$ ,  $\text{Nd}_2\text{Ti}_2\text{O}_7$ , and frustrated ferroelectricity in  $\text{Y}_2(\text{Nb}_{0.86}\text{Y}_{0.14})_2\text{O}_{6.91}$ ,  $\text{CaYNb}_2\text{O}_7$ , and  $\text{Y}_2\text{NbTiO}_7$ . [3–22] Unlike the perovskite materials, the origin of ferroelectricity in pyrochlore oxides is not well understood, and the knowledge gained through studies of this origin will contribute to advancements in the design of novel ferroelectric materials.

#### 4.1.2 Introduction to the Ferroelectric Pyrochlore Series $\text{Cd}_2\text{Nb}_2\text{O}_{7-x}\text{S}_x$

Ferroelectricity was first observed in  $\text{Cd}_2\text{Nb}_2\text{O}_7$  in 1952 and a ferroelectric transition temperature of 185 K was confirmed shortly after. [10,23] Numerous studies have since been carried out on this

material; it has been reported as an improper and relaxor ferroelectric, and evidence of  $\text{Cd}^{2+}$  displacement has been presented on single crystals and powders.[8,11,13,14,16] Exhibiting the  $Fd\bar{3}m$  pyrochlore phase at room temperature, there are a total of four reported phase transitions: the first at  $T_1 \approx 205$  K to an orthorhombic  $Fdd2$  phase, the second at  $T_2 \approx 195$  K to an orthorhombic  $Ima2$  phase, the third at  $T_3 \approx 85$  K to an uncharacterized monoclinic phase, and the fourth at  $T_4 \approx 45$  K to a different monoclinic phase.[6,7,24] It is proposed that the ferroelectric behavior arises from the interaction of the  $\text{NbO}_6$  and  $\text{Cd}_2\text{O}'$  interpenetrating networks of the pyrochlore structure, and the first distortion is that of the  $\text{NbO}_6$  octahedra ( $T_1$ ) followed by an induced distortion in the  $\text{Cd-O}'$  chains ( $T_2$ ).

$\text{Cd}_2\text{Nb}_2\text{O}_6\text{S}$  (illustrated in Figure 4.3) and a solid solution  $\text{Cd}_2\text{Nb}_2\text{O}_{7-x}\text{S}_x$  ( $x = 0-1$ ) was reported to exhibit ferroelectricity, and the origin of ferroelectricity across the solution was attributed to dynamic displacement of the  $\text{Cd}^{2+}$ . [25–27] A total of four phase transitions were determined in the solid solution (labeled as  $\alpha$ ,  $\beta$ ,  $\gamma$ , and  $\delta$ ) but detailed structural characterization on the low temperature phases was not reported.

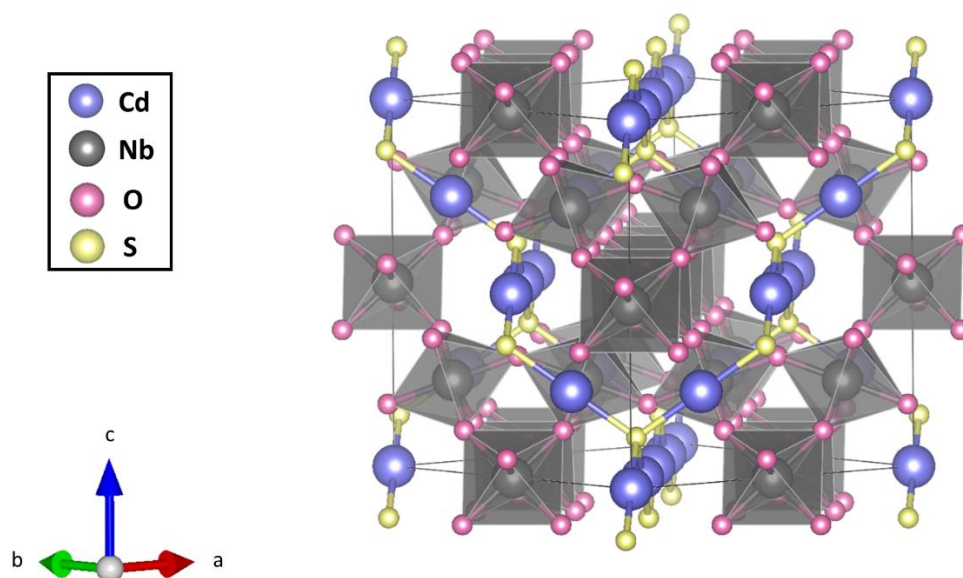


Figure 4.3 The ferroelectric pyrochlore  $\text{Cd}_2\text{Nb}_2\text{O}_6\text{S}$  at room temperature, space group  $Fd\bar{3}m$ .

There is a large amount of literature on the structural characterization of  $\text{Cd}_2\text{Nb}_2\text{O}_7$ . However, the vast majority of the available literature is on single crystal samples, and the propensity towards twinning in these crystals necessitates the analysis of powder diffraction data. The lack of literature on the low temperature structure of the solid solution  $\text{Cd}_2\text{Nb}_2\text{O}_{7-x}\text{S}_x$  may be a result of the complex patterns that are seen upon phase transformations. In order to observe well-resolved phase transitions, high-resolution powder diffraction is needed. As Cd is a strong absorber of neutron radiation, synchrotron radiation is the best alternative source to provide the necessary resolution. This chapter presents work on the structural characterization of the ferroelectric pyrochlore series  $\text{Cd}_2\text{Nb}_2\text{O}_{7-x}\text{S}_x$  through synchrotron diffraction experiments.

#### 4.2 Structural Characterization of $\text{Cd}_2\text{Nb}_2\text{O}_{7-x}\text{S}_x$ at Room Temperature

Room temperature synchrotron diffraction measurements were carried out on samples of  $\text{Cd}_2\text{Nb}_2\text{O}_{7-x}\text{S}_x$  for nominal values  $x = 0, 0.25, 0.5,$  and  $0.7$ . All compositions index to a cubic space group of  $Fd\bar{3}m$ . The presence of a  $\text{CdNb}_2\text{O}_6$  impurity phase was detected in all compositions and included in the fit. The Rietveld fits for the samples can be seen in Figure 4.4, and a summary of all refined parameters in Table 4.1. Values close to the nominal compositions were obtained; a small Cd deficiency was determined for the nominal  $x = 0$  sample, and a sulfur content of 0.64 was determined for the nominal  $x = 0.5$  sample. Deviations from the nominal stoichiometry are attributed to the formation of the stable impurity phase and the volatility of Cd at elevated temperatures.

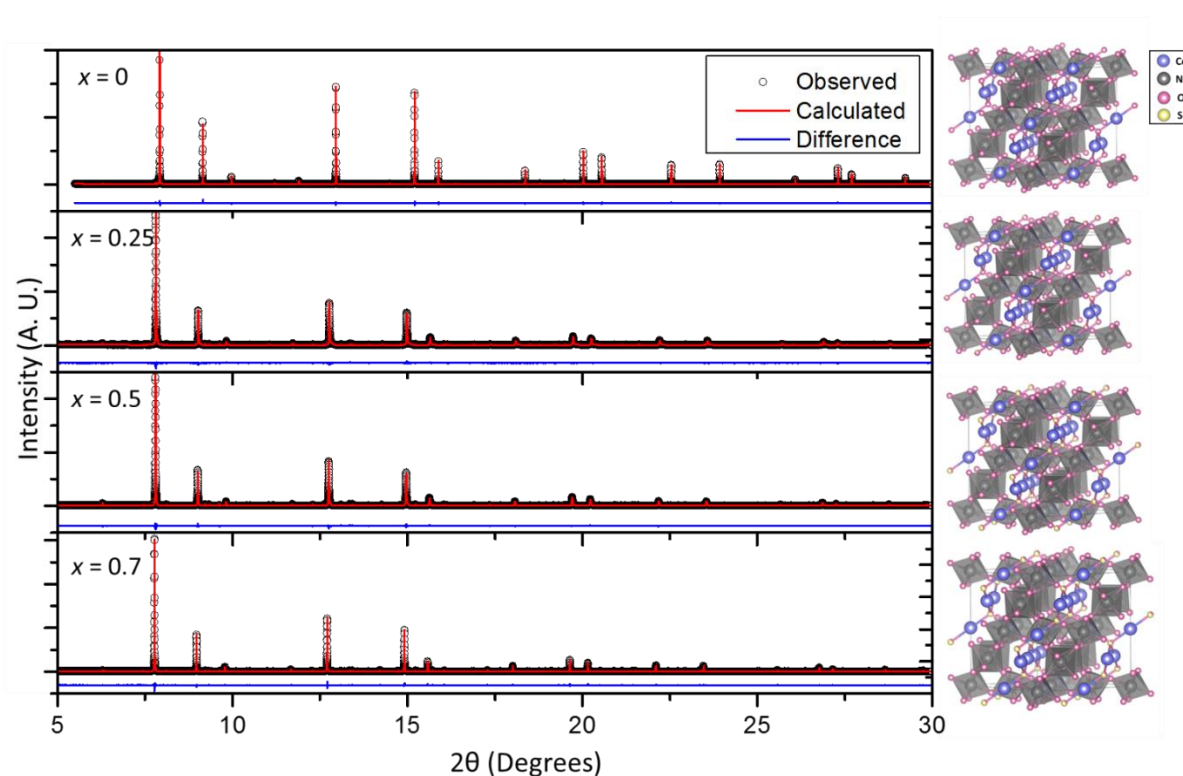


Figure 4.4 Room temperature Rietveld fits and unit cells for the series  $\text{Cd}_2\text{Nb}_2\text{O}_{7-x}\text{S}_x$ . Labels for  $x$  are nominal values.

Table 4.1 Refined crystallographic details for the series  $\text{Cd}_2\text{Nb}_2\text{O}_{7-x}\text{S}_x$ .

Refined Formula	$\text{Cd}_{1.94(2)}\text{Nb}_2\text{O}_{6.5(1)}$	$\text{Cd}_2\text{Nb}_2\text{O}_{6.88(1)}\text{S}_{0.22(1)}$	$\text{Cd}_2\text{Nb}_2\text{O}_{6.36(1)}\text{S}_{0.64(1)}$	$\text{Cd}_2\text{Nb}_2\text{O}_{6.28(1)}\text{S}_{0.72(1)}$
$a$ (Å)*	10.37371(2)	10.52151(1) 10.51106(1)	10.53438(1) 10.52380(1)	10.57097(2)
Volume (Å <sup>3</sup> )	1116.356(2)	1164.754(2)	1169.033(2)	1181.260(2)
Z	8	8	8	8
Formula Weight	519.10	526.04	532.82	534.16
Space Group	$Fd\bar{3}m$	$Fd\bar{3}m$	$Fd\bar{3}m$	$Fd\bar{3}m$
Temperature (K)	340	340	340	440
Density (g/cm <sup>3</sup> )	6.18	6.00	6.05	6.01
Cd-O'/S (Å)	2.2459(1)	2.2779(1)	2.2807(1)	2.2886(1)
Nb-O (Å)	1.9624(1)	2.0017(1)	2.0042(1)	1.9892(1)
Cd $U_{\text{iso}}$ (Å <sup>2</sup> )	0.0112(1)	0.0440(1)	0.0436(1)	0.0537(2)
Nb $U_{\text{iso}}$ (Å <sup>2</sup> )	0.0086(1)	0.0104(1)	0.0096(1)	0.0115(2)
R (%)	7.56	6.14	5.88	7.83
$R_{\text{wp}}$ (%)	10.14	8.29	8.14	9.36

\* Multiple phases were used to simulate the asymmetric strain in the sample for nominal  $x = 0.25$  and  $0.5$ , and lattice parameters for all phases used are reported.

An increase in S content was accompanied by an increase in the lattice parameter and Cd-O'/S bond length. Figure 4.5a illustrates the change in the lattice parameter as a function of S-doping,  $x$ . Nominal samples of  $\text{Cd}_2\text{Nb}_2\text{O}_6\text{S}$  were attempted, but the highest phase-pure sample achieved was the  $x = 0.72$  sample. Due to the large space inside the pyrochlore channels, it was predicted that S substitution would take place on the  $8b$  O' site in the pyrochlore lattice. Refinements of S occupancy on the  $8b$  site yielded better agreement with the experimental data than occupancy on the  $48f$  site. An expansion of the cell edge is anticipated as the larger S is substituted for O, and while this is observed, it does not strictly obey Vegard's Law and deviates from linearity. This can be explained by a large amount of strain in the nominal  $x = 0.25$  and  $x = 0.5$  sample, evident by large asymmetric tailing in the peaks (Figure 4.5b and c). The degree of strain was too large to be modeled by fitting a Lorentzian strain broadening term, and multiple pyrochlore phases were incorporated into the fit in order to accurately model the tailing. This is but one way to model the system; attempts are in progress to fit these samples with a single phase and strain modeling with different profile terms, but thus far multiple phases provides the best fit. The origin of the sample strain may be due to a gradient or pockets of S-rich regions throughout the bulk material. These regions modeled as "different phases" may be a result of the sample attempting to phase-separate, but cooling was too rapid to resolve the various phases. This hypothesis can be tested by slow-cooling the sample and observing the diffraction pattern for the presence of two or more resolved pyrochlore phases.

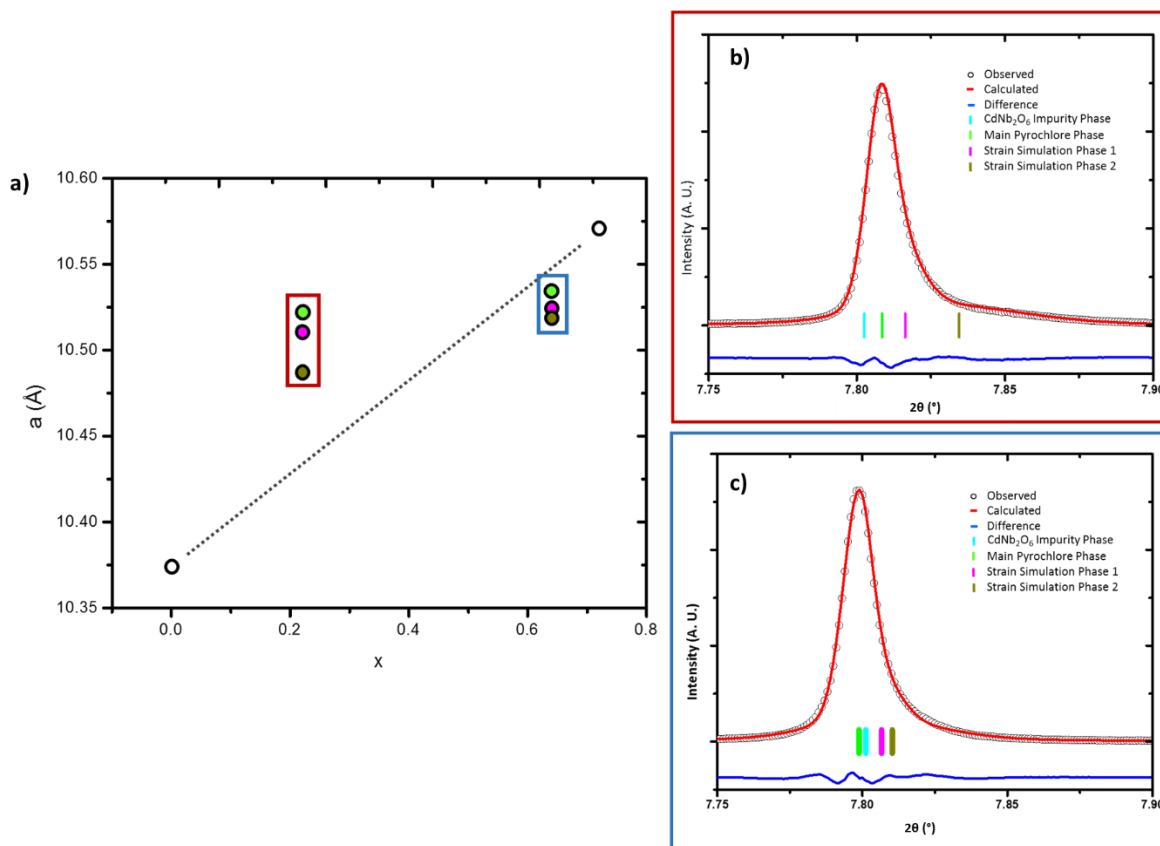


Figure 4.5 Lattice parameter evolution for the series  $\text{Cd}_2\text{Nb}_2\text{O}_{7-x}\text{S}_x$ . Deviation from a linear trend in the nominal  $x = 0.25$  (red outlined box) and  $x = 0.5$  (blue outlined box) can be attributed to large amounts of strain in the samples, which were modeled through multiple pyrochlore phases.

Calculations of the bond valence sums (BVS) of the cations throughout the solid solution (Figure 4.6) reveal under-bonded Cd in the nominal  $\text{Cd}_2\text{Nb}_2\text{O}_7$ . This under-bonded situation is remedied upon the addition of S, as a steady increase in the BVS of Cd is observed with increasing S-content. This also indicates that the degree of covalency between the Cd and  $8b$  atom is higher when more S is present, which agrees with the expected trend based on the electronegativities and sizes of O and S. The BVS variation of Nb does not appear to be as systematic based on the S-content, which is expected as S-substitution is exclusively on the Cd-O' chain.

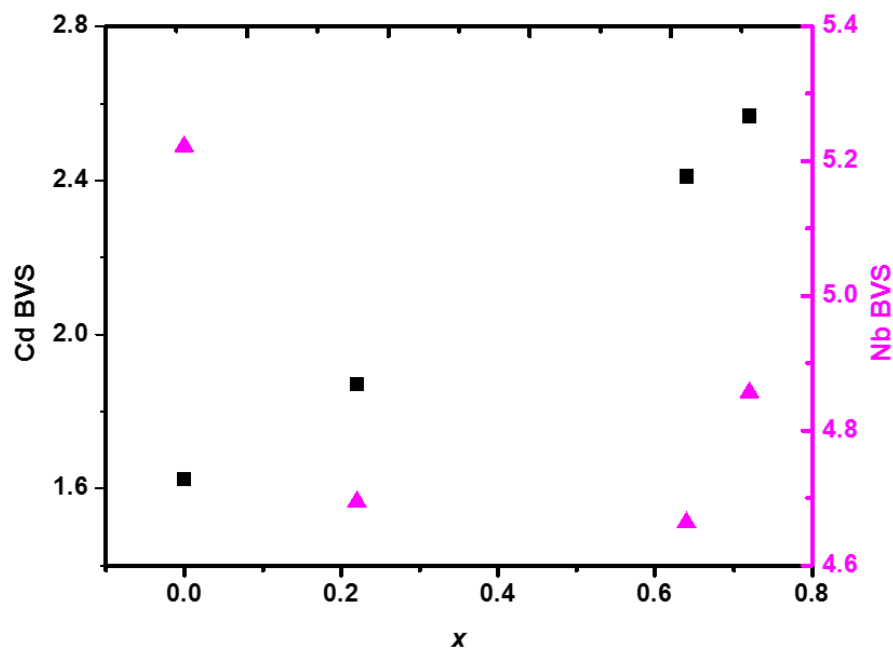


Figure 4.6 Bond valence sums of Cd (black) and Nb (magenta) as a function of refined S-content ( $x$ ) for the series  $\text{Cd}_2\text{Nb}_2\text{O}_{7-x}\text{S}_x$  at room temperature.

### 4.3 Structural Characterization of $\text{Cd}_2\text{Nb}_2\text{O}_{7-x}\text{S}_x$ at 100 K

#### 4.3.1 Qualitative Analysis of $\text{Cd}_2\text{Nb}_2\text{O}_{7-x}\text{S}_x$ at 100 K

A comparison of the room temperature and 100 K data can be seen in Figures 4.7 and 4.8. Peak splitting in the low temperature phases is observed for nominal samples of  $x = 0, 0.25, 0.5$ . In the  $x = 0.7$  sample, no peak splitting is observed, but instead the emergence of new peaks. Both peak splitting and new peaks suggest a lowering in symmetry, but the lack of peak splitting indicates the  $x = 0.7$  is still retaining a cubic space group.

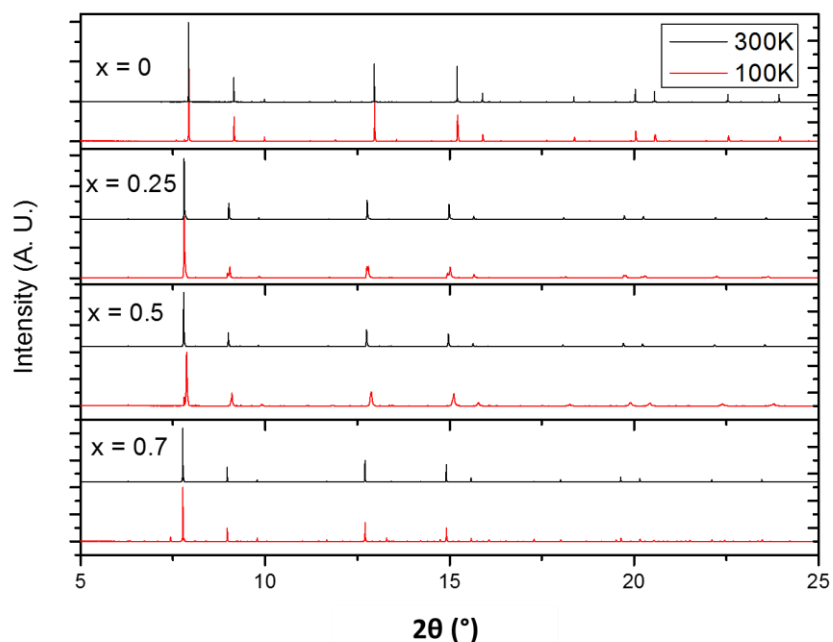


Figure 4.7 Comparison of the room temperature and 100 K diffraction data for the series  $\text{Cd}_2\text{Nb}_2\text{O}_{7-x}\text{S}_x$ .

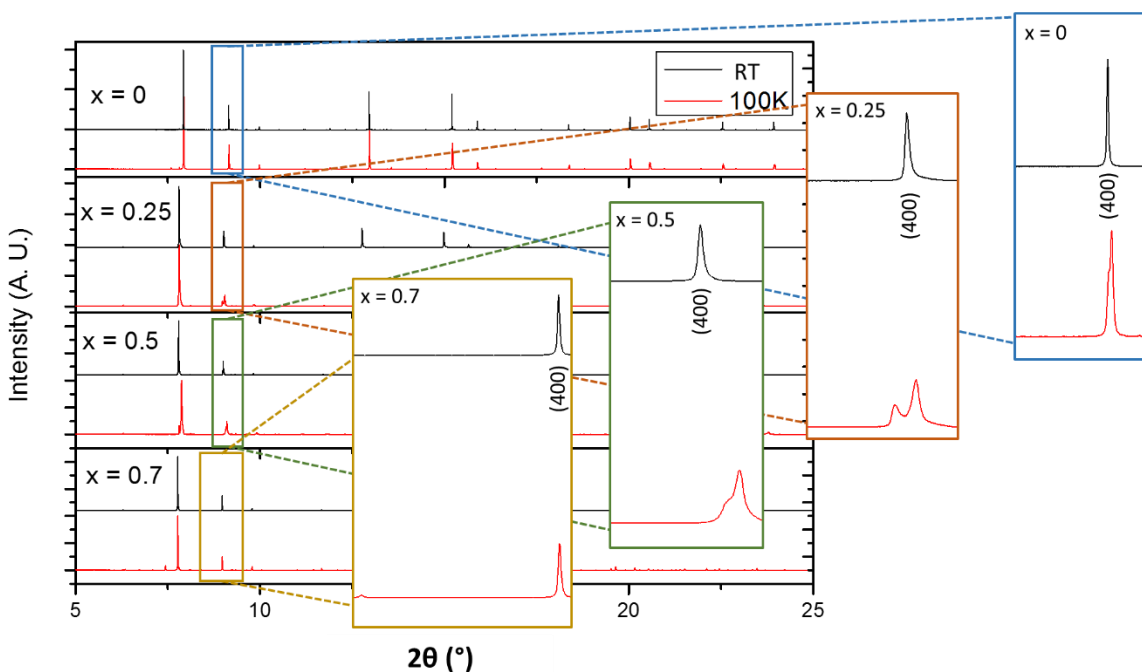


Figure 4.8 Comparison of the room temperature and 100 K data for the series  $\text{Cd}_2\text{Nb}_2\text{O}_{7-x}\text{S}_x$ . Enlarged areas from  $8\text{--}10^\circ 2\theta$  highlight the structural changes observed in each sample. For  $\text{Cd}_{1.96(2)}\text{Nb}_2\text{O}_7$  (blue outline),  $\text{Cd}_2\text{Nb}_2\text{O}_{6.88(1)}\text{S}_{0.22(1)}$  (orange outline), and  $\text{Cd}_2\text{Nb}_2\text{O}_{6.36(1)}\text{S}_{0.64(1)}$  (green outline) various degrees of peak splitting are observed. While no peak splitting is present in  $\text{Cd}_2\text{Nb}_2\text{O}_{6.28(1)}\text{S}_{0.72(1)}$  (yellow outline), the emergence of new peaks is observed.

The space groups of the low temperature phases should be subgroups of the high temperature phase  $Fd\bar{3}m$ , as transition at lower temperature involves the loss of symmetry elements from the high-symmetry phase. A breakdown of some of the possible subgroups for  $Fd\bar{3}m$  can be found in Figure 4.9. Of the space groups considered,  $F\bar{4}3m$ ,  $P\bar{4}3m$ ,  $I4_1md$ ,  $Fdd2$ ,  $Ima2$ , and  $Cc$  are non-centrosymmetric and could give rise to ferroelectricity.

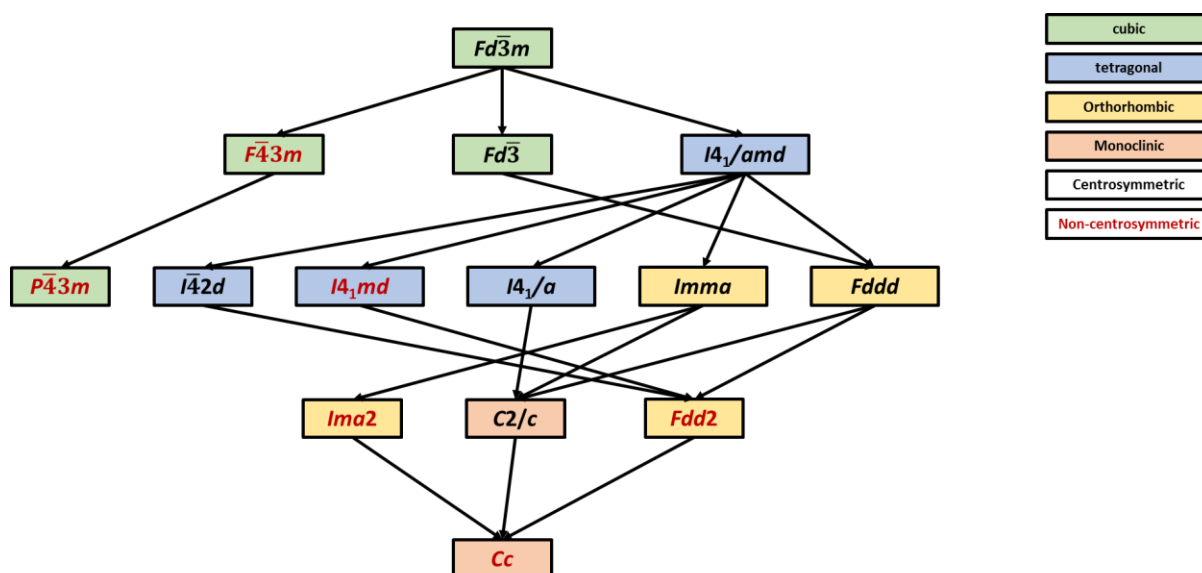


Figure 4.9 Subgroups of the  $Fd\bar{3}m$  subgroup. Space groups in red indicate non-centrosymmetric groups.

#### 4.3.2 Structural Characterization of $Cd_2Nb_2O_7$ at 100 K

The space group  $Ima2$  is widely reported as the low temperature phase at 100 K and was therefore used for the low temperature refinements. Lattice parameters and bond lengths are in reasonable agreement with the literature.[6,7] Upon cooling, Cd and Nb split from the fixed  $16d$  and  $16c$  positions, respectively, to the variable  $4a$  and  $4b$  sites each. In this new configuration, refinements indicate Cd1 and

Cd2 displace by 0.049 Å and 0.131 Å from the ideal positions, while Nb1 and Nb2 displace by 0.173 Å and 0.144 Å, respectively. The units cells before and after the phase transition are illustrated in Figure 4.10.

Table 4.2 Comparison of room temperature and 100 K data for nominal Cd<sub>2</sub>Nb<sub>2</sub>O<sub>7</sub>.

Refined Formula	Cd <sub>1.94(2)</sub> Nb <sub>2</sub> O <sub>6.5(1)</sub>	Cd <sub>1.97(1)</sub> Nb <sub>2</sub> O <sub>7</sub>
<i>a</i> (Å)	10.37371(2)	7.32114(2)
<i>b</i> (Å)	10.37371(2)	10.37099(3)
<i>c</i> (Å)	10.37371(2)	7.33098(1)
Volume (Å <sup>3</sup> )	1116.356(2)	556.623(3)
Space Group	<i>Fd</i> $\bar{3}$ <i>m</i>	<i>Ima</i> 2
Temperature (K)	340	100
Cd1 <i>z</i>		0.507(1)
Cd2 <i>y</i>		0.257(3)
Cd2 <i>z</i>		0.265(2)
Nb1 <i>z</i>		0.024(1)
Nb2 <i>y</i>		0.736(2)
Nb2 <i>z</i>		0.253(2)
Cd1-O1/S1 (Å)	2.2459(1)	2.18(2)
Cd2-O1/S1 (Å)		2.30(2)
Cd2-O1/S1 (Å)		2.30(2)
Nb1-O3 (Å)	1.9624(1)	1.96(2)
Nb1-O4 (Å)		2.08(2)
Nb1-O5 (Å)		1.92(1)
Nb2-O2 (Å)		1.92(2)
Nb2-O2 (Å)		2.01(2)
Nb2-O4 (Å)		1.87(2)
Nb2-O5 (Å)		2.02(2)
Cd1 U <sub>iso</sub> (Å <sup>2</sup> )	0.0121(1)	0.004(2)
Cd2 U <sub>iso</sub> (Å <sup>2</sup> )		0.0053(3)
Nb1 U <sub>iso</sub> (Å <sup>2</sup> )	0.0086(1)	0.0022(4)
Nb2 U <sub>iso</sub> (Å <sup>2</sup> )		0.0015(3)
R (%)	7.43	8.75
R <sub>wp</sub> (%)	10.06	11.10

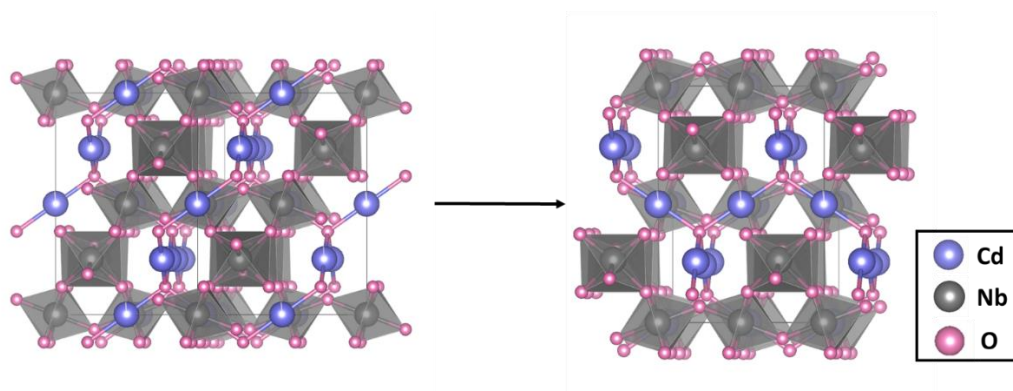


Figure 4.10 Phase transition from  $Fd\bar{3}m$  at 330 K (left) to  $Ima2$  at 100 K for nominal  $Cd_2Nb_2O_7$ .

Illustrated in Figures 4.11 and 4.12, the  $Cd_2O'$  and  $NbO_6$  networks undergo significant distortions in the low temperature structures. In the  $Fd\bar{3}m$  phase there is one Cd-O' bond throughout the  $Cd_2O'$  network. Upon transition to  $Ima2$ , there is a displacement of the Cd2 cations along the (011) plane, causing alternating short and long bonds in the Cd-O' chain. Chains of  $Cd_{12}O'$  along the (001) plane retain a single Cd-O' bond. Calculations of BVS at room and low temperatures indicates that the average BVS of Cd is slightly raised from 1.62 at room temperature to 1.66 in the low temperature structure, indicating that the alternating short and long Cd2-O' bonds help alleviate the under-bonded nature of Cd.

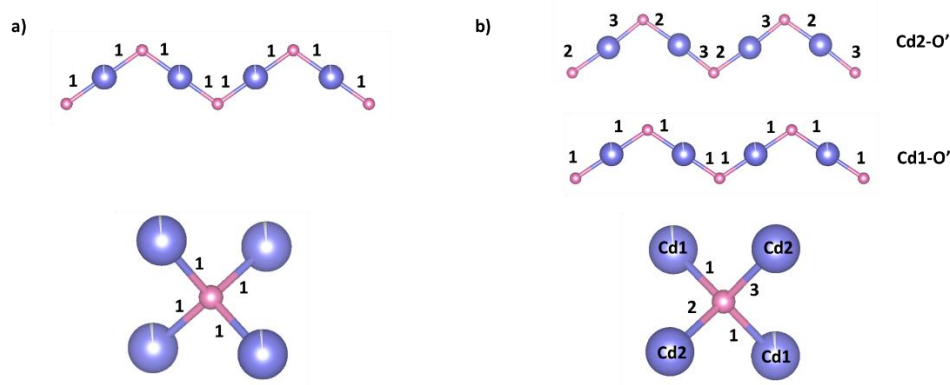


Figure 4.11 a) Cd-O' chain (top) and  $OCd_4$  tetrahedra (bottom) in nominal  $Cd_2Nb_2O_7$  obtained from the room temperature refinement in space group  $Fd\bar{3}m$ . b) Cd1-O' and Cd2-O' chains (top) and  $OCd_4$  tetrahedra (bottom) in nominal  $Cd_2Nb_2O_7$  obtained from the 100 K refinement in space group  $Ima2$ .

At room temperature, the NbO<sub>6</sub> octahedra are very regular and uniform with the presence of only one Nb-O bond. This number is increased to four bonds upon transition to the lower *Ima2* phase, resulting in a slight increase in the average BVS for Nb (5.22 at room temperature and 5.23 at 100 K). The coordination environment around the Nb2 atom shows less distortion with more similar bond lengths, while there is an overall displacement of Nb2 along the (100) plane, resulting in the observed distorted coordination environment.

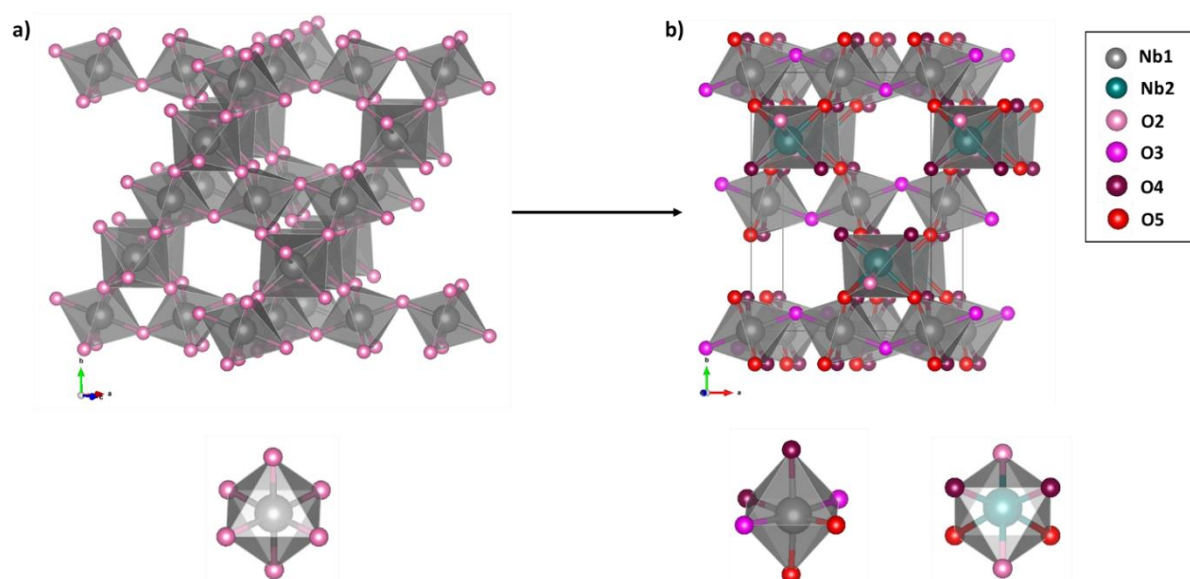


Figure 4.12 a) NbO<sub>6</sub> network in the room temperature *Fd* $\bar{3}$ *m* phase and b) in the *Ima2* phase at 100 K.

To investigate the relationship between the Cd-O' and NbO<sub>6</sub> networks, refinements on the phase transitions in the non-ferroelectric Cd<sub>2</sub>Ta<sub>2</sub>O<sub>7</sub> are in progress. A *Fd* $\bar{3}$ *m* pyrochlore at room temperature, this material undergoes a phase transition at low temperatures.[28] This is evidenced by the peak broadening in the data shown in Figure 4.13. The structure of the low temperature phase has not yet been reported, and the nature of this phase transition will provide insight on the behavior of the Cd-O' network in the absence of Nb.

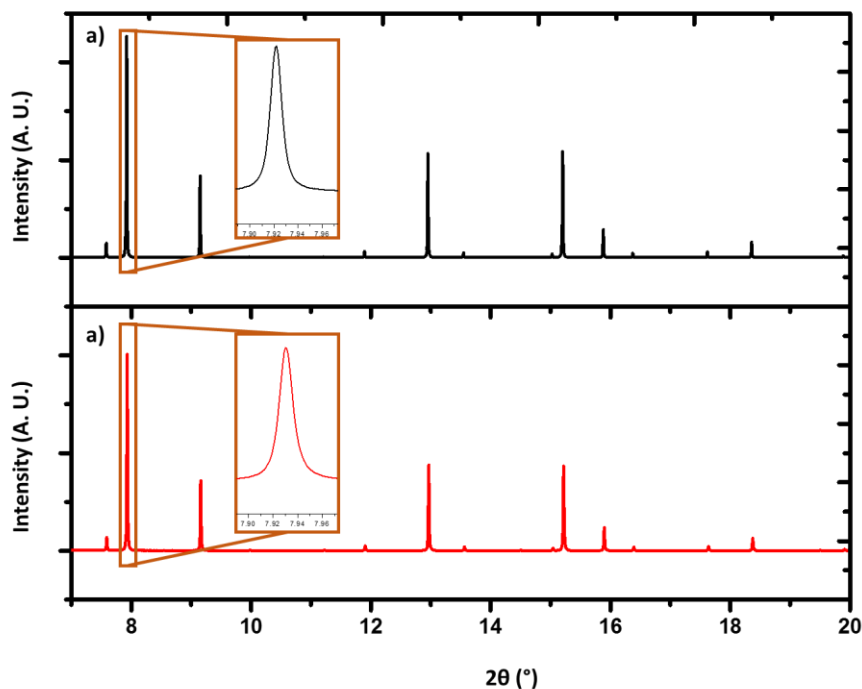


Figure 4.13 Room temperature (a) and 100 K data (b) for  $\text{Cd}_2\text{Ta}_2\text{O}_7$ . Inset shows (222) peak for both data.

#### 4.3.3 Structural Characterization of $\text{Cd}_2\text{Nb}_2\text{O}_{7-x}\text{S}_x$ ( $x = 0.25, 0.7$ ) at 100 K

Due to the complexity of the system upon S-substitution, characterization of the extreme ends of S-content ( $x = 0.25$  and  $0.7$ ) have thus far been analyzed. For the nominal  $x = 0.25$  sample, Le Bail fits were first attempted with an *Ima2* space group and lattice parameters were adjusted to incorporate the S content determined in the room temperature refinement. The *Ima2* space group was unable to index all peaks in the diffraction pattern (Figure 4.14a). Therefore, the orthorhombic space groups *Fddd* and *Fdd2* were considered, and successful peak indexing resulted from both (Figure 4.14b and c). Rietveld analysis (Figure 4.15) revealed better peak intensity in the *Fdd2* phase, particularly in the (222) peak.

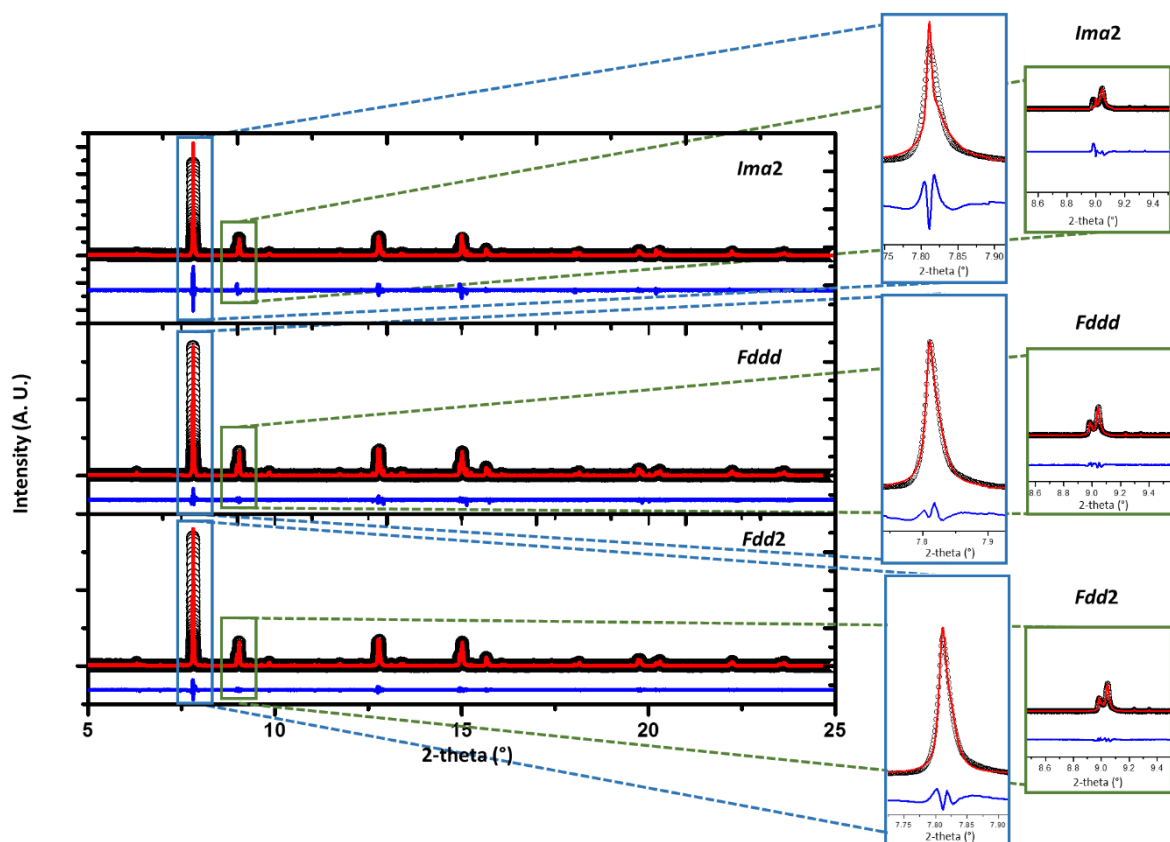


Figure 4.14 Le Bail fits with *Ima2*, *Fddd*, and *Fdd2* space groups for nominal  $\text{Cd}_2\text{Nb}_2\text{O}_{6.75}\text{S}_{0.25}$  at 100 K.

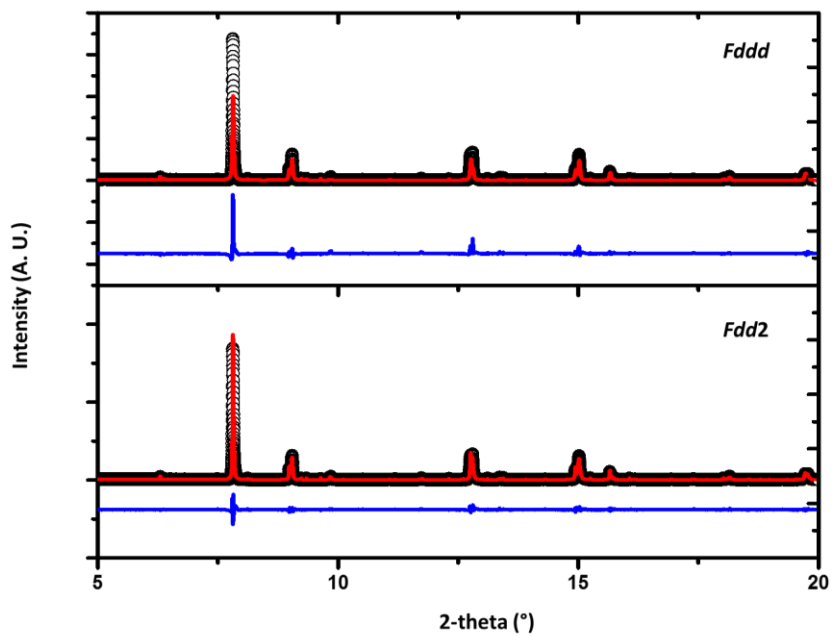


Figure 4.15 Rietveld fits with *Fddd*, and *Fdd2* space groups for nominal  $\text{Cd}_2\text{Nb}_2\text{O}_{6.75}\text{S}_{0.25}$  at 100 K.

Current results from the Rietveld analysis in *Fdd2* are shown in Table 4.3 and Figure 4.16. Refined positions in *Fdd2* results in a displacement of 0.065 Å for Cd and 0.092 Å for Nb from ideal positions in the room temperature structure. Efforts to reduce the R-values of the fit are in progress.

Table 4.3 Comparison of room temperature and 100 K data for nominal  $\text{Cd}_2\text{Nb}_2\text{O}_{6.75}\text{S}_{0.25}$ .

Refined Formula	$\text{Cd}_2\text{Nb}_2\text{O}_{6.88(1)}\text{S}_{0.22(1)}$	$\text{Cd}_2\text{Nb}_2\text{O}_{6.88(1)}\text{S}_{0.22(1)}$
<i>a</i> (Å)	10.52151(1)	10.5010(1)
<i>b</i> (Å)	10.52151(1)	10.4896(1)
<i>c</i> (Å)	10.52151(1)	10.5620(1)
Volume (Å <sup>3</sup> )	1164.754(2)	1163.428(2)
Space Group	<i>Fd</i> $\bar{3}m$	<i>Fdd2</i>
Temperature (K)	340	100
Cd <i>x</i>		0.877(1)
Cd <i>y</i>		0.120(1)
Cd <i>z</i>		0.252(1)
Nb <i>x</i>		0.882(1)
Nb <i>y</i>		0.876(1)
Nb <i>z</i>		0.003(1)
Cd-O'/S (Å)	2.2779(1)	2.3716(1)
		2.2030(1)
Nb-O1 (Å)	2.0017(1)	2.0011(1)
Nb-O2 (Å)		2.0689(1)
Nb-O3 (Å)		1.7898(1)
Nb-O3 (Å)		2.2053(1)
Nb-O4 (Å)		1.9863(1)
Nb-O4 (Å)		2.0749(1)
Cd $U_{\text{iso}}$ (Å <sup>2</sup> )	0.0440(1)	0.0099(1)
Nb $U_{\text{iso}}$ (Å <sup>2</sup> )	0.0104(1)	0.0117(1)
R (%)	6.14	15.43
$R_{\text{wp}}$ (%)	8.29	11.87

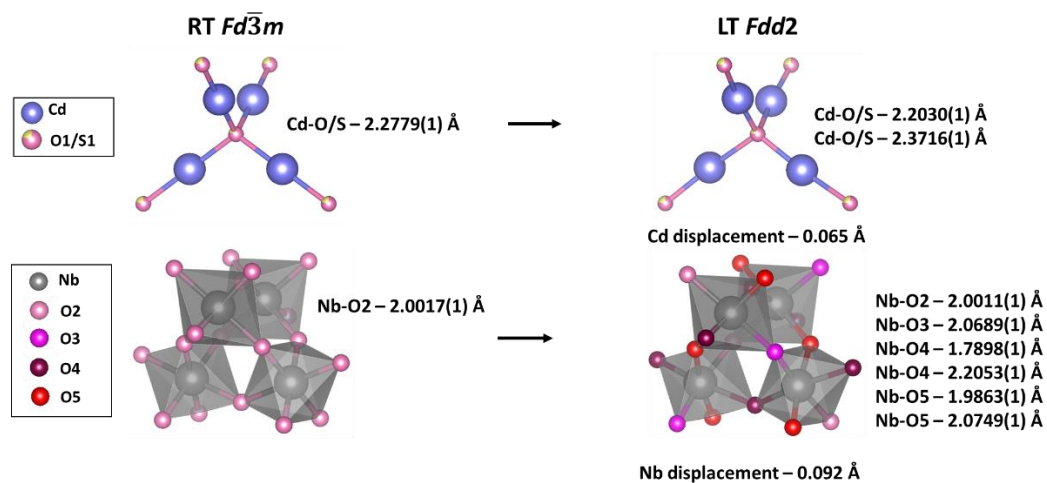


Figure 4.16 Phase transition from 330 K (left) to 100 K (right) for the networks in nominal  $Cd_2Nb_2O_{6.3}S_{0.7}$ .

The evolution of new peaks in the  $x = 0.7$  sample was observed upon cooling. To verify this was due to reduced symmetry and not displacements of the room temperature phase, LeBail analysis was first attempted with an  $Fd\bar{3}m$  space group (Figure 4.17a). This fit resulted in many unindexed peaks, so lower symmetry space groups  $F\bar{4}3m$  and  $P\bar{4}3m$  were considered. While able to index the (331) peak, many smaller peaks still remain unindexed with  $F\bar{4}3m$  (Figure 4.17b). Further reduction of symmetry to  $P\bar{4}3m$  properly indexes all peaks (Figure 4.14c), and Rietveld analysis in this space group is under investigation.

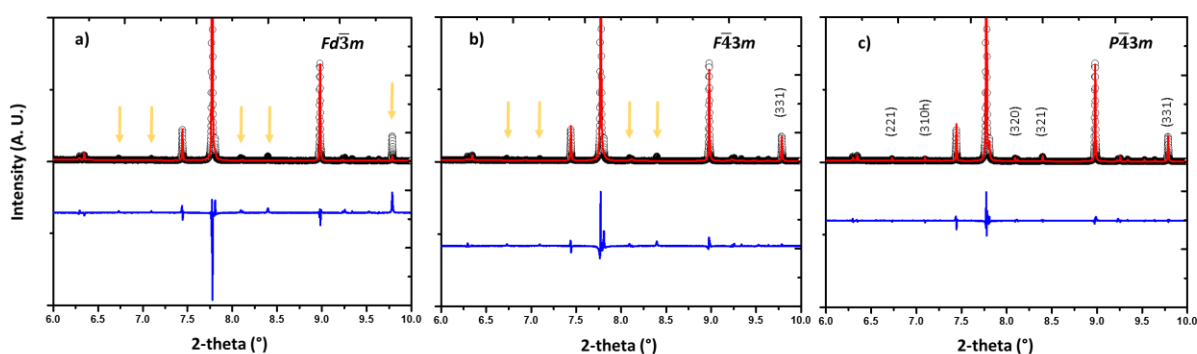


Figure 4.17 Le Bail fits for nominal  $Cd_2Nb_2O_{6.3}S_{0.7}$  at 100K: a) Le Bail fit with space group  $Fd\bar{3}m$  results in poor profile fits for major peaks and many smaller peaks remain unindexed; b) LeBail fit with space group  $F\bar{4}3m$  provides a better peak profile peak, but many smaller peaks still remain unindexed; c) Le Bail fit with space group  $P\bar{4}3m$  is able to index all peaks present and provide the best peak profile fit.

#### 4.5 Ferroelectricity in $\text{Cd}_2\text{Nb}_2\text{O}_{7-x}\text{S}_x$

Characterization of the dielectric constants of  $\text{Cd}_2\text{Nb}_2\text{O}_7$ ,  $\text{Cd}_2\text{Nb}_2\text{O}_{6.88(1)}\text{S}_{0.22(1)}$ , and  $\text{Cd}_2\text{Nb}_2\text{O}_{6.28(1)}\text{S}_{0.72(1)}$  (Figure 4.18) indicated the presence phase transitions, summarized and compared with the literature in Table 4.4.[25] Transitions in the literature were marked by much sharper  $T_c$  peaks. Sample density proved to be a major obstacle in the dielectric measurements, and may be responsible for the broad peaks observed around the transition temperatures.

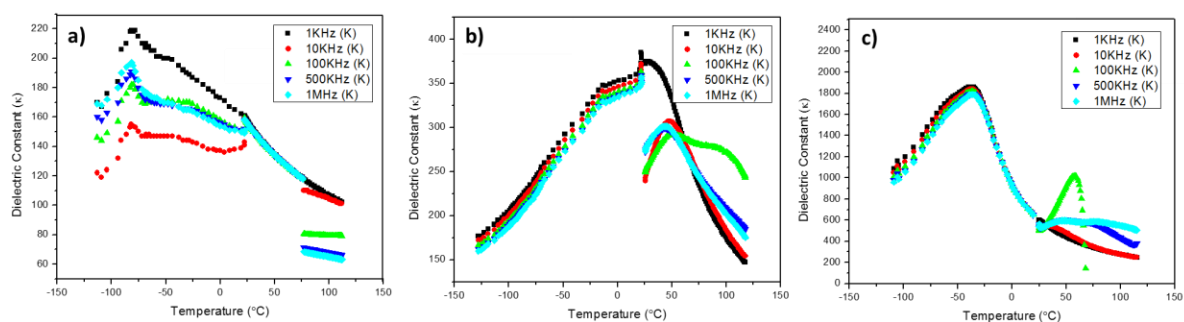


Figure 4.18 Dielectric measurements for  $\text{Cd}_2\text{Nb}_2\text{O}_7$  (a),  $\text{Cd}_2\text{Nb}_2\text{O}_{6.88(1)}\text{S}_{0.22(1)}$  (b), and  $\text{Cd}_2\text{Nb}_2\text{O}_{6.28(1)}\text{S}_{0.72(1)}$  (c).

Table 4.4 Observed and literature ferroelectric Curie temperatures for the series  $\text{Cd}_2\text{Nb}_2\text{O}_{7-x}\text{S}_x$

$x$	<b>0</b>	<b>0.22</b>	<b>0.72</b>
<b><math>T_c</math> 1 observed</b>	--	323 K	330 K
<b><math>T_c</math> 2 observed</b>	167 K	295 K	245 K
<b><math>T_c</math> 1 literature [25]</b>	--	~ 340 K	~ 415 K
<b><math>T_c</math> 2 literature [25]</b>	~ 250 K	~ 225 K	~ 320 K

As the S content increases, there is no general trend in the  $T_c$  for either  $T_c$  1 or  $T_c$  2. Structural characterization on the low temperature phases indicates that the same phase is not present throughout the solid solution at 100 K. This suggests that the sequence of phase transitions may not occur over the

same temperature (absolute or in magnitude) across the solution, and the observed  $T_c$  may not be comparing the same structural phases. It may be possible that all phase transitions ( $Fd\bar{3}m$ ,  $P\bar{4}3m$ ,  $Ima2$ , and  $Fdd2$ ) are occurring for each sample, but the degree of S substitution affects the temperature range or drives the stability of one structural transition over another. In-situ diffraction studies of the samples upon cooling would aid in the complete characterization of phase transitions present across the series.

#### 4.6 Conclusions

Synchrotron diffraction studies have been performed on the pyrochlore series  $Cd_2Nb_2O_{7-x}S_x$  ( $x = 0, 0.25, 0.25, \text{ and } 0.7$ ) at room temperature and 100 K. All samples can be fit with the space group  $Fd\bar{3}m$  at room temperature. Characterization at 100 K indicates a reduction in symmetry for all samples:  $Ima2$  for nominal  $x = 0$ ,  $Fdd2$  for nominal  $x = 0.25$ , and primitive cubic for  $x = 0.7$ . Dielectric measurements indicated the presence of multiple  $T_c$ 's in the samples, suggesting the phases investigated were indeed ferroelectric. From this investigation it is concluded that heat treatment and sample processing conditions are of paramount importance, as they will have a large effect on the structure and observed properties of the materials. Detailed processing and in-situ diffraction studies would greatly aid the determination of the origin of the ferroelectricity in pyrochlore materials, leading towards the design of novel ferroelectric materials.

#### 4.7 Materials and Methods

Polycrystalline samples of  $Cd_2Nb_2O_{7-x}S$  were prepared by mixing a stoichiometric ratio of  $2-x(CdO)$ ,  $x(CdS)$ , and  $Nb_2O_5$ .  $Cd_2Nb_2O_7$  was fired in air at 5000 °C for 10 h and 1000 °C for 122 h to prevent the volatilization of Cd. Samples containing S were sealed in evacuated quartz ampoules and annealed at 1050

°C for 24 h. Powders were first characterized through XRD with a Rigaku Miniflex II diffractometer using Cu K $\alpha$  radiation and a graphite monochromator. Powder samples were loaded onto a “zero background” oriented Si single crystal sample holder (MTI corp.) to maximize the detection of minor impurity phases. Data was collected from 10-120 ° 2 $\theta$  with a step size of 0.02 ° 2 $\theta$  and a dwell time of 2.0 s. Synchrotron diffraction studies were performed with a  $\lambda = 0.4137810$  on the 11BM beam line at the Advanced Photon Source, Argonne National Laboratory. Diffraction data was refined through the Le Bail method using the GSAS software and EXPGUI user interface.[29–31] Dielectric measurements were performed on an HP 4248 LCR meter using a home-made parallel plate capacitor setup from 150 – 400 K.

#### 4.8 References

- [1] Anthony R. West, *Solid State Chemistry and Its Applications*, Second, John Wiley & Sons. Ltd., West Sussex, 2014.
- [2] Anthony R. West, *Basic Solid State Chemistry*, 2nd ed., John Wiley & Sons. Ltd., New York, 1999.
- [3] A. Küster, J. Ihringer, W. Limper, T. Wroblewski, W. Prandl, *Mater. Sci. Forum* 79-82 (1991) 791.
- [4] M. Paściak, M. Wołczyr, A. Pietraszko, S. Leoni, *Phys. Rev. B* 81 (2010) 014107.
- [5] M. Tachibana, K. Fritsch, B.D. Gaulin, *J. Phys. Condens. Matter* 25 (2013) 435902.
- [6] M. Fischer, T. Malcherek, U. Bismayer, P. Blaha, K. Schwarz, *Phys. Rev. B* 78 (2008) 014108.
- [7] T. Malcherek, U. Bismayer, C. Paulmann, *J. Phys. Condens. Matter* 22 (2010) 205401.
- [8] G.A. Smolensky, N.N. Krainik, V.A. Trepakov, A. V. Babinsky, *Ferroelectrics* 26 (2011) 835.
- [9] Z.G. Ye, N.N. Kolpakova, J.-P. Rivera, H. Schmid, *Ferroelectrics* 124 (1991) 275.
- [10] F. Jona, G. Shirane, R. Pepinsky, *Phys. Rev.* 98 (1955) 903.
- [11] K. Łukaszewicz, A. Pietraszko, J. Stepień-Damm, N.N. Kolpakova, *Mater. Res. Bull.* 29 (1994) 987.
- [12] I.L. Shul, N.N. Kolpakova, M.P. Shcheglov, A.O. Lebedev, *Tech. Phys. Lett.* 25 (1999).

- [13] N.N. Kolpakova, S. Waplak, W. Bednarski, *J. Phys. Condens. Matter* 10 (1998) 9309.
- [14] E. Buixaderas, S. Kamba, J. Petzelt, M. Savinov, N.N. Kolpakova, *Eur. Phys. J. B* 19 (2001) 9.
- [15] N.N. Kolpakova, P.P. Syrnikov, A.O. Lebedev, P. Czarnecki, W. Nawrocik, C. Perrot, L. Szczepanska, *J. Appl. Phys.* 90 (2001) 6332.
- [16] N.N. KOLPAKOVA, P. CZARNECKI, W. NAWROCIK, M.P. SHCHEGLOV, L. SZCZEPANSKA, *Ferroelectrics* 302 (2004) 233.
- [17] A. Isupov, O.K. Khomutetskii, *Zhur. Sakharnoi Promysh.* 27 (1957) 2704-2717.
- [18] T.M. McQueen, D. V West, B. Muegge, Q. Huang, K. Noble, H.W. Zandbergen, R.J. Cava, *J. Phys. Condens. Matter* 20 (2008) 235210.
- [19] D. Liu, L. Lin, M.F. Liu, Z.B. Yan, S. Dong, J.-M. Liu, *J. Appl. Phys.* 113 (2013) 17D901.
- [20] X.W. Dong, K.F. Wang, S.J. Luo, J.G. Wan, J. –M. Liu, *J. Appl. Phys.* 106 (2009) 104101.
- [21] S. Saitzek, Z. Shao, A. Bayart, A. Ferri, M. Huvé, P. Roussel, R. Desfeux, *J. Mater. Chem. C* 2 (2014) 4037.
- [22] M. Kimura, S. Nanamatsu, T. Kawamura, S. Matsushita, *Jpn. J. Appl. Phys.* 13 (1974) 1473.
- [23] W. Cook, H. Jaffe, *Phys. Rev.* 88 (1952) 1426.
- [24] M. Tachibana, K. Fritsch, B.D. Gaulin, *J. Phys. Condens. Matter* 25 (2013) 435902.
- [25] D.B.J. Lucas, *Solid State Comm.* 18 (1976) 927.
- [26] J.-Y. Moisan, J. Pannetier, J. Lucas, *Comptes Rendus Des Seances l'Academie Des Sci. Ser. C Sci. Chim.* 271 (1970) 402.
- [27] D. Bernard, J. Pannetier, J. Lucas, *Solid State Comm.* 334 (1975) 328.
- [28] A.W. Sleight, *Mat. Res. Bull.* 9 (1974) 1437.
- [29] A. Le Bail, *Powder Diffr.* 20 (2005) 316.
- [30] A.C. Larson, R.B. Von Dreele, *Los Alamos Nat. Lab. Rep. LAUR* (1994) 89.
- [31] B.H. Toby, *J. Appl. Crystallogr.* 34 (2001) 210.

## CHAPTER 5

### Probing the local structure of Na-exchanged hollandites using total scattering techniques: $A_xRu_4O_8$ (A = K, Rb)

#### Abstract

The structure of the hollandites  $A_xRu_4O_8$  (A = K<sup>+</sup>, Rb<sup>+</sup>) has been studied through total scattering techniques upon cation exchange with Na<sup>+</sup> for the A-site cations. It is observed that the A-site of the hollandite structure is not fully occupied when A = K<sup>+</sup> or Rb<sup>+</sup>, but full A-site occupancy is achieved after ion exchange with NaNO<sub>3</sub>. The double chains of edge-shared RuO<sub>6</sub> octahedra and corner shared double chains found in the channel of the hollandite structure promotes two conduction mechanisms:  $\rho_{\parallel}$  (intra-chain metallic) and  $\rho_{\perp}$  (inter-chain hopping). The coexistence of  $\rho_{\parallel}$  and  $\rho_{\perp}$  gives rise to metallic conductivity below  $T_{max}$  (attributed to suppressed hopping at lower T) and semiconductivity above  $T_{max}$  (intra-chain mean-free-path becomes smaller than the inter-chain hopping distance), exhibiting quasi-one dimensional conduction along the RuO<sub>6</sub> chains at lower temperatures. The inter-chain distance is larger in the Rb-containing samples, and consequently the region dominated by intra-chain metallic conduction increases, along with an increase in  $T_{max}$ . All samples exhibit Pauli paramagnetism, explained primarily by the large low temperature range of metallic conduction.

Publications based on this chapter:

- 1) Laurita, G., Grajczyk, R., Coutinho, I., Stolt, M., Sleight, A. W., and Subramanian, M. A. Probing the local structure of sodium-exchanged hollandites using diffraction techniques:  $ARu_4O_8$  ( $A = K, Rb$ ). *Manuscript in Preparation*

## 5.1 Introduction to Quasi-One Dimensional Structures

The hollandites are a family of interest due to the one-dimensional nature of their structure. The tetragonal hollandite structure of  $A_xB_4O_8$  with symmetry  $I4/m$ , illustrated in Figure 5.1, consists of double chains of edge-shared  $BO_6$  octahedra. These corner-shared chains result in a one-dimensional (1D) tunnel structure that can house a variety of  $A^+$  cations.[1–4] The B-site and O atoms occupy variable  $8h$  sites and the A-site cation occupies the fixed  $2b$  site central to the tunnel structure.

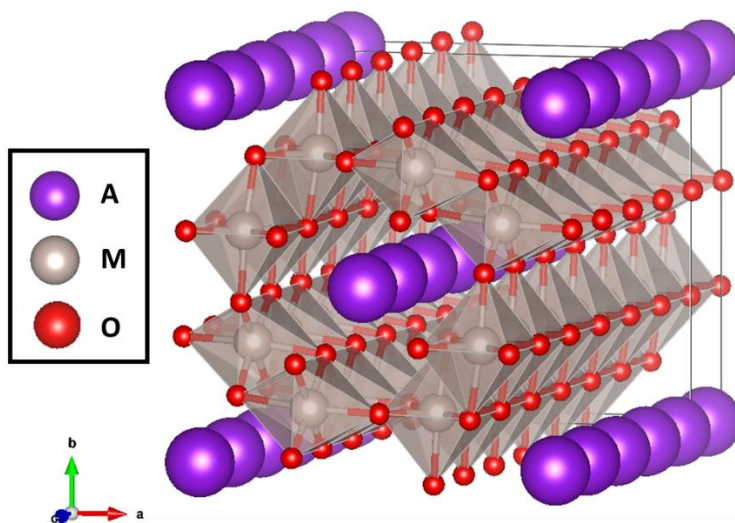


Figure 5.1 The tetragonal hollandite structure  $A_xB_4O_8$ . Edge-shared double chains of  $MO_6$  octahedra form a 1D tunnel structure which houses the A-cation.

Materials with quasi-one-dimensional (Q1D) structures can exhibit fascinating properties such as charge density waves in  $K_{0.3}MoO_3$  (Space group  $C2/m$ ), spin density waves in  $(TMTSF)_2PF_6$ , ballistic conduction in carbon nanotubes, and superconductivity in  $Nb_3Se_4$  (Space group  $P6_3/m$ ).[5–8] For a visual example, the structures of  $K_{0.3}MoO_3$  and  $Nb_3Se_4$  are shown in Figure 5.2

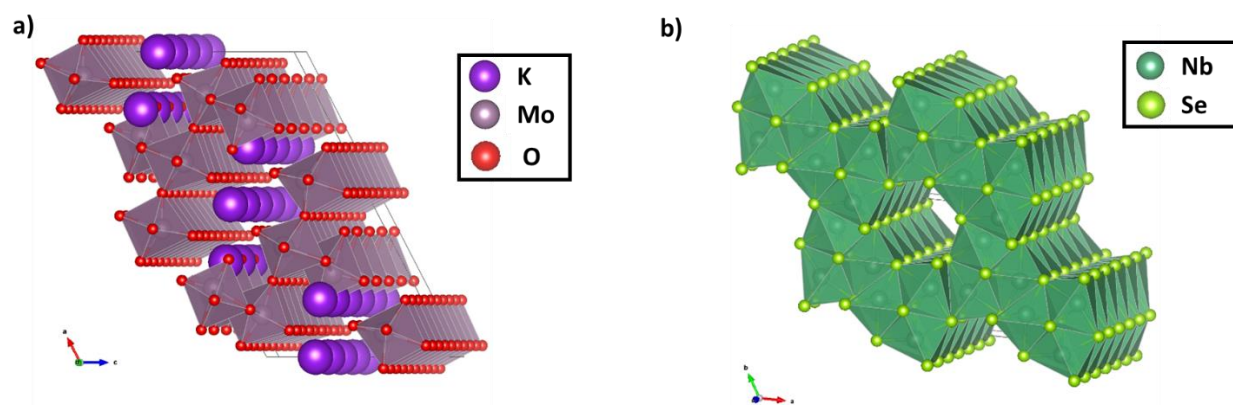


Figure 5.2 Q1D structures of  $K_{0.3}MoO_3$  (a) and  $Nb_3Se_4$  (b).

First reported in 1949, the  $KRu_4O_8$  hollandite is of interest as a strongly correlated Q1D oxide.[1–4,9] This material has been termed a “clean” conductor with a reported mean-free-path of 1300 - 2800 Å at low temperatures.[2,4] In addition to the Q1D nature of the tunnel structure, there is a large interest in studying *4d* and *5d* metal oxide materials, which exhibit high electron correlations such as spin-orbit coupling. Oxides of ruthenium exhibit a wealth of interesting electronic and magnetic properties, such as spin-glass behavior in  $Ca_2Ru_2O_7$ , high- $T_c$  superconductivity in  $Sr_2RuO_4$ , and simultaneous metallic conductivity and ferromagnetism in  $SrRuO_3$ . [10–13] This chapter focuses on the analysis of polycrystalline samples of  $ARu_4O_8$  hollandites, where  $A = Na^+$ ,  $K^+$ , and  $Rb^+$  through neutron total scattering techniques, four probe resistivity measurements, and magnetic susceptibility measurements.

## 5.2 Structural Analysis

Rietveld refinements on neutron total scattering data indicate all samples crystallize in the hollandite structure with space group symmetry  $I4/m$ , summarized in Table 5.1 and Figure 5.3. Lattice parameters for nominal  $KRu_4O_8$  are in agreement with the literature.[2] For samples of nominal composition  $KRu_4O_8$  and  $RbRu_4O_8$  it was found that the A site was not fully occupied, but upon Na-ion

exchange, full A-site occupancy was realized for both samples. Na exchange with the Rb hollandite resulted in a Na content of 40%, and this is the first report of Na substitution into the  $\text{RbRu}_4\text{O}_8$  hollandite. Due to the similarities in the neutron scattering cross section of Na and K (1.66 barn and 1.69 barn, respectively), it was impossible to determine the degree of Na substitution in the  $\text{K}_{1-x}\text{Na}_x\text{Ru}_4\text{O}_8$  sample.[14] Additional synchrotron data has recently been collected, and is in the process of being analyzed.

Table 5.1 Select crystallographic data from the powder neutron diffraction data.

Sample	$\text{KRu}_4\text{O}_8$	$\text{K}_{1-x}\text{Na}_x\text{Ru}_4\text{O}_8$	$\text{RbRu}_4\text{O}_8$	$\text{Rb}_{1-x}\text{Na}_x\text{Ru}_4\text{O}_8$
$a, b$ (Å)	9.8996(2)	9.9048(1)	10.0023(2)	9.9994(3)
$c$ (Å)	3.1196(2)	3.0871(2)	3.1175(2)	3.1167(3)
A Occ.	0.8(1)	1.0	0.79(3)	Rb = 0.61(3) Na = 0.39(3)
R (%)	5.27	5.74	8.96	8.88
$R_{\text{wp}}$ (%)	5.52	6.57	9.32	10.14

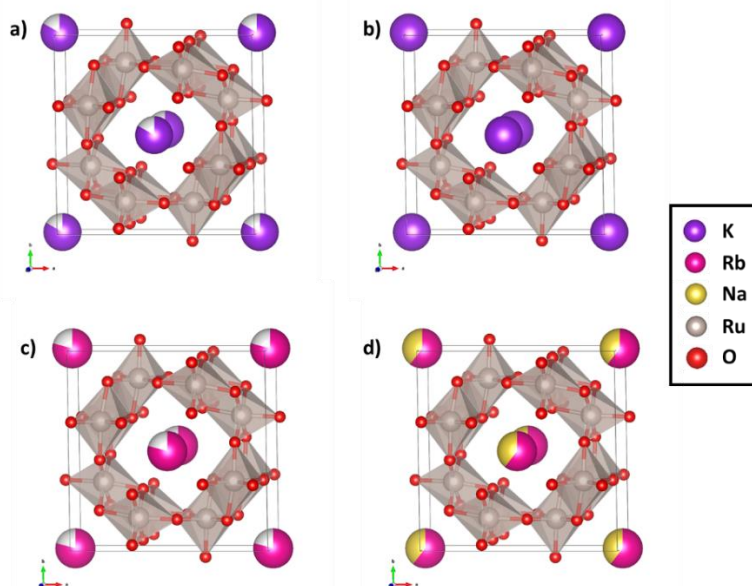


Figure 5.3 Unit cells obtained from Rietveld refinement of the neutron diffraction data for  $\text{K}_x\text{Ru}_4\text{O}_8$  (a),  $\text{K}_{1-x}\text{Na}_x\text{Ru}_4\text{O}_8$  (b),  $\text{Rb}_x\text{Ru}_4\text{O}_8$  (c), and  $\text{Rb}_{1-x}\text{Na}_x\text{Ru}_4\text{O}_8$  (d). For  $\text{K}_{1-x}\text{Na}_x\text{Ru}_4\text{O}_8$ , the A-site refined to full occupancy, but the degree of Na substitution requires X-ray analysis and is currently under investigation.

Due to the large channel in the hollandite structure, displacement parameters were modeled anisotropically for the A-site cations. Refinements indicated a dynamic displacement of all A-site cations parallel to the  $\text{RuO}_6$  tunnel structure, illustrated for each sample in Figure 5.5. Displacements of the A-site cation along the tunnels is documented in the literature and in agreement with these finding. [15]

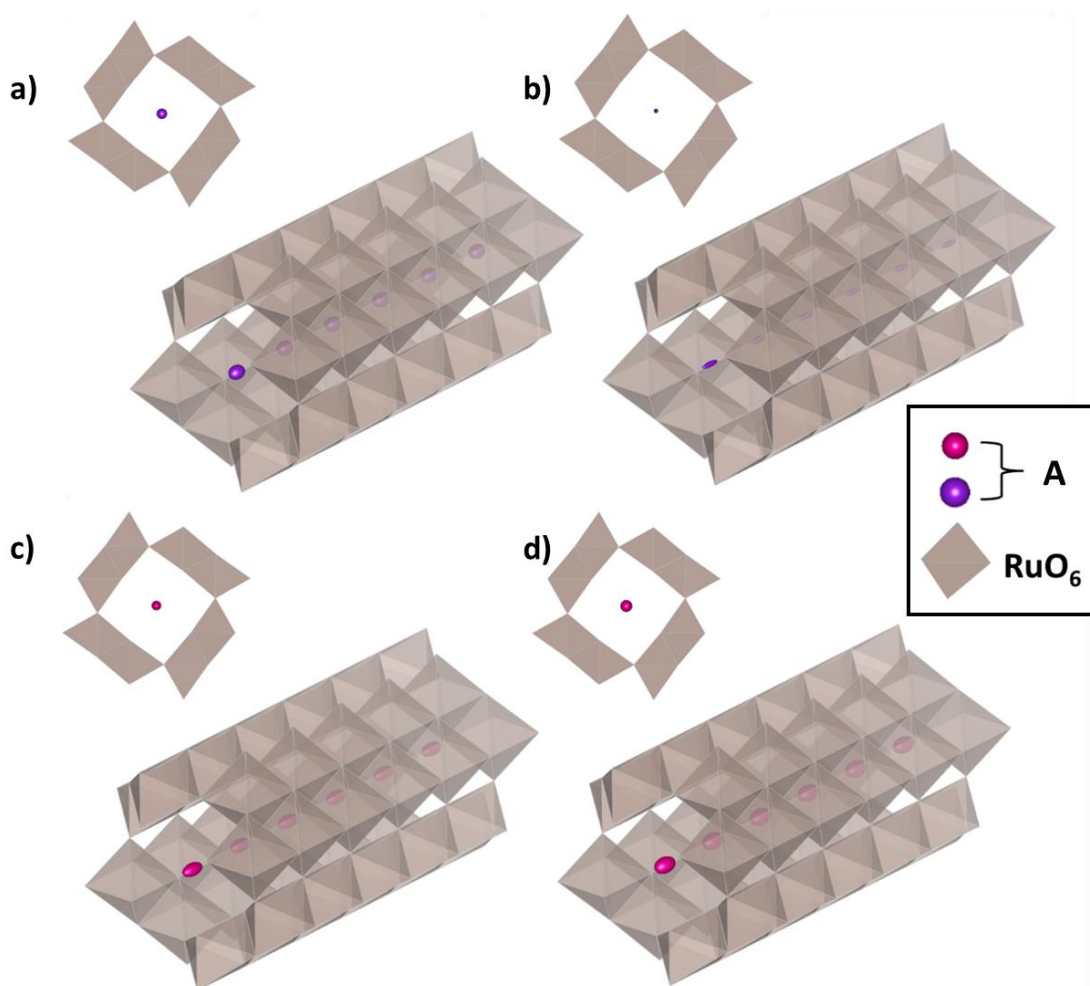


Figure 5.4 Anisotropic displacements of the A-site cations parallel to the  $\text{RuO}_6$  channel structure for  $\text{K}_x\text{Ru}_4\text{O}_8$  (a),  $\text{K}_{1-x}\text{Na}_x\text{Ru}_4\text{O}_8$  (b),  $\text{Rb}_x\text{Ru}_4\text{O}_8$  (c), and  $\text{Rb}_{1-x}\text{Na}_x\text{Ru}_4\text{O}_8$  (d).

The refined average structure was used as a starting point for local structure analysis, and refinements of the local structure over a  $r$ -range of  $10 \text{ \AA}$  against neutron PDFs (Figure 5.5) indicate similar atomic positions and displacements to those observed in the average structure refinements (Table 5.2). X-ray total scattering data has recently been collected, and analysis is still in progress and will provide contrast to any disorder in the channel structure between Na and K.

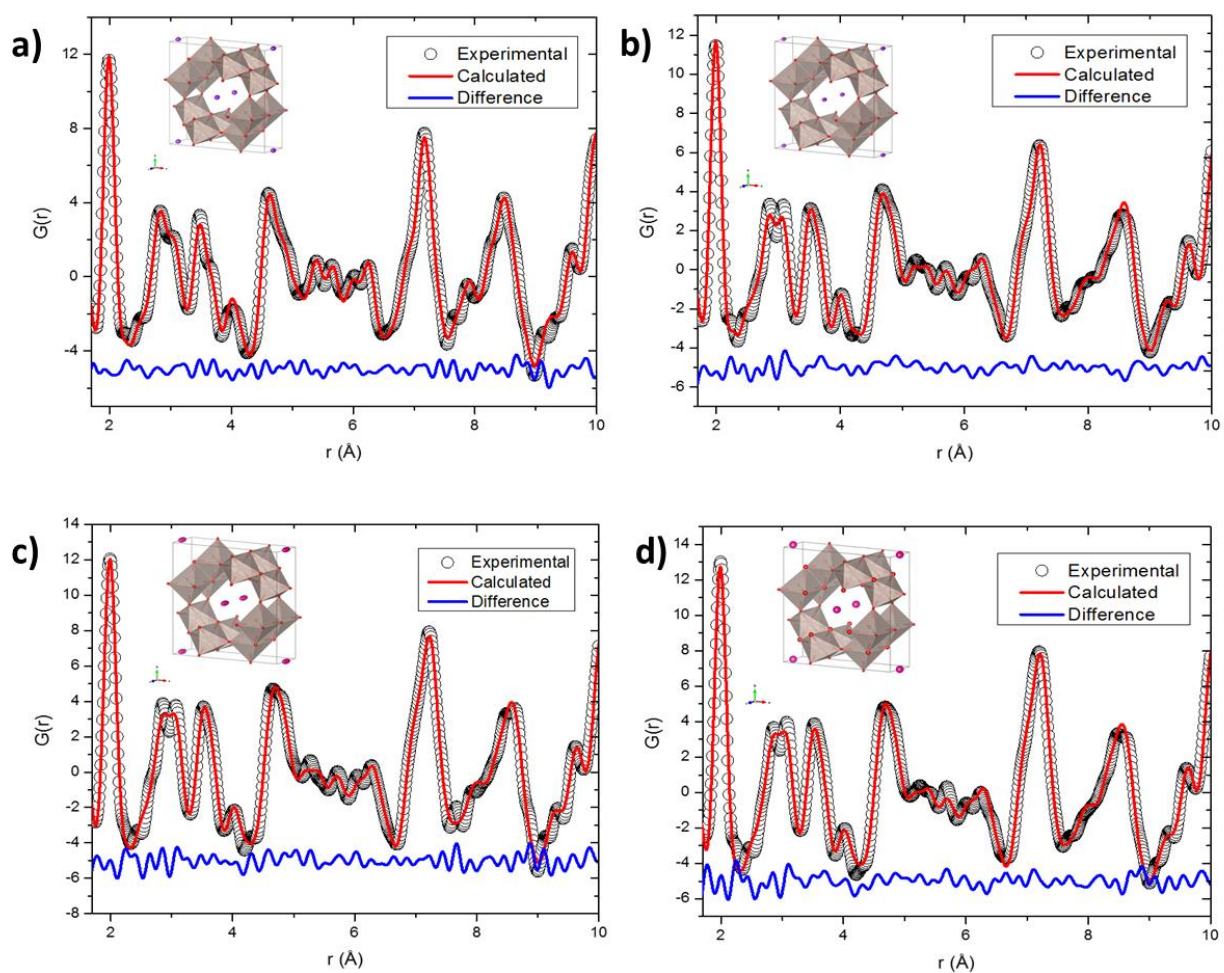


Figure 5.5 Fits to the neutron PDF data for  $K_xRu_4O_8$  (a),  $K_{1-x}Na_xRu_4O_8$  (b),  $Rb_xRu_4O_8$  (c), and  $Rb_{1-x}Na_xRu_4O_8$  (d). Insets: Resulting unit cells from the neutron PDF refinements.

Table 5.2 Comparison of the refined parameters for the local structure (refined over an r-range of 10 Å) and average structure (refined through Rietveld analysis) against neutron scattering data.

r-Range	$K_xRu_4O_8$		$K_{1-x}Na_xRu_4O_8$	
	10 Å	Rietveld	10 Å	Rietveld
Ru x	0.350(1)	0.3511(2)	0.349(1)	0.3512(1)
Ru y	0.166(1)	0.1675(2)	0.163(1)	0.1656(1)
O1 x	0.150(1)	0.1504(3)	0.153(1)	0.1532(1)
O1 y	0.201(1)	0.2004(3)	0.204(1)	0.2037(1)
O2 x	0.544(1)	0.5444(3)	0.542(1)	0.5428(1)
O2 y	0.157(1)	0.1586(3)	0.158(1)	0.1583(1)
Ru $U_{iso}$ (Å <sup>2</sup> )	0.0033(2)	0.0067(2)	0.003(1)	0.0056(1)
A $U_{11}$ (Å <sup>2</sup> )	0.019(2)	0.038(1)	0.012(1)	0.005(1)
A $U_{22}$ (Å <sup>2</sup> )	0.019(2)	0.038(1)	0.012(1)	0.005(1)
A $U_{33}$ (Å <sup>2</sup> )	0.047(2)	0.07(1)	0.04(2)	0.090(1)
O1 $U_{iso}$ (Å <sup>2</sup> )	0.007(2)	0.008(1)	0.005(1)	0.005(1)
O2 $U_{iso}$ (Å <sup>2</sup> )	0.0050(1)	0.0082(1)	0.0045(1)	0.0056(2)
Ru-O1	2.010(1)	2.012(4)	2.003(1)	1.996(4)
	2.040(1)	2.035(3)	2.034(1)	2.015(3)
Ru-O2	1.925(1)	1.915(4)	1.918(1)	1.899(3)
	1.980(1)	1.981(3)	1.994(1)	1.967(3)
A-O1	2.938(1)	2.930(3)	3.011(1)	2.959(3)
A-O2	3.416(1)	3.407(3)	3.444(1)	3.410(4)
r-Range	$Rb_xRu_4O_8$		$Rb_{1-x}Na_xRu_4O_8$	
	10 Å	Rietveld	10 Å	Rietveld
Ru x	0.349(1)	0.3510(3)	0.349(1)	0.3512(3)
Ru y	0.164(1)	0.1659(4)	0.165(1)	0.1658(4)
O1 x	0.153(1)	0.1536(4)	0.152(1)	0.1540(4)
O1 y	0.204(1)	0.2032(4)	0.207(1)	0.2020(4)
O2 x	0.542(1)	0.5433(3)	0.542(1)	0.5445(4)
O2 y	0.158(1)	0.1576(4)	0.159(1)	0.1584(4)
Ru $U_{iso}$ (Å <sup>2</sup> )	0.003(1)	0.0096(3)	0.0039(1)	0.0092(4)
A $U_{11}$ (Å <sup>2</sup> )	0.02(1)	0.032(4)	0.03(1)	0.050(5)
A $U_{22}$ (Å <sup>2</sup> )	0.02(1)	0.032(4)	0.03(1)	0.050(5)
A $U_{33}$ (Å <sup>2</sup> )	0.06(1)	0.134(4)	0.04(1)	0.13(2)
O1 $U_{iso}$ (Å <sup>2</sup> )	0.007(1)	0.0102(4)	0.0166(1)	0.0073(4)
O2 $U_{iso}$ (Å <sup>2</sup> )	0.005(1)	0.0107(4)	0.0049(1)	0.0116(5)
Ru-O1	2.004(1)	2.010(4)	2.017(1)	2.004(5)
	2.041(1)	2.035(3)	2.019(1)	2.043(4)
Ru-O2	1.934(1)	1.924(4)	1.934(1)	1.934(3)
	1.980(1)	1.985(4)	1.996(1)	1.977(4)
A-O1	2.995(1)	2.987(3)	3.0131(1)	2.980(3)
A-O2	3.448(1)	3.451(4)	3.438(1)	3.444(4)

Resolution of the total PDF into partial contributions (Figure 5.6) reveals the first atomic correlation of Ru-O ( $\sim 2 \text{ \AA}$ ) remains relatively unchanged through A-site substitution. This first correlation is the coordination environment of Ru: the  $\text{RuO}_6$  octahedra. A perfect octahedra would result in a narrow peak, and the observed broadness of the peak can be explained by the geometry of the  $\text{RuO}_6$  octahedra, which are composed of four distinct Ru-O bonds. The peak width remains relatively unchanged throughout the series of samples, suggesting the A-site cation has little influence on the geometry of the  $\text{RuO}_6$  octahedra. Minor variations by sample composition were observed in higher-r Ru-O correlations, which correspond to the octahedral arrangements in the structure. As different sized A cations are substituted into the  $\text{RuO}_6$  channel, the channel size will vary. This will have an effect on the Ru-O correlations in the edge-shared double chains ( $3 - 4 \text{ \AA}$ ) and the Ru-O correlations across the corner shared chains ( $4.8 - 5 \text{ \AA}$ ).

The first A-O correlation ( $\sim 2.5 - 4 \text{ \AA}$ ) is broader in distribution than the first Ru-O correlation, and indicates there is more disorder in the A cation coordination environment than that of the Ru atoms. This disorder is most likely due to the large dynamic displacements of the A cations inside the channel structure, as well as any disorder induced through Na- substitution. This is particularly noticeable in the  $\text{Rb}_{1-x}\text{Na}_x\text{Ru}_4\text{O}_8$  sample, as the partial  $G(r)$  between  $2.5 - 4 \text{ \AA}$  is quite broad compared to the other samples, and can be attributed to the disorder of the smaller Na cation in the large tunnel cavity. Bond valence sum (BVS) calculations of Na in the fixed  $8h$  position reveal a BVS of 0.38, indicating Na is severely under-bonded in the  $2b$  site. For comparison, the BVS of Rb in the  $2b$  site is 1.3, slightly over-bonded, but much closer to the expected valence of Rb. Therefore, the investigation of Na occupying the variable  $4e$  site to create some shorter Na-O distances and raise the BVS of Na is underway.

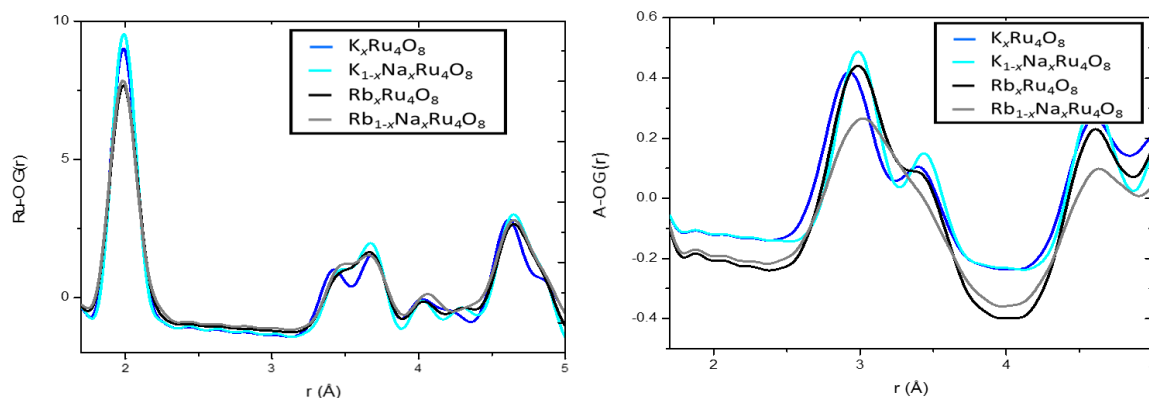


Figure 5.6 Partial contributions to the neutron PDF for samples  $A_x\text{Ru}_4\text{O}_8$  ( $A = \text{Na}^+$ ,  $\text{K}^+$ , and  $\text{Rb}^+$ ).

### 5.3 Physical Property Characterization

#### 5.3.1 Electrical Characterization

To perform four-probe resistivity measurements, well sintered bars need to be synthesized from the polycrystalline material. Sintering temperatures exceed the synthesis temperatures of the metastable Na-exchanged samples, so sample stability was assessed through thermogravimetric analysis (TGA) before sintering (Figure 5.7). Samples were heated to duplicate the sintering process, and weight loss was observed in all samples except  $\text{K}_x\text{Ru}_4\text{O}_8$ . XRD analysis of the samples after TGA treatment revealed the hollandite structure remained intact for the  $\text{Rb}_x\text{Ru}_4\text{O}_8$ , while the evolution of  $\text{RuO}_2$  peaks in the Na-exchanged samples was observed. Therefore, it was determined that the Na-exchanged samples were not stable under normal sintering procedures. Alternative room temperature procedures were attempted, including prolonged pressure treatment and isostatic cold pressing, but the resulting pellets were not robust enough to attach electrodes. Consequently, four-probe resistivity measurements were only carried out on sintered samples of  $\text{K}_x\text{Ru}_4\text{O}_8$  and  $\text{Rb}_x\text{Ru}_4\text{O}_8$ .

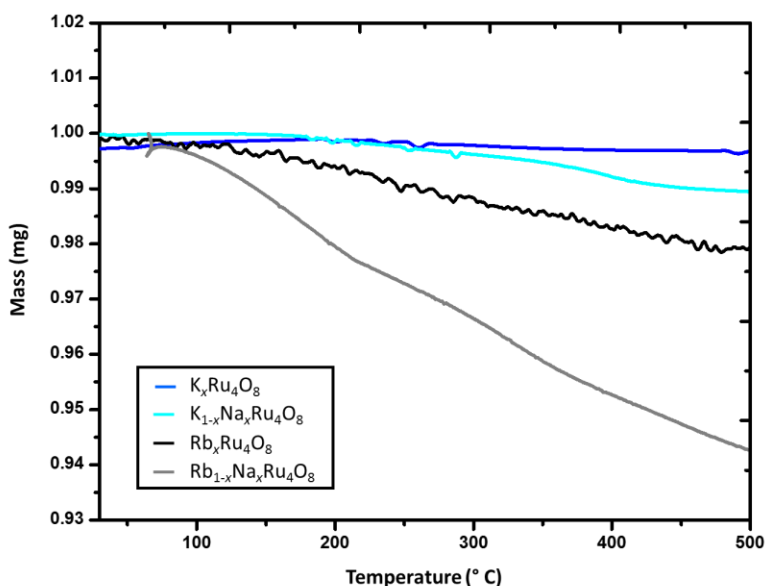


Figure 5.7 TGA curves up to 500 °C under  $N_2$  flow for hollandite samples  $A_xRu_4O_8$  ( $A = Na^+, K^+, \text{ and } Rb^+$ ).

The resistivity as a function of temperature for  $K_xRu_4O_8$  and  $Rb_xRu_4O_8$  can be seen in Figure 5.8. Two regions can be observed in the data: metallic behavior at low temperatures and semiconducting behavior at high temperatures. The arrangement of  $RuO_6$  octahedra in the hollandite structure gives rise to the two different conduction mechanisms. The double chains of edge-shared  $RuO_6$  octahedra result in intra-chain metallic conductivity,  $\rho_{||}$ , while the corner-shared chains result in an inter-chain hopping mechanism,  $\rho_{\perp}$ , and semiconducting behavior.[2–4] The coexistence of  $\rho_{||}$  and  $\rho_{\perp}$  gives rise to metallic conductivity below  $T_{max}$  due to suppressed carrier hopping at lower temperatures. As the temperature rises, the carrier mean-free path will decrease for metallic conduction. At the resistivity maximum, the intra-chain mean free path becomes smaller than the inter-chain hopping distance, and semiconductivity becomes dominant. This behavior is observed in the literature in single crystals of  $KRu_4O_8$  when the resistivity is measured along the  $a$ -axis of the single crystal, and the presence of both regions on the polycrystalline samples indicates preferential orientation of the needle-shaped crystallites (shown in

Figure 5.9). Measurement down the c-axis (along the  $\text{RuO}_6$  chains) of single crystals results in metallic conductivity throughout the entire temperature region, and this anisotropic behavior of the resistivity is indicative of Q1D conduction, with one dimensional conduction reinforced at lower temperatures.

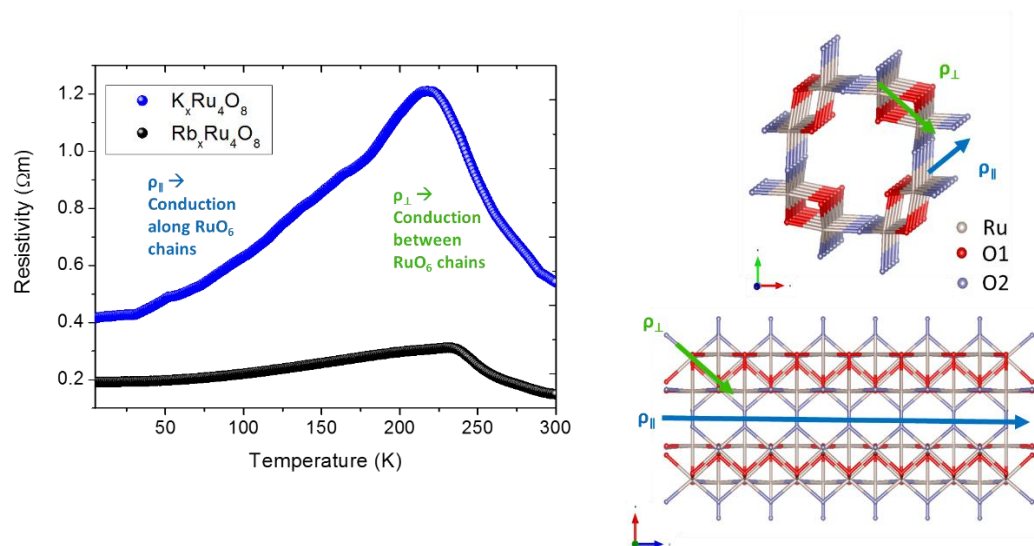


Figure 5.8 Left: Resistivity vs. temperature for polycrystalline samples of  $\text{K}_x\text{Ru}_4\text{O}_8$  and  $\text{Rb}_x\text{Ru}_4\text{O}_8$ . Right: conduction pathways in the hollandite structure.

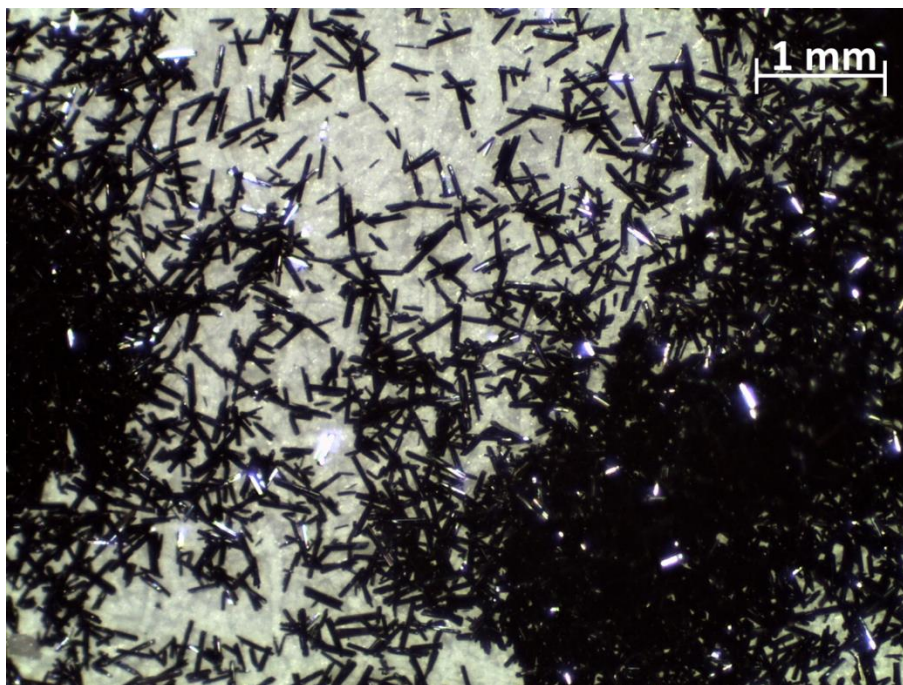


Figure 5.9 Microscope image of the small needle-shaped single crystals of  $\text{K}_x\text{Ru}_4\text{O}_8$ .

Substitution into the A-site of the hollandite structure has an observable effect on the electronic properties of the material. Occupancy of the A-site with cations of varying atomic radii have an impact on the lattice parameters and size of the tunnel structure. As the lattice parameters  $a$  and  $b$  increase to incorporate a larger cation, the distance between Ru atoms in corner-shared  $\text{RuO}_6$  chains also increases. As this inter-chain distance ( $d$ ) gets larger, the hopping distance needed for  $\rho_{\perp}$  increases and  $\rho_{\perp}$  is observed over a larger temperature region with a corresponding shift in  $T_{max}$  to higher temperatures. A larger Ru-Ru distance is observed in  $\text{Rb}_x\text{Ru}_4\text{O}_8$  in comparison to  $\text{K}_x\text{Ru}_4\text{O}_8$ , along with a larger temperature region of metallic conductivity and a higher  $T_{max}$  (Figure 5.10 and Table 5.3). Based on the Ru-Ru distances present in the Na-exchanged samples, the order of increasing  $T_{max}$  is expected to be  $\text{K}_x\text{Ru}_4\text{O}_8$ ,  $\text{K}_{1-x}\text{Na}_x\text{Ru}_4\text{O}_8$ ,  $\text{Rb}_x\text{Ru}_4\text{O}_8$ , and  $\text{Rb}_{1-x}\text{Na}_x\text{Ru}_4\text{O}_8$ .

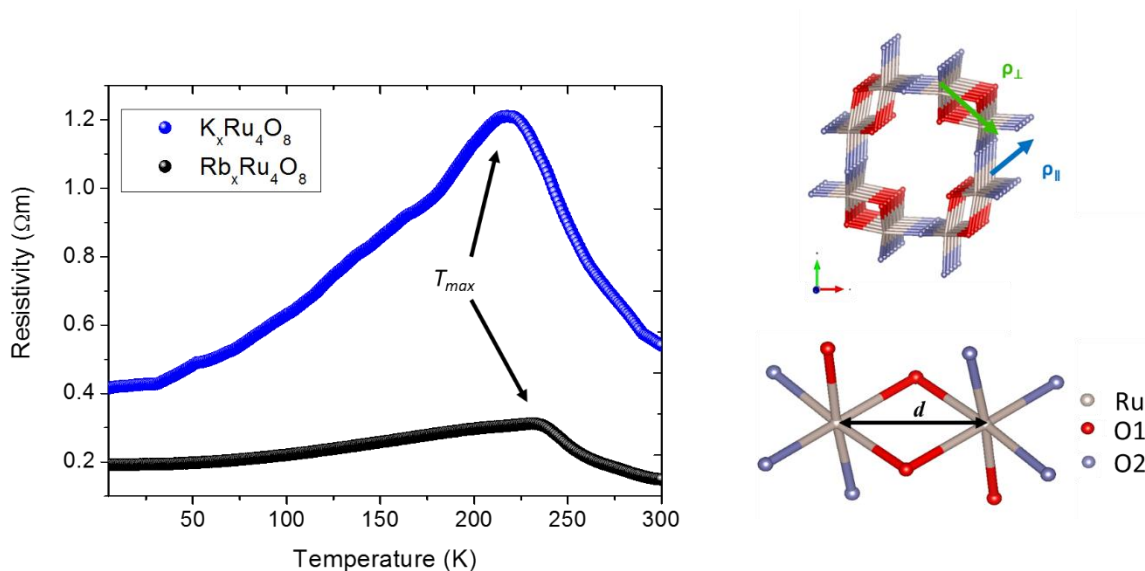


Figure 5.11 A shift in the  $T_{max}$  observed in the resistivity data (left) can be explained by a change in the inter-chain distance,  $d$ , or the distance between Ru-Ru atoms in the corner-shared chains.

Table 5.3 Inter-chain Ru-Ru distance ( $d$ ) and corresponding observed and predicted  $T_{max}$  values.

Sample	Ru-Ru Distance (Å)	$T_{max}$
$\text{K}_x\text{Ru}_4\text{O}_8$	3.018(2)	215.08 K
$\text{K}_{1-x}\text{Na}_x\text{Ru}_4\text{O}_8$	3.032(2)	230 K > T > 215 K
$\text{Rb}_x\text{Ru}_4\text{O}_8$	3.057(2)	234.07 K
$\text{Rb}_{1-x}\text{Na}_x\text{Ru}_4\text{O}_8$	3.059(2)	T > 235K

### 5.3.2 Magnetic Characterization

All measured samples indicate the presence of temperature-independent Pauli paramagnetism, with a slight increase in the magnetic susceptibility at the lowest temperatures, Figure 5.11a. This paramagnetic behavior is a result of the delocalized electrons in a metallic sample, and the observation of Pauli paramagnetism in the Na-exchanged samples suggests that they would have a similar resistivity trend as the parent compounds. The temperature dependence and magnitude of the susceptibility for the parent compounds are in good agreement with the data previously reported by Foo *et al.*[1] The slight increase in susceptibility below 50 K could be fit using the modified Curie-Weiss Law and is believed to be the result of impurity  $\text{Ru}^{4+}$  spins ( $S = 2$ ). With the exception of one composition, the modified Curie-Weiss Law is an appropriate model for all samples, shown by the linear trends in Figure 5.11b.

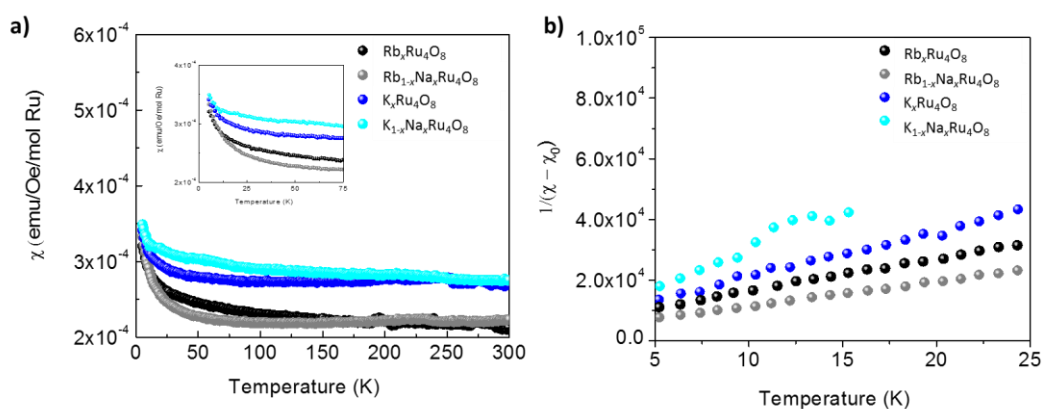


Figure 5.11 Magnetic susceptibility (a) and modified Curie-Weiss fits (b) for hollandite samples  $\text{ARu}_4\text{O}_8$  ( $A = \text{Na}^+, \text{K}^+, \text{and Rb}^+$ ).

## 5.4 Conclusions

Ion exchange methods can provide a successful route to achieving structures that are otherwise unattainable through standard solid state synthesis routes. In this chapter, hollandite samples  $A_x\text{Ru}_4\text{O}_8$  ( $A = \text{Na}, \text{K}, \text{Rb}$ ) were synthesized through both solid state and ion-exchanged procedures, and subsequently characterized through neutron scattering techniques, 4-probe resistivity measurements, and magnetic susceptibility measurements. It was determined that the 1D nature of the tunnel structure influenced an anisotropic displacement of A cations in the tunnel, as well as the observed Q1D conduction in the bulk samples. This Q1D conduction consists of two mechanisms: intra-chain metallic conduction and inter-chain carrier hopping. All samples exhibited Pauli paramagnetism above 50 K, and the low temperature region indicated a contribution from impurity  $\text{Ru}^{4+}$  spins. However, resistivity measurements could only be performed on samples synthesized through standard solid state reactions, as the stability of the ion-exchanged samples proved to be insufficient to withstand sintering procedures. This chapter illustrates that while ion-exchange routes can provide access to new compounds, the metastability of these previously undiscovered compositions can introduce unexpected changes to a full characterization. This progression allows for alternative routes to be utilized and a better understanding of the structure-property relationship to be found.

## 5.5 Materials and Methods

Polycrystalline samples of nominal  $\text{KRu}_4\text{O}_8$  and  $\text{RbRu}_4\text{O}_8$  were prepared by thoroughly grinding stoichiometric amounts of  $\text{RuO}_2$  and excess  $\text{A}_2\text{CO}_3$ , where  $A = \text{K}^+$  (15% excess) and  $\text{Rb}^+$  (30% excess) in an agate mortar and pestle. The samples were then annealed under  $\text{N}_2$  at  $800^\circ\text{C}$  for 12 hours in an alumina boat with intermediate grindings. Samples of  $\text{A}_{1-x}\text{Na}_x\text{Ru}_4\text{O}_8$  ( $A = \text{K}^+, \text{Rb}^+$ ) were prepared through the molten

salt ion exchange method. Approximately 0.2000g of ARu<sub>4</sub>O<sub>8</sub> was combined with NaNO<sub>3</sub> in a 1:5 metal to Na<sup>+</sup> molar ratio. Exchanges were performed at 350 °C for 12 hours. Samples were rinsed with deionized water to remove any exchanged or excess salts.

Powders were first characterized through XRD with a Rigaku Miniflex II diffractometer using Cu K $\alpha$  radiation and a graphite monochromator. Powder samples were loaded onto a “zero background” oriented Si single crystal sample holder (MTI corp.) to maximize the detection of minor impurity phases. Data was collected from 10-120 ° 2 $\theta$  with a step size of 0.02 ° 2 $\theta$  and a dwell time of 2.0 s. Room temperature lattice parameters were refined through the Le Bail method[16] using the GSAS software and EXPGUI user interface.[17,18] Powder neutron diffraction experiments were performed on the Nanoscale Ordered Materials Diffractometer (NOMAD) at the Spallation Neutron Source located at Oak Ridge National Laboratory.[19] Samples were loaded in a quartz capillary, and an empty capillary was collected and subtracted as background. The pair distribution function (PDF),  $G(r)$ , was obtained by the transformation of the total scattering function,  $S(Q)$ , according to the equation:

$$g(r) - 1 = \frac{1}{2\pi^2 r \rho \sum b^2} \int_{Q_{min}}^{Q_{max}} (S(Q) - 1) Q \sin(Qr) dQ$$

where  $G(r) = r(g(r) - 1)$  and  $Q_{max} = 31.5$ .

Room temperature synchrotron X-ray PDF measurements were collected on the 11-ID-B beam line at the Advanced Photon Source, Argonne National Laboratory with a photon wavelength of 0.2114 Å. Corrections to obtain the  $I(Q)$  and subsequent Fourier Transform with a  $Q_{max}$  of 35 Å<sup>-1</sup> to obtain the  $G(r)$  was performed using the program PDFgetX2.[20]

Least-squares refinements were performed on the average and local structure using GSAS software with the interface EXPGUI and PDFgui, respectively.[17,18,21] While local refinements were performed for various ranges of real space data ( $r = 1.7-5\text{Å}$ ,  $r = 1.7-10\text{Å}$  and  $r = 1.7-20\text{Å}$ ), the dependency

of the parameters on the range was determined to be negligible. Therefore, the reported PDF refinements have been completed with a 1.7 to 10 Å range.

The temperature stability of the compounds was studied through thermogravimetric analysis (TGA) using a TA Instruments Q50 TGA. Powdered starting materials were loaded in an alumina crucible and heated under N<sub>2</sub> flow to 900°C, with a ramp rate of 10°C/minute.

Four-probe resistivity and magnetic susceptibility were collected on bulk polycrystalline samples upon warming with a Quantum Design Physical Properties Measurement System (QD PPMS) from 5-300 K. Samples were prepared for resistivity measurements by pressing into bars and sintering to 500 °C under N<sub>2</sub> flow for 12 h. Ag electrodes were painted onto the samples, and Cu wires were used to perform the measurement. Zero-field-cooled (ZFC) DC magnetization data were collected using the ACMS mode with a magnetic field of 0.5 Tesla.

## 5.6 References

- [1] M.. Foo, W.-L. Lee, T. Siegrist, G. Lawes, a. . Ramirez, N.. Ong, R.. Cava, Mater. Res. Bull. 39 (2004) 1663.
- [2] W. Kobayashi, Phys. Rev. B 79 (2009) 155116.
- [3] T. Toriyama, M. Watanabe, T. Konishi, Y. Ohta, Phys. Rev. B 83 (2011) 195101.
- [4] A. Pautrat, W. Kobayashi, EPL 97 (2012) 67003.
- [5] G. Grüner, Rev. Mod. Phys. 60 (1988) 1129.
- [6] K. Mortensen, Y. Tomkiewicz, T. Schultz, E. Engler, Phys. Rev. Lett. 46 (1981) 1234.
- [7] A. Bachtold, M. Fuhrer, S. Plyasunov, M. Forero, E. Anderson, A. Zettl, P. McEuen, Phys. Rev. Lett. 84 (2000) 6082.
- [8] I.N. T. Ishida, K. Kanoda, H. Mazaki, Phys. Rev. B Condens. Matter Mater. Phys. 29 (1984) 1183.
- [9] A. Bystrom, A.M. Bystrom, Nature 164 (1949) 1128.

- [10] Y. Maeno, H. Hashimoto, K. Yoshida, S. Nishizaki, T. Fujita, J.G. Bednorz, F. Lichtenberg, *Nature* 372 (1994) 532.
- [11] Y. Maeno, T.M. Rice, M. Sigrist, *Phys. Today* 54 (2001) 42.
- [12] A. Callaghan, C.W. Moeller, R. Ward, *Inorg. Chem.* 5 (1966) 1572.
- [13] Y. Noro, S. Miyahara, *J. Phys. Soc. Japan* 27 (1969) 518A.
- [14] A. Munter, NIST Center for Neutron Research Neutron Scattering Lengths and Cross Sections, [Http://www.ncnr.nist.gov/resources/n-Lengths/](http://www.ncnr.nist.gov/resources/n-Lengths/), 2011.
- [15] T. Endo, S. Kume, N. Kinomura, M. Koizumi, *Mater. Res. Bull.* 11 (1976) 609.
- [16] A. Le Bail, *Powder Diffr.* 20 (2005) 316.
- [17] A.C. Larson, R.B. Von Dreele, Los Alamos Nat. Lab. Rep. LAUR (1994) 89.
- [18] B.H. Toby, *J. Appl. Crystallogr.* 34 (2001) 210.
- [19] J. Neufeind, M. Feygenson, J. Carruth, R. Hoffmann, K.K. Chipley, *Nucl. INSTRUMENTS METHODS Phys.* 287 (2012) 68.
- [20] X. Qiu, J.W. Thompson, S.J.L. Billinge, *J. Appl. Crystallogr.* 37 (2004) 678.
- [21] C.L. Farrow, P. Juhas, J.W. Liu, D. Bryndin, E.S. Božin, J. Bloch, T. Proffen, S.J.L. Billinge, *J. Phys. Condens. Matter* 19 (2007) 335219.

## General Conclusions and Future Work

This dissertation presented the characterization of a series of materials for energy and electronic applications. The structure-property relationships in the visible-light photocatalyst  $\text{Ag}_2\text{Sb}_2\text{O}_6$  were investigated through substitution with cations of varying valency, size, and electronegativity. A complete solid solution was formed between the anion-deficient pyrochlore  $\text{Ag}_2\text{Sb}_2\text{O}_6$  and the ideal pyrochlore  $\text{Cd}_2\text{Sb}_2\text{O}_7$ ; a plethora of characterization techniques including thermogravimetric analysis, computational studies, and Mössbauer Spectroscopy were employed to investigate anomalous behavior in the Cd-rich end. In conjunction with Electron Paramagnetic Resonance, it was determined this behavior was due to the presence of a small radical species, proposed as  $\text{O}^-$ . Total scattering neutron techniques were applied to the series  $\text{Ag}_{1-x}\text{M}^n_x\text{SbO}_{3+x[(n-1)/2]}$  ( $\text{M} = \text{Na}^+, \text{K}^+, \text{and } \text{Ti}^{+/3+}$ ), and it was observed that both  $\text{Na}^+$  and  $\text{Ti}^+$  statically displace from the ideal position in the channels of the pyrochlore structure. Photocatalytic activity was evaluated for all substituted samples, and an increase was observed upon Na-substitution due to a favorable orbital overlap and sample morphology.

Synchrotron diffraction studies were performed on the anion-substituted pyrochlore series  $\text{Cd}_2\text{Nb}_2\text{O}_{7-x}\text{S}_x$  ( $x = 0, 0.25, 0.25, \text{ and } 0.7$ ) at ambient temperatures and 100 K. While all samples were fit with the space group  $Fd\bar{3}m$  at room temperatures, different space groups were observed for the low temperature data across the series. It was suggested that the varying degree of S-content may be influencing the temperature range at which the transitions occur or may be driving the stability of one phase over another. Detailed processing and *in situ* characterization studies are needed to verify this hypothesis.

Structure-property relationships were investigated for hollandites  $\text{A}_x\text{Ru}_4\text{O}_8$  ( $\text{A} = \text{Na}^+, \text{K}^+, \text{Rb}^+$ ) synthesized through standard solid state and molten salt ion exchange routes. Neutron scattering, four-probe resistivity, and magnetic susceptibility measurements were performed on the samples. The one-

dimensional nature of the structure was confirmed by anisotropic displacements of the large A-site cations along the channel, as well as an observed quasi-one dimensional behavior in the resistivity as a function of temperature. Further characterization through X-ray scattering techniques are in progress and will benefit the total structural analysis of the samples.

Through this dissertation it was demonstrated that cation and anion substitution can be a promising route for manipulating the structure and consequently the properties of a material. However, each system has its own unique challenges, and one must be flexible and creative to solve the problems at hand. For example, sample processing for quality transport property characterization of samples in this dissertation was a major obstacle. Of the samples, metastable phases prepared through ion exchange routes were not viable for sintering, and therefore alternate routes of characterization had to be employed. Scattering techniques are a powerful tool for the structural characterization of a material, but as observed in Chapter 3, not all methods (such as neutron scattering for Cd-containing samples) can be employed for certain elements. While challenging, these obstacles can facilitate the exploration of new techniques, allowing for the development of a well-rounded scientific knowledge. It is through this open-minded and multi-disciplinary approach that novel materials with fascinating properties will be discovered.

## BIBLIOGRAPHY

- B.J. Alder, T.E. Wainwright, *J. Chem. Phys.* 31 -1959 459
- J.P. Allen, M.K. Nilsson, D.O. Scanlon, G.W. Watson, *Phys. Rev. B Condens. Matter* 83 -2011 35207
- T. Arai, K. Tani, R.L. McGreevy, *J. Phys. Condens. Matter* 22 -2010 404204
- A. Bachtold, M. Fuhrer, S. Plyasunov, M. Forero, E. Anderson, A. Zettl, P. McEuen, *Phys. Rev. Lett.* 84 -2000 6082
- R. Berthelot, W. Schmidt, S. Muir, J. Eilertsen, L. Etienne, A.W. Sleight, M.A. Subramanian, *Inorg. Chem.* 51 -2012 5377
- D. Bernard, J. Pannetier, J. Lucas, *Solid State Comm.* 334 (1975) 328.
- T. Birchall, B. Della Valle, *Chem. Commun.* -1970 675
- P.E. Blochl, *Phys. Rev. B* 50 -1994 17953
- E. Bonera, G. Scarel, M. Fanciulli, *J. Non. Cryst. Solids* 322 -2003 105
- K.B. Borisenko, Y. Chen, S.A. Song, D.J.H. Cockayne, *Chem. Mater.* 21 -2009 5244
- K.B. Borisenko, Y. Chen, D.J.H. Cockayne, S.A. Song, H.S. Jeong, *Acta Mater.* 59 -2011 4335
- M. Bouchama, M. Tournoux, *Rev. Chim. Miner.* 12 -1975 80
- R.A. Brand, NORMOS Mössbauer Fitting Program, Universitat Duisburg, Duisburg, Germany, 2007
- F. Brisse, D.J. Stewart, V. Seidl, O. Knop, *Can. J. Chem.* 50 -1972 3648
- W.S. Brower, D.B. Minor, H.S. Parker, R.S. Roth, J.L. Waring, *Mater. Res. Bull.* 9 -1974 1045
- S. Brunauer, P.H. Emmett, E. Teller, *J. Am. Chem. Soc.* 60 -1938 309
- E. Buixaderas, S. Kamba, J. Petzelt, M. Savinov, N.N. Kolpakova, *Eur. Phys. J. B* 19 -2001 9
- A. Bystrom, B. Hok, B. Mason, *Ark. Kemi, Mineral. Och Geol.* 15B -1941 8
- A. Bystrom, A.M. Bystrom, *Nature* 164 -1949 1128
- A. Callaghan, C.W. Moeller, R. Ward, *Inorg. Chem.* 5 -1966 1572
- W. Cook, H. Jaffe, *Phys. Rev.* 88 -1952 1426
- S.A. Corr, R. Seshadri, in: *Compr. Inorg. Chem. II, Second*, Elsevier, 2013, pp. 1–15.
- B.D. Cullity, S.R. Stock, *Elements of X-Ray Diffraction*, 3rd ed., Prentice Hall, Upper Saddle River, NJ, 2001
- X.W. Dong, K.F. Wang, S.J. Luo, J.G. Wan, J. -M. Liu, *J. Appl. Phys.* 106 -2009 104101
- T. Egami, S.J.L. Billinge, *Underneath the Bragg Peaks: Structural Analysis of Complex Materials*, Pergamon, New York, 2003
- T. Endo, S. Kume, N. Kinomura, M. Koizumi, *Mater. Res. Bull.* 11 -1976 609
- C. Fan, P. Liaw, V. Haas, J. Wall, H. Choo, A. Inoue, C. Liu, *Phys. Rev. B* 74 -2006 14205
- C.L. Farrow, P. Juhas, J.W. Liu, D. Bryndin, E.S. Božin, J. Bloch, T. Proffen, S.J.L. Billinge, *J. Phys. Condens. Matter* 19 -2007 335219
- M. Fischer, T. Malcherek, U. Bismayer, P. Blaha, K. Schwarz, *Phys. Rev. B* 78 -2008 14108
- M. Foo, W.-L. Lee, T. Siegrist, G. Lawes, a. . Ramirez, N.. Ong, R.. Cava, *Mater. Res. Bull.* 39 -2004 1663
- J. George, *Preparation of Thin Films*, M. Dekker, New York, NY, 1993
- R. Gillen, J. Robertson, *Phys. Rev. B* 85 -2012 14117
- R. Grajczyk, M.A. Subramanian, *Prog. Solid State Chem.* (2014).
- S.M.A. Greaves, C. Katib, *Mater. Res. Bull.* 25 -1990 1175
- J.E. Greedan, *J. Mater. Chem.* 11 -2001 37
- G. Grüner, *Rev. Mod. Phys.* 60 -1988 1129
- P. T. Hang, G. W. Brindley, *Clays and Clay Min.* 18 (1970) 203.
- P. Hanrahan, W. Krueger, *SIGGRAPH '93 Proceedings*, J. T. Kajiya 27 -1993 165
- J. Heyd, G.E. Scuseria, M. Ernzerhof, *J. Chem. Phys.* 118 -2003 8207

- A. Houas, H. Lachheb, M. Ksibi, E. Elaloui, C. Guillard, J. Herrmann, 31 -2001 145
- M. Inukai, Y. Noda, K. Takeda, J. Magn. Reson. 213 -2011 192
- A. Isupov, O.K. Khomutetskii, Zhur. Sakharnoi Promysh. 27 (1957) 2704-2717.
- Y.M. Jansen, J. Pebler, K. Dehnicke, Zeitschrift Für Anorg. Und Allg. Chemie 495 -1982 120
- R. Jin, J. He, S. McCall, C. Alexander, F. Drymiotis, D. Mandrus, Phys. Rev. B Condens. Matter 64 -2001 180503
- F. Jona, G. Shirane, R. Pepinsky, Phys. Rev. 98 -1955 903
- F. Jona, G. Shirane, R. Pepinsky, Phys. Rev. 98 -1955 903
- T. Kako, N. Kikugawa, J. Ye, Catal. Today 131 -2008 197
- M. Kaneko, I. Okura, Photocatalysis: Science and Technology, Springer, New York, NY, 2002
- M. Kimura, S. Nanamatsu, T. Kawamura, S. Matsushita, Jpn. J. Appl. Phys. 13 -1974 1473
- C. Kittel, Introduction to Solid State Physics, John Wiley & Sons. Ltd., Hoboken, NJ, 2005
- W. Kobayashi, Phys. Rev. B 79 -2009 155116
- N.N. Kolpakova, S. Waplak, W. Bednarski, J. Phys. Condens. Matter 10 -1998 9309
- N.N. Kolpakova, P.P. Syrnikov, A.O. Lebedev, P. Czarnecki, W. Nawrocik, C. Perrot, L. Szczepanska, J. Appl. Phys. 90 -2001 6332
- N.N. KOLPAKOVA, P. CZARNECKI, W. NAWROCIK, M.P. SHCHEGLOV, L. SZCZEPANSKA, Ferroelectrics 302 - 2004 233
- G. Kresse, Phys. Rev. B 59 -1999 1758
- G. Kresse, J. Furthmuller, Phys. Rev. B 54 -1996 11169
- G. Kresse, J. Hafner, Phys. Rev. B 49 -1994 14251
- A.V Krukau, O. a Vydrov, A.F. Izmaylov, G.E. Scuseria, J. Chem. Phys. 125 -2006 224106
- P. Kubelka, F. Munk, Zeitschrift Für Tech. Phys. 12 -1931 593
- A. Küster, J. Ihringer, W. Limper, T. Wroblewski, W. Prandl, Mater. Sci. Forum 79-82 -1991 791
- A.C. Larson, R.B. Von Dreele, Los Alamos Nat. Lab. Rep. LAUR -1994 89
- A. Le Bail, Powder Diffr. 20 -2005 316
- B.R. Li, J.L. Zhang, J. Mater. Sci. Lett. 9 -1990 109
- P.E. Lippens, Solid State Commun. 113 -2000 399
- Y.-F. Liu, X. Liu, J. Yu, Sensors Actuators B Chem. 61 -1999 208
- D. Liu, L. Lin, M.F. Liu, Z.B. Yan, S. Dong, J.-M. Liu, J. Appl. Phys. 113 -2013 17D901.
- D.B.J. Lucas, Solid State Comm. 18 (1976) 927.
- K. Lukaszewicz, A. Pietraszko, J. Stepien-Damm, N.N. Kolpakova, Mater. Res. Bull. 29 -1994 987
- Y. Maeno, H. Hashimoto, K. Yoshida, S. Nishizaki, T. Fujita, J.G. Bednorz, F. Lichtenberg, Nature 372 -1994 532
- Y. Maeno, T.M. Rice, M. Sigrist, Phys. Today 54 -2001 42
- T. Malcherek, U. Bismayer, C. Paulmann, J. Phys. Condens. Matter 22 -2010 205401
- A.R. Mather, G. C. Smith, R. I., Skakle, J. M. S Fletcher, J. G Castellanos, M. A. Gutierrez, M. P. West, J. Solid State Chem. 10 -2000 2219
- Y. Matsumoto, K. Funaki, J. Hombo, Y. Ogawa, J. Solid State Chem. 99 -1992 336
- R.L. McGreevy, J. Phys. Condens. Matter 13 -2001 R877.
- T.M. McQueen, D. V West, B. Muegge, Q. Huang, K. Noble, H.W. Zandbergen, R.J. Cava, J. Phys. Condens. Matter 20 -2008 235210
- N. Media, [http://www.nobelprize.org/nobel\\_prizes/physics/laureates/1915/index.html](http://www.nobelprize.org/nobel_prizes/physics/laureates/1915/index.html) (2014).
- J.-Y. Moisan, J. Pannetier, J. Lucas, Comptes Rendus Des Seances l'Academie Des Sci. Ser. C Sci. Chim. 271 (1970) 402.

- Rigaku, X-Ray Diffractometer Miniflex II Instruction Manual, Manual No. ME14966A02, 2006.
- R. Mishra, R. Pottgen, R.-D. Hoffmann, T. Fickenscher, M. Eschen, H. Trill, B.D. Mosel, *Zeitschrift Fuer Naturforschung, B Chem. Sci.* 57 -2002 1215
- D. Mitzi, *Solution Processing of Inorganic Materials*, Wiley, Hoboken, NJ, 2009
- H. Mizoguchi, H.W. Eng, P.M. Woodward, *Inorg. Chem.* 43 -2004 1667
- J.-Y. Moisan, J. Pannetier, J. Lucas, *Comptes Rendus Des Seances l'Academie Des Sci. Ser. C Sci. Chim.* 271 -1970 402
- K. Mortensen, Y. Tomkiewicz, T. Schultz, E. Engler, *Phys. Rev. Lett.* 46 -1981 1234
- A. Munter, NIST Center for Neutron Research Neutron Scattering Lengths and Cross Sections, <Http://www.ncnr.nist.gov/resources/n-Lengths/>, 2011
- J. Neufeind, M. Feygenson, J. Carruth, R. Hoffmann, K.K. Chipley, *Nucl. INSTRUMENTS METHODS Phys.* 287 -2012 68
- S. Nishiyama, A. Ichikawa, T. Hattori, *J. Ceram. Soc. Japan* 112 -2004 298
- K. Nomura, T. Kamiya, H. Ohta, T. Uruga, M. Hirano, H. Hosono, *Phys. Rev. B* 75 -2007 35212
- Y. Noro, S. Miyahara, *J. Phys. Soc. Japan* 27 -1969 518A.
- P.G. Pai, *J. Vac. Sci. Technol. A Vacuum, Surfaces, Film.* 4 -1986 689
- M. Pasciak, M. Wolczyk, A. Pietraszko, S. Leoni, *Phys. Rev. B* 81 -2010 14107
- A. Patterson, *Phys. Rev.* 56 -1939 978
- L. Pauling, *J. Am. Chem. Soc.* 51 -1929 1010
- A. Pautrat, W. Kobayashi, *EPL* 97 -2012 67003
- A. Pautrat, W. Kobayashi, *EPL* 97 -2012 67003
- J.P. Perdew, K. Burke, M. Ernzerhoff, *Phys. Rev. Lett.* 77 -1996 3865
- P.F. Peterson, M. Gutmann, T. Proffen, S.J.L. Billinge, *J. Appl. Crystallogr.* 33 -2000 1192
- P.Y. Piffard, M. Dion, M. Tournoux, *Acta Crystallogr. Sect. B Struct. Crystallogr. Cryst. Chem.* B34 -1978 366
- P.Y. Piffard, M. Tournoux, *Acta Crystallogr. Sect. B Struct. Crystallogr. Cryst. Chem.* B35 -1979 1450
- T. Proffen, T. Egami, S.J.L. Billinge, A.K. Cheetham, D. Louca, J.B. Parise, *Appl. Phys. A* 74 -2002 s163.
- X. Qiu, J.W. Thompson, S.J.L. Billinge, *J. Appl. Crystallogr.* 37 -2004 678
- Anthony R. West, *Solid State Chemistry and Its Applications*, Second, John Wiley & Sons. Ltd., West Sussex, 2014
- H.M. Rietveld, *J. Appl. Crystallogr.* 2 -1969 65
- J. Rodríguez-Carvajal, *Phys. B Condens. Matter* 192 -1993 55
- J.A. Russell, *Measurement of Optical Bandgap Energies of Semiconductors*, 2011
- S. Saitzek, Z. Shao, A. Bayart, A. Ferri, M. Huvé, P. Roussel, R. Desfeux, *J. Mater. Chem. C* 2 -2014 4037
- H.-Y. Sang, J.-F. Li, *J. Alloys Compd.* 493 -2010 678
- I. Schellenberg, T. Nilges, R. Pöttgen, 67 -2008 1
- O.F. Schirmer, *Solid State Commun.* 18 -1976 1349
- N. Schrewelius, *Zeitschrift Fur Anorg. Chemie* 238 -1938 241
- P. Seminario, *Modern Density Functional Theory: A Tool for Chemistry*, Elsevier, New York, NY, 1995
- R.D. Shannon, *Acta Crystallogr. Sect. A Found.* 32 -1976 751
- I.L. Shul, N.N. Kolpakova, M.P. Shcheglov, A.O. Lebedev, *Tech. Phys. Lett.* 25 (1999).
- J. Singh, S. Uma, *J. Phys. Chem. C* 113 -2009 12483
- D.S. Sivia, *Elementary Scattering Theory for X-Ray and Neutron Users*, Oxford University Press, 2011
- D.A. Skoog, F.J. Holler, S.R. Crouch, *Principles of Instrumental Analysis*, Sixth, Thompson Higher Education, Belmont, CA, 2007
- A.W. Sleight, *Inorg. Chem.* 7 -1968 1704

- A.W. Sleight, *Mater. Res. Bull.* 4 -1969 377
- A.W. Sleight, *Mat. Res. Bull.* 9 (1974) 1437.
- J.P. Smit, P.C. Stair, K.R. Poeppelmeier, *Chemistry* 12 -2006 5944
- G.A. Smolensky, N.N. Krainik, V.A. Trepakov, A. V. Babinsky, *Ferroelectrics* 26 -2011 835
- D.J. Stewart, O. Knop, C. Ayasse, F.W.D. Woodhams, *Can. J. Chem.* 50 -1972 690
- M.A. Subramanian, G. Aravamudan, G.V. Subba Rao, *Prog. Solid State Chem.* 15 -1983 55
- S.M. Sze, K.N. Kwok, *Physics of Semiconductor Devices*, John Wiley & Sons. Ltd., 2008
- I.N. T. Ishida, K. Kanoda, H. Mazaki, *Phys. Rev. B Condens. Matter Mater. Phys.* 29 -1984 1183
- M. Tachibana, K. Fritsch, B.D. Gaulin, *J. Phys. Condens. Matter* 25 -2013 435902
- M. Tachibana, K. Fritsch, B.D. Gaulin, *J. Phys. Condens. Matter* 25 -2013 435902
- J. Telser, *Pers. Commun.* (2012).
- R. Tilley, *Understanding Solids: The Science of Materials*, John Wiley & Sons. Ltd., West Sussex, 2004
- B.H. Toby, *J. Appl. Crystallogr.* 34 -2001 210
- T. Toriyama, M. Watanabe, T. Konishi, Y. Ohta, *Phys. Rev. B* 83 -2011 195101
- T. Toriyama, M. Watanabe, T. Konishi, Y. Ohta, *Phys. Rev. B* 83 -2011 195101
- International Union of Crystallography, <http://www.iycr2014.org/> (2014).
- B. van Akin, A. Meetsma, T. Palstra, *Acta Crystallogr. Sect. C Cryst. Struct. Commun.* 57 -2001 230
- B. van Akin, A. Meetsma, T. Palstra, *Cond. Mat.* -2001 106298
- B. van Akin, A. Meetsma, T. Palstra, *Acta Crystallogr. Sect. E Struct. Reports Online* 57 -2001 87
- J.K.R. Weber, C.J. Benmore, a. N. Taylor, S.K. Tumber, J. Neuefeind, B. Cherry, J.L. Yarger, Q. Mou, W. Weber, S.R. Byrn, *Chem. Phys.* 424 -2013 89
- A.R. West, *Basic Solid State Chemistry*, 2nd ed., John Wiley & Sons. Ltd., New York, 1999
- A.R. West, *Solid State Chemistry and Its Applications*, Second, John Wiley & Sons. Ltd., West Sussex, 2014
- M. Winterer, *J. Appl. Phys.* 88 -2000 5635
- J.B. Wooten, G.G. Long, L.H. Bowen, *J. Inorg. Nucl. Chem.* 36 -1974 2177
- H.L. Yakel, W.C. Koehler, E.F. Bertaut, E.F. Forrat, *Acta Crystallogr.* 16 -1963 957
- N. Yan, X.Q. Liu, L. Zhang, Z. Zhang, X.D. Han, *Chem. Phys. Lett.* 556 -2013 108
- K. Yanagawa, Y. Ohki, T. Omata, H. Hosono, N. Ueda, H. Kawazoe, *Jpn. J. Appl. Phys.* 33 -1994 L238.
- M. Yasukawa, H. Hosono, N. Ueda, H. Kawazoe, *Solid State Commun.* 95 -1995 399

## APPENDICES

## Appendix A

### Investigation of the Local Cation Environments in Thin Films of Amorphous IGZO

#### Abstract

The structure of thin films of amorphous  $\text{InGaZnO}_4$  (IGZO) for electronic applications has been studied through Reverse Monte Carlo modeling. Despite the use of consistent synthesis conditions, it is found that sample-to-sample structural variations for thin films are large. As a result modeling has been performed on the X-ray PDF only. It is observed that the amorphous structure retained similar local environments to that of crystalline IGZO, and characterization of longer range correlations requires additional datasets to constrain the fit.

#### A.1 Introduction to Amorphous IGZO

$\text{InGaZnO}_4$  crystallizes in the  $\text{YbFe}_2\text{O}_4$  structure with space group symmetry  $R\bar{3}m$ . [1] Single crystals with the formula  $\text{InGaZnO}_3(\text{ZnO})_5$  were implemented into TFTs in 2003, and amorphous thin films of IGZO were soon reported that exhibited high mobility ( $8.3 \text{ cm}^2/\text{Vs}$ ) and flexibility, laying the foundation for implementation into modern electronic devices. [2,3] With a maximum reported mobility of  $26.85 \text{ cm}^2/\text{Vs}$ , IGZO films are being incorporated in to electronics from name brand companies including Samsung and LG Electronics. [4–6]

While there is a plethora of literature on the transport properties and device performance of IGZO, little has been done to understand the structure of these amorphous films. Hosono et al. presented work on XAFS data in conjunction with *ab initio* calculations, revealing that the short range ordering and coordination structures in amorphous IGZO are similar to those in the crystalline material, and that a degree of the the edge-sharing structures of In-O polyhedral remain intact. [7] Other XAFS work by Cho et

al. reports local coordination environments of  $\text{ZnO}_5$ ,  $\text{GaO}_5$ , and  $\text{InO}_6$ , maintaining a similar local motif to that found in the crystalline material.[8] This work found the  $\text{ZnO}_5$  trigonal bipyramids to be highly distorted, but did not provide any information on the mid- to long-range order of the samples.

The broad literature on IGZO highlights the range of properties that can be observed based on synthesis route, which highly influences the degree of structural disorder present in these samples. Therefore, a detailed study on the local-, mid-, and long-range order of this promising material is needed for streamlining further technological advancements. This appendix presents work performed on the analysis of PDF data collected on amorphous films of  $\text{InGaZnO}_4$  and the subsequent modeling through Reverse Monte Carlo (RMC) simulations.

## **A.2 Structural Characterization**

### *A.2.1 Qualitative Analysis of the Experimental PDFs*

Both X-ray and neutron total scattering data was collected on exfoliated films of IGZO, and this exfoliation process is detailed in Section A1.5. The high acquisition speed of the 1D area detector on the synchrotron beam line allowed for time-resolved variable X-ray data in addition to measurements at ambient temperatures.[9] The variable temperature synchrotron PDFs are shown in Figure A.1. Two major qualitative observations can be made from the variable temperature data: 1) below 5 Å, the peaks are retained throughout the annealing process and 2) above 5 Å, the peak positions at room temperature are similar to those at 750 C, just broader in distribution. The first observation suggests that the basic polyhedral units in crystalline IGZO are retained in this amorphous phase, and the second observation suggests a relaxation of the crystalline cell is an appropriate model for the room temperature data.

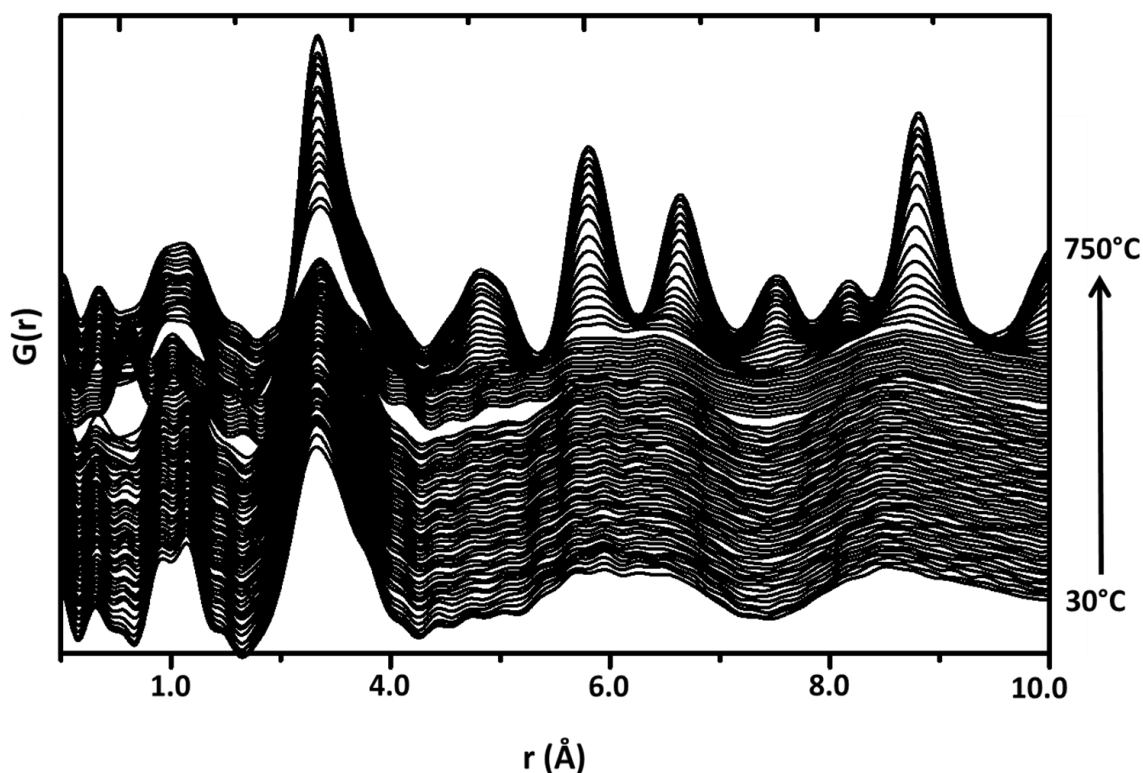


Figure A.1 Overlay of the variable temperature synchrotron PDF for an amorphous film of IGZO. The sample was heated at a ramp rate of 10°C/min up to 750°C, and data was collected every minute.

A comparison of the simulated crystalline partial PDFs and the experimental data (30 °C and 750 °C) can be seen in Figure A.2. It can be observed that the first peak in the PDF is comprised entirely of M-O partials, and the relative intensity compared to other peaks is a result of the insensitivity of X-ray radiation to oxygen-dependent partials. The similarities in intensity and peak position further indicate that the local coordination environments surrounding the metal cation remains relatively constant during the transition from an amorphous to crystalline phase. The second peak in the PDF is largely comprised of M-M partial contributions. The room temperature data is similar to that of the crystallized sample, but the slightly broader distribution and lower intensity is indicative of imperfect translational symmetry in the material, and it is at this point in the  $r$ -range where a relaxation of the crystal structure is observed. Due to X-ray scattering, the remaining peaks in higher  $r$ -ranges provide observations of primarily M-M

correlations. In the amorphous data, the maximum correlations are seen at  $\sim 5.7$ ,  $6.4$ , and  $8.5$  Å. The most notable change from the amorphous to crystalline data in this range is the resolved contributions of Ga/Zn-In correlations in the latter, whereas in the former it is impossible to resolve any of the contributing partials. These quantitative observations can be used to help analyze the simulation results.

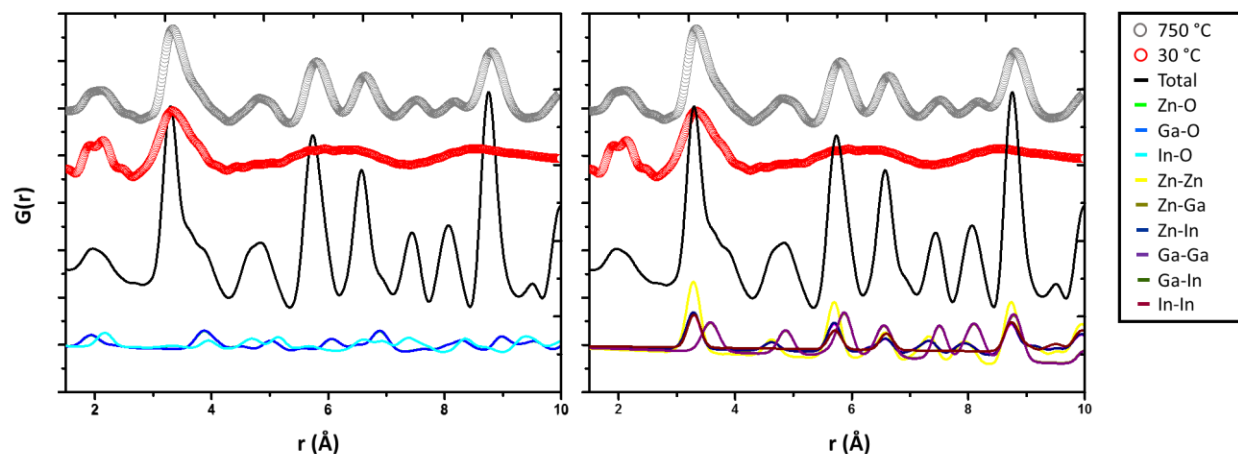


Figure A.2 Comparison of the simulated crystalline M-O partials (left) and M-M partials (right) to the experimental data collected at 30 °C and 750 °C. Simulated total and partial PDFs are represented by lines and experimental data by open circles. Zn-O partials fall directly underneath the Ga-O partials due to same site-occupancy in the crystal structure.

In contrast to crystalline materials, sample variability presents a major obstacle in the analysis of amorphous films of the same composition. While it seems reasonable for this to be the case between samples made through different synthesis routes (for example, vapor deposition vs. prompt inorganic condensation), differences in the X-ray and Neutron PDFs (Figure A.3) indicate this is also true for samples prepared under the same synthesis conditions. Due to the nature of the synthesis process, only small sample sizes (less than 20 mg) can be obtained for analysis, which necessitated the preparation of two samples for the two different experiments. It is evident that there is substantial variation in the samples. It can be observed that the X-ray PDF exhibits longer range correlations than the neutron PDF, evidenced by the presence of peaks at higher  $r$ -ranges, indicating that the sample prepared for X-ray PDF has more

mid-range ordering. Discrepancies in the data sets are not likely from differences in the scattering source, as all correlations should be strongly present in the neutron data due to the neutron scattering ability of the elements (5.8 fm for O, 5.6 fm for Zn, 7.2 fm for Ga, and 4.06 fm for In).[10] It is more likely that differences are arising from either variations in the preparation of the thin films (e. g. minor atmospheric variations in the deposition chamber) or during the film lift-off procedure for measurement preparation (e. g. deuterated acetone solvent for neutron experiments). This illustrates that even with the same preparation parameters, sample variation in amorphous materials is possible and the same sample should be used for experiments if at all possible.

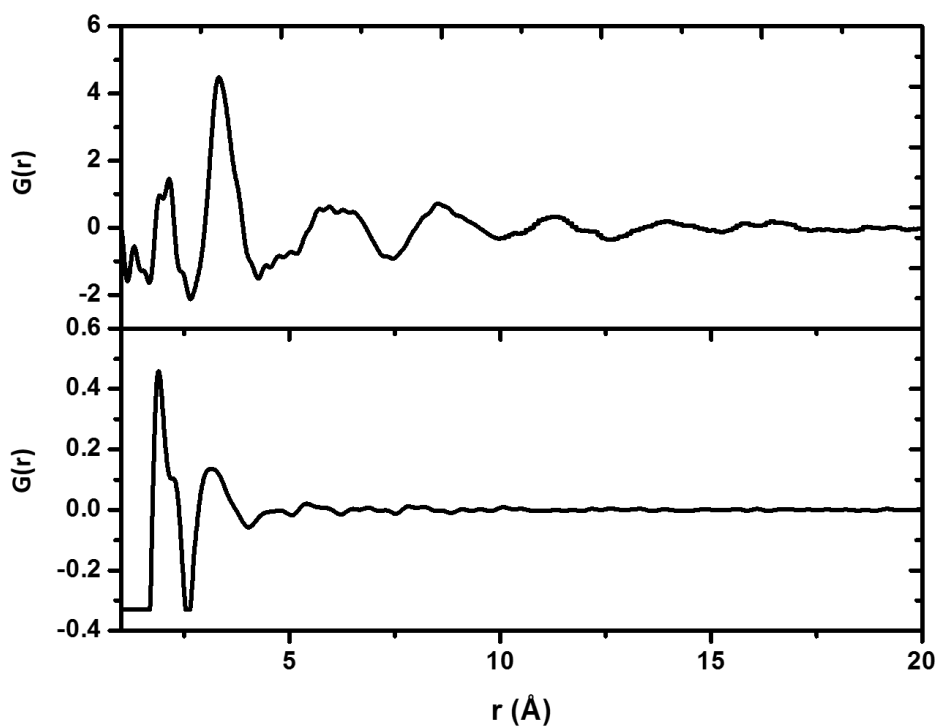


Figure A.3 Comparison of the X-ray (top) and neutron (bottom)  $G(r)$  reveals the X-ray sample has more peaks present in the higher- $r$  range, indicating more mid-range order than in the neutron sample.

Based on the differences in the sample, it was concluded that RMC simulations could not be performed simultaneously on both data sets. The following section details the RMC simulations against the X-ray PDF and the resulting configurations.

### A.2.2 Reverse Monte Carlo Simulations

To begin an RMC simulation, a supercell with dimensions large enough to capture the structural disorder in a sample must be generated. To determine an appropriate starting configuration, least squares analysis was performed on the synchrotron diffraction data and PDF collected at 750 °C (Figure A.4). This analysis indicated a good fit with a space group of  $R\bar{3}m$  ( $R_{wp}$  of 7.05%), so the crystalline structure of  $\text{InGaZnO}_4$  was used for supercell generation. A correction for the density of the thin films (~90 % theoretical density) was made by expanding the  $c$ -axis of crystalline IGZO by 10%.

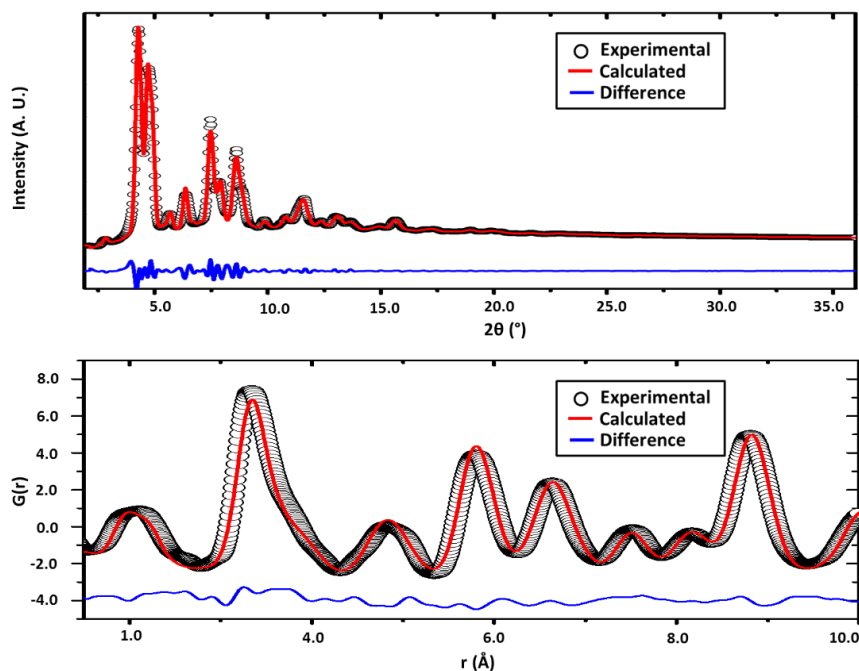


Figure A.4 Least-squares refinements of the synchrotron diffraction (top) and PDF (bottom) data collected at 750 °C on an amorphous film of IGZO.

To obtain similar  $a$ ,  $b$ , and  $c$  parameters for the simulation, a  $17 \times 17 \times 2$  supercell was generated from crystalline IGZO, illustrated in Figure A.5a. For comparison to a disordered starting configuration, a  $2 \times 2 \times 2$  supercell was generated from a randomized structure of IGZO obtained through a Molecular Dynamics (MD) liquid quench procedure (Figure A.5b). To facilitate this comparison, the crystalline and amorphous starting configurations were adjusted to have a similar number of atoms and the same number density ( $\rho_0$ , the number of atoms per  $\text{\AA}^3$ )

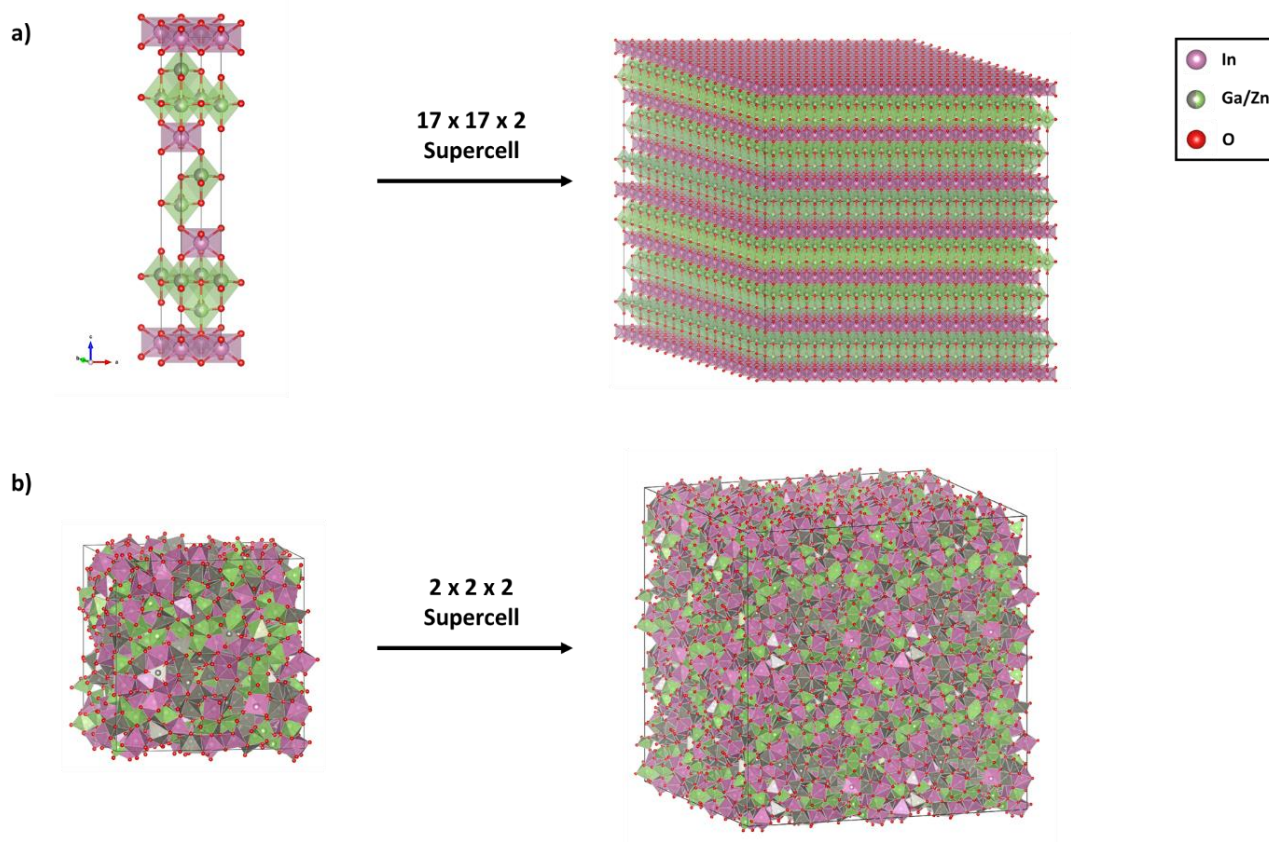


Figure A.5 Starting configurations for RMC simulations generated by creating (a) a  $17 \times 17 \times 2$  supercell of crystalline  $\text{InGaZnO}_4$  and (b) a  $2 \times 2 \times 2$  supercell of a randomized structure of  $\text{InGaZnO}_4$  obtained through MD simulations.

Very similar fits were obtained from the RMC simulations against the crystalline and MD starting configurations (Figure A.6 a and b,  $\chi^2 = 4.12$  and 4.11, respectively). Partial distributions, shown in Figure A.6b and c, show similar M-O partial contributions, with the strongest contribution below than 4.0 Å. These partial M-O correlations indicate that both configurations contain similar metal coordination environments. A quick analysis of the coordination number (CN) distributions for both models yield similar average CNs: 4.22 for Zn, 4.34 for Ga, and 5.67 for In from the crystalline simulation and 4.21 for Zn, 4.38 for Ga, and 5.73 for In from the MD simulation. A major difference in the two partials arises from the In-dependent partials: Zn-In, Ga-In, and In-In. These partials exhibit stronger correlations at high-r in the crystalline simulation, and this can be explained by visualizing the final configurations (Figure A.6e and f). The In-O layers are still retained in the crystalline model, and this gives rise to the high-r correlation; in the MD simulation, the InO<sub>6</sub> are randomly distributed throughout the supercell, and this remains present in the final model.

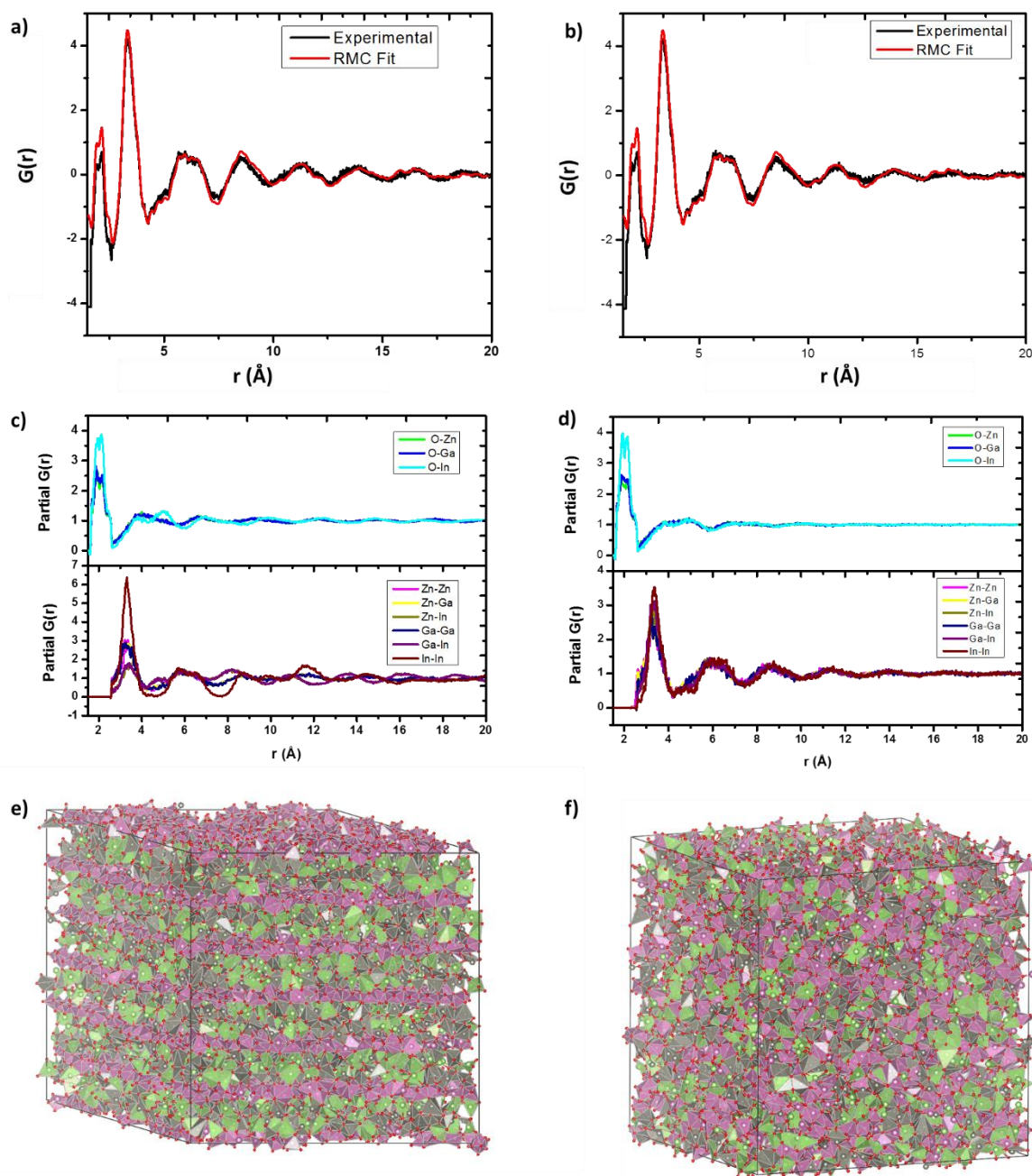


Figure A.6 Total RMC fit against the X-ray PDF of an amorphous IGZO film with a crystalline starting configuration (a) and a MD starting configuration (b). Calculated partials from the crystalline (c) and MD fit (d), and final configurations obtained from the crystalline (e) and MD (f) fit.

### A.3 Discussion and Future Directions

With RMC modeling, it is quite possible to obtain good fits of experimental data regardless of the starting configuration. The independent simulations against a crystalline and MD starting configuration illustrate the importance of including multiple data sets. However, it is equally important to ensure that multiple data sets are collected on the same sample. Several constraints were attempted in the simulations, including minimum approach distances, coordination number and bond valence constraints, but even with the inclusion of these, similar results were obtained for both starting models. In both situations, chemically realistic structures were obtained with distinct differences in the mid- to long-range order. In order to obtain the “true” structure of these amorphous materials, more rigorous constraints in the form of multiple data sets need to be applied.

In the RMC simulations of crystalline data, it is often common to simultaneously fit the diffraction and PDF data. The diffraction data provides a constraint to the long range order, but as amorphous materials do not provide meaningful diffraction patterns, another source of mid-to long range constraints must be applied. Simultaneous fitting of both X-ray and neutron PDF data to a high  $r$ -range (at least 20 Å) can provide this, and including XAFS, NMR, IR, or Raman data can provide constraints on the local order. Investigations employing STEM may help give sight into the mid-range order of the materials, and could provide a further constraint for the RMC simulation. Future studies should incorporate as many of these corroborating experiments as a means of minimizing the RMC solution space, and will lead to more accurate determination of realistic amorphous structures in IGZO and related materials.

#### A.4 Conclusions

The structure of amorphous IGZO was investigated through RMC modeling against experimental X-ray PDF data. Both crystalline and MD supercells were used as starting configurations for the simulations. A similar fit was obtained for both starting models, but differences in the mid-range ordering of the final configurations illustrates the necessity for simultaneous modeling of multiple data sets. Once incorporated, a more feasible solution of the room-temperature structure of IGZO can be determined, which will lead to more accurate calculations of the electronic structure and subsequent analysis of the structure-property relationships in this up-and-coming material.

#### A.5 Materials and Methods

1 x 1 inch samples of PMMA on Si substrates were prepared and placed into the AJA Orion 5 system. Deposition of IGZO was performed via radio frequency (RF) sputtering, where an RF power of 75 W was used on a two-inch target at a frequency of 13.56 MHz. A deposition process pressure of 5 mTorr with an Ar:O<sub>2</sub> ratio of 9:1 was maintained for the duration of IGZO sputtering. Composition of the sputtering target used was InGaZnO<sub>4</sub>.

Samples were prepared for PDF analysis through exfoliation of the thin films by submersion in acetone (deuterated acetone was used for the neutron sample to avoid effects due to incoherent scattering of hydrogen) to dissolve the PMMA layer between the sample and the Si substrate. Once exfoliated, the films were drawn through a Kapton capillary while suspended in acetone. For the X-ray PDF, samples remained in the Kapton capillaries and were allowed to dry. For the neutron PDF, samples were then transferred from the Kapton to a quartz capillary and allowed to dry. A total of 12 1 x 1 inch samples were used for each measurement, resulting in a total sample mass of ~10 mg.

Room temperature neutron PDF measurements were collected on the NOMAD beam line at the Spallation Neutron Source, Oakridge National Laboratory. A  $Q_{\max}$  of  $18 \text{ \AA}^{-1}$  was selected to balance between resolution and termination ripples in the reduced data, and further details of the reduction process are described elsewhere. [11] An empty quartz capillary was collected and subtracted as background.

Variable temperature synchrotron X-ray PDF measurements were collected on the 11-ID-B beam line at the Advanced Photon Source, Argonne National Laboratory with a photon wavelength of  $0.2114 \text{ \AA}$ . Corrections to obtain the  $S(Q)$  and subsequent Fourier Transform with a  $Q_{\max}$  of  $24 \text{ \AA}^{-1}$  to obtain the  $G(r)$  was performed using the program PDFgetX2. [12] An empty Kapton capillary was collected and subtracted as background.

The unit cell obtained from the MD liquid quench was performed using the General Utility Lattice Program (GULP). A total of 243 formula units of  $\text{InGaZnO}_4$  were randomly placed inside a box, which was then ran for 10 ps at 4000 K to equilibrate the atomic positions. The box was then quenched at 300 K at a rate of 100 K/ps, and finally ran for 10 ps at 300 K. Pair potentials used for the simulation are in the process of publication and were produced via a similar methodology to that of Pedone et al. [13]

Peak indexing was performed on the synchrotron diffraction data collected at  $750 \text{ }^\circ\text{C}$  through the Le Bail method using the GSAS software and EXPGUI user interface. [14–16] Fit of the PDF of the  $750 \text{ }^\circ\text{C}$  data was performed using the PDFgui software package. [17] Reverse Monte Carlo measurements were performed with RMCProfile software package. [18] RMC fits were performed against a  $17 \times 17 \times 2$  supercell with 12,138 atoms generated from crystalline IGZO and a  $2 \times 2 \times 2$  supercell with 13,608 atoms generated from the MD cell. Minimum pair approach distances were applied to prevent bond distances less than  $1.65 \text{ \AA}$  for Zn/Ga/In-O. Runs were performed with maximum translational steps of  $0.6 \text{ \AA}$  for each atom, alternated with Ga/Zn swapping attempts. A typical simulation was run for approximately 4,000,000 steps over a six hour period.

## A.6 References

- [1] N. Kimizuka, *J. Solid State Chem.* 203 (1985) 2.
- [2] T. Kamiya, K. Nomura, H. Hosono, *Sci. Technol. Adv. Mater.* 11 (2010) 044305.
- [3] K. Nomura, H. Ohta, K. Ueda, T. Kamiya, M. Hirano, H. Hosono, *Science* 300 (2003) 1269.
- [4] J.-S. Park, T.-W. Kim, D. Stryakhilev, J.-S. Lee, S.-G. An, Y.-S. Pyo, D.-B. Lee, Y.G. Mo, D.-U. Jin, H.K. Chung, *Appl. Phys. Lett.* 95 (2009) 013503.
- [5] M. Ito, M. Kon, C. Miyazaki, N. Ikeda, M. Ishizaki, R. Matsubara, Y. Ugajin, N. Sekine, *Phys. Status Solidi* 205 (2008) 1885.
- [6] H.-N. Lee, J. Kyung, M.-C. Sung, D.Y. Kim, S.K. Kang, S.-J. Kim, C.N. Kim, H.-G. Kim, S.-T. Kim, *J. Soc. Inf. Disp.* 16 (2008) 265.
- [7] K. Nomura, T. Kamiya, H. Ohta, T. Uruga, M. Hirano, H. Hosono, *Phys. Rev. B* 75 (2007) 035212.
- [8] D.-Y. Cho, J. Song, K.D. Na, C.S. Hwang, J.H. Jeong, J.K. Jeong, Y.-G. Mo, *Appl. Phys. Lett.* 94 (2009) 112112.
- [9] P.J. Chupas, K.W. Chapman, P.L. Lee, *J. Appl. Crystallogr.* 40 (2007) 463.
- [10] A. Munter, NIST Center for Neutron Research Neutron Scattering Lengths and Cross Sections, <http://www.ncnr.nist.gov/resources/n-Lengths/>, 2011.
- [11] J. Neufeind, M. Feygenson, J. Carruth, R. Hoffmann, K.K. Chipley, *Nucl. INSTRUMENTS METHODS Phys.* 287 (2012) 68.
- [12] X. Qiu, J.W. Thompson, S.J.L. Billinge, *J. Appl. Crystallogr.* 37 (2004) 678.
- [13] A. Pedone, G. Malavasi, M.C. Menziani, A.N. Cormack, U. Segre, *J. Phys. Chem. B* 110 (2006) 11780.
- [14] A. Le Bail, *Powder Diffr.* 20 (2005) 316.
- [15] B.H. Toby, *J. Appl. Crystallogr.* 34 (2001) 210.
- [16] A.C. Larson, R.B. Von Dreele, Los Alamos Nat. Lab. Rep. LAUR (1994) 89.
- [17] C.L. Farrow, P. Juhas, J.W. Liu, D. Bryndin, E.S. Božin, J. Bloch, T. Proffen, S.J.L. Billinge, *J. Phys. Condens. Matter* 19 (2007) 335219.
- [18] M.G. Tucker, D.A. Keen, M.T. Dove, 335218 (n.d.).

## APPENDIX B:

### Thermoelectric Characterization of Tetrahedrites $\text{Cu}_{10}\text{TM}_2\text{Sb}_4\text{S}_{13}$ (TM = Mn, Fe, Co, Ni, Zn)

#### Abstract

Electrical and thermal transport properties of tetrahedrites  $\text{Cu}_{10}\text{TM}_2\text{Sb}_4\text{S}_{13}$  (TM = Mn, Fe, Co, Ni, Zn) have been evaluated as potential thermoelectric materials. Of the transition metals studied, substitution with Mn exhibited the highest ZT. Therefore, the series  $\text{Cu}_{12-x}\text{Mn}_x\text{Sb}_4\text{S}_{13}$  ( $0 \leq x \leq 2$ ) was investigated to tune the ZT. Changing the Mn concentration to  $\text{Cu}_{11}\text{MnSb}_4\text{S}_{13}$  produces the highest ZT of 1.13 at 575 K. The relatively high value is attributed to a favorable balance between a low thermal conductivity and a relatively high power factor.

#### B.1 Introduction

##### *B.1.1 Introduction to Thermoelectricity*

A thermoelectric (TE) material converts thermal energy to electrical energy by utilizing a thermal gradient to produce an electric potential, or vice-versa. These materials have numerous applications as electric generators and heating/cooling systems. While TE materials present a promising solution to grand energy problems faced by the world, practical utilization is limited by material efficiencies. The conversion efficiency of a TE material is often described by a dimensionless figure of merit, ZT.[1] The ZT is a temperature-dependent quantity that depends on several material properties, as seen in Equation 1:

$$ZT = \frac{S^2 \sigma T}{\kappa}$$

To optimize ZT, a material must exhibit a high electrical conductivity and Seebeck coefficient (together referred to as the power factor) while simultaneously possessing a low thermal conductivity. This balance presents a challenge for the design of optimized thermoelectric materials, and several solutions have been presented in the literature. As a result of this challenge, the ZT of commercial TE materials has hovered around 1, despite the fact that theoretically there is no upper limit. One solution to this challenge is to utilize a structure that promotes a low thermal conductivity through phonon scattering while still maintaining a network for high conductivity. An example of a structure that exhibits these characteristics is the tetrahedrite structure, which provides a promising counter-balance between thermal and electrical conductivity.

### *B.1.2 The Tetrahedrite Structure*

The tetrahedrite  $\text{Cu}_{12}\text{Sb}_4\text{S}_{13}$  crystallizes in a cubic structure with space group  $I4\bar{3}m$ , shown in Figure B.1a.[2] The structure can be described as a sphalerite-like framework of corner-shared  $\text{CuS}_4$  distorted tetrahedra containing large cavities that are occupied by isolated structural units of  $\text{CuS}_3$  and  $\text{SbS}_3$  groups, illustrated in Figure B.1b. The  $\text{CuS}_4$  framework maintains the interconnected framework needed for high conductivity while the asymmetrically coordinated Cu and Sb in the isolated cavity groups act as phonon scattering centers, promoting low thermal conductivity.[3]

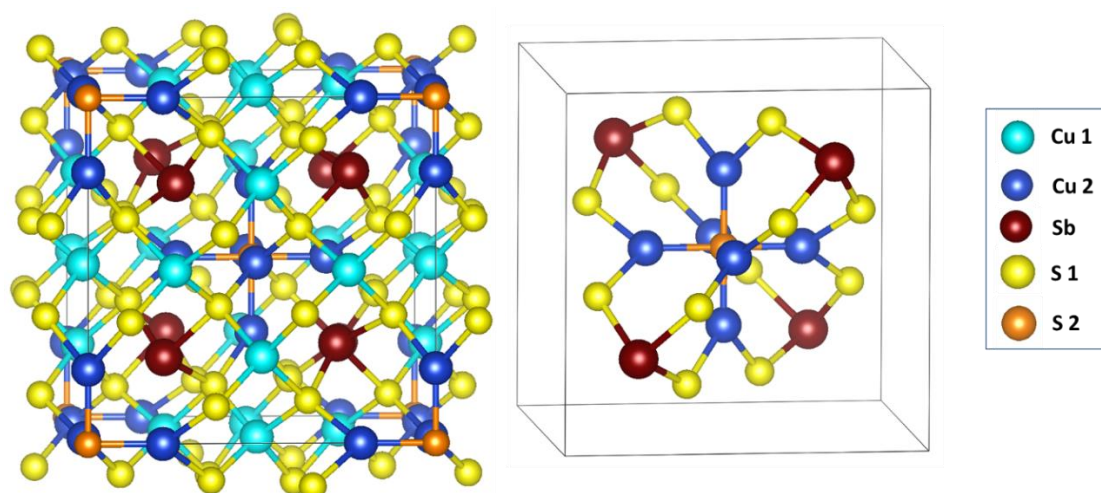


Figure B.1 Crystal structure of the tetrahedrite,  $\text{Cu}_{12}\text{Sb}_4\text{S}_{13}$  and b) isolated  $\text{CuS}_3$  and  $\text{SbS}_3$  polyhedron.

Recent thermoelectric evaluation of tetrahedrite derivatives containing Fe, Ni, and Zn have been reported to exhibit a maximum ZT of 0.95 at 700 K, exhibiting these materials are comparable to current conventional materials.[3–6] This appendix presents the characterization of the thermoelectric properties of  $\text{Cu}_{10}\text{TM}_2\text{Sb}_4\text{S}_{13}$  (TM = Mn, Fe, Co, Ni, Zn), revealing that a relatively high ZT can be achieved at modest temperatures through tuning the amount of TM present.

## B.2 Results and Discussion

### B.2.1 Electrical Properties

A broad range in the conductivity and Seebeck coefficients are observed for the series (Figure B.2b and c), indicating a large degree of property tunability based on the transition metal present. Of the series,  $\text{Cu}_{12}\text{Sb}_4\text{S}_{13}$  exhibits the highest power factor (Figure B.2c), and this is attributed to elevated conduction due to mixed valency of Cu. The Low power factors observed in Zn arises from complete valence band filling due to the  $d^{10}$  electronic configuration of Zinc, making this sample an intrinsic semiconductor with reduced conductivity. The reduced power factor of the Fe-substituted sample cannot be attributed to

band-filling, and it is proposed that the reducing power of  $\text{Fe}^{2+}$  may be resulting in hole trapping, and further lowering of the conductivity may be due to localized impurity scattering. Of the substituted samples, Mn displayed the highest power factor. When substituted into the tetrahedrite lattice  $\text{Mn}^{6+}$  is in a high-spin configuration, confirmed through low temperature magnetic susceptibility measurements. Diffuse reflectance measurements indicate a band gap of  $\sim 1.8$  eV, lower than the rest of the TM samples, giving rise to easier thermal excitation and higher conductivity.

All measured Seebeck coefficients are positive, indicating that holes are the minority carries in all samples. The highest Seebeck coefficient is observed in the Zn-substituted sample due to its intrinsic semiconducting nature, but a reduced power factor for this sample is observed due to the major suppression of the conductivity. There is no appreciable trend in the Seebeck coefficient across the transition metal series, indicating that the varying behavior is likely due to changes in the orbital overlap near the band edges, band filling near the Fermi level, and reduction potential of the various metals.

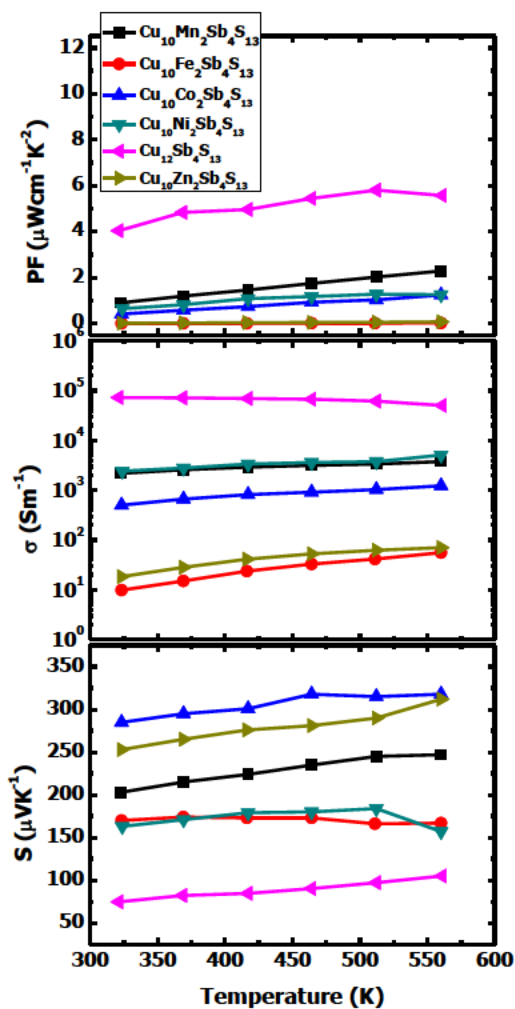


Figure B.2. Temperature dependences of (a) power factor (PF), (b) electrical conductivity ( $\sigma$ ), and (c) Seebeck Coefficient (S) for  $\text{Cu}_{10}\text{TM}_2\text{Sb}_4\text{S}_{13}$  (TM = Mn, Fe, Co, Ni, Cu, Zn).

### B.2.2 Thermal conductivity

A low thermal conductivity of  $\sim 1.1$  W/mK (Figure B.3a) is observed in the parent compound  $\text{Cu}_{12}\text{Sb}_4\text{S}_{13}$  and is in good agreement with the work of Lu et Al.[3] Upon substitution with various transition metals this value is decreased even farther. The thermal low conductivity in this structure is attributed to the complex crystal structure and the asymmetric isolated polyhedral units. Substitution further decreases

the thermal conductivity in the sample by creating disorder on the substituted sites. Thermal conductivity arises from two major components: an electronic component arising from heat transport by the carries and a lattice component arising from energy transport by lattice phonons. Isolation of the lattice component (Figure B.3) reveals that this is the main contribution to the transport properties of these samples. This is expected, as the electronic contribution should be low due to the low electronic transport properties.

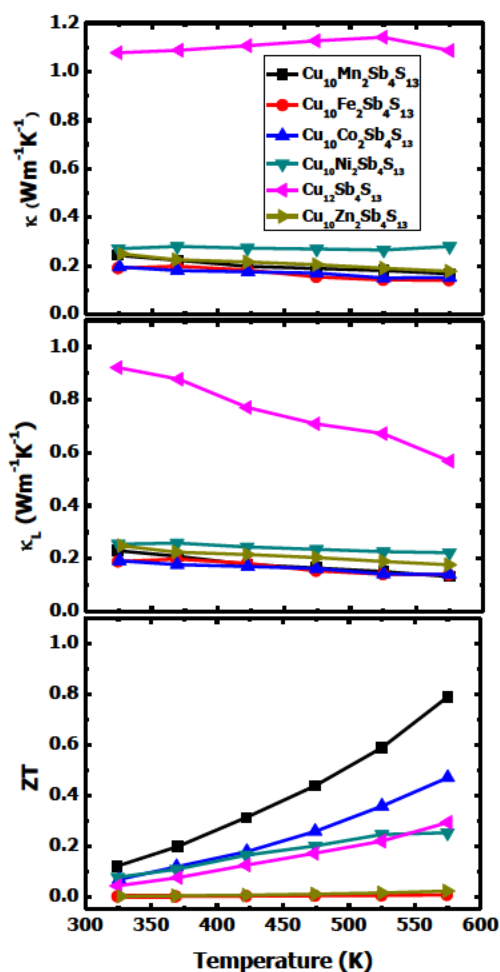


Figure B.3 (a) Total thermal conductivity ( $\kappa$ ), (b) lattice thermal conductivity ( $\kappa_L$ ), and (c) the thermoelectric figure of merit ZT for  $\text{Cu}_{10}\text{TM}_2\text{Sb}_4\text{S}_{13}$  (TM = Mn, Fe, Co, Ni, Cu, Zn) as a function of temperature.

### B.2.3 Figures of merit

Compiling the power factor and thermal conductivity data reveals that the Mn-substituted sample displays a maximum ZT of  $\sim 0.8$  at 575 K (Figure B.3 c). While all samples show low thermal conductivities, the elevated conductivity and resultant power factor at higher temperatures drives an increase in the observed ZT. Due to this elevated ZT, a solid solution  $\text{Cu}_{12-x}\text{Mn}_x\text{Sb}_4\text{S}_{13}$  ( $0 \leq x \leq 2$ ) was investigated to determine the effect of Mn concentration on the thermoelectric properties (Figure B.4). A maximum ZT of 1.13 for the  $x = 1$  sample was observed at 575 K. A plot of the ZT, power factor, Seebeck coefficient, conductivity, and thermal conductivity at 575 K as a function of Mn-content is shown in Figure B.5. A decrease in the thermal conductivity is observed with increasing Mn content along with an increase in the Seebeck coefficient and electrical conductivity. The maximum ZT at  $x = 1$  is attributed to an optimized balance of these correlated properties, and further studies are needed to characterize the detailed orbital compositions near the valence band maximum and conduction band minimum.

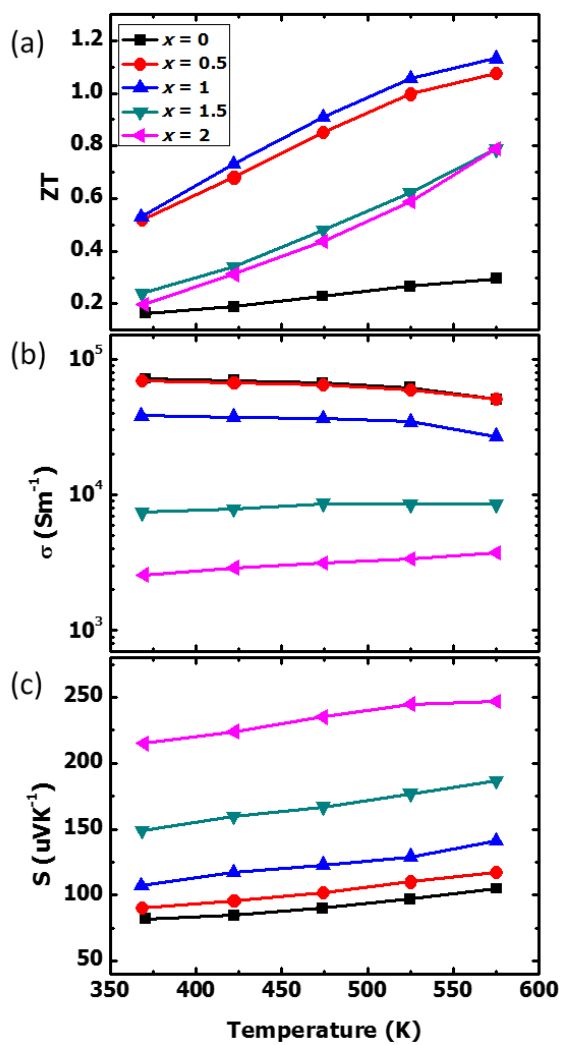


Figure B.4 (a) The thermoelectric figure of merit ZT, (b) electrical conductivity ( $\sigma$ ), and (c) thermopower ( $S$ ) for  $\text{Cu}_{12-x}\text{Mn}_x\text{Sb}_4\text{S}_{13}$  ( $0 \leq x \leq 2$ ) as a function of temperature.

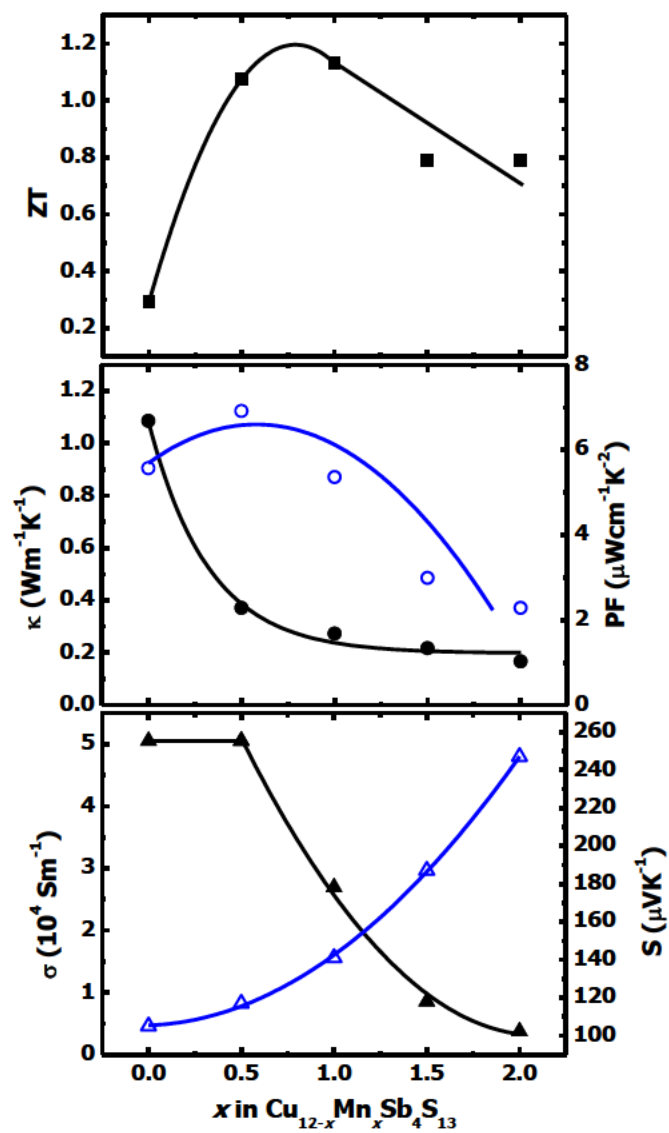


Figure B.5 (a) Thermoelectric figure of merit  $ZT$  (black filled squares), (b) thermal conductivity ( $\kappa$ , black filled circles), power factor ( $PF$ , blue open circles), (c) electrical conductivity electrical conductivity ( $\sigma$ , black filled triangles), and thermopower ( $S$ , blue open triangles) as a function of Mn concentration in  $\text{Cu}_{12-x}\text{Mn}_x\text{Sb}_4\text{S}_{13}$  ( $0 \leq x \leq 2$ ) at 575 K.

### B.3 Conclusion

The tetrahedrite  $\text{Cu}_{12}\text{Sb}_4\text{S}_{13}$  exhibits a low thermal conductivity that is further suppressed through substitution of various transition metals. A wide range in electrical conductivity is observed with the identity of the metal, as well as the Seebeck coefficient. By substitution across a transition metal series, these different electrical properties can be used to tune the overall thermoelectric properties, and as a result the ZT was maximized in the Mn-substituted sample. Subsequent variation of the Mn content in the tetrahedrite structure revealed a maximum ZT of 1.13 at 575 K for  $\text{Cu}_{11}\text{MnSb}_4\text{S}_{13}$ , illustrating that not only identity but concentration of a substituent is vital for the observed properties. This appendix serves as an excellent illustration of how a structure can be manipulated through doping to achieve optimized properties for material applications.

### B.4 Methods and Materials

Polycrystalline samples were synthesized by standard solid-state reaction of appropriate combinations of the elements Mn, Fe, Co, Ni, Cu, Zn, Sb, and S (purity > 99.95 %; Alfa Aesar) and heated at 450 °C for 3 weeks in evacuated, sealed fused-silica tubes. The resulting polycrystalline powders were sintered at 450 °C under 100 MPa pressure in a pellet mold to produce sample densities  $\geq 85$  % of theoretical values. Sample purity was verified through X-ray diffraction data collected on a Rigaku Ultima IV diffractometer with a 0.02 rad slit and Cu  $K\alpha$  radiation ( $\lambda = 1.5418 \text{ \AA}$ ), a step size of  $0.02^\circ 2\theta$ , and a dwell time of 1 s at each step.

Electrical and thermal properties ( $S$ ,  $\sigma$ , and  $\kappa$ ) were measured from 325 to 575 K. The  $S$  and  $\sigma$  data were collected on an ULVAC-RIKO ZEM-3 under a helium atmosphere (instrumental error = 5 %). Thermal diffusivity ( $\alpha$ ) was measured on a Netzsch LFA 457 Micro Flash under flowing  $\text{N}_2$  (instrumental error = 10 %). Upon cooling, the properties were measured again at 325 K to ensure the samples did not degrade or

display hysteresis. Specific heat capacity ( $C_p$ ) was measured for  $\text{Cu}_{12}\text{Sb}_4\text{S}_{13}$  and  $\text{Cu}_{10}\text{Mn}_2\text{Sb}_4\text{S}_{13}$  with a Netzsch DSC-200PC differential scanning calorimeter, and a  $C_p = 0.45 \text{ J g}^{-1} \text{ K}^{-1}$  was found for each sample. This value was used for all samples to calculate  $\kappa$  from the relationship  $\kappa = C_p \times \alpha \times d$ , where  $d$  is the sample bulk density.

Low-temperature magnetic and electrical measurements carried out on a Quantum Design Physical Properties Measurement System (QD PPMS). Magnetic susceptibility data were collected from 5-300 K on warming with a 0.5-Tesla field. Diffuse reflectance measurements collected with a balanced deuterium/tungsten halogen source (DH-2000-BAL) and an Ocean Optics HR400 UV-Vis/IR spectrophotometer. MgO powder (99.95 %, Cerac) was used as a white reflectance standard.

## B.5 References

- [1] Anthony R. West, *Solid State Chemistry and Its Applications*, Second, John Wiley & Sons. Ltd., West Sussex, 2014.
- [2] Bernhardt J. Wuensch, *Zeitschrift Fur Krist.* 119 (1964) 437.
- [3] X. Lu, D.T. Morelli, Y. Xia, F. Zhou, V. Ozolins, H. Chi, X. Zhou, C. Uher, *Adv. Energy Mater.* 3 (2013) 342.
- [4] T.M. Tritt, *Recent Trends in Thermoelectric Materials Research*, Academic, 2001.
- [5] K. Suekuni, K. Tsuruta, T. Ariga, M. Koyano, *Appl. Phys. Express* 5 (2012) 051201.
- [6] K. Suekuni, K. Tsuruta, M. Kunii, H. Nishiate, E. Nishibori, S. Maki, M. Ohta, A. Yamamoto, M. Koyano, *J. Appl. Phys.* 113 (2013) 043712.